A generalized two dimensional quasigeostrophic model of thermal convection

by

Thomas Daniel Laycock

A thesis submitted in partial fulfillment of the requirements for the degree of

Doctor of Philosophy

in

Geophysics

Department of Physics

University of Alberta

Abstract

The processes responsible for generating the mean azimuthal atmospheric winds observed on Jupiter and Saturn, which feature large prograde equatorial jets and jets of alternating direction at higher latitudes, have yet to be conclusively resolved. Results from three dimensional numerical models of thermal convection in a thin spherical shell have supported the theory that they are a surface manifestation of organized flow deep within the planets. While these models have been able to reproduce the general features of the observed zonal flow, computational limits restrict them to parameter regimes many orders of magnitude more modest than those thought to exist in the planets. A more efficient numerical model is required to study this phenomenon at more realistic parameter values, and would permit an investigation of the dependence of the solution on the parameters of the system and initial conditions, as well as the long time scale dynamics of zonal winds. The current thesis takes advantage of the rigid columnar flow structures that are produced by the rapid planetary rotation, as observed in the results of 3D simulations, to develop a two dimensional quasigeostrophic model of the system for a Boussinesq fluid. By averaging the equations of motion over Taylor columns in the axial direction, and simulating the mean variables in a 2D virtual equatorial plane, the essential dynamics can be modeled while collapsing the problem into one fewer dimension. To develop such a model, the standard quasigeostrophic framework, and existing numerical models based upon it, have been generalized to the geometry inside the tangent cylinder which circumscribes the inner spherical boundary of the convecting shell. Here, buoyancy in the axial direc-

tion, which is not considered in the traditional QG framework, is responsible for forcing axial convection and the turbulence which leads to jet generation. Thus, in addition to the traditional QG equations, we must also solve the averaged axial flow equation to model this effect. Numerical simulations of our 2D QG model demonstrate that this approach can capture much of the dynamics of 3D convection. The system variables all have amplitudes which are the same order of magnitude as solutions from full three dimensional models. Additionally, alternating zonal jets similar to those observed on Jupiter can be produced.

Acknowledgements

First and foremost I would like to thank my supervisor, Dr. Mathieu Dumberry, for his support and encouragement throughout the course of my studies at the University of Alberta. The guidance of the two additional members of my supervisory committee, Dr. Moritz Heimpel and Dr. Bruce Sutherland, was also invaluable to keeping my project on track. A particular thanks to Dr. Heimpel for his willingness to share his deep knowledge of my project with me, and for simulating data to which to verify our model against.

Thanks to my officemates and colleges over the years, particularly Martin Veasey, Colin More and Drew Chorney, with whom I've shared many interesting and insightful conversations about science and beyond.

Finally, thanks to my parents for always supporting me.

Table of Contents

List of Tables

List of Figures

Chapter 1

Introduction

The study of convecting fluids under rotation is a very important one due to its wide range of applicability to fields such as geophysics, meteorology, oceanography and astrophysics. Since the Earth, all the other planets of the Solar System and the Sun all spin with periods ranging from fractions of the Earth's day to nearly the Earth's year, understanding problems as diverse as dynamo generation in planetary interiors, to jet formation in the atmospheres of the gas giant planets, to stellar evolution depend on knowledge of how fluids behave under rotation, which turns out to have profound implications on their dynamics [21].

1.1 Convection

Count Rumford was the first to observe in 1797 that when a fluid was heated from below, hot regions would float to the surface and cold regions would sink to the bottom, transporting heat across the fluid layer much more effectively than would be possible exclusively by conduction through a static fluid. Rum-

ford correctly deduced that this motion was being driven by changes in the local density of the fluid with the temperature. Warmer fluid, being less dense and hence more buoyant, rises in a gravitational field and vice versa for cooler fluid [11][68]. We now call this motion thermal convection.

Henri Bénard carried out a number of experiments at the turn of the twentieth century studying the onset of thermal convection in a horizontal fluid layer [7][8], which were subsequently explained theoretically by Lord Rayleigh in 1916 [76]. They found that thermal convection is driven by an unstable thermal gradient, such that the lower fluid is hotter and thus more buoyant than the higher fluid, and is inhibited by the fluid's viscosity. Only for sufficiently large thermal gradients, which are capable of overcoming both the fluid's capacity to conduct heat across the layer and its viscosity inhibiting motion, will convection commence. It was later found that convection can also be driven by other sources of buoyant instabilities, such as variations in chemical composition which lead to changes in density. If the fluid is electrically conductive, convection is referred to as magnetohydrodyamics and in planetary scale systems can lead to the generation of a dynamo, in which the kinetic energy generated by convection is transformed into magnetic energy.

1.2   Fluids under rotation

When fluids in motion are subject to rapid rotation, their dynamics are significantly impacted. Strong Coriolis forces tend to organize flow such that it is invariant parallel to the direction of rotation. This phenomenon was first described by Lord Kelvin in 1868, though he did not publish his results [35]. Several decades later the subject was revisited most notably by Sydney

Samuel Hough, Sir Geoffrey Ingram Taylor and Joseph Proudman, who would provide an explanation for the effect [53][75][92]. It would become known as the Taylor-Proudman theorem after the latter two.

Taylor conducted a number of groundbreaking experiments which demonstrated the consequences of this theorem [91][93][94]. Of particular significance was his observation that if a solid body within a rotating fluid was slowly displaced perpendicularly to the axis of rotation, the entire fluid column parallel to the rotation axis above and below the body was rigidly dragged along with it as if it was a single solid body. These elongated structures, invariant in the axial direction but with small scales perpendicular to the axis of rotation, became known as Taylor columns after him.

The Taylor-Proudman theorem has important implications to the onset of convection. In the 1950s Subrahmanyan Chandrasekhar derived the conditions under which a fluid under rotation could become unstable and begin to convect [23][25][24]. While non-rotating fluids need only overcome their viscosity, the rigidity imposed on a fluid by rotation inhibits convection parallel to the rotation axis and must be broken for convection to begin. This is because convection requires that there be axial variations in the velocity to match boundary conditions. Therefore, under rotation viscosity actually promotes, rather than hinders, the onset of convection since if it is sufficiently large it breaks the Taylor-Proudman rigidity constraint, which strictly only holds for an inviscid fluid.

Paul Roberts considered the related problem of convection within a rotating sphere in the 1960s, though in this case the thermal gradient was supported by internal heat sources rather than applied externally [79][80]. This work was taken up by Friedrich Busse, who extended it to spherical shells in 1970

3

[13][21]. Busse noted that the tangent cylinder (TC), which is coaxial to the axis of rotation and circumscribes the inner boundary of the convection shell, divided the shell into two regions (see figure 2.1) in which the dynamics were starkly different. Inside the TC, convection is approximately equivalent to the Rayleigh-Bénard problem, plane layer convection aligned with the rotation axis, which is suppressed until the Taylor-Proudman theorem is broken. Meanwhile, outside the TC convection is perpendicular to the rotation axis. Here, at the onset of convection columnar structures aligned with the rotation axis, known as Busse rolls, are formed since they are not significantly inhibited by the rigidity constraints of rotation. The non-rigidities required by the interaction of these columnar rolls with the sloping boundaries are balanced by a time dependence of the flow, leading to the rolls drifting in the azimuthal direction. Much lower forcing is required for convection to begin outside the TC. These results were consistent with numerical simulations [41] and experiments [19][20][22].

In experimental studies of this effect an effective gravitational centrifugal forcing is used to drive convection rather than a Newtonian gravitation field. The reason for this is that it is very difficult to generate a sufficiently large gravitational field in the lab with any reasonable volume of mass due to the weakness of the gravitational constant. Provided that the centrifugal gravity is large enough to dominate the Earth's gravitational field, inverting the applied thermal gradient makes this system analogous to convection in a planetary shell, though the gravitational forcing is cylindrical rather than spherical. Formally the systems are only exactly equivalent in the equatorial plane, but the analogue is approximately applicable elsewhere outside the TC where the cylindrical component of the gravitational field is much larger than

4

the axial component.

1.3   2D turbulence

The Taylor-Proudman theorem showed that rapid rotation tends to promote two dimensional structures in a three dimensional system. Aside from rotational systems, 2D turbulent convection has been investigated in a number of inherently 3D systems in which some force plays the role of the Coriolis term in inhibiting the development of a shear in the flow in one direction [90][58]. When a conducting fluid is subject to strong magnetic fields, the frozen flux theorem requires that the flow drags magnetic field lines around with it. Shearing of the flow in the direction parallel to the field induces currents by Lenz's law which in turn produces Lorentz forces that act as a restoring force to the shearing. This effect has been shown to produce 2D flow [62][88][87]. Layerwise 2D flow can be produced if the fluid is strongly stably stratified or has a large aspect ratio [100][26]. The latter is exploited by shallow layer models, widely used to model the dynamics of oceans and the atmosphere [70], which assume that for motion with a wavelength that is much larger that the fluid depth the velocity across the layer must be small relative to its velocity along the layer. These assumptions lead to 2D horizontal motion within the layer.

Due to the extremely complicated nature of fully developed 3D turbulence, 2D turbulence, which is a more tractable problem numerically, is frequently studied to gain insight into turbulence in general [90]. However, there are fundamental differences between 3D and 2D turbulence beyond one fewer dimension. In 1967 Robert Kraichnan proved a unique property of flow in a 2D system [61]. For an unforced incompressible fluid, he showed that in the in-

viscid limit the advection of vortices leads to the energy of the flow cascading from small scales to large scales. This result is a direct consequence of the conservation of both total energy and enstrophy, the square of the vorticity, in 2D. This is quite different than the usual behaviour in 3D where the cascade is from large to small scales. For example, when one stirs a liquid with a large spoon, eddies are spun off from the edges, and those eddies spin off smaller eddies and so on until the kinetic energy is eventually converted to other forms of energy through viscous dissipation at the smallest scales. The difference is that enstrophy is not conserved in 3D due to vortex stretching into the third dimension, which is not possible in 2D.

The inverse cascade predicted by Kraichnan has been observed in both experiments [87][69] and numerical simulations [34][67][9] by continuously forcing a system at small scales. In these systems, large scale viscosity must be included since otherwise the constant injection of energy would lead to energy accumulating at the maximal scale of the system and no steady state ever being reached. Numerical models of fully three dimensional convectively forced systems under rapid rotation have also been shown to undergo an inverse energy cascade, leading to the development of large-scale vortices (LVS) [45][81][32]. Experimental observations suggest that the dominant mechanism of the cascade is not the successive merging of small vortices into larger vortices, as one might naively expect, but rather the clustering of same-signed small vortices such that there are regions of dominantly positive vortices and others of negative vortices [69]. These small correlated vortices act coherently, leading to the large scale structures observed.

1.4 Rhines scaling

When a rotating fluid is driven by some forcing, such as a pressure gradient, flow is deflected either to the right or left with respect to its direction of motion, depending on the sign of the Coriolis parameter f. This parameter appears in the Coriolis term of the Navier-Stokes momentum equation, which arises from the conservation of the fluid's momentum. In general, the value of the Coriolis parameter can depend on a spatial dimension. For example, in a planetary shallow layer model of a spherical shell, the Coriolis parameter varies with latitude due to the changing direction of the local normal. In spherical coordinates, $f = 2\Omega \sin \theta$, where Ω is the planetary angular velocity and θ is the latitude.

With a constant Coriolis parameter, flow is deflected until the Coriolis term forcing the curvature equilibrates with the pressure gradient in a geostrophic balance, which results in steady flow perpendicular to the pressure gradient. For a shallow layer model, expanding about a latitude of θ_0 by a small angular perturbation α gives a Coriolis parameter of

$$
\begin{aligned}
f &= 2\Omega \sin (\theta_0 + \alpha) \\
&= 2\Omega (\sin \theta_0 \cos \alpha + \cos \theta_0 \sin \alpha) \\
&\sim 2\Omega (\sin \theta_0 + \alpha \cos \theta_0) \\
&= f_0 + \beta n,
\end{aligned}
\tag{1.1}
$$

where we have used the angular addition formula and Taylor expanded the result about the value θ_0, keeping up to first order in α. $f_0 = 2\Omega \sin \theta_0$ is the Coriolis parameter at the expansion latitude θ_0, and $n = \alpha R$ is the Carte-

sian coordinate in the northward direction with respect to θ_0, where R is the planetary radius. β is the coefficient of the linear expansion term, and in this prescription is equal to

$$\beta = \frac{2\Omega \cos \theta_0}{R}. \tag{1.2}$$

This parameterization is referred to as the beta-plane approximation.

In this approximation, the Coriolis forcing in the local vertical (aligned with the gravitational field) vorticity equation, which is equal to the curl of the momentum equation, is

$$\left(\boldsymbol{\nabla}_\perp \times \left(f \begin{pmatrix} v_n \\ -v_e \\ 0 \end{pmatrix} \right) \right) \cdot \hat{\mathbf{z}}$$

$$= \left(f\boldsymbol{\nabla} \times \begin{pmatrix} v_n \\ -v_e \\ 0 \end{pmatrix} + \boldsymbol{\nabla}f \times \begin{pmatrix} v_n \\ -v_e \\ 0 \end{pmatrix} \right) \cdot \hat{\mathbf{z}}$$

$$= -v_n \frac{\partial f}{\partial n} = -v_n \beta, \tag{1.3}$$

where v_n and v_e are the velocities in the northward and eastward directions respectively, the derivative with respect to n is a northward directional derivative, z is the coordinate in the local vertical direction, and $\hat{\mathbf{z}}$ is a unit vector pointing in the local vertical. Here the curl in the second line is zero for an incompressible flow. Therefore, for a constant Coriolis parameter (i.e. $\beta = 0$), the Coriolis term does not generate vorticity, but if the Coriolis parameter has some spatial dependence (i.e $\beta \neq 0$) then fluid parcels moving in opposite

8

directions generate vorticity of opposite signs.

It was shown by Peter Rhines in 1976 that for a system under rotation with a Coriolis parameter which varies in one direction, the 2D inverse turbulent energy cascade can only proceed up to a maximal length scale in that direction [78]. This length scale subsequently became known as the "Rhines length" after him. Beyond this scale energy from the cascade is converted into the excitation of Rossby waves, transverse waves whose restoring force is the linear variation of the Coriolis term which is proportional to β.

(a)   (b)
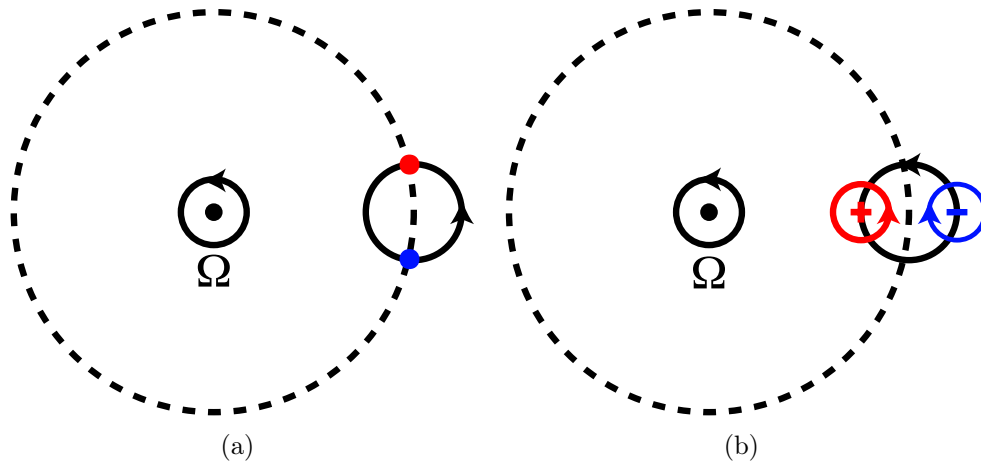
Figure 1.1: The generation of Rossby waves for the case of a Coriolis parameter which depends on the radius from the rotation axis, marked with a black dot, such that $\beta < 0$. The gravitational field forcing convection is pointing away from the axis of rotation. On the left (1.1(a)) two fluid elements located at a reference cylindrical radius, indicated by a dashed line, are highlighted in blue and red. As the fluid circulates around a convection cell (solid line), oppositely signed vorticity is generated depending on its direction of motion, as seen on the right (1.1(b)). The case illustrated is for counterclockwise circulation.

If f varies in a certain direction, when a fluid element in geostrophic balance moves sufficiently far away from its original location in that direction, β leads to the generation of vorticity as illustrated in figure 1.1. The sign of the vorticity generated depends on the sign of β. Fluid elements displaced in

opposite directions generate oppositely signed vorticity. As can be seen in figure 1.2, this vorticity has the effect of forcing neighbouring fluid elements to become displaced in the same direction from the reference cylindrical radius, which then acquire their own vorticity from the beta-effect. In this way, any disturbance to the geostrophically balanced fluid propagates in the form of Rossby waves [17][18]. In the case of figure 1.2, the wave will propagate to the left of the image. On Earth, Rossby waves are frequently seen in the meanders of the jet stream.
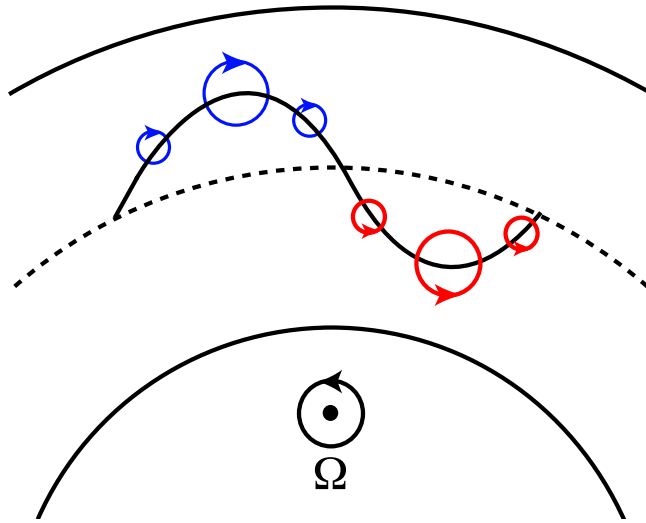
Figure 1.2: The propagation of Rossby waves in the geometry of figure 1.1. The Coriolis parameter depends on the radius from the rotation axis such that $\beta < 0$. The black dot indicates the direction of planetary rotation. Outward moving (blue) and inward moving (red) fluid, originally located at a reference cylindrical radius indicated by a dashed line, generate oppositely signed vorticity, leading to the propagation of Rossby waves. The waves travel to the left in the case of this image.

Rossby waves are only generated if the variation in the Coriolis parameter is sufficiently large, or if the fluid is exploring a large enough range such that it experiences the variation in the Coriolis parameter. Therefore, as the inverse

cascade proceeds, Rossby wave excitation becomes more important. If the non-linear advection terms in the momentum equation are larger than the beta term, the inverse cascade will dominate. However, once structures become large enough such that the beta term dominates, rather than further growing the structures, energy from the cascade will go into the excitation of Rossby waves. This prevents the cascade from continuing indefinitely. The transition occurs when the two terms in the momentum equation are of roughly equal magnitude. For the beta-plane approximation, assuming that the Coriolis parameter varies with latitude and using the evaluation of the beta term in equation 1.3 gives a balance between the advection and beta term in the local vertical vorticity equation of

$$\mathbf{u} \cdot \boldsymbol{\nabla} \omega_z \sim \beta v_n$$

$$v_n k_\beta^2 v_e \sim \beta v_n. \tag{1.4}$$

Here we have assumed that v_e is a large eastward geostrophically balanced flow which only depends on n, which is perturbed by a small northward velocity v_n. The wavenumber in the latitudinal direction at the balance has been defined to be k_β.

Using U as a typical magnitude for the eastward velocity, this balance implies

$$k_\beta^2 \sim \frac{\beta}{U}. \tag{1.5}$$

11

Inverting the wavenumber to get a maximal wavelength, we obtain

$$\lambda_\beta = \frac{2\pi}{Rk_\beta} \sim \frac{2\pi}{R}\sqrt{\frac{U}{\beta}}, \qquad (1.6)$$

where we have divided by the planetary radius R to get an angular wavelength on the planetary surface. There is some ambiguity in this definition, with some authors choosing to neglect the factor of 2π. Thus the limiting angular scale depends on the ratio of the fluid velocity and the gradient of the Coriolis parameter (β) in the beta-plane approximation. Numerical simulations have observed that the beta-effect does indeed act as a barrier limiting further growth of vortices beyond the Rhines length [52][67]. An alternative formulation for the limiting length scale, based on the large scale viscous dissipation, has also been proposed [95][36].

Raymond Hide argued that if a rotating fluid with constant Coriolis parameter undergoing convection is confined within a rigid container, boundary geometry can induces a similar effect to variations of the Coriolis parameter [51]. In 1983 Busse published results which demonstrated this. He studied convection driven by a thermal gradient within a cylindrical shell coaxial to the rotation axis, which was bounded from above and below [15]. When the top and bottom boundaries were flat, rigid Busse rolls effectively transported heat across the shell. However, if the top and bottom of the shell had sloping boundaries, the axial container height varying with cylindrical radius, convection across the shell broke the Taylor-Proudman theorem since the boundary conditions necessitate non-rigidities. Thus, temporal variations in the flow are necessary to balance the non-geostrophic residual forcing. As illustrated in figure 1.3, the shell's slope forces radially displaced fluid columns to adjust

their height as they circulate around a convection cell. To conserve poten-
tial vorticity, which for a Boussinesq fluid in this system is equal to the ratio
of the absolute vorticity to the fluid column depth (see equation 3.85), this
change in column height must be accompanied by a change in vorticity. Thus,
the boundary geometry induces vortex stretching in convecting fluids just as
variations in the Coriolis terms does. For a constant sloping boundary, equal
magnitudes of opposite signed relative vorticity are generated by inward and
outward moving flow.
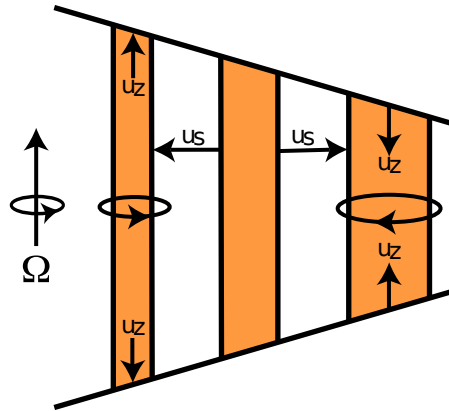
Figure 1.3: Vorticity generation from the topographic beta-effect with constant
sloping boundaries.

Mathematically, this effect leads to a term in the vorticity equation that is
of identical form to the β term from the beta-plane approximation of a varying
Coriolis parameter. In this mechanism it is the fractional change in container
height with cylindrical radius multiplied by the planetary angular rotation rate
that plays the role of the β parameter. To differentiate it from the beta-plane
approximation, it is often termed the topographic beta-effect. Traditionally,
the topographic beta is defined as the geometric factor, with the rotation rate
considered separately. Like the beta-plane β, the topographic β generates

Rossby waves and thus limits the growth of structures. The analogous Rhines length is similar to equation 1.6, with the replacement of the beta-plane β with the product of the topographic β and planetary rotation rate. However, since in this geometry β models variations in cylindrical radius, rather than latitude, the calculated wavelength is also in the cylindrical radial direction and must be projected onto the planetary surface to compare with observations [49]. This gives an extra factor of $\sin\theta$ in the denominator, leading to a Rhines length for a spherical shell of

$$\lambda_\beta \sim \frac{2\pi}{R\sin\theta}\sqrt{\frac{U}{\Omega\beta}}, \tag{1.7}$$

where θ is the latitude.

One final mechanism, adiabatic expansion, can also play a role in Rossby wave generation. It works similarly to vortex stretching, except here radial variations in the equilibrium density profile of the fluid force radially displaced fluid parcels to expand or contract to adapt to the local pressure [54][43][37][97]. Once again, to conserve potential vorticity the fluid's rotation rate must adapt and vorticity is created or quenched. The relative importance of these two processes is not well understood [97].

1.5 Mean flows

In 1981 Ruby Krishnamurti and Louis Howard showed that as the thermal forcing applied across a non-rotating, horizontal fluid layer undergoing cellular convection is increased, a regime is entered which features a turbulent wind [63][12]. This consists of mean flows of opposite directions near the bound-

aries. Random tilting of the convection cells across the fluid layer leads to a correlation of orthogonal velocity components, as seen in figure 1.4. These correlations generate Reynolds stresses that force a mean flow parallel to the boundary.

In the untilted case, as seen in figure 1.4(a), as fluid elements circulate around a given convection cell outward moving fluid parcels (green arrows) have roughly the same radial velocity magnitude but opposite sign as inward moving fluid parcels (red arrows) as they cross a reference depth. Meanwhile, the outward and inward flow's velocity component along the reference depth is of comparable amplitude and the same sign in each cell, so the product of the two velocity components will be of comparable amplitude but opposite sign. Thus, as fluid elements circulate around an untilted convection cell their contributions to the Reynolds stresses, equal to the correlation of the orthogonal velocity components at a given depth, cancel each other. However, once the convection cell is tilted the two contributions no longer cancel. As seen in figure 1.4(b), the magnitude of the components of the velocity for inward and outward moving fluid elements are no longer comparable. This leads to non-zero Reynolds stresses, which forces a mean flow. The mean flow is oriented such that once it is established it tends to tilt the convection cells even further, leading to larger correlations and stronger Reynolds stresses and a positive feedback loop of mean flow generation. These mean flows have been reproduced by numerical simulations [44].

Busse showed that boundary geometry could induce an asymmetry to the system leading to mean flows through the topographic beta-effect [15]. If the generated Rossby waves create a correlation between velocities, the resulting Reynolds stresses force a mean flow which in turn further tilts the convection
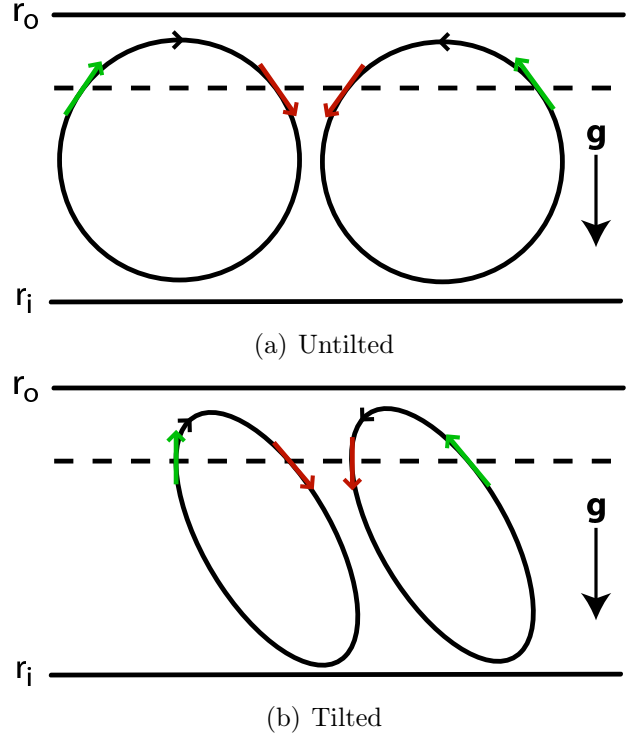
Figure 1.4: The velocity correlations contributing to Reynolds stress for untilted plane layer convection cells on the top (1.4(a)) and tilted plane layer convection cells on the bottom (1.4(b)). The dashed line represents an arbitrary reference depth.

cells. If the boundary has a varying slope as in figure 1.5, so that β is non-uniform, fluid parcels generate different magnitudes of vorticity when moving in opposite directions while circulating around a convection cell, as seen in figure 1.6. In addition to the Rossby wave generation described in the previous section for a constant β, an asymmetry in vorticity generation leads to the tilting of convection cells, such that the tilting axis is aligned with the rotation axis. In the constant-beta case the induced vorticity of circulating fluid elements leads to drifting of the convection cells as a result of the viscous stresses from neighbouring fluid elements. However, if the vorticity generation is non-uniform, then so too is the drift rate since the net viscous stress on a

fluid element from its neighbours will vary. This differential drift rate leads to tilting of the convection cells, which again results in a correlation of velocities, Reynolds stresses and a mean wind. Analogously, the adiabatic expansion beta-effect can also lead to mean wind generation.
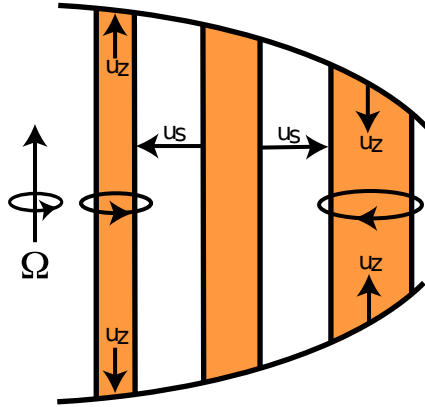
Figure 1.5: Vorticity generation from the topographic beta-effect with boundaries whose slope varies.

There are three distinct regimes of mean wind generation. With moderate thermal forcing, the viscous dissipation is sufficient to prevent the jets from growing too large and a steady state is reached with the forcing of the mean flow in balance with the viscous stresses. If the system is subject to larger thermal forcing, the mean flow will continue to grow until it is so large that it tears apart the convection cells that are forcing it. This leads to the mean flow decaying until it is small enough that the convection cells can re-establish themselves. A burst in convection and rapid growth of the mean flow follows, which again tears apart the convection cells. These bursting vacillations repeat themselves [29][18][6][44]. Finally, at larger thermal forcing still, a non-episodic mean flow state can be reached [29].
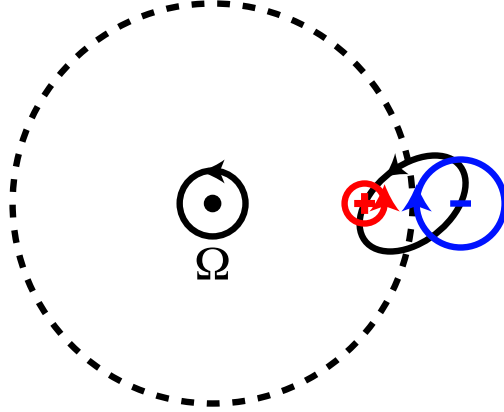
Figure 1.6: Unlike in the case of a homogeneous beta, as in figure 1.1, if beta varies in a particular direction then different magnitudes of vorticity are generated by fluid parcels with oppositely signed velocity in that direction. This image illustrates the case of a β which varies with cylindrical radius such that $\beta < 0$ and $\frac{\partial \beta}{\partial s} < 0$, where s is the radius from the rotation axis, marked with a black dot. Counterclockwise circulation of fluid parcels original located at a reference cylindrical radius, indicated by a dashed line, is depicted.

1.6   Zonal winds on the gas giant planets

In this thesis we investigate some aspects of turbulence in a rapidly rotating fluid. Specifically, we study turbulent flows in a spherical shell geometry, driven by thermal convection. The motivation for the present work is to understand further the organization of the atmospheres of the gas giant planets into differentially rotating bands of wind circling the planet. These are referred to as zonal winds, and have eluded a comprehensive explanation.

Observations of the gas giant planets of Jupiter, Saturn, Uranus and Neptune by a variety of missions, most notably Voyager 2, Galileo and Cassini [65][73][96], have revealed that the surface winds on these planets are dominated by their mean azimuthal (or zonal) component. All four planets feature multiple zonal jets of latitudinally varying amplitude, as measured with respect to the frame of reference fixed to the magnetic field generated in the planet's

18

core. However, important differences exist between the planets. While the ice giants of Neptune and Uranus are characterized by a broad retrograde equatorial jet, this is contrasted by a broad prograde jet on Jupiter and Saturn. As well, the ice giants have only a single broad, prograde high latitude jet in each hemisphere of comparable wind speed to the central jet, while Jupiter and Saturn have numerous smaller amplitude jets of alternating prograde and retrograde motion in the polar region. In the current work we will focus on the dynamics of Jupiter and Saturn.

The mean zonal winds on Jupiter's surface as a function of latitude were measured by both the Voyager 2 and Cassini missions [96]. Their observations show that the central jet, referred to as the Equatorial Zone, spans $\sim \pm 15°$ in latitude about the equator with wind speeds up to 150 m/s. At high latitudes, roughly up to $\sim 80°$, there are on the order of ten jets with a much lower maximum velocity of 50 m/s. Additionally, these jets are significantly narrower than the central jet. There is an equatorial asymmetry in the wind profile, with a fast retrograde jet at $\sim 20°$ S and a fast prograde jet at $\sim 20°$ N. The significance of this asymmetry is unknown. The zonal wind structure is correlated with the darkly coloured bands (called belts) and lightly coloured bands (called zones) observed on Jupiter's surface. Each band is bound by a local extremum of the zonal flow, with prograde jets at the equatorward edge of belts and retrograde jets at the poleward edge of belts. Saturn has a similar zonal wind structure as Jupiter, although its wind speeds are larger and central jet broader. The zonal wind of Jupiter changed very little during the twenty years between observations, indicating that it is a relatively stable feature of the planet's atmosphere. The existence of these jets, and their steadiness, demands an explanation.

It has yet to be conclusively resolved whether the observed jets are confined to the outermost atmospheric layers or originate deep within the planet. If the jets are the result of deep thermal convection, then observations of the surface flow could provide a window into the inner workings of the planet and act as an excellent constraint for models of the planet's internal dynamics. Voyager 1's infrared measurements showed that the heat flux emitted by Jupiter is approximately twice as large as its insolation [48][72], suggesting that convection is transporting heat from deep within the planet. Additionally, the observed radiative heat flux is roughly constant with latitude, while the solar energy is deposited primarily near the equator. One possibility is that convection could make up the difference, since it preferentially transports heat axially in the polar regions. This is due to the fact that cylindrical radial convection cells, the dominant form of convection in the equatorial regions, are inhibited by the shearing of the zonal flow [4]. When combined with the insolation, this could lead to a uniform heat flux with latitude. However, surface observations alone cannot definitively determine the depth to which the zonal jets extend. The Galileo mission directly measured Jupiter's wind speed as a function of atmospheric depth in 2003 by crashing a probe into the planet in the equatorial region. It found that the zonal wind speed remained large well below the surface layers to a depth of $\sim 21 bar$ (140km or 0.2% of the planetary radius below the 1bar surface), and was roughly constant with depth [1]. It is unclear whether this observation also applies to the polar regions.

Numerous models have been developed to study both deep and shallow layer scenarios. Shallow layer models, where fluid motion is constrained to a thin 2D spherical layer near the planetary surface, have been successful in generating multiple high-latitude jets, but usually feature a retrograde central

jet as opposed to the observed prograde jet of Jupiter [28][27][98][99]. However, ad hoc forcing functions can produce a prograde jet [99].

In deep layer models the convection layer is much thicker. In this class of models, first proposed by Busse in 1976 [14][16], the jets are driven by thermal convection within a three dimensional spherical shell, and the resulting zonal flow extends uniformly across the entire depth of the shell axially. These models can be described in cylindrical coordinates by specifying an axial fluid depth which varies with cylindrical radius. They generally produce a large prograde equatorial zonal jet, but though the high latitude jets in these models tend to be the right amplitude, they are usually broader and fewer than observations require [29][6]. Convection in these models is generally driven by a spherical radial thermal gradient across the shell due to the hot inner planet. The latitudinally varying insolation of the planet has also been considered as a mechanism for generating zonal flows deep within the planet, even though the deposition of solar energy is limited to surface layers [64].

In deep layer models the shell thickness plays a key role in the structure of the zonal winds produced. The thickness physically corresponds to the depth to which the convection which drives zonal flow generation extends. For Jupiter and Saturn the inner boundary is taken at the location of a phase transition from molecular to metallic hydrogen, which occurs as a result of increased pressure with depth [46]. Due to the higher electrical conductivity of metallic hydrogen, magnetic braking becomes important below the phase transition. Any zonal flow in the conducting region shears magnetic field lines and thus induces large electrical currents. By Lenz's law these currents are oriented such that the Lorentz forces they generate resist further shearing of the field and hence limit the growth of zonal winds. Therefore, the large zonal

winds generated in the outer non-conducting region cannot extend into the inner conducting region. Numerical results [55][39] and observational constraints support this picture. If the zonal winds remained large in the conducting region, the large Ohmic dissipation that would result would exceed the observed luminosity of the planet [66].

It is thought that magnetic braking should become important at $\sim 85-95\%$ of the planetary radius in Jupiter [47], though it is unknown how abrupt the phase change is. To model the effects of this phase transition, and the shear in the flow it creates, in a model which does not include magnetic fields, mechanical boundary conditions are applied. A sharp transition would be akin to no-slip boundary conditions, which strongly damp zonal winds. Numerical models that use such a boundary condition typically find that zonal winds are suppressed, especially inside the TC [56][3][6]. This could be due in part to the unphysically large viscous dissipation used in simulations due to numerical constraints, which overdamps the zonal flow. It is possible that with lower, more physically realistic viscous dissipation, jets could still be produced with no-slip boundary conditions. Experiments studying thermal convection in a rotating tank with sloping boundaries, mimicking the geometry outside Jupiter's TC, are able to produce alternating jets with no slip boundary conditions [86]. Alternatively, the dynamics associated with a gradual phase transition, which would be the case if the differentiation of hydrogen was ongoing, would perhaps be better captured by stress-free boundary conditions. At the outer boundary the fluid is surrounded by a near vacuum, so free-slip boundary conditions are the most physically realistic choice here.

While the wind speeds on Jupiter and Saturn are large, their rapid planetary rotation ensures that their Rossby numbers, which is the ratio of their

inertial and Coriolis forces ($Ro = U/\Omega R$), remain small (~ 0.01) and the planet is in the rapid rotation limit. Here U is the typical fluid velocity, Ω is the planet's angular velocity and R is its outer radius. In this limit the first order balance of forces in the system, assuming that the viscosity and thermal forcing are small, is between the Coriolis force and pressure gradient (a geostrophic balance). As described in Section 1.2, the Taylor-Proudman theorem states that for a homogeneous inviscid fluid the resulting flow in such a balance will be invariant in the direction parallel to the rotation axis. At very high rotation rates axial fluid columns move rigidly and extend across the entire width of the convection shell. Even if the fluid is moderately forced thermally, breaking the Taylor-Proudman constraint and leading to 3D turbulence, the zonal flow remains axially invariant. This can be clearly seen in the numerical results of the deep layer Boussinesq model of Moritz Heimpel [50] presented in figure 1.7, with the zonal wind forming a series of nested differentially rotating cylinders. Though the zonal flow is mostly invariant, or rigid, across the shell in the axial direction, there is a noticeable asymmetry between the high latitude jets in the northern and southern hemispheres. This is due to the fact that inside the TC the two polar regions are dynamically separated by the interior of the planet, so the flow need not be rigid between the two. The chaotic nature of turbulence will naturally lead to differences in the pattern of jets in the two hemispheres even though the underlying physics governing their dynamics is identical. Numerical models have shown that initial conditions influence the number of jets that are ultimately generated [56]. The Rossby numbers of the ice giants are significantly larger (~ 0.1), so it is not clear that they are in the rapid rotation limit. This could explain their different wind patterns [5]. Simulations by Jonathan Aurnou found that when

23

the buoyant forces are larger than the Coriolis forces, convection becomes fully three dimensional and the equatorial jet reverses direction [5].
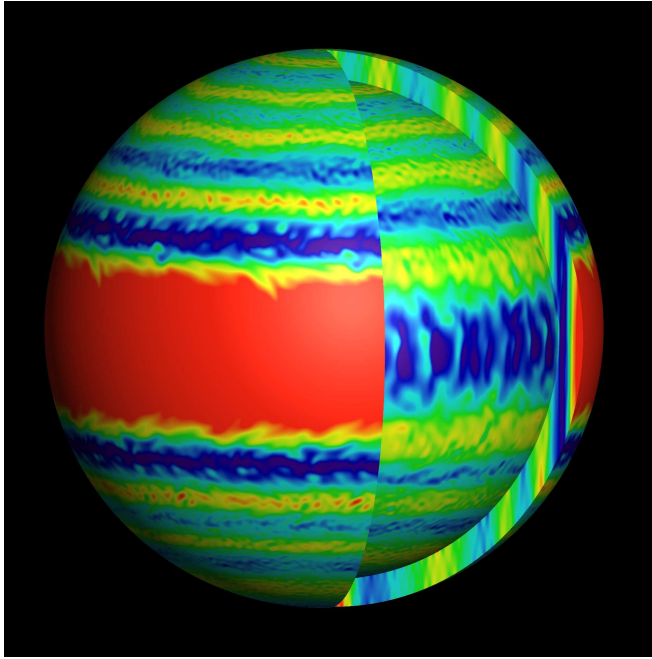
Figure 1.7: Figure 2 of Heimpel [50] showing a snapshot of the fluid's azimuthal velocity on the outer boundary of the convection shell. The cutaway reveals the flow on the inner shell surface and a meridional cross section. Red indicates prograde motion and blue retrograde.

As described in previous sections, the zonal wind in the deep layer models is the result of a turbulent cascade of energy from small scales to large scales under rapid rotation. The mean flow is generated by Reynolds stresses from tilting in the azimuthal direction of the turbulent 2D convection cells. Both the topographic beta-effect and adiabatic expansion contribute to tilting the convection cells, and thus the generation of a zonal wind [37]. The jets grow until their latitudinal width is equal to the Rhines wavelength. This length scale depends on the topographic β parameter, which equals the fractional change in axial column length with cylindrical radius for a homogeneous fluid

[49]. There is a discontinuity in β at the planet's TC due to a doubling of axial height of the shell outwards across the TC, since fluid elements span both hemispheres outside the TC but are restricted to one inside. This leads to differential vorticity generation in the two regions, providing a natural mechanism for producing jets of different widths. Additionally, the sign of β changes across the TC so that the Reynolds stresses forcing the mean flow are oriented in opposite directions in the two regions. Recent simulations of thermal convection by Heimpel using a thinner shell ($\sim 10\%$ of the planetary radius) than previous work, such that the TC is located at the observed discontinuity in the jet widths, have been able to generate zonal winds broadly in agreement with observations of Jupiter in both the equatorial and high latitude regions, as seen in figure 1.8 [50][49]. The thin shell increases the number of high latitude jets both due to an enlargement of the high latitude region and also because the lower jet velocities in a thin shell lead to decreased jet widths. Saturn's broader central jet could be explained by its relatively smaller metallic core and hence thicker convection shell [46]. A thicker convection shell could also explain the larger jet amplitudes on Saturn, since the magnetic braking would be less effective due to the lower surface-area-to-volume ratio for a given axial fluid column.

While laboratory experiments have been carried out to study zonal wind generation [77], size and energy constraints do not allow for realistic Jovian scale parameters to be studied for rotationally dominated systems. As turbulent convection is a highly non-linear process, analytical attempts to study it are mostly restricted to the onset of convection, where the non-linear effects are minimal. Direct numerical simulations (DNS) also face limitations due to the vast range of scales that must be considered. While current models have been
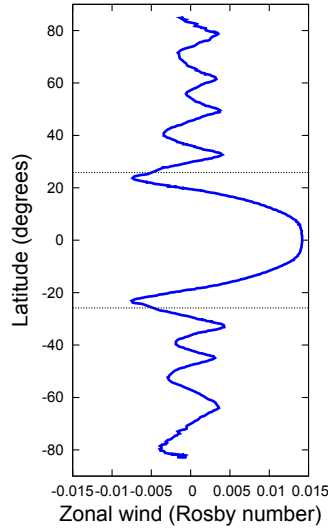
Figure 1.8: Replotted data from figure 2 of Heimpel [50] showing a snapshot of the surface mean zonal wind from numerical results. The model simulated deep layer thermal convection with a shell thickness of 10% of the planetary radius. The solid black line indicates the location of the intersection of the TC with the surface.

successful in generating zonal winds broadly in agreement with observations, they too have not been able to explore realistic Jovian parameter regimes due to computation limits. There is no prospects for substantial improvement numerically in the foreseeable future. The extremely small viscous dissipation of Jupiter's atmosphere requires very fine resolution to resolve the viscous length scale. Such a large number of grid points cannot be achieved by present day machines. Current models must compensate for this by overstating the viscous dissipation by many orders of magnitude relative to the predicted planetary values, to ensure that the viscous dissipation scale is sufficiently large enough to be resolvable. It is unclear whether the results of these models can be extrapolated to more realistic scenarios. Since the zonal winds are generated by an energy cascade from small to large scales, this approach of neglecting the small scale flow could very well be missing important dynamics. Additionally,

these models generally simulate an idealized incompressible Boussinesq fluid. Finally, due to numerical constraints they have been unable to explore the long time scale dynamics of the flow, which would help to resolve whether the asymmetry observed on Jupiter is just a fluctuation about some steady state.

1.7 Quasigeostrophic models of convection

Since rotation imparts a 2D organization to a homogeneous fluid in the direction of rotation, it is reasonable to postulate that it could be possible to capture the essential ingredients of the dynamics of zonal flow generation using a 2D quasigeostrophic (QG) approach. In such a model the fluid is assumed to be in geostrophic balance to first order, with the nonlinear terms being much smaller. Ageostrophic perturbations about this state are also included. Under rapid rotation the geostrophic flow is dominantly 2D, provided the thermal forcing is not too large. However, numerical simulations have shown that if the buoyant forcing is large enough this axial coherence is broken [89]. In the present work we will consider the rapid rotation and modest thermal forcing limit, leading to axially invariant flow.

By averaging the equations of motion in the axial direction over the entire shell, and simulating the evolution of the axially averaged variables on a 2D polar coordinate grid (a virtual equatorial plane), the geostrophic component of the flow can be modeled in one fewer dimension. The non-rigid ageostrophic flow, which is required to meet the boundary conditions, must be parameterized in this framework so that its effects on the geostrophic flow components can be accounted for in the model.

There are two main categories of QG models that have been developed.

Shallow layer QG models have been built to describe the Earth's atmosphere and ocean. In these models a local coordinate system is chosen to describe a patch of the Earth's surface. The local Coriolis parameter varies in latitude using these coordinates since the angle made by the local vertical with the planetary rotation vector changes due to the curvature of the planetary surface. The velocity in the local vertical direction is taken to be small and the horizontal flow is assumed to be balanced to first order with the Coriolis term, leading to dominantly 2D flow. Generalizations which allow for continuous stratification and vertical variations in the flow across the layer have also been developed [71].

In deep layer QG models, flow is modeled in a 3D spherical shell. In this case a global coordinate system oriented such that the vertical is aligned with the rotation axis is used. In such a coordinate system the Coriolis parameter is constant with latitude, since the vertical does not vary with latitude. This leads to the flow being dominantly 2D aligned with the rotation axis, rather than with the local vertical as in the shallow layer models.

In both shallow and deep layer modes, only the rigid geostrophic component of the flow is dynamically simulated, with the effects of non-rigidities of the flow on the rigid flow variables parameterized. By exploiting the expected 2D rigid structure of the flow in this way, a more efficient numerical model of zonal wind generation can be developed. The computational demands for a 2D model scale as N^2, where N is the number of grid points in each dimensions. This is much more gradual than 3D models, which scale as N^3, allowing for an exploration of significantly more computationally demanding regimes of parameter space which are currently inaccessible to 3D models. Additionally, the greatly reduced computational requirements allows for the dependence of

the solution on other parameters of the system, such as the shell thickness, to be explored in more detail than is possible with 3D models. If scaling laws for the solution can be established, more realistic extrapolations of existing results to Jovian-like parameters could be possible. Furthermore, the effects of initial conditions and the long time scale dynamics of the system can be more thoroughly investigated.

Another advantage of a 2D model is that since it allows for better resolved simulations, subgrid-scale processes are less of a problem. Generally, 3D models must use special techniques to deal with unresolved small scale flow to avoid numerical instabilities. If flow at these small scales plays an important role in the dynamics of the system, their effects on the larger resolved scales of interest must be parameterized. Examples of this are the various different types of large eddy simulation (LES) parameterizations. Alternatively, hyperdiffusion can be used, as for example is done in both the shallow layer models of Richard Scott [84][85] and deep layer model of Heimpel [50]. If a numerical simulation is underresolved the small scale modes tend to become overexcited. To compensate for this, a viscosity which is inversely proportional to the length scale is used to preferentially damp out the small scale flow. This approach assumes that there are limited interactions between the small scales, where viscous diffusion dominates, and the large scales. Since the zonal wind is generated by an energy cascade from the small scale turbulence, it is unclear whether this assumption is valid, and the use of hyperdiffusion could influence the resulting zonal wind produced. In particular, since hyperdiffusivity introduces an anisotropy into the flow by enhancing the diffusion of small scale structures on spherical surfaces but not small scale structures in the radial direction, this could lead to unphysical Reynolds stresses and zonal flows.

1.8   Thesis outline

In the present thesis we develop a generalized 2D QG model of thermal convection in a deep spherical shell, and use it to study Jovian-like systems. As a first approach we will consider the simplified case of a Boussinesq fluid, where only vortex stretching plays a role in zonal wind generation. QG models have been formulated in the past to study other problems [40], and have been shown to produce results broadly in agreement with both 3D models and laboratory experiments at the onset of convection and in fully turbulent flow [2]. However, existing QG models only consider flow outside the convection shell's TC. This is due to the fact that the primary application for such models to date has been to study the flow in planetary cores. In these systems a thick convection shell is appropriate, resulting in most of the volume of the shell being located in the region outside the TC. Conversely, for the scenario we are interested in (the generation of atmospheric jets on the gas giant planets) a thin shell is required. In such a geometry much of the shell volume is located within the TC, making a model of the dynamics here much more critical. Therefore, the existing QG framework must be extended to the region inside the TC. We develop a model of thermally forced convection throughout the shell, which allows for the model to be used to study the thermal properties of the system, including the heat flux out the surface of the planet. An alternative approach would be to utilize random mechanical forcing inside the TC, and future work could examine the difference in the jets generated by different forcings. Due to the distinct dynamics of convection aligned with the rotation axis inside the TC, as compared to convection perpendicular to the rotation axis outside the TC, this generalization involves more than just different geometry.

The thesis is structured as follows. Chapter 2 presents the geometry and fundamental equations for thermal convection of a Boussinesq fluid in a 3D shell. In Chapter 3 the generalized QG framework is developed. The fundamental equations are axially averaged to derive 2D QG equations for the mean geostrophic flow. The details of the numerical implementation of these QG equations which has been utilized in the present work is described in Chapter 4. The numerical code is a modified version of the code originally written by Nathanael Schaeffer, which itself was based on codes written by Philippe Cardin [82][83], that implemented the QG model of thermal convection in a spherical shell outside the TC of Nicolas Gillet and Chris Jones [40]. This code has been adapted to also model QG flow inside the TC. Chapter 5 presents the numerical results of this implementation. Two sets of parameters are investigated with the QG model, both chosen such that the resulting wind speeds are comparable to the gas giants. The results from one of these scenarios are directly compared to results from a 3D model run at analogous parameters. The similarities and differences of the amplitudes and length scales of all the flow variables are examined. Finally, in Chapter 6 the results of our model are discussed and conclusions are drawn on which features of the flow our 2D model captures well and which need improvement. Suggestions for future work to improve upon our QG model are also presented. While none of the work presented in this thesis has been published, it is currently being prepared for submission.

Chapter 2

Equations of motion

2.1 Geometry

In the present work we consider thermal convection of a fluid under rapid rotation within a shell that is assumed to be axisymmetric. Such a system has two natural coordinate systems, which are depicted in figure 2.1. Spherical coordinates (r, θ, ϕ) are useful for describing the geometrical structure of the shell. Meanwhile, cylindrical coordinates (s, ϕ, z), with the z axis defined such that it is coaxial with the axis of rotation of the shell so that the angular velocity vector is given by $\boldsymbol{\Omega} = \Omega \hat{\mathbf{z}}$, where the hat indicates a unit vector, are simpler for describing the flow, which is expected to be organized such that it is dominantly invariant parallel to the axis of rotation. Here r and s are the spherical and cylindrical radius respectively, θ and ϕ are the co-latitude and azimuthal angles respectively, and z is the axial height. These coordinates are related by the relations $s = r\sin(\theta)$, $z = r\cos(\theta)$ and $r = \sqrt{s^2 + z^2}$. The domain of the angular variables is taken to be $\theta \in [0, \pi]$ and $\phi \in [0, 2\pi)$.

Since we are simulating convection in a shell, and not the entire spheri-
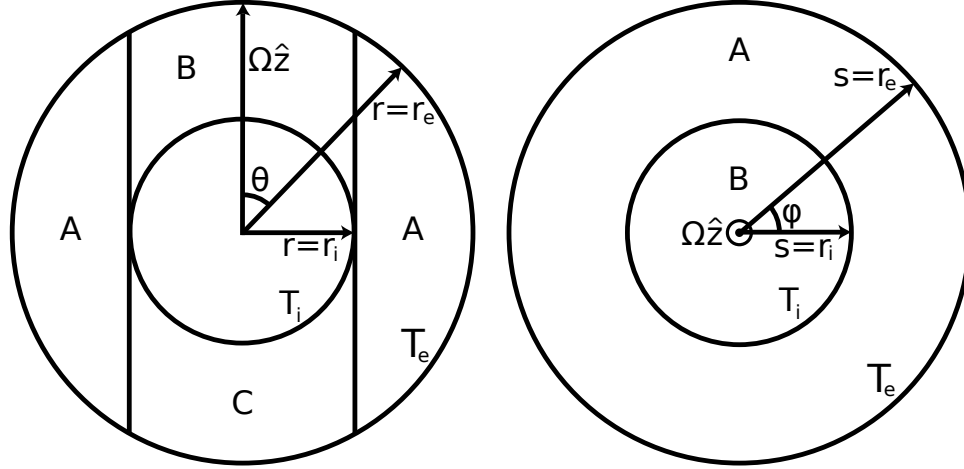
(a) Meridional slice

(b) Equatorial slice
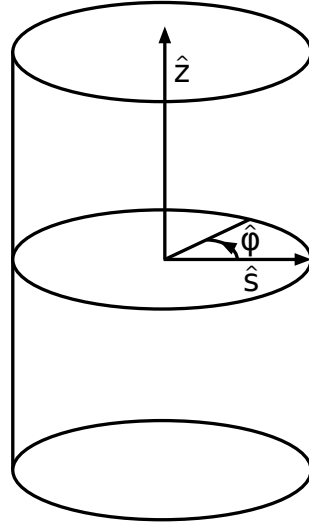
(c) Cylindrical coordinates

Figure 2.1: The geometry of the system. The tangent cylinder (TC) has a cylindrical radius equal to the radius of the inner shell boundary r_i. Figure 2.1(a) depicts the three dynamical regions of the system: A (outside the tangent cylinder), B (upper endcap) and C (lower endcap). Note that the shell thickness has been exaggerated for ease of illustration.

cal volume within the outer boundary of the shell, we can separate the shell volume into two distinct convective regions. The regions are divided by the tangent cylinder (TC), the cylinder that is coaxial with the axis of rotation and circumscribes the inner shell boundary. At cylindrical radial values out-

side the TC the flow spans both hemispheres and is bound on both ends in z by the outer shell boundary. Meanwhile, inside the TC the flow is restricted to a single hemisphere and is bound on one end by the inner shell boundary. In each of these two regions we define two variables, $L^+(s)$ and $L^-(s)$, which are equal to the z-coordinate of the upper and lower boundary of the shell at specific values of s. For simplicity we assume that both variables are monotonic within each region, though there can be a change in the sense of monotonicity across the TC since the variables can correspond to a different spherical boundary on either side of the TC.

We will work in the frame of reference co-rotating with the shell, and utilize a Eulerian specification fixed in space, rather than a Lagrangian specification fixed to the fluid parcels. Fixed temperature boundary conditions will be utilized, with the value at the inner and outer shell boundaries, T_i and T_e respectively, giving an external temperature difference imposed across the shell of $\Delta T = T_i - T_e$. $T^+(s)$ and $T^-(s)$ are defined to be the boundary values at the points where the z coordinate equals $L^+(s)$ and $L^-(s)$ respectively.

Of particular interest from a geophysical perspective is a spherically symmetric shell, though we will derive the equations of motion for the more general case before specifying the boundary geometry. Figure 2.1 depicts two dimensional cross sections of the 3D spherical shell to be modeled. In this case, the inner shell boundary is located at a spherical radius of r_i, and the outer shell boundary is at a radius of r_e, giving it a thickness of $d = r_e - r_i$ and non-dimensional radius ratio of $\chi = r_i/r_e$. We will label the co-latitude at which the TC intersects the outer shell boundary θ_{TC}, which is given by $\theta_{TC}^\pm = \arccos\left(\frac{L^\pm(r_i)}{r_e}\right)$.

To express the shell boundary in cylindrical coordinates we must divide the

shell into three regions, labeled A, B and C in figure 2.1, separated by the TC. In the equatorial region A, outside the TC, the fluid is bound from above and below by the outer shell at $z = L^+ = \sqrt{r_e^2 - s^2}$ and $z = L^- = -\sqrt{r_e^2 - s^2} = -L^+$. In the endcap regions B and C, the fluid is bound on one end by the inner shell and on the other by the outer shell. In region B the boundaries are at $L^+ = \sqrt{r_e^2 - s^2}$ and $L^- = \sqrt{r_i^2 - s^2}$, while in region C they are the negative of this, $L^+ = -\sqrt{r_i^2 - s^2}$ and $L^- = -\sqrt{r_e^2 - s^2}$. For generality of notation we will define $r^+(s)$ and $r^-(s)$ to be the spherical radius of the upper and lower boundary of the shell at a given cylindrical radius s. In region A and B, $r^+ = r_e$, and in region C, $r^+ = r_i$, while the lower boundary in region A and C is located at $r^- = r_e$, and in region B at $r^- = r_i$. The temperature boundary conditions in cylindrical coordinates are $T^+ = T_e$ in region A and B and $T^+ = T_i$ in region C, while the lower value in region A and C is $T^- = T_e$ and in region B is $T^- = T_i$. Due to the symmetry of the system it is expected that the dynamics in the two endcap regions B and C will be identical, thus to simplify the model we will only consider the positive z polar region B in this work.

2.2   Continuum hypothesis

At a fundamental level, fluids are comprised of discrete point-like molecules separated by a vacuum, each interacting with every other molecule. Unfortunately, directly modeling the dynamics of such a system is beyond the capabilities of modern computing due to the extremely large number of molecules that are present in any realistic volume of fluid. However, experiments have shown that if the system of interest has a separation of scales such that the

scale of the flow structures of interest are much larger than the mean-free-path of the molecules, then the precise details of the dynamics of individual particles do not play a major role in the larger scale dynamics of the fluid. The average state of the particles over some scale much smaller than the flow structures of interest is sufficient to describe the macroscopic flow. Given that the mean-free-path of molecules is usually quite small for most fluids of interest, this is generally a good assumption. This allows for a greatly simplified description of fluids, with discrete particle variables approximated by continuous fluid variables. This formulation has many advantages, not least of which is that it allows for the harnessing of the full power of calculus, which requires smoothly defined variables.

2.3   Conservation laws

A rotating, continuous fluid subject to gravity conserves three quantities: mass, momentum and internal energy. Conservations laws for each of these variables are listed below for a fluid parcel per unit volume, written in differential form.

Conservation of mass (continuity equation)

$$\frac{\partial \rho}{\partial t} + \boldsymbol{\nabla} \cdot (\rho \mathbf{u}) = 0 \tag{2.1}$$

Conservation of momentum (Cauchy equation)

$$\rho \frac{\partial \mathbf{u}}{\partial t} + \rho \left(\mathbf{u} \cdot \boldsymbol{\nabla} \right) \mathbf{u} + 2\rho \boldsymbol{\Omega} \times \mathbf{u} = \boldsymbol{\nabla} \cdot \mathbf{T} + \rho \mathbf{g} \tag{2.2}$$

Conservation of energy (Heat equation)

$$\rho \frac{\partial e}{\partial t} + \rho \left(\mathbf{u} \cdot \boldsymbol{\nabla} \right) e = -\boldsymbol{\nabla} \cdot \mathbf{q} - P(\boldsymbol{\nabla} \cdot \mathbf{u}) + \Phi \tag{2.3}$$

In these equations, t is the time, ρ is the fluid density, $\mathbf{u}$ is the fluid velocity, $\boldsymbol{\Omega} = \Omega\hat{\mathbf{z}}$ is the shell's angular velocity, which is assumed to be both spatially and temporally constant, $\mathbf{T}$ is the stress tensor, e is the internal energy per unit mass, $\mathbf{q}$ is the heat flux, P is the pressure and Φ is the kinetic energy viscous dissipation rate per unit volume. The only body force that has been included in the momentum equation is buoyancy. $\mathbf{g}$ is the effective gravitational field, which is the sum of the Newtonian gravity $(\mathbf{g}_n)$ and centrifugal acceleration $(s\Omega^2\hat{\mathbf{s}})$, $\mathbf{g} = \mathbf{g}_n + s\Omega^2\hat{\mathbf{s}}$. We have assumed that the electrical conductivity of the fluid is small, so that Lorentz forces do not play a significant role in the dynamics, and do not allow for phase changes of the fluid. In each of these equations the temporal and spatial derivatives can be combined and rewritten in terms of a material derivative, denoted with a capital D, which is defined for a general variable f as

$$\frac{Df}{Dt} = \frac{\partial f}{\partial t} + (\mathbf{u} \cdot \boldsymbol{\nabla})f, \tag{2.4}$$

where f can be either scalar or vector valued. This notation will be utilized in this thesis.

In equation 2.3, Φ can be parameterized in terms of the velocities, $\mathbf{q}$ is a function of the energy, and the stress tensor is related to the velocities and pressure by a constitutive relation. Thus we have a system of five equations (one each for the density and energy and three for the velocity from each of the components of the vector equation) for six independent dynamic variables

37

(density, pressure, energy, and three components of the velocity.) To close the system, we need one final equation. This can be provided by an equation of state relating pressure, temperature and density, such as for example the ideal gas law.

2.4 Boussinesq approximation

To these fundamental conservation laws we apply a series of approximations collectively known as the Boussinesq approximation. First proposed by Joseph Valentin Boussinesq [10], they start with the premise that convection acts over a relatively long time scale and does not depend on the details of faster processes such as acoustic waves. As such, the equations of motion can be simplified by assuming that the fluid's thermodynamic variables are governed by small perturbations about a static reference state. This has the effect of filtering out the influence of fast processes.

In particular, the density is assumed to be constant throughout the fluid except in the buoyancy term, since here it is multiplied by the large (for example order 10 at Earth's surface) gravitational field. Also, since it is only the variations in density, and not the total density, which drives buoyancy, we must retain first-order perturbations in density to model the dynamics of convection since this is the leading order contribution. In the other terms the first order perturbations are minor corrections and can be safely neglected. The Boussinesq approximation also ignores the feedback of changes in density on the gravitational field, which is assumed to be static, and assumes that the properties of the fluid, such as viscosity, are constant. These assumptions have been shown to be valid provided that several conditions are met. Specifically,

they require that fluid velocities be not too large relative to the speed of sound. Generally this is taken to mean a Mach number M, the ratio of the fluid speed to the local sound speed, which is $M \lesssim 0.3$. Obviously it is important that we not be interested in the effects of compressional waves, such as sound or shock waves, which propagate via pressure (and thus density) variations and and as such get filtered out in the Boussinesq approximation. Also, the vertical length scale cannot be so large that the hydrostatic pressure results in significant density variations across the fluid layer.

In effect, these assumptions allow us to assume that the fluid is incompressible so that the density does not change significantly with changes in pressure. However, the density can still vary with temperature, and these variations are vital to retain since they are responsible for the buoyancy which drives convection. If these thermal variations in the fluid are small, then the resulting density perturbations will also be small and need only be considered in the buoyancy term. We will not consider other possible variables on which the density could depend, such as chemical composition, thus restricting our model to a single-component fluid. In this approximation only the topographic beta-effect, and not adiabatic expansion, leads to vortex stretching and plays a role in zonal wind generation.

In reality the density variations across planetary scale shells are significant. While the Boussinesq approximation might seem like a drastic oversimplification, these assumptions are widely used and are quite successful at capturing much of the dynamics of convection. An alternative to the Boussinesq approximation is the more general anelastic approximation [42], which assumes that the momentum density, rather than the velocity, is divergenceless: $\boldsymbol{\nabla}\cdot(\rho\mathbf{u}) \sim 0$. An adiabatic density profile is assumed. This approach allows for some of the

effects of compressibility to be retained, including vortex stretching via adiabatic expansion and contraction in addition to the topographic beta-effect [30]. However, it has been shown that qualitatively similar zonal flows are obtained using an anelastic model as compared with a Boussinesq fluid [56][38]. The results of Chris Jones showed that with a 5 efold variation in density across the shell the zonal flow remained largely invariant, even though the non-axisymmetric velocities were no longer rigid [56].

Since this work is a first step in the development of a model of QG flow inside the TC, we will restrict our consideration to a Boussinesq fluid. This allows us to avoid the complexities inherent to compressible flow so that we can instead focus on the dynamics essential to zonal wind generation. Once the model is successful in this simplified scenario, the effects of compressibility can be incorporated into it.

2.5 Continuity equation

The Boussinesq approximation allows us to make a number of simplifications. By assuming that the variations in density of a fluid parcel as the flow advects it are small relative to gradients of the velocity

$$
\frac{1}{\rho}\frac{D\rho}{Dt} \equiv \frac{1}{\rho}\left(\frac{\partial \rho}{\partial t} + (\mathbf{u}\cdot\boldsymbol{\nabla})\rho\right) \ll \boldsymbol{\nabla}\cdot\mathbf{u}, \tag{2.5}
$$

we can simplify the continuity equation by replacing it with the incompressibility condition

$$
\frac{\partial \rho}{\partial t} + \boldsymbol{\nabla}\cdot(\rho\mathbf{u}) = \frac{D\rho}{Dt} + \rho\boldsymbol{\nabla}\cdot\mathbf{u} = 0,
$$

$$\boldsymbol{\nabla} \cdot \mathbf{u} \approx 0. \tag{2.6}$$

2.6 Navier-Stokes equation

If we assume that we are working with a Newtonian fluid, the constitutive equation relating the deviatoric stress and the strain rate tensors is linear, with the total stress tensor given by

$$T_{ij} = -\left(P + \frac{2}{3}\mu\boldsymbol{\nabla} \cdot \mathbf{u}\right)\delta_{ij} + 2\mu e_{ij}, \tag{2.7}$$

where $e_{ij} \equiv \frac{1}{2}\left(\frac{\partial u_i}{\partial x_j} + \frac{\partial u_j}{\partial x_i}\right)$ is the symmetric strain rate tensor, P is the pressure and μ is the dynamic viscosity. Using the incompressibility condition in equation 2.6 simplifies this to

$$T_{ij} = -P\delta_{ij} + 2\mu e_{ij}. \tag{2.8}$$

Substituting this into the Cauchy equation in equation 2.2 gives the Navier-Stokes (NS) momentum equation for a buoyant incompressible fluid in a rotating frame of reference

$$\rho\frac{\partial \mathbf{u}}{\partial t} + \rho\left(\mathbf{u} \cdot \boldsymbol{\nabla}\right)\mathbf{u} + 2\rho\boldsymbol{\Omega} \times \mathbf{u} = -\boldsymbol{\nabla}P + \rho\nu\boldsymbol{\nabla}^2\mathbf{u} + \rho\mathbf{g}, \tag{2.9}$$

where $\nu = \frac{\mu}{\rho}$ is the kinematic viscosity, which is assumed to be constant. It is important to note that the operator in the second last term of equation 2.9 is a vector Laplacian, which differs from the scalar Laplacian in curvilinear coordinates.

We will write the gravitational field as $\mathbf{g} = g_0 g_r(r)\hat{\mathbf{g}}$, where g_0 is the grav-

itational field strength at the outer boundary, $g_r(r)$ is the non-dimensional radial dependence of the field, and $\hat{\mathbf{g}}$ is a unit vector in the direction of the field. There are several choices on how to parameterize $\mathbf{g}$. In planetary scale systems the Newtonian gravity dominates. For a perfectly spherically symmetric planet the Newtonian gravitational field at a given radius r is in the negative spherical radial direction $\hat{\mathbf{r}}$. From the divergence theorem its magnitude is proportional to the mass enclosed by a spherical shell at that radius, $M_{enc}(r)$, giving $\mathbf{g}_n = -\frac{GM_{enc}(r)}{r^2}\hat{\mathbf{r}}$. Thus, in this geometry $g_0 = \frac{GM_{enc}(r_e)}{r_e^2}$, where G is the universal gravitational constant, $g_r(r) = \frac{r_e^2}{r^2}\frac{M_{enc}(r)}{M_{enc}(r_e)}$ and $\hat{\mathbf{g}} = -\hat{\mathbf{r}}$. Since we are considering a relatively thin convection shell at the surface of the planet, where the density is much less than in the core, most of the planet's mass should be contained within the inner shell radius at $r = r_i$. In this case $M_{enc}(r_e) \sim M_{enc}(r_i)$, and so $g_r(r_e) \sim \left(\frac{r_i}{r_e}\right)^2 g_r(r_i)$. For a shell of thickness $d = 0.1$, this amounts to a decrease in the gravitational field strength of roughly $1 - \left(\frac{r_i}{r_e}\right)^2 \sim 20\%$ across the shell. In reality there will be some mass within the shell, and this unaccounted for mass will partially cancel the decrease in field strength. Thus one reasonable approach is to assume that the gravitational field is spherically symmetric and invariant across the thin shell, $g_r \sim 1$. Alternatively, the other extreme is to assume that the density is constant throughout the entire planet and calculate the enclosed mass explicitly from $M_{enc} = \int \rho \, dV$. This gives $M_{enc}(r) = \frac{4}{3}\pi r^3 \rho$, and thus $g_r = \frac{r}{r_e}$.

Conversely, in experimental setups the Newtonian gravity is negligible and the centripetal acceleration dominates, giving a cylindrically symmetric effective gravitational field. The centripetal acceleration is in the cylindrical radial direction $\hat{\mathbf{s}}$. In this case $g_0 = \Omega^2 s_e$, $g_r = \frac{s}{s_e}$, where s_e is the cylindrical radius of the external boundary, and $\hat{\mathbf{g}} = \hat{\mathbf{s}}$. In the present work we will consider a

constant, spherically symmetric gravitational field, but the equations will be developed for the more general case.

2.6.1   Reference state

One of the important assumptions of the Boussinesq approximation is that the fluid layer is not so deep that the hydrostatic density gradient is significant. However, for convection in a shell spanning a significant fraction of the planetary radius it is clear that this is not the case. We can get around this difficulty by recasting the equations as a perturbation about the hydrostatic, thermally conducting state.

We label the static reference density, temperature and pressure profiles as ρ_c, T_c and P_c, which are defined as the solutions of the hydrostatic conducting state equations. The specific choice of background profiles depends on the symmetries of the system. In planetary scale systems the spherically symmetric gravitational field gives rise to hydrostatic pressure and density profiles which depend only on r, while fluctuations about these profiles can depend on all the coordinates. For a centripetal acceleration dominated system, cylindrically symmetric background profiles are more natural. The choice of a conductive thermal profile depends on the shell structure and thermal boundary conditions. A spherical shell with constant temperature boundary conditions leads to a spherically symmetric profile. Regardless of the details of the profiles, we can expand the full ρ, T, P variables as

$$\rho = \rho_c + \tilde{\rho}, \tag{2.10}$$

$$T = T_c + \tilde{T}, \tag{2.11}$$

$$P = P_c + \tilde{P}, \tag{2.12}$$

where the variables with tildes are dynamic perturbations about the background hydrostatic, conducting profiles, indicated by c subscripts. We will assume that the perturbations are much smaller than the background profiles: $\rho_c >> \tilde{\rho}$, $T_c >> \tilde{T}$ and $P_c >> \tilde{P}$. The hydrostatic thermally conducting solution obeys the NS equation with $\mathbf{u} = \mathbf{0}$, which allows us to write

$$\mathbf{0} = -\boldsymbol{\nabla} P_c + \rho_c \mathbf{g} = -\boldsymbol{\nabla} P_c + \rho_c g_0 g_r \hat{\mathbf{g}}. \tag{2.13}$$

2.6.2 Perturbation equation

Making use of the hydrostatically balanced reference state in equation 2.13 and the decomposition of the hydrostatic and dynamic perturbations of the variables in equation 2.10-2.12, the full dynamic forcing in equation 2.9 can be written as

$$
\begin{aligned}
-\boldsymbol{\nabla} P + \rho \mathbf{g} &= -\boldsymbol{\nabla}(P_c + \tilde{P}) + (\rho_c + \tilde{\rho})g_0 g_r \hat{\mathbf{g}} \\
&= -\boldsymbol{\nabla} P_c + \rho_c g_0 g_r \hat{\mathbf{g}} - \boldsymbol{\nabla}\tilde{P} + \tilde{\rho} g_0 g_r \hat{\mathbf{g}} \\
&= -\boldsymbol{\nabla}\tilde{P} + \tilde{\rho} g_0 g_r \hat{\mathbf{g}}.
\end{aligned} \tag{2.14}
$$

The full NS equation in terms of the perturbations in the variables is

$$\rho\frac{\partial \mathbf{u}}{\partial t} + \rho\left(\mathbf{u}\cdot\boldsymbol{\nabla}\right)\mathbf{u} + 2\,\rho\boldsymbol{\Omega}\times\mathbf{u} = -\boldsymbol{\nabla}\tilde{P} + \rho\nu\boldsymbol{\nabla}^2\mathbf{u} + \tilde{\rho}g_0 g_r\hat{\mathbf{g}}. \tag{2.15}$$

We have thus eliminated the hydrostatic pressure from our equations in favour of the dynamic pressure, which allows us to proceed with making the Boussi-

nesq approximation since the dynamic pressure should not vary significantly across the shell relative to the hydrostatic pressure.

We will now demonstrate why the Boussinesq approximation lets us neglect density perturbations except in the buoyancy term. Expanding the density in the NS equation we get

$$(\rho_c + \tilde{\rho}) \left(\frac{\partial \mathbf{u}}{\partial t} + (\mathbf{u} \cdot \boldsymbol{\nabla}) \mathbf{u} + 2\boldsymbol{\Omega} \times \mathbf{u} \right) = -\boldsymbol{\nabla}\tilde{P} + (\rho_c + \tilde{\rho})\,\nu\boldsymbol{\nabla}^2\mathbf{u} + \tilde{\rho}g_0 g_r\hat{\mathbf{g}},$$

$$\left(1 + \frac{\tilde{\rho}}{\rho_c} \right) \left(\frac{\partial \mathbf{u}}{\partial t} + (\mathbf{u} \cdot \boldsymbol{\nabla}) \mathbf{u} + 2\boldsymbol{\Omega} \times \mathbf{u} \right)$$

$$= -\frac{1}{\rho_c}\boldsymbol{\nabla}\tilde{P} + \left(1 + \frac{\tilde{\rho}}{\rho_c} \right) \nu\boldsymbol{\nabla}^2\mathbf{u} + \frac{\tilde{\rho}}{\rho_c}g_0 g_r\hat{\mathbf{g}}, \quad (2.16)$$

where we have divided through by the conducting density profile. This makes it clear why we must retain the density perturbations in the buoyancy term. In the inertial, Coriolis and viscous terms the contributions from the relative density perturbations $\left(\frac{\tilde{\rho}}{\rho_c} \right)$ are small corrections to the background state. However, in the buoyancy term the leading order contribution is the perturbation and not the background state. The background buoyancy force is cancelled by the background hydrostatic pressure gradient, and thus it is the residual which dominates this term. Small density perturbations in the buoyancy term play a major role in driving convection. Thus, to leading order in the density perturbations the NS equation is

$$\frac{\partial \mathbf{u}}{\partial t} + (\mathbf{u} \cdot \boldsymbol{\nabla}) \mathbf{u} + 2\boldsymbol{\Omega} \times \mathbf{u} = -\frac{1}{\rho_c}\boldsymbol{\nabla}\tilde{P} + \nu\boldsymbol{\nabla}^2\mathbf{u} + \frac{\tilde{\rho}}{\rho_c}g_0 g_r\hat{\mathbf{g}}. \quad (2.17)$$

From the Boussinesq approximation we have assumed that the density does not change significantly with pressure and thus its dependence on temperature is dominant. The thermal and density perturbations for a given fluid parcel

45

can be related via the volumetric thermal expansion coefficient, α, which is defined as

$$\alpha \equiv \frac{1}{V}\left(\frac{\partial V}{\partial T}\right)_P = \frac{1}{V}\left(\frac{\partial V}{\partial \rho}\right)_P\left(\frac{\partial \rho}{\partial T}\right)_P = -\frac{1}{\rho}\left(\frac{\partial \rho}{\partial T}\right)_P,$$

where the P subscript indicates the derivative is performed with the pressure being held constant. Here we have utilized the definition of density $\rho = \frac{m}{V}$, where m and V are the mass and volume of the fluid element respectively, and have assumed isotropic expansion. Though for an ideal gas the equation of state $P = \rho R T$, with R the idea gas constant, gives $\alpha = \frac{1}{T}$, we will take α to be constant over the shell for simplicity. Also, since we are assuming that the density does not vary significantly with pressure or other variables, we can replace the partial derivative with a full one. Therefore, to first order, for small thermal perturbations, an approximate relation between the thermal perturbations and the resulting density perturbations about the background profile is

$$\Delta\rho = \Delta T\left(\frac{\partial \rho}{\partial T}\right)_P = -\rho\alpha\Delta T. \tag{2.18}$$

This allows us to write

$$\tilde{\rho} \equiv \rho - \rho_c = -\rho_c\alpha(T - T_c) = -\rho_c\alpha\Theta, \tag{2.19}$$

where $\Theta \equiv \tilde{T} = T - T_c$ is the temperature fluctuation.

Thus, we can write the full NS equation as

$$\frac{\partial \mathbf{u}}{\partial t} + (\mathbf{u}\cdot\boldsymbol{\nabla})\,\mathbf{u} + 2\boldsymbol{\Omega}\times\mathbf{u} = -\frac{1}{\rho_c}\boldsymbol{\nabla}\tilde{P} + \nu\boldsymbol{\nabla}^2\mathbf{u} - \frac{\rho_c}{\rho_c}\alpha\Theta g_0 g_r\hat{\mathbf{g}}. \tag{2.20}$$

46

As we have recast the density perturbations in the buoyancy term in terms of the thermal perturbations, we can now apply the Boussinesq approximation to assume the density is invariant across the shell in the remaining terms in which it appears. Formally, this involves taking $\tilde{\rho} = 0$, and defining the constant ρ_0 to be the radially averaged ρ_c. Thus we get

$$\frac{\partial \mathbf{u}}{\partial t} + (\mathbf{u} \cdot \boldsymbol{\nabla}) \mathbf{u} + 2\boldsymbol{\Omega} \times \mathbf{u} = -\frac{1}{\rho_0} \boldsymbol{\nabla} \tilde{P} + \nu \boldsymbol{\nabla}^2 \mathbf{u} - \alpha \Theta g_0 g_r \hat{\mathbf{g}}. \tag{2.21}$$

Since this equation only depends on the perturbations in pressure we will drop the tilde from here onward for simplicity of notation.

2.7 Heat equation

The viscous dissipation term (Φ) in the heat equation (equation 2.3) is small under the Boussinesq approximation, since it assumes that the velocities of the fluid are not too large. For an ideal gas $e = C_V T$, where C_V is the specific heat at constant volume. The volumetric expansion term can be combined with the material derivative of the thermal energy, using the continuity equation and the relation derived above between density and thermal perturbations in equation 2.18, to give

$$\rho C_P \frac{DT}{Dt} = -\boldsymbol{\nabla} \cdot \mathbf{q}, \tag{2.22}$$

where C_P is the specific heat at constant pressure.

The heat flux is given by Fourier's law of thermal conduction, which takes the form

$$\mathbf{q} = -k \boldsymbol{\nabla} T, \tag{2.23}$$

where k is the thermal conductivity which is assumed to be constant. There-
fore, the heat equation is given by

$$\frac{\partial T}{\partial t} + \mathbf{u} \cdot \boldsymbol{\nabla} T = \kappa \nabla^2 T. \tag{2.24}$$

Here $\kappa = \frac{k}{\rho C_P}$ represents the thermal diffusivity and is assumed to be constant.
We have ignored internal thermal sources, such as radioactivity, as well as
adiabatic heating from the compression and decompression of sinking and
rising fluid.

As before, we can expand the temperature about the reference profile. Since
this profile was defined to be the static conducting solution in the absence of
motion, it can be determined by solving the resulting Laplace's equation. For
a spherically symmetric shell we get

$$0 = \kappa \nabla^2 T_c = \kappa \frac{1}{r^2} \frac{\partial}{\partial r} \left(r^2 \frac{\partial T_c}{\partial r} \right). \tag{2.25}$$

The general solution to this equation, found by integrating twice, is

$$T_c(r) = C + \frac{D}{r}, \tag{2.26}$$

where C and D are constants of integration. Applying the constant tempera-
ture boundary conditions yields

$$T_c(r) = \frac{r_e T_e - r_i T_i}{d} + \frac{\Delta T r_i r_e}{dr}. \tag{2.27}$$

A thermal conducting profile for a cylindrically symmetric thermal forcing can
be derived using a similar approach, though this would only be applicable to

length	$l \sim r_e$
time	$t \sim \Omega^{-1}$
velocity	$U \sim r_e\Omega$
temperature	$T \sim \Delta T$

Table 2.1: Characteristic scales used in non-dimensionalizing the equations.

cylindrical gravitationally forced systems outside the TC.

By assuming that the density is constant except in the buoyancy term, where it has been parameterized in terms of the thermal perturbations, we have reduced the system to solving five equations (continuity, three velocities and temperature) for five variables (pressure, three velocities and temperature).

2.8   Non-dimensionalization

For numerical computations it is preferable to recast the variables into order unity dimensionless units. This helps to avoid overflow and underflow errors. It also simplifies the analysis since the Buckingham Π theorem provides for a reduction in the number of independent parameters necessary to describe the system. In this case our system depends on ten physical parameters: outer radius, shell thickness, viscosity, thermal expansion coefficient, gravitational field strength, thermal diffusivity, velocity, temperature, density and pressure. However, the pressure and density only appear as a ratio, while the gravitational field strength and thermal expansion coefficient only appear as a product, reducing the number of independent parameters to eight. These variables depend on four dimensional units: length, time, temperature and mass. Thus, we we can recast the problem in terms of $8 - 4 = 4$ independent non-dimensional numbers.

We will take the characteristic length, time, velocity and temperature scales

to be those given in Table 2.1. Our equations of motion are invariant to a constant shift in temperature, since they only depend on relative temperatures, either with respect to the conductive profile or in the form of a thermal gradient across the shell. Thus we have the additional freedom to fix the absolute temperature by specifying that the outer boundary temperature is zero, $T'_e = 0$. Here the prime indicates a non-dimensionalized variable. Together, these non-dimensionalizations give the remaining boundary values of $r'_e = 1$, $r'_i = r_i/r_e$ and $T'_i = 1$. The dynamic variables become $\mathbf{u} = (r_e\Omega)\mathbf{u}'$, $T = (\Delta T)T'$ and $P = (\rho_0 r_e^2 \Omega^2)P'$ in non-dimensional units. This leads to the dimensionless equations of motion of

$$\frac{\partial \mathbf{u}}{\partial t} + (\mathbf{u} \cdot \boldsymbol{\nabla})\,\mathbf{u} + 2\hat{\mathbf{z}} \times \mathbf{u} = -\boldsymbol{\nabla}P + E\boldsymbol{\nabla}^2\mathbf{u} - Ra^* g_r \Theta\hat{\mathbf{g}}, \qquad (2.28)$$

and

$$\frac{\partial T}{\partial t} + \mathbf{u} \cdot \boldsymbol{\nabla}T = \frac{E}{Pr}\nabla^2 T. \qquad (2.29)$$

Formally the dynamic variables should have primes in the two preceding equations, but to simplify the notation we have dropped all primes and non-dimensionalized variables are implied from this point forward. The non-dimensionalized spherically symmetric conducting temperature profile in equation 2.27, and its radial derivative, are

$$T_c(r) = \frac{r_i}{d}\left(-1 + \frac{1}{r}\right) \qquad \text{and} \qquad \frac{\partial T_c}{\partial r} = -\frac{r_i}{dr^2}. \qquad (2.30)$$

These equations depend on the dimensionless Ekman number E (the ratio of viscous and Coriolis forces), Rayleigh number Ra (the ratio of buoyancy forces and the product of thermal and momentum diffusivities), and Prandtl

Input parameters	
Ekman number	$E = \frac{\nu}{\Omega r_e^2}$
Rayleigh number	$Ra = \frac{\alpha \Delta T g_o r_e^3}{\nu \kappa}$
Prandtl number	$Pr = \frac{\nu}{\kappa}$
Radius ratio	$\chi = \frac{r_i}{r_e}$
Output parameters	
Rossby number	$Ro = \frac{U}{\Omega r_e}$
Convective Rossby number	$\sqrt{Ra^*} = \sqrt{E^2 Ra Pr^{-1}} = \sqrt{\frac{\alpha \Delta T g_0}{\Omega^2 r_e}}$

Table 2.2: Definition of non-dimensional numbers of the system.

number Pr (the ratio of momentum and thermal diffusivity), which are defined in Table 2.2. Note that some authors use a length scale equal to the shell thickness to non-dimensionalize, rather than the shell radius, which leads to slightly different definitions of the Ekman and Rayleigh numbers. Care must be taken when comparing results to ensure that equivalent values are considered. The fourth non-dimensional number is the radius ratio χ.

While the four numbers defined above are the four independent non-dimensional parameters of the system, additional diagnostic or non-independent non-dimensional numbers can also be defined. The previously defined Rossby number is one example of this. In the vorticity equation above we have also defined the modified Rayleigh number, Ra^*, which is the ratio of buoyancy and Coriolis forces and depends on three non-dimensional parameters. The square root of the modified Rayleigh number is referred to as the convective Rossby number. When its value is less than unity the global force balance suggests that the system is rotationally dominated. However, experimental and numerical results demonstrate that the dynamics of the system are better predicted by the thicknesses of the boundary layers [60]. In this framework, if the Ekman viscous boundary layer is thinner then the thermal boundary layer then the

system is dominated by rotation.

2.9   Vorticity equation

While all of the dynamics of the system are specified by the continuity, momentum and heat equations, it will prove more convenient to work with the vorticity, rather than the velocity, of the flow. The vorticity, which is defined as $\boldsymbol{\omega} = \boldsymbol{\nabla} \times \mathbf{u}$, can be expanded in cylindrical coordinates as

$$\boldsymbol{\omega} = \begin{cases} \left(\dfrac{1}{s} \dfrac{\partial u_z}{\partial \phi} - \dfrac{\partial u_\phi}{\partial z} \right) \hat{\mathbf{s}} \\[2ex] \left(\dfrac{\partial u_s}{\partial z} - \dfrac{\partial u_z}{\partial s} \right) \hat{\boldsymbol{\phi}} \\[2ex] \left(\dfrac{1}{s} \dfrac{\partial s u_\phi}{\partial s} - \dfrac{1}{s} \dfrac{\partial u_s}{\partial \phi} \right) \hat{\mathbf{z}} \end{cases} . \tag{2.31}$$

Note that since the divergence of a curl is zero, the vorticity is divergenceless: $\boldsymbol{\nabla} \cdot \boldsymbol{\omega} = \boldsymbol{\nabla} \cdot (\boldsymbol{\nabla} \times \mathbf{u}) = 0$.

The curl of the dimensionless NS equation 2.28 gives the vorticity equation

$$\frac{\partial \boldsymbol{\omega}}{\partial t} - (\boldsymbol{\omega} \cdot \boldsymbol{\nabla}) \mathbf{u} + (\mathbf{u} \cdot \boldsymbol{\nabla}) \boldsymbol{\omega} - 2 \frac{\partial \mathbf{u}}{\partial z} = E \boldsymbol{\nabla}^2 \boldsymbol{\omega} - Ra^* \boldsymbol{\nabla} \times (g_r \Theta \hat{\mathbf{g}}) . \tag{2.32}$$

See Appendix A for the details of this calculation.

Since we are considering the $E \ll 1$ and $Ra^* \ll 1$ limits, the dominant linear term in this equation is the Coriolis: $\frac{\partial \mathbf{u}}{\partial z}$. In the steady state this term must be nearly zero, since there are no other large linear terms to balance it and the non-linear terms are small. Therefore the flow is rigid in the axial direction, which is consistent with the Taylor-Proudman theorem.

2.10 Boundary conditions

To completely specify the system, the four equations must be complemented by appropriate conditions for the temperature and velocity on the boundary of the shell at r_i and r_e. Since we are solving a second order differential equation, we require either the values or the radial derivative of all variables on both boundaries.

We have already fixed the value of the temperature on the shell to be $T(r_i) = 1$ and $T(r_e) = 0$ in non-dimensional units. The boundary is also taken to be impenetrable, which gives

$$u_n(L^{\pm}) \equiv \mathbf{u} \cdot \hat{\mathbf{n}}_{bc}\big|^{L^{\pm}} = 0, \tag{2.33}$$

where $\hat{\mathbf{n}}_{bc}$ is a unit vector normal to the surface directed outwards from the volume. Finally, we require that the flow at the boundary be stress free, which for a spherical shell gives in spherical coordinates

$$\frac{\partial u_\phi}{\partial r}\bigg|^{L^{\pm}} = \frac{u_\phi}{r} \qquad \frac{\partial u_\theta}{\partial r}\bigg|^{L^{\pm}} = \frac{u_\theta}{r}. \tag{2.34}$$

These conditions can be combined to impose constraints on the vorticity at the boundary. See Appendix B for their full derivation.

Chapter 3

Two dimensional equations

3.1   Limiting geostrophic cases

In the rapid rotation limit, with $E << 1$, the dominant steady state balance near onset, where the non-linear terms are small, in the Navier-Stokes equation 2.28 is a balance between the Coriolis term, pressure gradient and buoyancy

$$2\hat{\mathbf{z}} \times \mathbf{u} = -\boldsymbol{\nabla}P - Ra^* g_r \Theta \hat{\mathbf{g}}. \tag{3.1}$$

The equivalent dominant balance in the vorticity equation 2.32 is

$$-2\frac{\partial \mathbf{u}}{\partial z} = -Ra^* \boldsymbol{\nabla} \times (\Theta g_r \hat{\mathbf{g}}) . \tag{3.2}$$

If we decompose the buoyant forcing into cylindrical coordinates as $g_r \hat{\mathbf{g}} = -g_r \hat{\mathbf{r}} \equiv -g_s \hat{\mathbf{s}} - g_z \hat{\mathbf{z}}$ for a spherical gravitational field, we can write the cylindrical components of these momentum and vorticity balances as

$$-2u_\phi = -\frac{\partial P}{\partial s} + Ra^* g_s \Theta \tag{3.3}$$

$$2u_s = -\frac{1}{s}\frac{\partial P}{\partial \phi} \tag{3.4}$$

$$0 = -\frac{\partial P}{\partial z} + Ra^* g_z \Theta, \tag{3.5}$$

and

$$2\frac{\partial u_s}{\partial z} = -Ra^* \left(\frac{1}{s}\frac{\partial (\Theta g_z)}{\partial \phi} \right) \tag{3.6}$$

$$2\frac{\partial u_\phi}{\partial z} = -Ra^* \left(\frac{\partial (\Theta g_s)}{\partial z} - \frac{\partial (\Theta g_z)}{\partial s} \right) \tag{3.7}$$

$$2\frac{\partial u_z}{\partial z} = -Ra^* \left(-\frac{1}{s}\frac{\partial (\Theta g_s)}{\partial \phi} \right). \tag{3.8}$$

In the following subsections we will consider three illustrative limits of these equations for thermal convection under rotation.

3.1.1 No buoyant forcing

The first case we will consider is the unforced $Ra^* = 0$ limit. This can be understood as the limit of $\Delta T \to 0$. In this limit we recover the Taylor-Proudman theorem from the vorticity equation

$$\frac{\partial \mathbf{u}}{\partial z} = \mathbf{0}, \tag{3.9}$$

so the steady state flow is invariant along the axis of rotation.

From the momentum equation we find that

$$\frac{\partial P}{\partial z} = 0, \tag{3.10}$$

55

and thus the planar velocities

$$u_\phi = \frac{1}{2}\frac{\partial P}{\partial s} \quad \text{and} \quad u_s = -\frac{1}{2}\frac{1}{s}\frac{\partial P}{\partial \phi}, \tag{3.11}$$

must be a rigid geostrophic wind, balanced by a rigid pressure. Also, the axial velocity must be constant with z. So in summary, in an unforced geostrophic system the flow is invariant parallel to the rotation axis.

3.1.2 Buoyant forcing perpendicular to the rotation axis

In the case of buoyant forcing perpendicular to the rotation axis $g_z = 0$, and we can take $g_s = 1$ for a constant gravitational field. Formally, this case is only valid for convection in the equatorial plane outside the TC. However, even for the relatively thick spherical shell that will be used in some simulations in the present thesis with $d = 0.25$, for spherically symmetric gravitational forcing $|g_z| = |\cos\theta| < |\cos\theta_{TC}| = |L^+(r_i)| \sim 0.66$ everywhere outside the TC. The axially averaged magnitude for any Taylor column will be much less than this. Thus, this limit is generally applicable outside the TC. In this case the momentum equation gives

$$-2u_\phi = -\frac{\partial P}{\partial s} + Ra^*\Theta \tag{3.12}$$

$$2u_s = -\frac{1}{s}\frac{\partial P}{\partial \phi} \tag{3.13}$$

$$0 = -\frac{\partial P}{\partial z}, \tag{3.14}$$

while the vorticity equation gives

$$2\frac{\partial u_s}{\partial z} = 0 \tag{3.15}$$

$$2\frac{\partial u_\phi}{\partial z} = -Ra^*\frac{\partial \Theta}{\partial z} \tag{3.16}$$

$$2\frac{\partial u_z}{\partial z} = +Ra^*\frac{1}{s}\frac{\partial \Theta}{\partial \phi}. \tag{3.17}$$

In this case the geostrophic balance is modified by buoyancy. However, if $Ra^* << 1$ we expect that the first order flow will still be rigid. If we assume that the thermal perturbations are also rigid to first order, which is sensible since they are generated by the advection of the background thermal profile by the rigid u_s, then we can conclude that

$$\frac{\partial \mathbf{u}_\perp}{\partial z} = \mathbf{0} \qquad \text{and} \qquad \frac{\partial u_z}{\partial z} = f(s,\phi), \tag{3.18}$$

where $\mathbf{u}_\perp = (u_s, u_\phi)$ is the planar velocities. Thus, the thermal forcing does not alter the rigidity of the planar flow, but introduces a z-dependence to the axial velocity. If the thermal perturbations are rigid to first order, the axial velocity will have a linear variation with z.

3.1.3 Buoyant forcing parallel to the rotation axis

In the case of gravitational forcing parallel to the rotation axis $g_s = 0$, and for a constant gravitational field we can take $g_z = 1$. This is the geometry of the canonical Rayleigh-Bénard problem, which is exactly applicable at the pole. However, analogous to the argument in the previous subsection this picture is approximately applicable inside the TC since in this region the buoyant forcing is dominantly aligned with the rotating axis. In this limit the momentum equation is

$$-2u_\phi = -\frac{\partial P}{\partial s} \tag{3.19}$$

$$2u_s = -\frac{1}{s}\frac{\partial P}{\partial \phi} \tag{3.20}$$

$$0 = -\frac{\partial P}{\partial z} + Ra^*\Theta, \tag{3.21}$$

and the vorticity equation gives

$$2\frac{\partial u_s}{\partial z} = -Ra^*\frac{1}{s}\frac{\partial \Theta}{\partial \phi} \tag{3.22}$$

$$2\frac{\partial u_\phi}{\partial z} = +Ra^*\frac{\partial \Theta}{\partial s} \tag{3.23}$$

$$2\frac{\partial u_z}{\partial z} = 0. \tag{3.24}$$

In this case we find that the axial velocity remains rigid. Meanwhile, the buoyant forcing is balanced by a pressure gradient in the axial direction. The planar flow still obeys a geostrophic balance, however because the pressure now varies with z so too does the planar flow. This shear in the geostrophic wind is referred to as a thermal wind. If we again assume that the thermal perturbations are rigid, then the pressure and planar flow must both vary linearly in z. Thus, the first order velocities are

$$\frac{\partial \mathbf{u}_\perp}{\partial z} = \mathbf{f}(s, \phi) \qquad \text{and} \qquad \frac{\partial u_z}{\partial z} = 0. \tag{3.25}$$

If the second result was strictly true then there could be no convection across the fluid layer, since this requires variations in u_z to meet the boundary conditions. However boundary layers can develop in which additional forces become large, breaking this constraint.

3.1.4 Summary

In summary, for a rapidly rotating system $(E << 1)$ with modest thermal forcing $(Ra^* << 1)$, the first order picture of convective flows in a spherical shell is a geostrophic balance with

$$
\left.
\begin{array}{l}
\mathbf{u}_\perp = \text{linear in } z \\[1em]
u_z = \text{independent of } z
\end{array}
\right\} \qquad s < r_i \qquad \text{inside TC}, \qquad (3.26)
$$

$$
\left.
\begin{array}{l}
\mathbf{u}_\perp = \text{independent of } z \\[1em]
u_z = \text{linear in } z
\end{array}
\right\} \qquad s > r_i \qquad \text{outside TC}. \qquad (3.27)
$$

Since the linear terms are proportional to Ra^*, we expect that the flow will be dominantly rigid in the mid-latitude regions where the buoyancy in both directions contributes.

To describe fully the dynamics we must also consider the viscous forces and non-linear terms in the momentum balance. Viscosity should not alter this first order description provided we are in the $E << 1$ limit. If the fluid is not too far beyond the onset of convection, such that the buoyancy forcing remains small relative to the Coriolis force $(Ra^* << 1)$, the fluid velocities should also be small as measured by the Rossby number: $Ro << 1$. In this case the non-linear terms will be small and we should not be too far from the first order geostrophic balance described above.

QG models have been developed which assume the fluid is dominantly geostrophic, with ageostrophic perturbations about this state. However, existing QG models only consider convection outside the TC. They simulate rigid, geostrophic planar velocities and thermal perturbations in a 2D equatorial slice, while parameterizing the effects of the non-rigid axial velocities on

the rigid variables. Also, only the cylindrical radial buoyancy component is considered, so that the axial velocity is not forced. To extend the QG model inside the TC we will take an analogous approach. The rigid temperatures and axial velocities generated by axial buoyancy will be evolved on a 2D $s - \phi$ domain, while parameterizing the effects of the non-rigid planar velocities on the dynamics of the rigid variables. Since convection inside the TC is not purely that of a plane layer heated from below, but rather is some intermediate state between the two extreme cases presented in the previous subsections, we will also model the cylindrical radial buoyancy, and the rigid planar velocities it generates, inside the TC. It is hoped that by simulating all the rigid variables we can capture the leading order dynamics of rotationally dominated convection, including the generation of zonal jets, both inside and outside the TC.

3.2 Interactions of rigid flows with boundaries

In the previous section it was shown that the first order geostrophic flow is rigid. In addition to the shear induced by buoyancy, the boundary conditions of the convection shell prevent the flow from being completely rigid. This ageostrophic effect turns out to play a much more significant role for rotationally dominated flow. Let us assume that the flow can be decomposed into a geostrophic component and an ageostrophic perturbation about this state

$$\mathbf{u} = \mathbf{u}^g + \mathbf{u}^a, \tag{3.28}$$

where a superscript g (x^g) indicates the geostrophic component of a variable, and a superscript a (x^a) indicates the ageostrophic component. We will assume that the non-rigidities induced by buoyancy are small, so that the geostrophic component is rigid. Thus,

$$\frac{\partial \mathbf{u}^g}{\partial z} \sim \mathbf{0} \qquad \text{but} \qquad \frac{\partial \mathbf{u}^a}{\partial z} \neq \mathbf{0}. \qquad (3.29)$$

As described in the previous section, in the present work we will simulate the dynamics of only the geostrophic flow. To do so we must parameterize the effects of the ageostrophic flow on the geostrophic flow. In the following subsections we will use the impenetrability of the boundary and the incompressibility of the flow to derive a relationship between the two components.

3.2.1   Impenetrability of boundary induced flow

On the upper and lower shell boundary, for a general flow,

$$u_n(L^\pm) \equiv \mathbf{u} \cdot \hat{\mathbf{n}}_{bc}\big|^{L^\pm}$$
$$= u_z(L^\pm)\, \hat{\mathbf{z}} \cdot \hat{\mathbf{n}}_{bc}\big|^{L^\pm} + u_s(L^\pm)\, \hat{\mathbf{s}} \cdot \hat{\mathbf{n}}_{bc}\big|^{L^\pm} + u_\phi(L^\pm)\, \hat{\boldsymbol{\phi}} \cdot \hat{\mathbf{n}}_{bc}\Big|^{L^\pm}. \qquad (3.30)$$

Rearranging for the axial flow gives

$$u_z(L^\pm) = \frac{\mathbf{u} \cdot \hat{\mathbf{n}}_{bc}\big|^{L^\pm}}{\hat{\mathbf{z}} \cdot \hat{\mathbf{n}}_{bc}\big|^{L^\pm}} - u_s(L^\pm)\frac{\hat{\mathbf{s}} \cdot \hat{\mathbf{n}}_{bc}\big|^{L^\pm}}{\hat{\mathbf{z}} \cdot \hat{\mathbf{n}}_{bc}\big|^{L^\pm}} - u_\phi(L^\pm)\frac{\hat{\boldsymbol{\phi}} \cdot \hat{\mathbf{n}}_{bc}\big|^{L^\pm}}{\hat{\mathbf{z}} \cdot \hat{\mathbf{n}}_{bc}\big|^{L^\pm}}. \qquad (3.31)$$

An arbitrary surface geometry can be implicitly defined as the collection of points which satisfy the relation $f(s, \phi, z) = 0$. The normal vector to level sets of the function f is equal to the gradient of f, provided that it is not the null

vector, so at any point on the surface the normal is

$$\mathbf{n}_{bc}|^{L^\pm} = (\boldsymbol{\nabla} f)|^{L^\pm} \qquad \text{and} \qquad \hat{\mathbf{n}}_{bc}|^{L^\pm} = \frac{(\boldsymbol{\nabla} f)|^{L^\pm}}{|\boldsymbol{\nabla} f|^{L^\pm}}. \qquad (3.32)$$

This allows us to write equation 3.31 as

$$u_z(L^\pm) = \frac{\mathbf{u}\cdot\hat{\mathbf{n}}_{bc}|^{L^\pm}}{\hat{\mathbf{z}}\cdot\hat{\mathbf{n}}_{bc}|^{L^\pm}} - u_s(L^\pm)\frac{|\boldsymbol{\nabla} f|^{L^\pm}\frac{\partial f}{\partial s}\big|^{L^\pm}}{|\boldsymbol{\nabla} f|^{L^\pm}\frac{\partial f}{\partial z}\big|^{L^\pm}} - u_\phi(L^\pm)\frac{|\boldsymbol{\nabla} f|^{L^\pm}\frac{1}{s}\frac{\partial f}{\partial\phi}\big|^{L^\pm}}{|\boldsymbol{\nabla} f|^{L^\pm}\frac{\partial f}{\partial z}\big|^{L^\pm}}. \qquad (3.33)$$

If we assume that the surface is axisymmetric then $\frac{\partial f}{\partial\phi} = 0$ and the third term is zero. If we utilize no-penetration boundary conditions, $\mathbf{u}\cdot\hat{\mathbf{n}}_{bc}|^{L^\pm} = 0$ on the boundary and the first term can be dropped.

Provided that our surface is mathematically smooth and the first derivatives of f are non-zero throughout the domain, we can use the fact that f is constant on the surface to perform a chain rule differentiation to get

$$0 = df|^{L^\pm} = ds\left.\frac{\partial f}{\partial s}\right|^{L^\pm} + dz\left.\frac{\partial f}{\partial z}\right|^{L^\pm}, \qquad (3.34)$$

and thus

$$\frac{\frac{\partial f}{\partial s}\big|^{L^\pm}}{\frac{\partial f}{\partial z}\big|^{L^\pm}} = -\left.\frac{dz}{ds}\right|^{L^\pm} \equiv -\frac{\partial L^\pm}{\partial s}. \qquad (3.35)$$

This allows us to write the unit surface normal (again assuming axisymmetry) as

$$\hat{\mathbf{n}}_{bc}|^{L^\pm} = (\hat{\mathbf{n}}_{bc}\cdot\hat{\mathbf{s}}|^{L^\pm}, \hat{\mathbf{n}}_{bc}\cdot\hat{\boldsymbol{\phi}}\big|^{L^\pm}, \hat{\mathbf{n}}_{bc}\cdot\hat{\mathbf{z}}|^{L^\pm}) = \hat{\mathbf{n}}_{bc}\cdot\hat{\mathbf{z}}|^{L^\pm}\left(\frac{\hat{\mathbf{n}}_{bc}\cdot\hat{\mathbf{s}}|^{L^\pm}}{\hat{\mathbf{n}}_{bc}\cdot\hat{\mathbf{z}}|^{L^\pm}}, 0, 1\right)$$

$$= \hat{\mathbf{n}}_{bc}\cdot\hat{\mathbf{z}}|^{L^\pm}\left(\frac{\boldsymbol{\nabla} f\cdot\hat{\mathbf{s}}|^{L^\pm}}{\boldsymbol{\nabla} f\cdot\hat{\mathbf{z}}|^{L^\pm}}, 0, 1\right) = \hat{\mathbf{n}}_{bc}\cdot\hat{\mathbf{z}}|^{L^\pm}\left(-\frac{\partial L^\pm}{\partial s}, 0, 1\right), \qquad (3.36)$$

except when $\hat{\mathbf{n}}_{bc} \cdot \hat{\mathbf{z}}\big|^{L^\pm} = 0$ on vertical surfaces. Thus,

$$u_z(L^\pm) = -\frac{\hat{\mathbf{s}} \cdot \hat{\mathbf{n}}_{bc}\big|^{L^\pm}}{\hat{\mathbf{z}} \cdot \hat{\mathbf{n}}_{bc}\big|^{L^\pm}} u_s(L^\pm) = \frac{dz}{ds}\bigg|^{L^\pm} u_s(L^\pm) \equiv \frac{dL^\pm}{ds} u_s(L^\pm). \tag{3.37}$$

In the case of spherical boundaries,

$$u_z(L^\pm) = -\frac{s}{L^\pm} u_s(L^\pm) = -\tan(\theta^\pm) u_s(L^\pm), \tag{3.38}$$

where we have utilized the explicit definition of $L^\pm$ for the spherical shell surface. Here $\theta^\pm$ is the angle made by $\hat{\mathbf{n}}_{bc}$ with the vertical $\hat{\mathbf{z}}$ on the boundary at $z = L^\pm$.

Now we can clearly see that if u_s, for example, is purely rigid, then $u_s(L^+) = u_s(L^-) \equiv u_s^g$ and thus in general $u_z(L^+) \neq u_z(L^-)$, except in the case that $\theta^+ = \theta^-$, since the tan function is injective over the domain. For our geometry, this implies that u_z cannot be rigid unless $\frac{s}{L^+} = \frac{s}{L^-}$ which can be rearranged to $L^+ = L^-$. Since this is only satisfied in the degenerate case of a shell of vanishing thickness, $d = 0$, and at the equator, we must allow for some non-rigidity in the axial velocity to satisfy the boundary conditions. Thus, an axially invariant component of u_s necessarily generates a non-rigid component of u_z. Likewise, a rigid u_z generates non-rigid u_s.

3.2.2 Incompressibility of boundary induced flow

In addition to the impenetrable boundary condition, we must also ensure that these non-rigid boundary induced flows remain incompressible. Figure 3.1 shows a Gaussian surface located at the outer spherical boundary, which is assumed to be infinitely small. A, B and C are the surface areas of the $s - \phi$,

$z - \phi$ and $\theta - \phi$ surfaces respectively, while α is the angle made by the boundary with respect to the horizontal. From similar triangles we can conclude that $\alpha = \theta^+$. For an infinitely small Gaussian surface we can ignore the curvature of surface C to get $\frac{B}{A} \sim -\frac{\partial L^+}{\partial s}$.

Using the integral form of the incompressible condition gives

$$
\begin{aligned}
0 &= \iiint_V (\boldsymbol{\nabla} \cdot \mathbf{u}) \, dV \\
&= \oint_S (\mathbf{u} \cdot \hat{\mathbf{n}}) \, dS \\
&= - Alu_z(L^+) - Blu_s(L^+) + Cl \, \mathbf{u} \cdot \hat{\mathbf{n}}|^{L^+} ,
\end{aligned}
\tag{3.39}
$$

where l is the length of the surface in the $\hat{\boldsymbol{\phi}}$ direction. From the impenetrability condition we know that $\mathbf{u} \cdot \hat{\mathbf{n}}|^{L^+} = 0$, so the incompressibility relation is

$$
\begin{aligned}
Alu_z(L^+) &= -Blu_s(L^+) \\
u_z(L^+) &= \frac{\partial L^+}{\partial s} u_s(L^+).
\end{aligned}
\tag{3.40}
$$

The same argument applies to the flow at the inner boundary.

This is exactly the same relation between the velocity components as derived in equation 3.37 from the impenetrable condition. Therefore, this prescription accounts for both the impenetrability of the boundary and for the necessity for flow to escape along the boundary to remain divergenceless. Had this not been the case, a non-rigid u_ϕ component would have been required to ensure the fluid remained incompressible. Since such a flow is not induced by an axisymmetric boundary in the present framework, we will assume that the non-rigid azimuthal velocity vanishes.
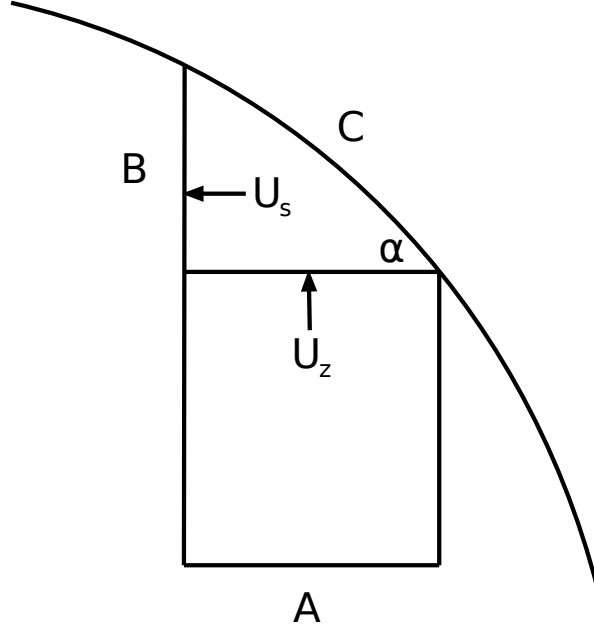
Figure 3.1: This image shows a $s-z$ cross section of the flow though a Gaussian surface located at the boundary.

3.3 Z-averaging

Now that we have the equations of the system developed, we would like to exploit the expected 2D flow structure. We do this by integrating the equations of motion over Taylor columns aligned with the rotation axis and spanning the entire width of the shell to average over small departures from rigid two-dimensionality. The ageostrophic components will contribute to the boundary conditions of the integral.

The z average of variables is defined as

$$\langle f \rangle (s, \phi) = \frac{1}{\Delta L} \int_{L^-}^{L^+} f(s, \phi, z) dz, \tag{3.41}$$

where $\Delta L = L^+ - L^-$. For variables which are independent of z averaging has

no effect, so

$$\langle f(s, \phi) \rangle = f(s, \phi). \tag{3.42}$$

While z averaging commutes with time and azimuthal derivatives, it does not with s-derivatives, since the limits of integration at the shell boundary are themselves functions of s. Using the Leibniz integral theorem,

$$\frac{\partial}{\partial s} \int_{a(s)}^{b(s)} f(s, z) dz = \int_{a(s)}^{b(s)} \frac{\partial}{\partial s} f(s, z) dz + f(s, b) \frac{\partial b}{\partial s} - f(s, a) \frac{\partial a}{\partial s}, \tag{3.43}$$

which in our notation is equivalent to

$$\frac{\partial}{\partial s} \left(\Delta L \langle f \rangle \right) = \Delta L \left\langle \frac{\partial f}{\partial s} \right\rangle + f(z = L^+) \frac{\partial L^+}{\partial s} - f(z = L^-) \frac{\partial L^-}{\partial s}. \tag{3.44}$$

Therefore, the average of the cylindrical radial derivative of a variables is

$$\left\langle \frac{\partial f}{\partial s} \right\rangle = \frac{\partial}{\partial s} \langle f \rangle + \beta \langle f \rangle - \frac{1}{\Delta L} \left(f(L^+) \frac{\partial L^+}{\partial s} - f(L^-) \frac{\partial L^-}{\partial s} \right). \tag{3.45}$$

Here we have defined

$$\beta \equiv \frac{1}{H} \frac{\partial H}{\partial s}, \tag{3.46}$$

where $H \equiv \Delta L = L^+ - L^-$ is the axial height of the convection shell.

For spherical shell geometry the commutation rule is

$$\left\langle \frac{\partial f}{\partial s} \right\rangle = \frac{\partial}{\partial s} \langle f \rangle - \frac{1}{\Delta L} \left(-\frac{s}{L^+} \left[f(L^+) - \langle f \rangle \right] + \frac{s}{L^-} \left[f(L^-) - \langle f \rangle \right] \right), \tag{3.47}$$

where we have used

$$\frac{dL^\pm}{ds} = -\frac{s}{L^\pm} \qquad \text{and thus} \qquad \beta = \frac{s}{L^+ L^-}. \tag{3.48}$$

66

These relations are valid both inside and outside the TC.

3.3.1   Limits of integration

The limits of integration utilized for evaluating the averages depends on the physics of the variables being averaged. This choice is dictated by the philosophy discussed in previous sections: to model the rigid components of variables and parameterize the effects of the non-rigidities on the rigid components. For the velocities, we will assume stress free mechanical boundary conditions so there should not be a significant boundary layer for the flow and Ekman layers are neglected. The geostrophic velocities can be rigid across the entire shell. Since in this case the flow's dynamics are dictated by its interaction with shell boundary, we will average the flow equations over the entire shell. Conversely, while the thermal perturbations should be mostly rigid in the bulk, there will be a significant thermal boundary layer since while heat convects through the bulk it must conduct through the boundary layer due to the no-penetration condition. The dynamics of the rigid bulk thermal perturbations are influenced by its interaction with a thermal boundary layer. Thus for the heat equation we will only integrate over the bulk of the fluid, where the thermal perturbations are rigid, and parameterize the effects of the thermal boundary layer on the rigid thermal perturbations.

For the axial velocity the averaging is defined slightly differently. Since outside the TC we expect the axial velocity to be antisymmetric about the equatorial plane for a spherical shell due to the symmetry of the system, its full shell average would vanish. Instead, we take only the upper hemisphere average outside the TC. The lower bound of our half-shell integral is notated

as $L^{1/2}$, which is defined to be $L^{1/2} = L^-$ inside the TC and $L^{1/2} = 0$ outside.

3.4   Velocities

Since we will be axially averaging our equations of motion, we will need the averaged values of the velocities and their derivatives. To completely model the system with just the geostrophic variables, this requires a parameterization of the z dependence of the ageostrophic components in terms of the geostrophic variables.

Firstly, under the assumption that the flow is dominantly geostrophic, and that the geostrophic flow is rigid to first order as in equation 3.29, we have

$$\langle \mathbf{u} \rangle = \langle \mathbf{u}^g + \mathbf{u}^a \rangle \sim \langle \mathbf{u}^g \rangle \sim \mathbf{u}^g \qquad \text{or} \qquad \langle \mathbf{u}^a \rangle \sim \mathbf{0}. \tag{3.49}$$

For the axial flow the above averages are single hemisphere averages outside the TC since as discussed in the previous section the two hemisphere average would be zero due to the antisymmetry of the axial flow here. Formally, the assumption of equation 3.49 could break down when $|\beta| \gg 1$ and the geostrophic flow induces large ageostrophic components due to a large boundary slope, however the entire QG framework breaks down in this limit.

If u_s is purely geostrophic, and there is no geostrophic u_z, equation 3.37 gives the induced ageostrophic u_z at the boundaries to be

$$u_z(L^\pm) = u_z^a(L^\pm) = \frac{\partial L^\pm}{\partial s} u_s(L^\pm) = \frac{\partial L^\pm}{\partial s} u_s^g \sim \frac{\partial L^\pm}{\partial s} \langle u_s \rangle. \tag{3.50}$$

Conversely, if u_z is purely geostrophic, and there is no geostrophic u_s, the

ageostrophic u_s induced at the boundaries is

$$u_s(L^\pm) = u_s^a(L^\pm) = \frac{u_z(L^\pm)}{\frac{\partial L^\pm}{\partial s}} = \frac{u_z^g}{\frac{\partial L^\pm}{\partial s}} \sim \pm \frac{\langle u_z \rangle}{\frac{\partial L^\pm}{\partial s}}, \tag{3.51}$$

where the sign is positive inside the TC and on the upper boundary outside the TC, and negative outside the TC on the lower boundary due to the anti-symmetry of u_z outside the TC.

In general there will be both geostrophic components of u_s and u_z, each of which will induce an ageostrophic component when interacting with the impenetrable boundary. In this case the boundary velocities will be the superposition of the two components such that

$$u_z(L^\pm) = u_z^g + u_z^a(L^\pm) = \pm \langle u_z \rangle + \frac{\partial L^\pm}{\partial s} \langle u_s \rangle \tag{3.52}$$

$$u_s(L^\pm) = u_s^g + u_s^a(L^\pm) = \langle u_s \rangle \pm \frac{\langle u_z \rangle}{\frac{\partial L^\pm}{\partial s}} \tag{3.53}$$

$$u_\phi(L^\pm) = u_\phi^g + u_\phi^a(L^\pm) = \langle u_\phi \rangle, \tag{3.54}$$

where the sign is taken as previously specified. Here we have taken $u_\phi^a \sim 0$. In principle there could be an ageostrophic azimuthal velocity component. However, as discussed in Section 3.2.2, because such motion is not induced by an axisymmetric boundary and not required by incompressibility, it should be small and thus we will not consider it here.

The physical interpretation of this parameterization is as follows. Unlike in the traditional QG framework, in which only the cylindrical radial component of buoyancy is considered, including buoyancy forcing parallel to the rotation axis requires that we allow for the possibility of a rigid geostrophic u_z, in addition to the ageostrophic contribution from the topographic beta-effect.

69

However, such motion requires that our rigidity assumptions break down in a boundary layer so as to adjust to the boundary conditions. Inside the TC axial buoyancy can set up a scenario in which hot fluid rigidly floats upwards in the $\hat{z}$ direction out of the inner boundary layer, through the bulk of the fluid, and into the outer boundary layer. The boundary conditions force the rising fluid to disperse parallel to the surface within the boundary layer, giving rise to a shear in the fluid motion relative to the rigid columnar flow in the bulk in the form of an ageostrophic contribution to u_s. The boundary layer flow eventually cools and sinks back into the bulk of the fluid, allowing for the upwelling fluid to be returned downwards. This circulation feeds thermal plumes which transport heat across the shell, and acts as a feedback to reinforce the circulation. Hot rising fluid advects hot fluid from the inner boundary layer into the bulk and in the process raises the average temperature of the Taylor column. This increases its buoyancy and forces it to rise faster, and in the process advects even more hot fluid into the bulk.

Outside the TC this process is more complicated. Whereas inside the TC the geostrophic u_z is constant across the shell and the return flow is fed by circulation within the boundary layer, where geostrophy is expected to be broken, outside the TC symmetry demands that u_z must be antisymmetric across the equatorial plane. Therefore the return flow required by incompressibility would need to be along the equatorial plane, breaking the rigid geostrophic planar flow we expect in the bulk. Also, this flow would only be reinforced by buoyancy if there were thermal reserves along the equatorial plane, and it is unlikely that a hot layer could be sustained here. Once the fluid becomes well mixed in z it would not be possible for hot plumes to be formed by axial convection. Therefore, we will only allow for a geostrophic u_z inside the TC

in the present implementation.

Incompressibility requires equal quantities of fluid entering and exiting the bulk. For the non-axisymmetric components of the axial velocity this is automatically satisfied. In principal there could be axisymmetric axial velocity, provided that each region with a net axisymmetric flow into the boundary layer is compensated for by another region with a net axisymmetric flow out of the boundary layer. A surface integral over the interface between the boundary layer and the bulk must find no net flow into the boundary layer. The two regions would need to be connected by ageostrophic flow within the boundary layer. To simplify the model we will not consider such motion, instead taking the axisymmetric axial velocity to vanish $\overline{\langle u_z \rangle} = 0$, where the overbar indicates an azimuthal average. This guarantees that mass is conserved at each cylindrical radius.

The axial averages of the derivatives of the velocities are derived in Appendix C.1 using the parameterization of the flow on the boundary defined in equations 3.52-3.54. With $\langle u_z \rangle = 0$ outside the TC, two of these identities are

$$\left\langle \frac{\partial u_z}{\partial z} \right\rangle = \beta \langle u_s \rangle \qquad \text{and} \qquad \left\langle \frac{\partial u_s}{\partial s} \right\rangle = \frac{\partial \langle u_s \rangle}{\partial s}. \tag{3.55}$$

With these, the z-averaged incompressibility equation can be calculated to be

$$\langle \boldsymbol{\nabla} \cdot \mathbf{u} \rangle = \left\langle \frac{1}{s} \frac{\partial}{\partial s} (s u_s) + \frac{1}{s} \frac{\partial u_\phi}{\partial \phi} + \frac{\partial u_z}{\partial z} \right\rangle = \langle 0 \rangle$$

$$\frac{1}{s} \frac{\partial}{\partial s} (s \langle u_s \rangle) + \frac{1}{s} \frac{\partial \langle u_\phi \rangle}{\partial \phi} + \left\langle \frac{\partial u_z}{\partial z} \right\rangle = 0$$

$$\frac{1}{s} \frac{\partial}{\partial s} (s \langle u_s \rangle) + \frac{1}{s} \frac{\partial \langle u_\phi \rangle}{\partial \phi} + \beta \langle u_s \rangle = 0$$

$$\boldsymbol{\nabla}_\perp \cdot \langle \mathbf{u}_\perp \rangle + \beta \langle u_s \rangle = 0. \tag{3.56}$$

Here $\mathbf{u}_\perp$ and $\boldsymbol{\nabla}_\perp$ are the projections of $\mathbf{u}$ and $\boldsymbol{\nabla}$ respectively into the 2D equatorial plane.

3.5 Heat flux

The Nusselt number Nu is defined as the ratio of the total heat flux through a surface in the system to the heat flux through the same surface when only conduction transports heat. Mathematically it is defined as

$$\mathrm{Nu} = \frac{\mathbf{q} \cdot \hat{\mathbf{n}}}{\mathbf{q_c} \cdot \hat{\mathbf{n}}}, \tag{3.57}$$

where $\mathbf{q}$ is the total heat flux and $\mathbf{q_c}$ is the hydrostatic conductive heat flux, with $\hat{\mathbf{n}}$ the unit normal to the surface through which the heat flux is being evaluated. While Nu is a locally defined variable at each point in space, we will only consider its axisymmetric component by azimuthally averaging it, while retaining its s-dependence. The conductive heat flux is by definition axisymmetric for an axisymmetric convection shell and thermal boundary conditions.

In general the heat flux is comprised of two components, the conductive and convective heat fluxes. These can be determined in our non-dimensional units by writing the heat equation 2.29 as

$$\begin{aligned} \frac{\partial T}{\partial t} &= -\mathbf{u} \cdot \boldsymbol{\nabla} T + \frac{E}{Pr} \nabla^2 T \\ &= -\boldsymbol{\nabla} \cdot (T\mathbf{u}) + T \boldsymbol{\nabla} \cdot \mathbf{u} + \frac{E}{Pr} \nabla^2 T \\ &= -\frac{E}{Pr} \boldsymbol{\nabla} \cdot \left(-\boldsymbol{\nabla} T + \frac{Pr}{E} T\mathbf{u} \right) \\ &\equiv -\frac{E}{Pr} \boldsymbol{\nabla} \cdot \mathbf{q}, \end{aligned} \tag{3.58}$$

where we have used the incompressibility of the fluid. Thus, the local heat flux is

$$\mathbf{q} = -\boldsymbol{\nabla}T + \frac{Pr}{E}T\mathbf{u}. \tag{3.59}$$

The hydrostatic conductive heat flux in spherical coordinates is equal to $\mathbf{q_c} = -\boldsymbol{\nabla}T_c = \frac{r_i}{dr^2}\hat{\mathbf{r}}$, where we have used equation 2.30 for T_c. If we decompose Nu into cylindrical coordinates, and assume a spherical surface with unit normal $\hat{\mathbf{n}} = \hat{\mathbf{r}}$, we get an axisymmetric Nusselt number of

$$
\begin{aligned}
Nu(s) &= \frac{\overline{q_s}\hat{\mathbf{s}} \cdot \hat{\mathbf{r}} + \overline{q_z}\hat{\mathbf{z}} \cdot \hat{\mathbf{r}}}{\overline{\mathbf{q_c}} \cdot \hat{\mathbf{r}}} \\
&= \frac{\left(-\frac{\partial\overline{T}}{\partial s} + \frac{Pr}{E}\overline{Tu_s}\right)\frac{s}{r} + \left(-\frac{\partial\overline{T}}{\partial z} + \frac{Pr}{E}\overline{Tu_z}\right)\frac{z}{r}}{\frac{r_i}{dr^2}} \\
&= \left(-s\frac{\partial\overline{T}}{\partial s} - z\frac{\partial\overline{T}}{\partial z} + \frac{Pr}{E}\overline{T(zu_z + su_s)}\right)\frac{dr}{r_i}. \tag{3.60}
\end{aligned}
$$

Evaluating this further within our 2D QG framework forces us to address several difficulties with our parameterization. The Nusselt number is defined in terms of three dimensional variables, while the result of our model only provides us with their axially averaged values. We wish to calculate the heat flux at the outer shell boundary, so as to compare with both three dimensional results and surface observations, but it is precisely here that the QG rigidity assumptions break down. The temperature must be non-rigid near the boundary since while the heat flux through the bulk is dominantly convective, the impenetrability of the boundary requires that the heat flux be exclusively conductive through the boundary. Therefore, we will calculate the total heat flux, both convective and conductive, through a surface in the bulk near the

boundary and assume that this is equivalent to the surface heat flux, albeit in a different form.

The z-average of the 3D conducting temperature is equal to

$$\langle T_c \rangle = \left\langle \frac{r_i}{d} \left(-1 + \frac{1}{r} \right) \right\rangle \tag{3.61}$$

$$= \frac{r_i}{d} \left(-1 + \left\langle \frac{1}{r} \right\rangle \right)$$

$$= \frac{r_i}{d} \left(-1 + \frac{1}{\Delta L} \left(\operatorname{arcsinh} \left(\frac{L^+}{s} \right) - \operatorname{arcsinh} \left(\frac{L^-}{s} \right) \right) \right), \tag{3.62}$$

where we have used equation C.61 from Appendix C.5 to evaluate the average. This function, which is plotted in figure 3.2 for the two shell thicknesses considered in this thesis, has a prominent cusp at the TC. Inside the TC its value at points closer to the TC is larger because Taylor columns include a longer segment close to the inner boundary, whose tangent approaches vertical at the TC. Outside the TC its value at points closer to the TC also increases as all points on a Taylor column are closer to the inner boundary. Thus $\langle T_c \rangle$ has a local maximum at the TC. This implies that even though for all points in 3D $\frac{\partial T_c}{\partial s} > 0$, this does not hold for the derivative of the axially averaged conducting temperature. Were we to use a thermal profile like in figure 3.2 in the numerator of the Nusselt number as defined in equation 3.60, it would give a negative heat flux contribution inside the TC in the conductive case, a clearly nonsensical result.

An alternative would be to use the axially averaged conductive heat flux calculated in equation 3.62 in the denominator of the Nusselt number, rather than the 3D heat flux. However, since we will dynamically model the z-averaged temperature, and its gradients only in the s and ϕ directions, such

a cuspy conduction profile cannot be sustained: for a convection-diffusion problem initiated with such a profile this cusp will be diffused away, replaced with a smoother profile even in the absence of convection. Since again we would not get a Nusselt number of unity in the purely conductive case, this parameterization is also not satisfactory.
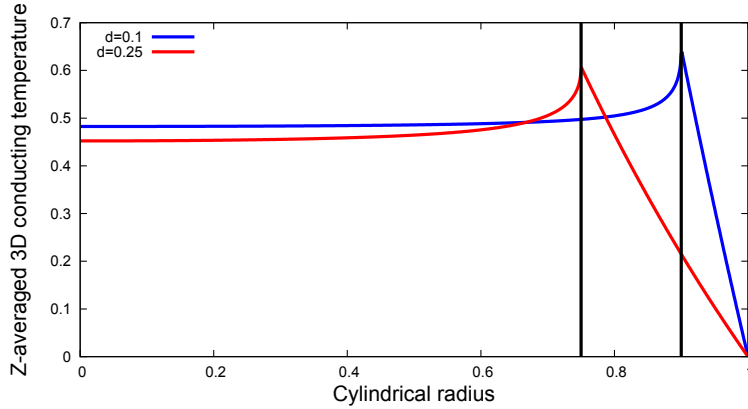
Figure 3.2: A plot of the z-averaged conducting temperature profile for the two shell thicknesses considered in this thesis: $d = 0.25$ and $d = 0.1$. The TCs for the two cases are indicated by black vertical lines.

Inside the TC, because $T^- = 1$ and $T^+ = 0$, we expect the z-averaged axisymmetric temperature to be $\overline{\langle T \rangle} \sim 0.5$, the average of the boundary values. Outside the TC, at $s = r_e$ the boundary conditions require that $\overline{\langle T \rangle} = T^+ = T^- = 0$. Thus a more realistic 2D profile of $\overline{\langle T \rangle}$ as a function of s is one which is approximately constant (~ 0.5) inside the TC and with a constant gradient $\frac{\partial T}{\partial s} \approx \frac{0 - 0.5}{r_e - r_i} = -\frac{1}{2d}$ outside the TC, connected smoothly at the TC with no cusp.

To ensure that we retrieve a Nusselt number of unity in the absence of convection we will compare our calculated 2D heat flux values to the 2D con-

duction profile which is the solution to our equations of motion in the absence of fluid motion. This solution is evaluated numerically, and is depicted in figure 3.3 for two shell thicknesses. The Nusselt number is then defined as ratio of the dynamic 2D heat flux to the 2D conducting heat flux

$$
Nu = \frac{\left(-\frac{\partial \overline{\langle T \rangle}}{\partial s} + \frac{Pr}{E} \overline{\langle T \rangle \langle u_s \rangle} \right) \frac{s}{r} + \left(-\frac{\partial \overline{\langle T \rangle}}{\partial z} + \frac{Pr}{E} \overline{\langle T \rangle \langle u_z \rangle} \right) \frac{z}{r}}{ - \left(\frac{\partial T_{2DC}}{\partial s} \right) \frac{s}{r} - \left(\frac{\partial T_{2DC}}{\partial z} \right) \frac{z}{r} }, \tag{3.63}
$$

where T_{2DC} is the 2D conduction profile. This definition also requires the z-derivative of the conduction profile, which is taken to be

$$
\frac{\partial T_{2DC}}{\partial z} = \begin{cases} \dfrac{T^+ - T^-}{L^+ - L^-} = -\dfrac{1}{\Delta L} & (s < r_i) \\[2ex] \dfrac{T^+ - T^{eq}}{L^+ - L^{eq}} = -\dfrac{r_i}{dL^+} \left(\dfrac{1}{s} - 1 \right) & (s \geq r_i) \end{cases} . \tag{3.64}
$$

Here the eq superscripts indicate values in the equatorial plane. Due to the antisymmetry of z-derivatives of T_{2DC} outside the TC we have averaged over only one hemisphere.

Once the Nusselt number is known, the thermal boundary layer thickness can be calculated by considering the heat flux in the boundary layer, where it is dominantly conductive. Assuming that the entire temperature drop across the shell occurs over the width of two boundary layers (at the top and bottom boundaries), with a well mixed constant temperature bulk, we get a Nusselt number of

$$
Nu = \frac{1/2\delta}{\left| \frac{\partial T_c}{\partial r} \right|}. \tag{3.65}
$$

Thus, for a spherical shell

$$
\delta^\pm = \frac{d(r^\pm)^2}{2 r_i N u^\pm}, \tag{3.66}
$$

76
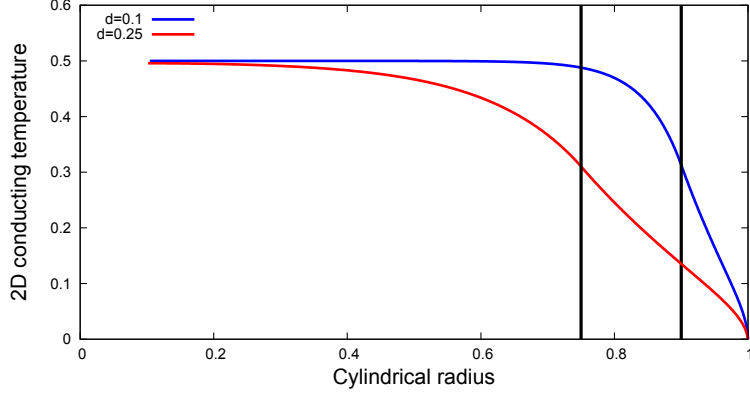
Figure 3.3: A plot of the 2D conducting temperature profile, T_{2DC}, for the two shell thicknesses considered in this thesis: $d = 0.25$ and $d = 0.1$. The TCs for the two cases are indicated by black vertical lines.

where the sign indicates which boundary the thickness is valid for. Due to geometry, the boundary layer is a factor of r_i^2 smaller at the inner shell. This ensures that the total heat flux, integrated over a spherical surface, is constant at all radii.

3.6 Heat equation

As discussed in Section 3.3.1, the heat equation is only averaged over the bulk of the flow. Taking the z-average of the heat equation 2.29 gives

$$\frac{\partial}{\partial t} \langle T \rangle + \langle \mathbf{u}_\perp \rangle \cdot \boldsymbol{\nabla}_\perp \langle T \rangle + \langle u_z \rangle \left(\frac{T(L^+) - T(L^-)}{\Delta L} \right) = \frac{E}{Pr} \left\langle \nabla^2 T \right\rangle, \quad (3.67)$$

77

where $\langle u_z \rangle$ is the rigid component of the axial fluid velocity crossing from the thermal boundary layer into the bulk. The full 2D diffusion term is

$$\langle \nabla^2 T \rangle = \nabla_\beta^2 \langle T \rangle + \frac{1}{\Delta L} \left(\left. \frac{\boldsymbol{\nabla} T \cdot \hat{\mathbf{n}}_{bc}}{\hat{\mathbf{z}} \cdot \hat{\mathbf{n}}_{bc}} \right|^{L^+} - \left. \frac{\boldsymbol{\nabla} T \cdot \hat{\mathbf{n}}_{bc}}{\hat{\mathbf{z}} \cdot \hat{\mathbf{n}}_{bc}} \right|^{L^-} \right), \qquad (3.68)$$

where we have defined

$$\nabla_\beta^2 \langle f \rangle = \nabla_\perp^2 \langle f \rangle + \beta \frac{\partial \langle f \rangle}{\partial s}, \qquad (3.69)$$

with

$$\nabla_\perp^2 \langle f \rangle = \frac{1}{s} \frac{\partial}{\partial s} \left(s \frac{\partial \langle f \rangle}{\partial s} \right) + \frac{1}{s^2} \frac{\partial^2 \langle f \rangle}{\partial \phi^2}, \qquad (3.70)$$

being the 2D Laplacian operator in the equatorial plane. See the full derivation of these equations in Appendix C. Here we have utilized rigidity boundary conditions, $T(L^+) \sim \langle T \rangle \sim T(L^-)$, in calculating the Laplacian. This is appropriate since we are attempting to model the rigid component of the temperature in the bulk. The last two terms of the Laplacian in equation 3.68 account for conduction of heat through the top and bottom of a given Taylor column, to the boundary layers. The terms are scaled by $\hat{\mathbf{z}} \cdot \hat{\mathbf{n}}_{bc}$, which is equal to $\frac{L^\pm}{r^\pm}$ in spherical geometry, to account for the fact that the surface area at the end of each column varies with s due to the slope of the boundary. The boundary conductive heat flux terms in this equation can be evaluated in terms of the thermal boundary layer thickness, $\delta^\pm$, which was specified in Section 3.5. For spherical geometry,

$$\left. \frac{\boldsymbol{\nabla} T \cdot \hat{\mathbf{n}}_{bc}}{\hat{\mathbf{z}} \cdot \hat{\mathbf{n}}_{bc}} \right|^{L^\pm} = \left. \frac{r^\pm}{L^\pm} \frac{\partial T}{\partial r} \right|^{L^\pm}. \qquad (3.71)$$

This can be further parameterized by taking

$$
\frac{\partial T}{\partial r}\bigg|^{L^+} = \begin{cases} \dfrac{0.5 - \langle T \rangle}{\delta^+} & s < r_i \\ -\dfrac{\langle T \rangle}{\delta^+} & s > r_i \end{cases},
$$

$$
\frac{\partial T}{\partial r}\bigg|^{L^-} = \begin{cases} \dfrac{\langle T \rangle - 0.5}{\delta^-} & s < r_i \\ -\dfrac{\langle T \rangle}{\delta^-} & s > r_i \end{cases}. \tag{3.72}
$$

These are defined so as to reproduce an equilibrium thermal profile of $\langle T \rangle \sim 0.5$ inside the TC, decaying to 0 at the equator. If we were to use the physical boundary temperatures of T_e and T_i, rather than 0.5, in equation 3.72 we would get a cuspier profile like $\langle T_c \rangle$, which as discussed in the previous section is not what is desired. The full details of this calculation are presented in Appendix C.

Integrating the advection term of the heat equation over Taylor columns results in the convective heat source term in equation 3.67 (the last term on the left hand side) which models the convective heat flux into the bulk of the fluid transported by the flow. Since the axisymmetric geostrophic axial velocity is taken to be zero, this term only contributes to the non-axisymmetric modes. Inside the TC warm fluid can rigidly rise under the force of buoyancy, carrying heat with it. As it rises, it further warms the Taylor column by advecting warm fluid from the inner boundary into the bulk. The same process works in reverse for cool, sinking fluid. This mechanism reinforces thermal perturbations and drives turbulence. However, outside the TC this forcing term is taken to be zero since, as discussed previously, we assume the rigid axial velocity vanishes here.

To evaluate this term further we must specify the boundary temperature

values $T(L^+)$ and $T(L^-)$. We cannot use rigidity boundary conditions for this term since this would lead to it vanishing, and we would not capture the effects of the convective heat flux mechanism described above. Another option would be to take these values to be the shell boundary values, $T(L^+) = T_e$ and $T(L^-) = T_i$. However, this choice would result in unbounded forcing and growth of the thermal perturbations, which would lead to further growth of the axial velocity, which in turn would lead to positive feedback to the thermal perturbations. The boundary values physically correspond the thermal difference across the bulk of the fluid. As a fluid column rises, its average temperature changes because the fluid exiting the bulk differs from that entering at the other end to replace it. As convection becomes more vigorous the fluid will become more well mixed, leading to the background thermal profile saturating. At some point the axial velocity becomes so large that as it transports heat across the shell it does not have time to deposit its heat within the shell, leading to equal amounts of heat entering and exiting the bulk. The exact details of how this happens are complicated, so we will instead parameterize its effects. We will define

$$\Gamma(Nu_z) \equiv \frac{T(L^+) - T(L^-)}{\Delta L}, \tag{3.73}$$

to be the axial thermal profile as a function of the axial Nusselt number, which only considers heat flux in the axial direction.

In the present work we will take Γ to be a Kelvin cooling profile superimposed on a background conducting profile linear in z. The Kelvin cooling profile is the thermal diffusion profile that would evolve in a solid body which initially has a homogeneous temperature, subject to $T = 0$ external bound-

ary conditions. This acts as a thermal sink and leads to the decay of the temperature, preferentially near the boundary. We assume that this profile is equivalent to the steady state thermal diffusion profile sustained by the axial advection of heat, which tends to homogenize the initial conductive thermal profile across the shell. To make this analogy with our system, we consider only the upper half of the shell and assume that it is initially at a temperature of $\frac{\Delta T}{2}$, with the profile in the lower half defined to be antisymmetric. The resulting profile is equal to

$$T_K(h, t_d) = \Delta T \left(\frac{h}{\Delta L} \left(\text{erf} \left(\frac{\Delta L}{2\sqrt{4Et_d}} \right) - 1 \right) - \frac{1}{2} \text{erf} \left(\frac{h}{\sqrt{4Et_d}} \right) \right), \quad (3.74)$$

where erf is the error function, and h is the $\hat{\mathbf{z}}$ coordinate measured with respect to the surface. Here t_d formally corresponds to the time the body has had to cool, but in this case we will take it to be a free parameter to be fitted. Since $h < 0$ in the shell, as $t_d \to 0$, $T_K \to \frac{\Delta T}{2}$, which corresponds to a well mixed homogeneous fluid, and as $t_d \to \infty$, $T_k \to -\frac{h\Delta T}{\Delta L}$, which is the hydrostatic linear conduction profile. The derivative of the profile in equation 3.74 with respect to h is

$$\frac{\partial T_K}{\partial h} = \Delta T \left(\frac{1}{\Delta L} \left(\text{erf} \left(\frac{\Delta L}{2\sqrt{4Et_d}} \right) - 1 \right) - \frac{1}{\sqrt{4\pi Et_d}} e^{-\frac{h^2}{4Et_d}} \right). \quad (3.75)$$

Since we also know that the thermal gradient at the boundary and in the middle of the shell are related by the fact that the axisymmetric axial heat flux should be constant across the shell,

$$\overline{q_z}|^{L^+} = -\left. \frac{\partial \overline{T}}{\partial z} \right|^{L^+} = \frac{Pr}{E} \overline{u_z \Theta} \Big|^{mp} - \left. \frac{\partial \overline{T}}{\partial z} \right|^{mp} = \overline{q_z}|^{mp}, \quad (3.76)$$

where the mp superscript indicates the midpoint of the shell, we can derive a relationship between the convective and conductive heat flux through the shell. Substituting equation 3.75 into this result, and using the fact that $h = -\frac{\Delta L}{2}$ at the mid-shell and $h = 0$ at the upper boundary, gives

$$\frac{\partial \overline{T}}{\partial z}\bigg|^{mp} \equiv \frac{\partial T_K}{\partial h}\bigg|^{h=-\frac{\Delta L}{2}}$$
$$= \frac{\partial T_K}{\partial h}\bigg|^{h=0} + \frac{Pr}{E}\overline{u_z \Theta}\bigg|^{h=-\frac{\Delta L}{2}}. \tag{3.77}$$

In our model both u_z and Θ are simulated in the bulk, so only t_d is unknown in this equation. While no explicit formula can be derived for t_d, equations 3.75 and 3.77 implicitly define it. In this thesis it is solved for using Newton's root finding method. Prior to the beginning of the simulation, t_d is evaluated for a series of values of the axial convective heat flux at the mid-shell, and these values are used to create a lookup table such that $t_d \equiv t_d(Nu_z)$. The mid-shell thermal gradient can then be evaluated using equation 3.75 to give

$$\Gamma(Nu_z) = \frac{\partial T_K}{\partial h}\bigg|^{h=-\frac{\Delta L}{2}}_{t_d=t_d(Nu_z)}. \tag{3.78}$$

The resulting Γ is plotted as a function of the axial convective heat flux $Nu_z = \frac{Pr}{E}\overline{u_z \Theta}$, normalized by the hydrostatic conductive heat flux, in figure 3.4. This figure shows that using this parameterization the thermal forcing in the axial velocity equation saturates when the axial convective heat flux reaches $2 - 3$ times the hydrostatic conductive heat flux. Therefore we expect that the model will produce a Nusselt number of this magnitude. A larger Nusselt number can be produced by utilizing an "effective" convective heat flux, scaled by some constant greater than 1, when calculating t_d.

82
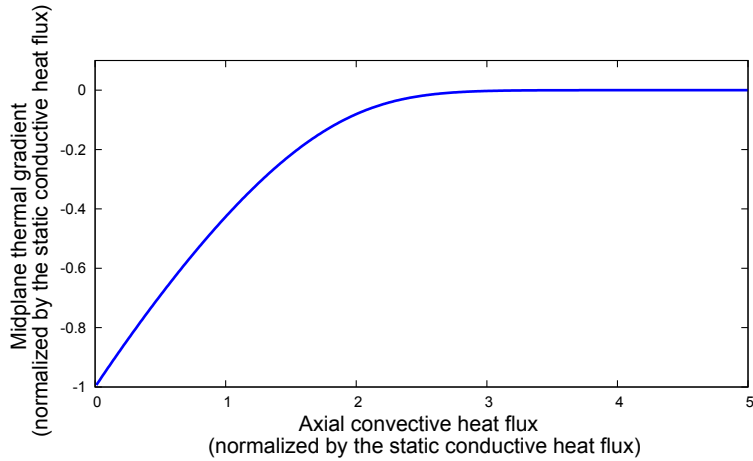
Figure 3.4: A plot of $\Gamma(Nu_z)$, the mid-shell thermal gradient, as a function of the convective heat flux as parameterized in this thesis. Both axis are normalized by the hydrostatic conductive heat flux.

A potential future refinement to this approach would be to utilize scaling laws for the unknown variables. Eric King has found a relationship between the Ekman and Rayleigh number of a rapidly rotating Rayleigh-Bénard system and the resulting Nusselt number from numerical and experimental data [59]. Additionally, the numerical simulations of Keith Julien using the same geometry have determined the steady state mean thermal gradient across the fluid layer for a number of Ekman, Rayleigh and Prandtl numbers [57].

3.7 Axial vorticity equation

The z-averaged vorticity can be written as

$$
\langle\boldsymbol{\omega}\rangle =
\begin{cases}
\left\langle \dfrac{1}{s}\dfrac{\partial u_z}{\partial \phi} - \dfrac{\partial u_\phi}{\partial z}\right\rangle \hat{\mathbf{s}} \\[2mm]
\left\langle \dfrac{\partial u_s}{\partial z} - \dfrac{\partial u_z}{\partial s}\right\rangle \hat{\boldsymbol{\phi}} \\[2mm]
\left\langle \dfrac{1}{s}\dfrac{\partial s u_\phi}{\partial s} - \dfrac{1}{s}\dfrac{\partial u_s}{\partial \phi}\right\rangle \hat{\mathbf{z}}
\end{cases}
=
\begin{cases}
\dfrac{1}{s}\dfrac{\partial \langle u_z\rangle}{\partial \phi}\hat{\mathbf{s}} \\[2mm]
\left(\eta\langle u_z\rangle - \left\langle \dfrac{\partial u_z}{\partial s}\right\rangle\right)\hat{\boldsymbol{\phi}} \\[2mm]
\left(\dfrac{1}{s}\dfrac{\partial \left(s\langle u_\phi\rangle\right)}{\partial s} - \dfrac{1}{s}\dfrac{\partial \langle u_s\rangle}{\partial \phi}\right)\hat{\mathbf{z}}
\end{cases}
. \quad (3.79)
$$

The vorticity equation 2.32 has three components. The z component, which specifies the time evolution of the axial vorticity, is

$$
\frac{\partial \omega_z}{\partial t} + (\mathbf{u}\cdot\boldsymbol{\nabla})\,\omega_z - (\boldsymbol{\omega}\cdot\boldsymbol{\nabla})u_z - 2\frac{\partial u_z}{\partial z} = E\boldsymbol{\nabla}^2\omega_z + Ra^*\hat{\mathbf{g}}\cdot\hat{\mathbf{s}}\frac{g_r}{s}\frac{\partial \Theta}{\partial \phi}. \quad (3.80)
$$

See Appendix A for the details of this calculation. The azimuthal average of ω_z gives the mean zonal wind.

Though strictly not correct, we will adopt the following approximation when evaluating the average of the buoyancy term

$$
\left\langle g_r\frac{\hat{\mathbf{g}}\cdot\hat{\mathbf{s}}}{s}\frac{\partial \Theta}{\partial \phi}\right\rangle \approx \left\langle g_r\frac{\hat{\mathbf{g}}\cdot\hat{\mathbf{s}}}{s}\right\rangle\left\langle \frac{\partial \Theta}{\partial \phi}\right\rangle. \quad (3.81)
$$

In spherical symmetry,

$$
\left\langle g_r\frac{\hat{\mathbf{g}}\cdot\hat{\mathbf{s}}}{s}\right\rangle = \left\langle -g_r\frac{\hat{\mathbf{r}}\cdot\hat{\mathbf{s}}}{s}\right\rangle = \left\langle -g_r\frac{s}{rs}\right\rangle = \left\langle -\frac{g_r}{r}\right\rangle. \quad (3.82)
$$

For a constant gravitational field, $g_r = 1$, this can be evaluated to give

$$
\left\langle g_r\frac{\hat{\mathbf{g}}\cdot\hat{\mathbf{s}}}{s}\right\rangle = \left\langle -\frac{g_r}{r}\right\rangle = \left\langle -\frac{1}{r}\right\rangle
$$

$$= -\frac{1}{\Delta L} \left[\text{arcsinh}\left(\frac{L^+}{s}\right) - \text{arcsinh}\left(\frac{L^-}{s}\right) \right]. \quad (3.83)$$

See Appendix C.5 for the full calculation as well as for the averaged buoyancy term for a linear spherical or cylindrical gravitational field.

The z average of equation 3.80 is

$$\frac{\partial \langle \omega_z \rangle}{\partial t} + \langle \mathbf{u}_\perp \rangle \cdot \boldsymbol{\nabla}_\perp \langle \omega_z \rangle - (\langle \omega_z \rangle + 2)\beta \langle u_s \rangle$$
$$= E \nabla_\beta^2 \langle \omega_z \rangle + Ra^* \left\langle g_r \frac{\hat{\mathbf{g}} \cdot \hat{\mathbf{s}}}{s} \right\rangle \frac{\partial \langle \Theta \rangle}{\partial \phi}. \quad (3.84)$$

The details of this calculation are presented in Appendix C.

This equation depends on the axially averaged temperature perturbation, while the thermal equation derived in the previous section gives the axially averaged total temperature. In general, $\langle T \rangle = \langle T_c \rangle + \langle \Theta \rangle \neq \langle \Theta \rangle$ since the average of the conducting profile is non-zero and depends on s. However, since the vorticity equation involves only the azimuthal derivative of the temperature, only the non-axisymmetric component contributes to vorticity generation. As the conductive profile is purely axisymmetric, its addition to the temperature does not change the buoyancy force in the vorticity equation, so the full temperature and thermal perturbations can be used interchangeably.

Ignoring the viscous dissipation and thermal forcing terms, equation 3.84 can be written

$$\frac{D \langle \omega_z \rangle}{Dt} \sim \langle u_s \rangle (\langle \omega_z \rangle + 2) \frac{1}{H} \frac{\partial H}{\partial s}$$
$$\frac{D \langle \omega_z \rangle}{Dt} \sim (\langle \omega_z \rangle + 2) \frac{1}{H} \frac{DH}{Dt}$$
$$\frac{D \left(\frac{(2 + \langle \omega_z \rangle)}{H} \right)}{Dt} \sim 0, \quad (3.85)$$

and thus the potential vorticity, $PV = \frac{(2+\langle\omega_z\rangle)}{H}$, is conserved. Here we have assumed an axisymmetric and time independent H. The potential vorticity is proportional to the absolute vorticity $(2 + \langle\omega_z\rangle)$, the sum of the planetary and local eddy vorticity. It appears in the last term on the left hand side of equation 3.84, which represents a vortex stretching term that generates or quenches vorticity depending on the sign of the existing absolute vorticity. As Taylor columns are displaced in the $\hat{\mathbf{s}}$ direction $(u_s \neq 0)$, their height is forced to adjust by the boundary. To conserve PV, the vorticity must likewise adapt, which is captured by the β coefficient from equation 3.55.

However, since the definition of β in equation 3.46 flips sign across the TC, due to L^- going from positive inside the TC to negative outside the TC, the geometry will induce vorticity of opposite signs in the two regions for the same direction of motion. This is due to the fact that outside the TC the boundary geometry forces outward moving fluid columns to shorten, and hence decrease their vorticity to conserve PV, whereas inside the TC the same displacement results in lengthening, and hence an increase in vorticity. This divides the shell into two distinct dynamical regions.

Had we assumed an anelastic fluid, rather than Boussinesq, one of the consequences is that we would have found an extra vortex stretching term of the form $2\left(\mathbf{\nabla} \cdot \mathbf{u}\right) = -\frac{1}{\rho}\mathbf{u} \cdot \nabla\rho$ in the vorticity equation, where the right-hand side follows from the static continuity equation with density variations retained [56]. This would give rise to changes in vorticity due to compressional effects, analogous the topographic beta-effect. This term can provide a balance with the Coriolis term, $2\frac{\partial u_z}{\partial z}$, meaning that the flow need not be dominantly rigid if the density gradient is large. However, for a spherically symmetric density profile the rigidity of the azimuthal velocity, and hence zonal wind, is not

impacted by this compressional term since it has no $\hat{\phi}$ component. Depending on the nature of convection, the adiabatic expansion term can be of the same or opposite sign as βu_s, leading to an enhancement or diminishment of the effective β. This term can also lead to a skewness of the vorticity, with opposite senses being generated in the outer regions than the inner regions [31].

The couplings of $\langle \omega_z \rangle$ in equation 3.84 with the other components of the vorticity, through the nonlinear term $\langle (\boldsymbol{\omega} \cdot \boldsymbol{\nabla}) u_z \rangle$ term, cancel in our 2D approach when taking the z-average. Thus, instead of solving two more equations for the other vorticity components ω_s and ω_ϕ, which both depend on u_z, we will instead solve for u_z directly using the Navier-Stokes equation. See Section 3.9 for the development of this equation.

3.8 Zonal flow equation

It will prove convenient to break the vorticity into its axisymmetric component, which corresponds to the mean zonal flow, and its non-axisymmetric component. The vorticity equation 3.84 is used to evolve the non-axisymmetric vorticity. The equation for the zonal flow is developed from the azimuthal component of the momentum equation 2.28

$$\frac{\partial u_\phi}{\partial t} + [(\mathbf{u} \cdot \boldsymbol{\nabla}) \mathbf{u}]_\phi + 2 (\hat{\mathbf{z}} \times \mathbf{u}) \cdot \hat{\phi} = -\frac{1}{s} \frac{\partial p}{\partial \phi} + E \left[\nabla^2 \mathbf{u} \right]_\phi. \qquad (3.86)$$

The individual terms can be expanded as

$$[(\mathbf{u} \cdot \boldsymbol{\nabla}) \mathbf{u}]_\phi = u_s \frac{\partial u_\phi}{\partial s} + \frac{u_\phi}{s} \frac{\partial u_\phi}{\partial \phi} + u_z \frac{\partial u_\phi}{\partial z} + \frac{u_\phi u_s}{s}, \qquad (3.87)$$

$$(\hat{\mathbf{z}} \times \mathbf{u}) \cdot \hat{\phi} = u_s, \qquad (3.88)$$

87

and

$$\left[\nabla^2 \mathbf{u}\right]_\phi = \nabla^2 u_\phi - \frac{u_\phi}{s^2} + \frac{2}{s^2}\frac{\partial u_s}{\partial \phi}. \tag{3.89}$$

To extract the equation for the axisymmetric component of the flow, equation 3.86 is azimuthally averaged, which allows us to drop terms which are full ϕ-derivatives since the integral of such terms around a closed loop is zero. The assumption of the absence of an ageostrophic component of u_ϕ can be used to drop terms which involve its z-derivative, and replace averages of its s-derivatives with derivatives of its average. Finally, we assume that we can approximate the z-average of the product of velocities with the product of the averages, due to the rigidity of the velocities. The resulting z and ϕ averaged equation 3.86 is

$$\frac{\partial \overline{\langle u_\phi \rangle}}{\partial t} = E\left(\overline{\langle \nabla^2 u_\phi \rangle} - \frac{\overline{\langle u_\phi \rangle}}{s^2}\right) - 2\overline{\langle u_s \rangle} - \overline{\langle u_s \rangle \frac{\partial \langle u_\phi \rangle}{\partial s}} - \frac{\overline{\langle u_s \rangle \langle u_\phi \rangle}}{s}, \tag{3.90}$$

where overbars $(\overline{x})$ indicate azimuthally averaged variables. Here we have taken $\overline{\langle u_s \rangle}$ to be zero due to incompressibility under our rigidity assumptions. See Appendix D for the proof of this identity.

Expanding equation 3.90 gives the equation for the axisymmetric zonal flow

$$\frac{\partial \overline{\langle u_\phi \rangle}}{\partial t} = E\left\langle\left(\frac{\partial^2}{\partial s^2} + \frac{1}{s}\frac{\partial}{\partial s} - \frac{1}{s^2}\right)\overline{u_\phi}\right\rangle - \overline{\langle u_s \rangle \frac{\partial \langle u_\phi \rangle}{\partial s}} - \frac{\overline{\langle u_s \rangle \langle u_\phi \rangle}}{s}. \tag{3.91}$$

It is convenient to introduce a new variable, $\tilde{\omega} = \overline{\langle u_\phi \rangle}/s$, to represent the azimuthally and z averaged angular velocity of the flow. The relationship between the axisymmetric component of the axial vorticity, $\overline{\langle \omega_z \rangle}$, and the

angular velocity is

$$\overline{\langle \omega_z \rangle} = \overline{\left\langle \frac{1}{s} \frac{\partial}{\partial s} (s u_\phi) - \frac{1}{s} \frac{\partial u_s}{\partial \phi} \right\rangle}$$

$$= \frac{1}{s} \frac{\partial}{\partial s} \left(s \overline{\langle u_\phi \rangle} \right) = \frac{1}{s} \frac{\partial}{\partial s} \left(s^2 \tilde{\omega} \right) = s \frac{\partial \tilde{\omega}}{\partial s} + 2\tilde{\omega}. \qquad (3.92)$$

Rewriting equation 3.91 in terms of this new variable gives the zonal flow equation

$$\frac{\partial \tilde{\omega}}{\partial t} = E \left(\frac{\partial^2}{\partial s^2} + \left(\frac{3}{s} + \beta \right) \frac{\partial}{\partial s} \right) \tilde{\omega} - \frac{1}{s} \overline{\left(\langle u_s \rangle \frac{\partial \langle u_\phi \rangle}{\partial s} + \frac{\langle u_s \rangle \langle u_\phi \rangle}{s} \right)}. \qquad (3.93)$$

See Appendix C for the calculation of the axial average of the Laplacian. The last two terms on the right, which involve the azimuthal average of the non-linear product of the planar flow components, are the Reynolds stress terms. These are the source terms for zonal flow generation.

3.9   Axial velocity equation

The standard set of QG equations were developed to model convection driven by thermal forcing perpendicular to the rotation axis outside the TC. In such a geometry, with no buoyant forcing of the axial velocity, u_z can be completely specified by the β term, allowing for its feedback on the vorticity equation to be incorporated without dynamically simulating it. However, inside the TC, where buoyancy is dominantly aligned with the rotation axis, this is no longer true. In this region, the rigid geostrophic axial velocity is forced by buoyancy and an adaption of the QG model is required to capture heat transport in the axial direction. Therefore, an equation for the geostrophic axial velocity must

be derived.

The z component of the Navier-Stokes equation is

$$\frac{\partial u_z}{\partial t} + \mathbf{u} \cdot \nabla u_z = -\frac{\partial P}{\partial z} + E\nabla^2 u_z - g_r Ra^* T \hat{\mathbf{g}} \cdot \hat{\mathbf{z}}. \qquad (3.94)$$

As discussed previously, we expect that u_z will be antisymmetric about the equatorial plane outside the TC for a spherical shell, so unlike the other equations we need to average this one over a single hemisphere outside the TC. Otherwise, the thermal forcing term, which is also antisymmetric, would vanish and no motion would result.

The full z-averaged equation is

$$
\begin{aligned}
\frac{\partial \langle u_z \rangle}{\partial t} &+ (\langle \mathbf{u}_\perp \rangle \cdot \boldsymbol{\nabla}_\perp) \langle u_z \rangle \\
&= E\left(\nabla_\perp^2 \langle u_z \rangle - \frac{\langle u_z \rangle}{\Delta L}\left(\frac{1}{\delta^+} + \frac{1}{\delta^-}\right)\right) \\
&- \left(\frac{P(L^+) - P(L^-)}{\Delta L}\right) - Ra^* \langle g_r \hat{\mathbf{g}} \cdot \hat{\mathbf{z}} \Theta \rangle.
\end{aligned}
\qquad (3.95)
$$

See Appendix C for the detailed calculation.

In spherical geometry

$$\langle g_r \hat{\mathbf{g}} \cdot \hat{\mathbf{z}} \Theta \rangle = \langle -g_r \hat{\mathbf{r}} \cdot \hat{\mathbf{z}} \Theta \rangle = \left\langle -g_r \frac{z}{r} \Theta \right\rangle, \qquad (3.96)$$

and with constant $g_r = 1$ this can be approximated as

$$\langle g_r \hat{\mathbf{g}} \cdot \hat{\mathbf{z}} \Theta \rangle = \left\langle -g_r \frac{z}{r} \Theta \right\rangle = \left\langle -\frac{z}{r} \Theta \right\rangle \sim \left\langle -\frac{z}{r} \right\rangle \langle \Theta \rangle = -\frac{\Delta r}{\Delta z} \langle \Theta \rangle. \qquad (3.97)$$

Inside the TC we have $\Delta z = \Delta L$ and $\Delta r = d$, while outside $L^{1/2} = 0$ and so

we get the single hemisphere values of $\Delta z = L^+ - 0 = L^+$ and $\Delta r = 1 - s$. See Appendix C.5 for the full calculation of the averaged buoyancy term as well as for the result for a linear gravitational field or in cylindrical symmetry. As discussed previously, we will only simulate the non-axisymmetric components of $\langle u_z \rangle$. Consequently, we have dropped the $Ra^* \langle g_r \hat{\mathbf{g}} \cdot \hat{\mathbf{z}} T_c \rangle$ term since it only contribute to the axisymmetric component.

3.9.1 Pressure

Unlike in the vorticity equation, where taking the curl leads to the elimination of the pressure gradient term, the pressure remains in the axial velocity equation. The pressure acts as a brake on the growth of the axial velocity: as the fluid contacts the boundary it is forced to slow down to match the impenetrable boundary conditions, which generates pressure that inhibits further axial flow. Since we do not directly simulate the pressure we need to parameterize its effects on the rigid flow in terms of the simulated variables.

The normal stress must be continuous across a free surface. For a spherical surface this gives

$$-P_l + 2E \left.\frac{\partial u_r}{\partial r}\right|^l = -P_u + 2E \left.\frac{\partial u_r}{\partial r}\right|^u, \qquad (3.98)$$

where l and u specify opposite sides of the interface. We will apply this equation at the interface between the bulk and boundary layer.

Inside the TC the radial derivative is predominantly in the axial direction. We will assume that the flow is rigid in the bulk, and that its radial derivative vanishes here, but non-rigid in the boundary layer so as to match the boundary conditions. Also, we will take the pressure at the boundary to be hydrostatic,

91

and thus the dynamic pressure to be zero here. Under these assumptions, using equation 3.98, the pressure in the bulk at the boundary layer is

$$P(L^\pm) = -2E \left.\frac{\partial u_r}{\partial r}\right|^{L^\pm} \sim \pm 2E \frac{L^\pm}{r} \frac{\langle u_z \rangle - u_z(L^\pm)}{\delta_\nu}, \tag{3.99}$$

where δ_ν is the boundary layer thickness. Thus the pressure boundary conditions are related to the rigidity of the flow perpendicular to the boundary.

As discussed in Section 1.2, the limiting factor preventing the onset of axial convection in a rotating system is the rigidity of the flow. In the case of very weak thermal forcing ($Ra^* << 1$), the fluid remains rigid and the pressure generated by equation 3.99 is insufficient to drive significant flow parallel to the boundary to relieve it. The presence of shear stress on the boundary also limits the flow parallel to the surface. Thus, if any $\langle u_z \rangle$ is generated it is not possible for non-rigid u_s to be generated to meet the impenetrable boundary conditions as required by equation 3.40. If the non-rigid $u_s(L^\pm) = 0$, impenetrability requires that $u_z(L^\pm) = 0$. Therefore, the boundary pressure is

$$P(L^\pm) \sim \pm 2E \frac{L^\pm}{r} \frac{\langle u_z \rangle}{\delta_\nu}. \tag{3.100}$$

As the thermal forcing is increased the rigidity constraints are loosened. Flow can escape along the boundary to reduce the pressure. Once the flow along the boundary can become large enough to satisfy equation 3.40 for the rigid axial flow $\langle u_z \rangle$

$$u_s(L^+) = \frac{\langle u_z \rangle}{\frac{\partial L^+}{\partial s}}, \tag{3.101}$$

the impenetrable boundary conditions no longer require the axial flow to change across the boundary layer. Since the flow is now being redirected along the boundary, rather than compressed, no pressure is generated.

In the present formulation we assume that the flow is being forced sufficiently hard so that the non-rigid flow takes the form of equation 3.40. To be consistent with this picture we must take the pressure boundary conditions to be zero

$$P(L^+) = P(L^-) = 0. \tag{3.102}$$

Note that here we have neglected variations in the geostrophic pressure due to a thermal wind, which should be small for the parameter regime we are investigating ($Ra^* < 1$).

Clearly this parameterization will not be valid near the onset of convection. In fact, this framework permits convection to commence well below the critical Rayleigh number. However it should be valid in the convective Taylor column regime, where rigidity is broken in the boundary layer but is generally still valid in the bulk.

To extend the model to capture the onset of convection we would need to parameterize the transition between the these two regimes. One possible way to achieve this is as follows. If the maximal non-rigid flow that is achievable is $\breve{u}_s(L^\pm)$ then the maximal axial velocity that can be accommodated incompressibly, from equation 3.40, is $\breve{u}_z(L^\pm) = \frac{\partial L^\pm}{\partial s} \breve{u}_s(L^\pm)$. If the rigid axial flow is larger than this, then the remainder will generate pressure at the boundary.

Thus, the boundary pressure would be

$$P(L^\pm) = \pm 2E \frac{L^\pm}{r} \frac{\langle u_z \rangle - \check{u}_z(L^\pm)}{\delta_\nu}. \tag{3.103}$$

Once $\check{u}_z(L^\pm) > \langle u_z \rangle$ the pressure boundary condition becomes zero since this picture only applies until the flow can completely diverge along the boundary and reduce the pressure to zero. If we assume that within the boundary layer the pressure gradient is balanced by the viscous diffusion then

$$\frac{\partial P}{\partial s} \sim E \frac{\partial^2 \check{u}_s}{\partial z^2} \sim \mp E \frac{\check{u}_s}{\delta_\nu^2} \sim \mp \check{u}_s, \tag{3.104}$$

where we have assumed that $\delta_\nu \sim \sqrt{E}$. Therefore,

$$P(L^\pm) \sim \pm 2E \frac{L^\pm}{r} \frac{\left(\langle u_z \rangle \pm \frac{\partial L^\pm}{\partial s} \frac{\partial P(L^\pm)}{\partial s} \right)}{\delta_\nu}. \tag{3.105}$$

This differential equation would need to be solved with appropriate boundary conditions at the pole and equator. If the solution gives a pressure of the opposite sign of $\langle u_z \rangle$ on the outer boundary, or the same sign on the inner boundary, it should be taken to be zero as it should not act as a source term. This generalization has not been incorporated into the present numerical implementation of the QG model.

3.10   Stream function

We will recast the fluid velocities and vorticities in terms of a stream function ψ. The stream function is a scalar field defined such that its level sets, which are known as streamlines, are at all points in space tangent to the fluid velocity

vector field. The velocities are defined in terms of derivatives of the stream function such that the incompressibility condition is automatically satisfied. This reduces by one the number of equations which must be simultaneously solved at the expense of having to solve a differential equation which is of order one larger.

Any vector field, such as the flow, can be written as the sum of the gradient of a scalar potential and the curl of a vector potential

$$\mathbf{u} = -\boldsymbol{\nabla}V + \boldsymbol{\nabla} \times \mathbf{A}. \tag{3.106}$$

If the field is divergenceless, as in a incompressible fluid, it can be completely specified by just the vector potential. In cylindrical coordinates

$$\mathbf{u} = \left(\frac{1}{s}\frac{\partial A_z}{\partial \phi} - \frac{\partial A_\phi}{\partial z}, \frac{\partial A_s}{\partial z} - \frac{\partial A_z}{\partial s}, \frac{1}{s}\left(\frac{\partial (sA_\phi)}{\partial s} - \frac{\partial A_s}{\partial \phi} \right) \right)$$

$$\langle \mathbf{u} \rangle = \left(\frac{1}{s}\frac{\partial \langle A_z \rangle}{\partial \phi} - \left\langle \frac{\partial A_\phi}{\partial z} \right\rangle, \left\langle \frac{\partial A_s}{\partial z} \right\rangle - \left\langle \frac{\partial A_z}{\partial s} \right\rangle, \frac{1}{s}\left\langle \frac{\partial (sA_\phi)}{\partial s} \right\rangle - \frac{1}{s}\frac{\partial \langle A_s \rangle}{\partial \phi} \right).$$

We are free to specify $\mathbf{A}$ as necessary to match the properties of $\mathbf{u}$ and the incompressibility condition is guaranteed to be satisfied. For purely 2D planar flow we would take $A_z = \psi(s, \phi)$ and $A_s = A_\phi = 0$, which gives $\langle u_s \rangle = \frac{1}{s}\frac{\partial \psi}{\partial \phi}$ and $\langle u_\phi \rangle = -\frac{\partial \psi}{\partial s}$. To ensure that $\left\langle \frac{\partial u_z}{\partial z} \right\rangle = \beta \langle u_s \rangle$ we can additionally define A_s such that $-\left\langle \frac{1}{s}\frac{\partial^2 A_s}{\partial z \partial \phi} \right\rangle = \frac{\beta}{s}\frac{\partial \langle A_z \rangle}{\partial \phi}$ or $\left\langle \frac{\partial A_s}{\partial z} \right\rangle = -\beta \langle A_z \rangle = -\beta \psi$. This couples the non-rigid axial flow to the azimuthal velocity through A_s.

We could also define the rigid axial velocity to be $\langle u_z \rangle = -\frac{1}{s}\frac{\partial \langle A_s \rangle}{\partial \phi}$, then the final boundary induced flow $\left\langle \frac{\partial u_s}{\partial z} \right\rangle = \eta \langle u_z \rangle$ could be accommodated by defining A_ϕ such that $-\left\langle \frac{\partial^2 A_\phi}{\partial z^2} \right\rangle = -\frac{\eta}{s}\frac{\partial \langle A_s \rangle}{\partial \phi}$. This would couple the non-rigid cylindrical radial flow to an at least quadratic in z component of the axial

velocity through $\langle A_\phi \rangle$. However, since only the non-rigid component of $\langle A_s \rangle$ have been defined in terms of the stream function ψ, this would require the introduction of a second independent stream function variable. Rather than doing this, we will solve the equations for the rigid axial velocity directly.

Our stream function parameterizations are thus

$$\langle u_s \rangle = \frac{1}{s} \frac{\partial \psi}{\partial \phi}, \tag{3.107}$$

and

$$\langle u_\phi \rangle = \overline{\langle u_\phi \rangle} - \frac{\partial \psi}{\partial s} - \beta \psi. \tag{3.108}$$

The vorticity in terms of this parameterization is

$$\langle \omega_z \rangle = \overline{\langle \omega_z \rangle} - \nabla_\perp^2 \psi - \beta \left(\frac{\partial \psi}{\partial s} + \frac{\psi}{s} \right) - \psi \frac{\partial \beta}{\partial s}, \tag{3.109}$$

where

$$\overline{\langle u_\phi \rangle} \qquad \text{and} \qquad \overline{\langle \omega_z \rangle} = \frac{1}{s} \frac{\partial s \overline{\langle u_\phi \rangle}}{\partial s}, \tag{3.110}$$

are the axisymmetric components of the variables. In the above parameterization we have separated the axisymmetric components of the flow from the higher order components. Since the axisymmetric components of $\langle u_\phi \rangle$ and $\langle \omega_z \rangle$ are completely specified by $\tilde{\omega}$, and the axisymmetric component of $\langle u_s \rangle = 0$ from incompressibility, the stream function only parameterizes the non-axisymmetric components of the flow. We can thus take the axisymmetric component of the stream function to be zero without loss of generality. When the full vorticity is required, as in the non-linear terms of the vorticity equa-

tion, the sum of the axisymmetric $\tilde{\omega}$ and non-axisymmetric ψ contributions must be taken.

The physical interpretation of this parameterization is as follows. A rigid geostrophic component of u_s induces an ageostrophic component of u_z. Since this component varies axially across the shell, differing amounts of fluid enter one end of a Taylor column as exit the other end and thus incompressibility dictates that this difference in the flow must diverge into the 2D plane. Due to rotation, this divergence in the plane will tend to be rigid. The parameterization which has been chosen above specifies that the flow diverges into the $\hat{\phi}$ direction uniformly across the width of the shell (since it induces an geostrophic component of u_ϕ). In this prescription the stream function is proportional to the geostrophic pressure. Comparing the above equations with equations 3.11 we find that $\psi = -\frac{P}{2}$.

3.11 Boundary conditions

While we have already applied the 3D boundary conditions at the edges of the convection shell to the equations when taking the z-average, we must also use them to derive boundary conditions for our 2D equations. The boundaries of the 2D domain are located at the point in the equatorial plane at $s = 1$, and a cylindrical surface concentric with the rotation axis located near the pole.

Symmetry across the pole of the planet requires that the boundary condition here be $u_s(s = 0) = 0$ and thus $\psi(s = 0) = constant$. Since we have defined the stream function such that it has no axisymmetric component, this constant must be zero. At both the TC and $s = 1$ we impose no penetration boundary conditions ($u_s = 0$) which again forces $\psi = 0$. Flow across the TC

should be inhibited by its rigidity, since such motion requires the splitting of a single fluid column into two halves (or merging two columns into one).

Two boundary conditions are required for the stream function because by parameterizing the vorticity in terms of a stream function we introduce an extra derivative into the equations. If we also specify that the flow is stress free on the boundaries we can set the shear components of the stress tensor equal to zero, which in cylindrical coordinates for a spherical shell gives

$$
e_{\phi s} = \frac{s}{2} \frac{\partial}{\partial s} \left(\frac{u_\phi}{s} \right) + \frac{1}{2s} \frac{\partial u_s}{\partial \phi} = 0 \qquad e_{zs} = \frac{1}{2} \frac{\partial u_z}{\partial s} + \frac{1}{2} \frac{\partial u_s}{\partial z} = 0
$$

$$
\frac{\partial u_\phi}{\partial s} = \frac{u_\phi}{s} \qquad\qquad\qquad \frac{\partial u_z}{\partial s} = 0, \qquad (3.111)
$$

where we have used the impenetrability of the boundary. The first condition, when expanded in terms of the stream function, gives a relation between the second and first derivative of ψ with respect to s. This is implemented by eliminating second derivatives in our definition of the vorticity in equation 3.109 at the boundary. When combined with the condition that ψ and u_s are zero on the boundary due to incompressibility this translates into a condition on the vorticity at the boundary of

$$
\langle \omega_z \rangle = \frac{2 \langle u_\phi \rangle}{s} = \overline{\langle \omega_z \rangle} - \frac{2}{s} \frac{\partial \psi}{\partial s}. \qquad (3.112)
$$

The first condition in equation 3.111 also gives the free-slip boundary condition for the zonal flow of

$$
\frac{\partial \tilde{\omega}}{\partial s} = \frac{1}{s} \frac{\partial \overline{\langle u_\phi \rangle}}{\partial s} - \frac{1}{s^2} \overline{\langle u_\phi \rangle} = 0. \qquad (3.113)
$$

For the axial flow we use the second condition in equation 3.111 to impose free-slip conditions. As argued previously, $\langle u_z \rangle$ is set to 0 outside the TC at $s \geq r_i$.

Conversely, we could take no-slip boundary conditions, in which case $u_\phi = 0$, and thus $\tilde{\omega} = 0$ and $\frac{\partial \psi}{\partial s} = 0$. This would give a vorticity condition of $w_z = -\frac{\partial^2 \psi}{\partial s^2}$. However, in the present thesis we will use free-slip boundary conditions on both boundaries.

At $s = 1$ the temperature is taken to be $\langle T \rangle = 0$, since the full 3D temperature is $T = 0$ here. At $s = 0$ we assume that there is no heat flux across the pole, giving a condition of $\boldsymbol{\nabla} T \cdot \hat{\mathbf{n}} = \frac{\partial \langle T \rangle}{\partial s} = 0$.

3.12 Summary of the model

The problem has now been reduced to simultaneously solving four non-linear equations for the temperature (T), vorticity $(\langle \omega_z \rangle)$, zonal flow $(\tilde{\omega})$ and axial velocity $(\langle u_z \rangle)$, which are given by equations 3.67, 3.84, 3.93 and 3.95 respectively. In the present implementation, for spherical geometry, they equal

$$(1): \quad \frac{\partial}{\partial t} \langle T \rangle + \langle \mathbf{u}_\perp \rangle \cdot \boldsymbol{\nabla}_\perp \langle T \rangle + \Gamma(Nu_z) \langle u_z \rangle$$
$$= \frac{E}{Pr} \left(\nabla_\beta^2 \langle T \rangle + \frac{1}{\Delta L} \left(\frac{r^+}{L^+} \left. \frac{\partial T}{\partial r} \right|^+ - \frac{r^-}{L^-} \left. \frac{\partial T}{\partial r} \right|^- \right) \right),$$

$$(2): \quad \frac{\partial \langle \omega_z \rangle}{\partial t} + \langle \mathbf{u}_\perp \rangle \cdot \boldsymbol{\nabla}_\perp \langle \omega_z \rangle - (\langle \omega_z \rangle + 2)\beta \langle u_s \rangle$$
$$= E\nabla_\beta^2 \langle \omega_z \rangle + Ra^* \left\langle g_r \frac{\hat{\mathbf{g}} \cdot \hat{\mathbf{s}}}{s} \right\rangle \frac{\partial \langle \Theta \rangle}{\partial \phi},$$

$$(3): \quad \frac{\partial \tilde{\omega}}{\partial t} = E \left(\frac{\partial^2}{\partial s^2} + \left(\frac{3}{s} + \beta \right) \frac{\partial}{\partial s} \right) \tilde{\omega} - \frac{1}{s} \left(\overline{\langle u_s \rangle \frac{\partial \langle u_\phi \rangle}{\partial s}} + \frac{\overline{\langle u_s \rangle \langle u_\phi \rangle}}{s} \right),$$

$$(4): \quad \frac{\partial \langle u_z \rangle}{\partial t} + (\langle \mathbf{u}_\perp \rangle \cdot \mathbf{\nabla}_\perp) \langle u_z \rangle$$

$$= E \left(\nabla_\perp^2 \langle u_z \rangle - \frac{\langle u_z \rangle}{\Delta L} \left(\frac{1}{\delta^+} + \frac{1}{\delta^-} \right) \right) + Ra^* \frac{\Delta r}{\Delta z} \langle \Theta \rangle .$$

Here $\mathbf{u}_\perp = (u_s, u_\phi)$ is the planar velocities and $\Gamma(Nu_z)$ is the thermal profile, which is defined in Section 3.6,

$$\left. \frac{\partial T}{\partial r} \right|^+ = \begin{cases} \dfrac{0.5 - \langle T \rangle}{\delta^+} & s < r_i \\[2mm] -\dfrac{\langle T \rangle}{\delta^+} & s > r_i \end{cases},$$

$$\left. \frac{\partial T}{\partial r} \right|^- = \begin{cases} \dfrac{\langle T \rangle - 0.5}{\delta^-} & s < r_i \\[2mm] -\dfrac{\langle T \rangle}{\delta^-} & s > r_i \end{cases}, \qquad (3.114)$$

$$\delta^\pm = \frac{d(r^\pm)^2}{2r_i Nu^\pm}, \qquad (3.115)$$

$$\left\langle g_r \frac{\hat{\mathbf{g}} \cdot \hat{\mathbf{s}}}{s} \right\rangle = -\frac{1}{\Delta L} \left[\operatorname{arcsinh} \left(\frac{L^+}{s} \right) - \operatorname{arcsinh} \left(\frac{L^-}{s} \right) \right], \qquad (3.116)$$

and

$$\Delta z = \begin{cases} \Delta L & s < r_i \\ L^+ & s > r_i \end{cases} \qquad \Delta r = \begin{cases} d & s < r_i \\ 1 - s & s > r_i \end{cases}. \qquad (3.117)$$

Having re-expressed $\langle u_\phi \rangle$, $\langle u_s \rangle$ and $\langle \omega_z \rangle$ in terms of the stream function ψ

and $\tilde{\omega}$,

$$\langle u_s \rangle = \frac{1}{s}\frac{\partial \psi}{\partial \phi} \qquad \langle u_\phi \rangle = \overline{\langle u_\phi \rangle} - \frac{\partial \psi}{\partial s} - \beta\psi \qquad (3.118)$$

$$\langle \omega_z \rangle = \overline{\langle \omega_z \rangle} - \nabla^2_\perp \psi - \beta\left(\frac{\partial \psi}{\partial s} + \frac{\psi}{s}\right) - \psi\frac{\partial \beta}{\partial s}, \qquad (3.119)$$

where

$$\tilde{\omega} = \overline{\langle u_\phi \rangle}/s \qquad \overline{\langle \omega_z \rangle} = s\frac{\partial \tilde{\omega}}{\partial s} + 2\tilde{\omega}, \qquad (3.120)$$

the independent variables of the system of equations are ψ, $\tilde{\omega}$, $\langle u_z \rangle$ and $\langle T \rangle$.

Chapter 4

Numerical implementation

The code used in the present thesis is based on a numerical implementation originally developed by Schaeffer and Cardin to simulate flow in the Earth's interior [83], and has been generalized to account for the geometry inside the TC. In addition, we have added the axial velocity equation to the code, which is coupled with the other equations through the buoyancy and advection terms. The parallelization of the code has also been improved to allow for more computationally demanding simulations.

4.1 Fourier expansion

The azimuthally dependent variables of the system (all but $\tilde{\omega}$) are expanded in ϕ with a Fourier decomposition in terms of spectral modes m

$$f(s, \phi) = \sum_{-\infty}^{+\infty} f_m(s)e^{im\phi}, \tag{4.1}$$

where the variables with subscript m are the spectral coefficients. These coefficients are the variables which are actually computed in the numerical implementation of our model. Working in spectral space has the advantage that azimuthal derivatives can be easily calculated since $\frac{\partial f}{\partial \phi} = \sum_{-\infty}^{+\infty} im f_m e^{im\phi}$. Thus the spectral coefficient of the azimuthal derivative is just im times the spectral coefficient of the function.

Due to computational limits the expansion is truncated at a maximal mode M_{max}. Thus, the expansions are

$$\psi(s, \phi) = \sum_{m=-M_{max}}^{m=M_{max}} \psi_m(s) e^{im\phi} \tag{4.2}$$

$$\langle T \rangle (s, \phi) = \sum_{m=-M_{max}}^{m=M_{max}} T_m(s) e^{im\phi} \tag{4.3}$$

$$\langle u_z \rangle (s, \phi) = \sum_{m=-M_{max}}^{m=M_{max}} \langle u_z \rangle_m (s) e^{im\phi}. \tag{4.4}$$

Both ψ and $\langle u_z \rangle$ have no $m = 0$ component, while the mean zonal flow, $\tilde{\omega}$, is independent of ϕ.

In general, both positive and negative modes must be evaluated to fully specify the variables. However, we can take advantage of the fact that all of the physical variables must be real. This gives the condition

$$f = f^* \tag{4.5}$$

$$\sum_{-\infty}^{+\infty} f_l(s) e^{il\phi} = \sum_{-\infty}^{+\infty} f_n^*(s) e^{-in\phi}, \tag{4.6}$$

and matching the coefficients of each spectral mode gives, at $l = -n \equiv m$,

$$f_{-m}(s) = f_m^*(s). \tag{4.7}$$

Thus, only the $m \geq 0$ coefficients must be dynamically computed to uniquely determine the state of the system, with the negative modes calculated from equation 4.7 when needed to transform variables into physical space.

For more aggressive parameter regimes the equations are solved subject to an eightfold azimuthal symmetry to reduce the computational demands. This is implemented by only simulating every eighth mode. Since the structures of interest, the Taylor columns and tilted convection cells, are smaller than the imposed symmetry (the Taylor columns should scale as $E^{\frac{1}{3}}$), this should not significantly alter the results. The exception is near the pole since by excluding the possibility of an $m = 1$ mode to the flow we effectively prohibit flow across the pole, which could be significant.

4.2 Radial grid

The variables are expanded on a uniformly spaced discrete lattice in the radial $\hat{s}$ direction. To avoid numerical stability issues with the coordinate singularity at the pole $s = 0$, the inner cylindrical boundary is fixed at $s = 0.1$. In principle we could expand variables in terms of cylindrical harmonic Bessel basis functions to address this issue, however this has not been done in the present work. The numerical implementation of our model only simulates the upper hemisphere inside the tangent cylinder. Symmetry dictates that the dynamics are equivalent in both hemispheres, so for numerical reasons only one

will be simulated. As discussed previously, the axial velocity is only simulated inside the TC.

Derivatives are calculated on the grid based on a second order centred finite difference method. The first and second derivatives in s are evaluated, respectively, by

$$f'(s) = \frac{\left(-\left(h^+\right)^2 f\left(s - h^-\right) + \left(h^-\right)^2 f\left(s + h^+\right)\right)}{h^+ h^- \left(h^+ + h^-\right)} + \left(\frac{h^+ - h^-}{h^+ h^-}\right) f(s) \quad (4.8)$$

$$f''(s) = \frac{2}{\left(h^+ + h^-\right)} \left(\frac{f\left(s - h^-\right)}{h^-} + \frac{f\left(s + h^+\right)}{h^+}\right) - \frac{2 f(s)}{h^+ h^-}. \quad (4.9)$$

These are derived in Appendix F.1.

4.3   Numerical integration

All four equations of the system can be written in the general form

$$\mathsf{A} \cdot \frac{\partial \mathbf{y}}{\partial t} = \mathsf{B} \cdot \mathbf{y} + \mathbf{N}, \quad (4.10)$$

where $\mathbf{y}$ is a vector of the dynamic variables on the radial grid for a specific mode m. The matrices A and B encode the linear terms, while the non-linear terms are represented by the vector $\mathbf{N}$.

The equations are numerically integrated in a two step process. The linear terms are advanced using the Crank-Nicholson finite difference method, while a second order Adams-Bashforth-Moulton (ABM) algorithm is used for the non-linear terms.

The initial state of the system, $\mathbf{y}^t$, must be prescribed. Here the superscript t represents the time step number. In the present work the simulation is

initiated by specifying small perturbations to the flow in a single mode. The solution is then advanced by a time step dt using a predictor step

$$\left(\frac{1}{dt}\mathsf{A} - \frac{1}{2}\mathsf{B}\right) \cdot \mathbf{y}^{t+1} = \left(\frac{1}{dt}\mathsf{A} + \frac{1}{2}\mathsf{B}\right) \cdot \mathbf{y}^t + \frac{3}{2}\mathbf{N}(\mathbf{y}^t) - \frac{1}{2}\mathbf{N}(\mathbf{y}^{t-1}). \quad (4.11)$$

For increased accuracy a higher order ABM routine could be utilized, in which a corrector step follows the predictor step. However, this would require a second calculation of the non-linear terms, which is costly due to the fact that it requires several Fourier transforms. Instead, we can decrease our time step size to compensate for the less accurate lower order routine.

All the terms on the right hand side of equation 4.11 can be calculated at step t. In principle the non-linear terms could be calculated in Fourier space as

$$\begin{aligned}
h(\phi) = f(\phi)g(\phi) &= \left(\sum_{m=-M_{max}}^{+M_{max}} f_m e^{im\phi}\right)\left(\sum_{n=-M_{max}}^{+M_{max}} g_n e^{in\phi}\right) \\
&= \sum_{m,n=-M_{max}}^{+M_{max}} f_m g_n e^{i(m+n)\phi} \\
&= \sum_{l=-M_{max}}^{+M_{max}} h_l e^{il\phi}.
\end{aligned} \quad (4.12)$$

The spectral coefficient of the non-linear term for a given mode, say l, is given by the sum of all contributions such that $m + n = l$

$$h_l = \sum_{n=-M_{max}}^{+M_{max}} f_{(l-n)}g_n. \quad (4.13)$$

Unfortunately, calculating all of the coefficients of the non-linear term becomes a costly $O(M_{max}^2)$ problem. Instead, the non-linear terms are computed using

106

a pseudo-spectral method. This approach takes advantage of the fact that in physical space multiplication of two functions only scales as $O(N)$. The spectral variables are inverse Fourier transformed into the spatial domain, multiplied pointwise on the azimuthal grid, and the result Fourier transformed back into spectral space. The Fourier transforms are performed using the Fastest Fourier Transform in the West (FFTW) software package [33], which scales like $O(M_{max} \ln(M_{max}))$, so this approach is much faster for large M_{max}. However, when only the axisymmetric component of a non-linear term is required, as in the zonal flow equation, it can be calculated directly without having to perform any costly Fourier transforms. As shown above, only the cross products in which $l = m + n = 0$, or $n = -m$, contribute to the axisymmetric mode. The coefficient of the axisymmetric product is

$$\overline{h(\phi)} = \overline{f(\phi)g(\phi)} \quad = h_0 = f_0 g_0 + \sum_{m=1}^{+M_{max}} 2(\Re(f_m)\Re(g_m) + \Im(f_m)\Im(g_m)).$$

See Appendix F.2 for the derivation of this equation.

Once the non-linear terms have been evaluated in spectral space the problem is a linear one of the form

$$\mathsf{C} \cdot \mathbf{y}^{t+1} = \mathbf{d}^t, \tag{4.14}$$

where we need to invert C to find $\mathbf{y}$.

The method used to solve this equation depends on the specific structure of each equation. For the zonal flow, temperature and axial velocity equations, the equation at a given radial point is only dependent upon variables evaluated at its nearest radial neighbours (to calculate the finite difference

```
f(1)=0.0
y(1)=d(1)/b(1)

do  i=2,N
    f(i)=c(i-1)/(b(i-1)-a(i-1)*f(i-1))
    y(i)=(d(i)-a(i)*y(i-1))/(b(i)-a(i)*f(i))
enddo

do  i=N-1,1
    y(i)=y(i)-f(i+1)*y(i+1)
enddo
```

Algorithm 4.1: Tridiagonal routine

derivatives). Thus C is tridiagonal and the system can be solved following the "tridag" algorithm in *Numerical Recipes* [74]. That the zonal flow equation is tridiagonal, and thus relatively easy to solve, is the rational for solving this mode separately from the rest of the vorticity. If we write a general tridiagonal matrix as

$$
C = \begin{bmatrix}
b_1 & c_1 & & & 0 \\
a_2 & b_2 & c_2 & & \\
& a_3 & b_3 & \ddots & \\
& & \ddots & \ddots & c_{N-1} \\
0 & & & a_N & b_N
\end{bmatrix},
\tag{4.15}
$$

the solution is found using a forward sweep to eliminate the as, followed by a backwards substitution sweep. Algorithm 4.1 gives an outline of the routine. This works well provided that the matrix C is diagonally dominant, so that dividing by b does not lead to overflow errors.

For the stream function (z vorticity) equation, the system depends on the nearest and next-nearest neighbours. This is due to the fact that it contains a

Laplacian of the vorticity, which itself depends on the Laplacian of the stream function. Each Laplacian requires one further pair of neighbouring points to evaluate. However, C is still a banded matrix with a bandwidth of five and can be solved using a LU decomposition. This allows us to write $\mathsf{C} = \mathsf{LU}$, where L is a lower triangular matrix and U is an upper triangular matrix, so that

$$
\mathsf{C} = \begin{bmatrix}
c_{11} & c_{12} & c_{13} & & & & 0 \\
c_{21} & c_{22} & c_{23} & c_{24} & & & \\
c_{31} & c_{32} & b_{33} & b_{34} & b_{35} & & \\
 & c_{42} & c_{43} & c_{44} & c_{45} & \ddots & \\
 & & \ddots & \ddots & \ddots & \ddots & c_{(N-2)N} \\
 & & & \ddots & \ddots & \ddots & c_{(N-1)N} \\
0 & & & & c_{N(N-2)} & c_{N(N-1)} & c_{NN}
\end{bmatrix} = \mathsf{LU}, \qquad (4.16)
$$

with

$$
\mathsf{L} = \begin{bmatrix}
1 & & & & & & 0 \\
l_{21} & 1 & & & & & \\
l_{31} & l_{32} & 1 & & & & \\
 & l_{42} & l_{43} & 1 & & & \\
 & & \ddots & \ddots & \ddots & & \\
 & & & \ddots & \ddots & \ddots & \\
0 & & & & l_{N(N-2)} & l_{N(N-1)} & 1
\end{bmatrix} \qquad (4.17)
$$

```
do j=1,N
   do i=1,j
      u(i,j)=c(i,j)-∑_{k=1}^{i-1}(l(i,k)u(k,j))
   enddo
   do i=j+1,N
      l(i,j)=(c(i,j)-∑_{k=1}^{j-1}(l(i,k)u(k,j)))/u(j,j)
   enddo
enddo
```

Algorithm 4.2: LU decomposition routine

$$
\mathsf{U} =
\begin{bmatrix}
u_{11} & u_{12} & u_{13} & & & & & 0 \\
& u_{22} & u_{23} & u_{24} & & & & \\
& & u_{33} & u_{34} & u_{35} & & & \\
& & & u_{44} & u_{45} & \ddots & & \\
& & & & \ddots & \ddots & u_{(N-2)N} & \\
& & & & & \ddots & u_{(N-1)N} & \\
0 & & & & & & u_{NN}
\end{bmatrix}.
\tag{4.18}
$$

Following the "ludcmp" algorithm in *Numerical Recipes*, which is outlined in algorithm 4.2, this proceeds as follows [74]. Writing the equation as $\mathsf{C}y = d = \mathsf{L}\mathsf{U}y = \mathsf{L}x$, where $x = \mathsf{U}y$, lets us solve the inversion by solving two simple inversions: first solving $\mathsf{L}x = d$ by forward substitution, and using the result to solve $\mathsf{U}y = x$ by backward substitution.

To implement the boundary conditions we utilize a phantom point, located one grid spacing outside the boundary. The boundary conditions are used to derive a relationship between the phantom point and the first two points within the domain. To evaluate the equations at the boundary point, which depends on the phantom point, we use this relation, eliminating the need to know the value of the phantom point.

To improve the scalability of the code it was parallelized using OpenMP. The simulations were run on WestGrid using Breezy, which has four sockets, each with six cores, for a total of 24 2.4 GHz AMD Istanbul processors with 256GB of memory per node.

Chapter 5

Numerical results

With our 2D model and its numerical implementation developed, we will now present numerical results that have been obtained to demonstrate its capabilities. All that remains to be specified is the values of the non-dimensional parameters of the system. For reference, the estimated non-dimensional parameters of Jupiter are listed in table 5.1. As discussed previously, these parameters are not realistically achievable numerically, even in our simplified 2D model. Thus we will investigate parameter regimes that are less computationally demanding, but still produce Jovian-like zonal wind structures. The limiting factor for numerical simulations is the Ekman number. The smaller the viscous diffusion coefficient, the smaller the viscous length scale ($\delta_\nu = \frac{\nu}{U}$) and the finer the necessary resolution. For a given available resolution, an achievable Ekman number can thus be calculated. Additionally, to ensure that the solution is converged the simulation should be run for a viscous diffusion time scale across the shell. For a purely diffusive system this can be

E	$\sim 10^{-17} - 10^{-23}$	Ra	$\sim 10^{26} - 10^{32}$
Pr	~ 0.1	χ	$0.8 - 0.95$

Table 5.1: Estimated non-dimensional parameters of Jupiter [49].

evaluated as

$$
\frac{\partial f}{\partial t} \approx E \frac{\partial^2 f}{\partial^2 r}
$$
$$
\frac{f}{t_\nu} \approx E \frac{f}{d^2}
$$
$$
t_\nu \approx \frac{d^2}{E}. \tag{5.1}
$$

Thus, the smaller the viscous diffusion, the longer the simulation must be run to reach convergence.

To compensate for the inevitable over-damping of the system from an overly large Ekman number, the thermal forcing must be taken to be smaller so that the system is not over-forced. The Rayleigh number can be adjusted such that the Rossby number, or amplitude of the zonal flow, is comparable to observations of Jupiter.

In the following sections we investigate the performance of the numerical implementation of our model at two distinct parameter regimes, both chosen to give Jovian-like wind amplitudes. First we consider a system with relatively modest non-dimensional parameters. Our results at this set of parameters are compared to results from a fully three dimensional model at analogous parameters. Following that we examine the results at a more computationally demanding set of non-dimensional parameters.

E	1×10^{-5}	Ra	4.8×10^8
Pr	1	χ	0.75

Table 5.2: Non-dimensional parameters used for the results in Section 5.1.

5.1 Large Ekman number run

In this section we present results of our model run at modest non-dimensional parameters, which are listed in Table 5.2. These are chosen such that the fluid is fully turbulent, so that non-linear effects play a role, but that are not so aggressive so as to make numerical simulations overly lengthy. The relatively large Ekman number also ensures that the typical size of the flow structures are large enough to allow for easy identification and comparison of features between the 3D and 2D results.

5.1.1 Three dimensional results

As a baseline to which to compare our 2D QG model results, this section will present the results of the model by Heimpel [49]. This data was generated and graciously provided by Heimpel. It was simulated on a spherical coordinate grid with $1024 \times 512 \times 129$ non-uniformly spaced grid points in the $\hat{\phi}$, $\hat{\theta}$ and $\hat{r}$ direction respectively.

To allow for a direct comparison with our 2D model, this 3D data has been processed using the following method prior to imaging. As the 3D data is simulated in spherical coordinates it must first be interpolated onto a cylindrical coordinate grid. The interpolation function is then sampled at 512 (the number of co-latitudinal grid points) uniformly spaced points in $\hat{z}$ for each point in the $\phi - s$ plane. The mean of these sampled values is then taken to give axially averaged quantities. In addition to these axial mean values, we

also plot the mid-shell ($z = \frac{L^-+L^+}{2}$) values projected into the $\phi - s$ plane to give a sense of how much the flow departs from the mean due to random fluctuations along Taylor columns. We also plot both the azimuthal mean values and cross sections for an arbitrarily chosen meridian, which is identical for all the flow variables plotted, in the $s - z$ plane. The 3D model gives results for both the northern and southern hemispheres, but for simplicity we have arbitrarily chosen to analyze only the results from the northern hemisphere in the following.

(a) Azimuthal mean   (b) Cross section
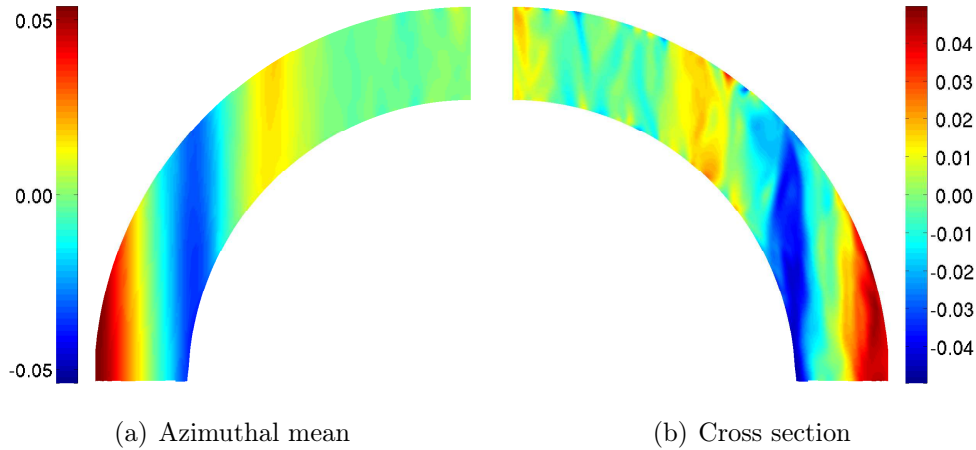
Figure 5.1: 3D azimuthal velocity plotted in the $s - z$ plane. On the left (5.1(a)) is the azimuthal mean and on the right (5.1(b)) is a cross section for an arbitrarily chosen meridian, depicted as a black line in figure 5.2.

Figure 5.1 shows the $s-z$ values of the azimuthal velocity. When compared with the azimuthal mean it is clear that azimuthal velocity is dominated by a rigid, axisymmetric mode, as expected. This is confirmed by figure 5.2, which shows the azimuthal velocity plotted in the $\phi - s$ plane. Both the axially averaged and mid-shell values projected into the plane are shown. These two figures are very similar, again confirming that the zonal wind is dominantly

rigid. The main differences are that the latter has slightly larger amplitudes and the former has less small scale features, which is to be expected due to random variations about the mean. A plot of the z-averaged zonal wind

(a) Axial mean
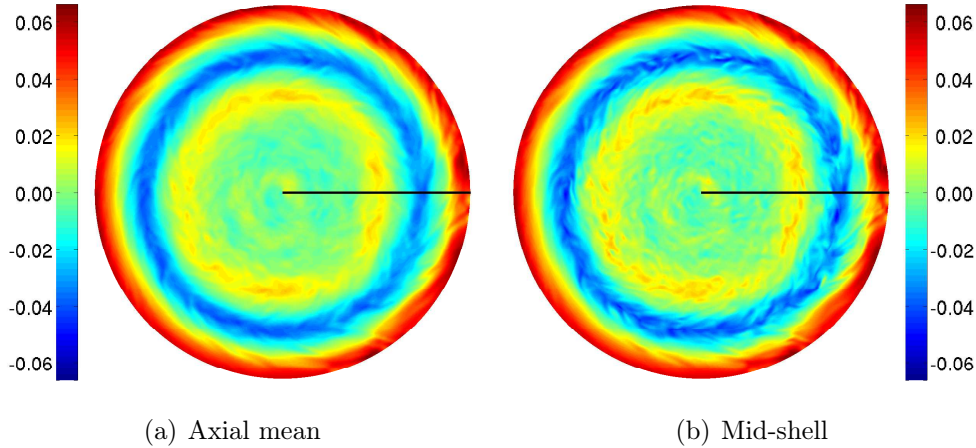
(b) Mid-shell

Figure 5.2: 3D azimuthal velocity plotted in the $\phi - s$ plane. On the left (5.2(a)) are the axially averaged values and on the right (5.2(b)) are the mid-shell values ($z = \frac{L^- + L^+}{2}$). The black line represents the location of the cross section plotted in figure 5.1(b).

as a function of latitude is given in figure 5.3. It features a strong prograde equatorial jet and two smaller jets of alternating directions at higher latitudes. North of $\sim 65°$, the mean zonal wind nearly vanishes. However, two additional weak high latitude jets are visible near the pole in figure 5.2, but since these jets are not concentric with the pole their presence is difficult to detect in figure 5.3. The absolute minimum amplitude of the wind, at the peak of the first retrograde high latitude jet, is located roughly at the TC.

If we consider only the non-axisymmetric component of the azimuthal velocity, more detailed structures become apparent. A cross section of the non-axisymmetric azimuthal velocity is plotted in figure 5.4. This image shows evidence that there is a significant z-varying component to the flow. Inside
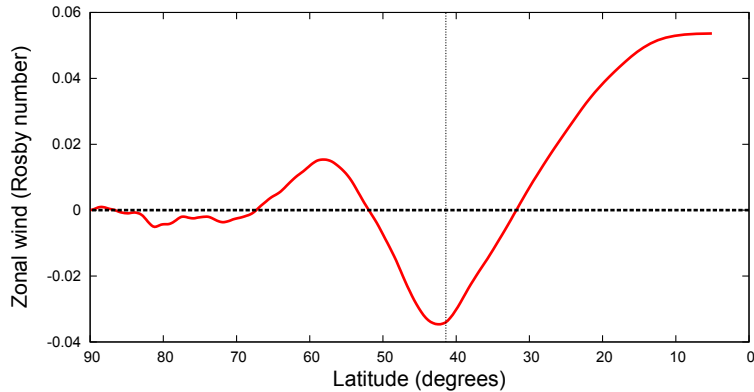
Figure 5.3: z-averaged 3D zonal flow plotted versus latitude. The dotted line is the location of the tangent cylinder.

the TC this variation is largest in thin layers adjacent to the spherical boundaries of the shell. However, there appears to be a smaller amplitude component of the azimuthal flow that varies in z through the bulk of the flow. This could be a thermal wind, which is not modelled in the present thesis.

Figure 5.5 shows the non-axisymmetric azimuthal velocity in the $\phi - s$ plane, again showing both the z-averaged and mid-shell values. The axial average has the effect of filtering out flow components that are antisymmetric about the mid-shell level. The similarity of axial average and mid-shell values in figure 5.5 strongly suggest that the non-axisymmetric component of the azimuthal flow is also dominantly rigid. This figure also shows that there is an asymmetry to the convection: outside the TC convection is noticeably stronger on the right hand side of the plots, where the amplitudes of the flow are larger.

Moving on to the cylindrical radial velocity, figure 5.6 shows the $s - z$ cross section of u_s for both the azimuthal mean and a specific meridian. This image
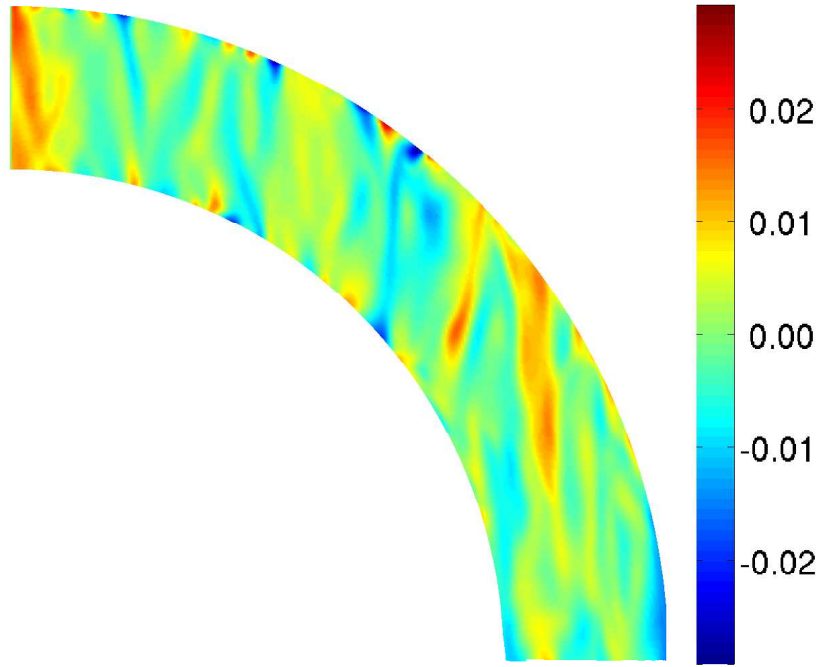
Figure 5.4: 3D non-axisymmetric azimuthal velocity plotted in the $s - z$ plane. This is a cross section for an arbitrarily chosen meridian, depicted as a black line in figure 5.5.

shows that the axisymmetric component is an order of magnitude smaller than the non-axisymmetric components. This justifies our assumption that it can be neglected in our QG parameterization. Similar to the azimuthal velocity in figure 5.4, the cross section of the cylindrical radial velocity in figure 5.6(b) shows some axial dependence. This non-rigid flow is again most significant in thin layers near the boundaries. While in the present numerical implementation of our QG mode we have assumed for numerical reasons that there is no flow across the TC, figure 5.6(b) suggests that the cylindrical radial velocity does not vanish here.

Figure 5.7 shows the $\phi - s$ plane values of the cylindrical radial velocity.

118

(a) Axial mean   (b) Mid-shell
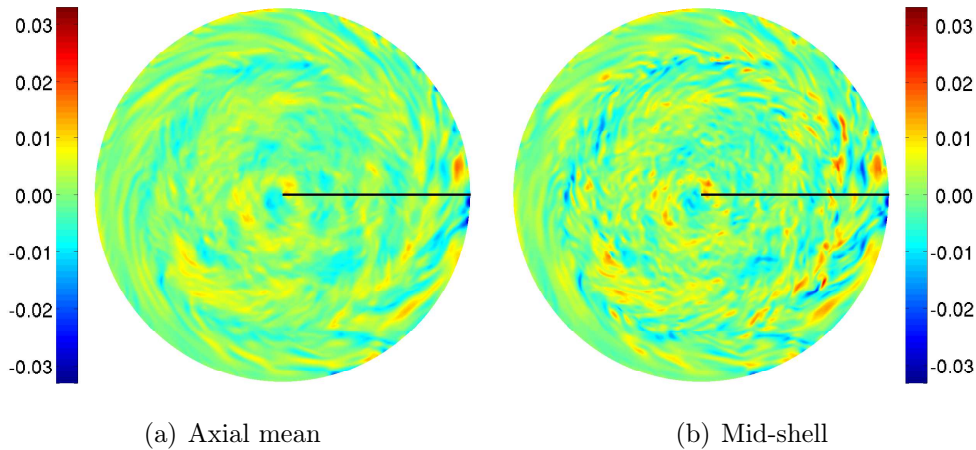
Figure 5.5: 3D non-axisymmetric azimuthal velocity plotted in the $\phi - s$ plane. On the left (5.5(a)) are the axially averaged values and on the right (5.5(b)) are the mid-shell values ($z = \frac{L^- + L^+}{2}$). The black line represents the location of the cross section plotted in figure 5.4.

Again we see that the axial mean has less small scale structure and slightly smaller amplitudes, and that there is enhanced convection on the right side outside the TC. The most significant feature of figure 5.7 is the large order one structure near the pole, representing horizontal flow across the pole. This feature also explains the large amplitude azimuthal flow near the pole in figure 5.5. As flow crosses the pole, a return azimuthal flow around the pole is established. Due to our choice of an inner boundary located outside the pole at $s = 0.1$, and impenetrable boundary conditions at this radius, our QG model cannot capture such an order one flow near the pole. It is possible that this flow is the cause of the offset of the inner jets from the rotation axis. We can also see the tilted convection cells quite well in this image, especially near the external boundary and tangent cylinder.

Figure 5.8 shows the axial velocity in the $s - z$ plane. There is significant axial variation outside the TC, however the axial velocity is mostly rigid in-

(a) Azimuthal mean   (b) Cross section
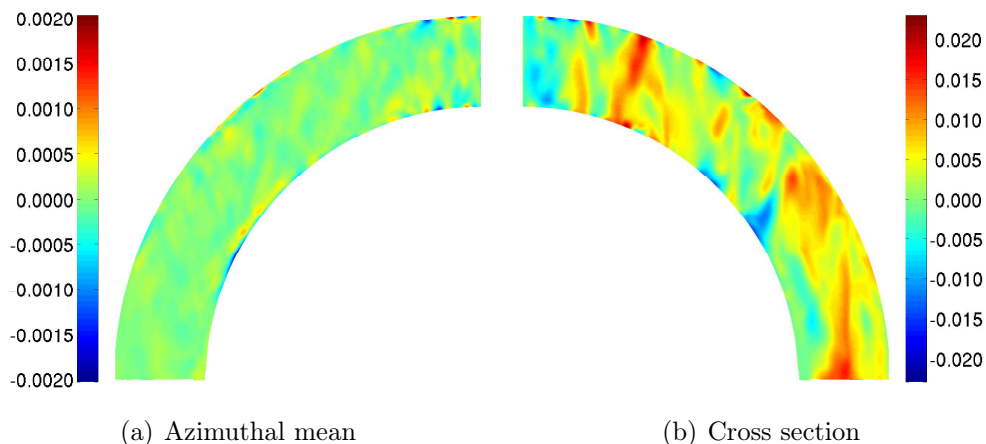
Figure 5.6: 3D cylindrical radial velocity plotted in the $s - z$ plane. On the left (5.6(a)) are the azimuthal mean values and on the right (5.6(b)) is a cross section for an arbitrarily chosen meridian, depicted as a black line in figure 5.7.

side. This is consistent with our QG framework, where outside the TC the axial velocity is predominantly linear in z due to the boundary induced flow, while inside it is dominantly a rigid buoyancy driven component. We again see that the azimuthal mean flow is an order of magnitude smaller than the non-axisymmetric flow. When the cross section of the azimuthal mean axial flow in figure 5.8(a) is compared with the analogous plot for the cylindrical radial flow in figure 5.6(a), the presence of a series of poloidal circulation cells can be observed, most clearly near the pole. This type of flow cannot be captured in the present implementation of our QG model since we do not allow for an axisymmetric mode of the axial velocity. However, since the magnitude of the axisymmetric flow is so much smaller this approximation is justifiable. The cylindrical radial locations with large amplitude rigid axial velocities seen in figure 5.8 correlate with the locations where the cylindrical radial and azimuthal velocities are large near the boundaries in figure 5.6 and

(a) Axial mean (b) Mid-shell
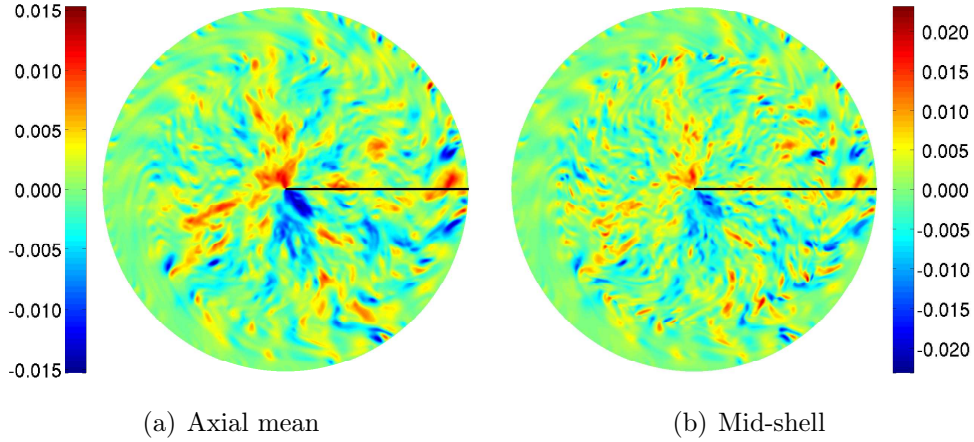
Figure 5.7: 3D cylindrical radial velocity in the $\phi - s$ plane. On the left (5.7(a)) are the axially averaged values and on the right (5.7(b)) are the mid-shell values ($z = \frac{L^- + L^+}{2}$). The black line represents the location of the cross section plotted in figure 5.6(b).

5.4 respectively. This is consistent with the picture that the rigid axial plumes are being fed by flow parallel to the boundary within the thermal boundary layer. While our QG model does not directly model this flow in the boundary layer, it does parameterize the effects of this flow on the rigid axial flow by accounting for the convective heat flux across the thermal boundary layer.

Figure 5.9 shows the $\phi - s$ plane values of the axial velocity. The z-averaged and mid-shell values are very similar, once more confirming that the flow is dominantly rigid, both inside and outside the TC. Figure 5.9 also shows that outside the TC the axial flow structures tend to have larger typical horizontal length scales than inside. Inside the TC the axial flow tends to appear as localized plumes, whereas outside it tends to be elongated structures that cross the shell from the TC to equator, tilted in the prograde direction. This is consistent with our QG framework in which a rigid axial velocity is forced by axial buoyancy inside the TC, so that localized thermal perturbations lead

121

to plumes. Outside the TC, the axial velocity is dominated by the boundary induced flow. Here, fluid parcels crossing the shell generate axial flow due to the topographic beta-effect, tilting in the process.

(a) Azimuthal mean   (b) Cross section
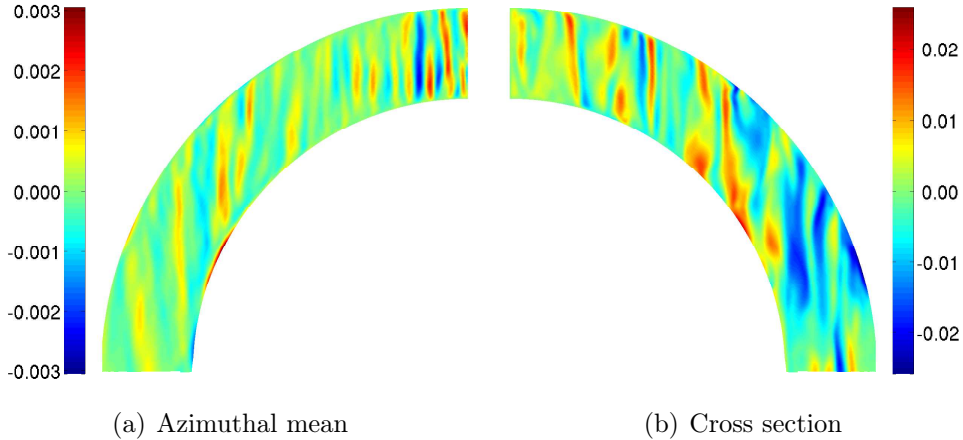
Figure 5.8: 3D axial velocity plotted in the $s - z$ plane. On the left (5.8(a)) are the azimuthal mean values and on the right (5.8(b)) is a cross section for an arbitrarily chosen meridian, depicted as a black line in figure 5.9.

Finally, we examine the thermal structure of the flow. As before, figure 5.10 depicts the $s - z$ plane values and figure 5.11 the $\phi - s$ plane values. Outside the TC the temperature is mostly rigid across the shell, but inside it much more closely resemble the conducting profile shifted by a z-independent constant. This will be discussed further shortly. The planforms of temperature look very similar to the equivalent images for the axial velocity shown in figure 5.9. This lends credence to our modeling of the thermal forcing from convective heat flux into the shell by a term proportional to the axial velocity.

Repeating the above analysis for the non-axisymmetric temperature, the rigidity of the thermal perturbations, especially inside the TC, is quite clear in the plot of their $s - z$ values in figure 5.12. We see a number of thermal plumes, both warm and cold, extending from the boundary through the bulk

(a) Axial mean   (b) Mid-shell
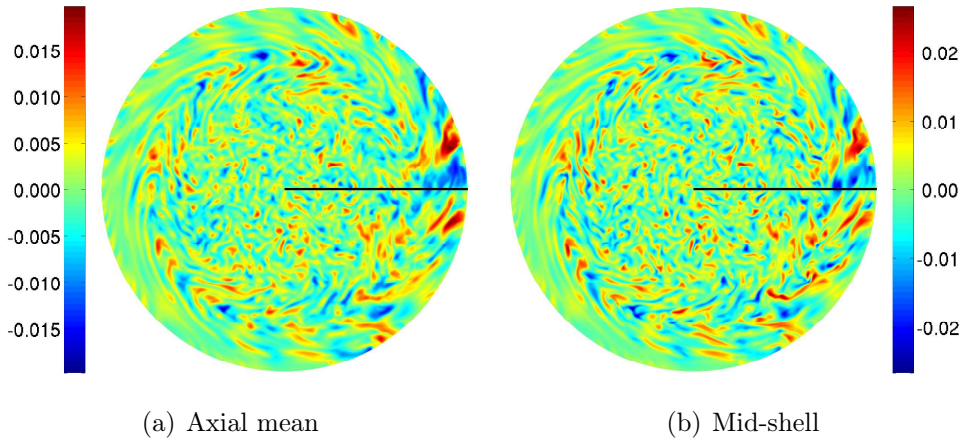
Figure 5.9: 3D axial velocity plotted in the $\phi - s$ plane. On the left (5.9(a)) are the axially averaged values and on the right (5.9(b)) are the mid-shell values ($z = \frac{L^- + L^+}{2}$). The black line represents the location of the cross section plotted in figure 5.8(b).

of the flow. A planform of the non-axisymmetric temperature is shown in figure 5.13. The similarity of the axially averaged and the mid-shell thermal perturbations is consistent with the premise that the perturbations are rigid. We can also see large thermal perturbations on the right outside the TC, which are driving the enhanced convection here. These perturbations tend to be tilted and aligned with the convection cells; as they are advected outwards their motion is deflected.

The axisymmetric spherical radial Nusselt number for the system is depicted in figure 5.14. This is calculated by taking the average thermal gradient near the boundary, normalized by the hydrostatic conducting gradient. The heat flux is roughly constant with latitude with a value of $\sim 6 - 8$.

(a) Azimuthal mean   (b) Cross section
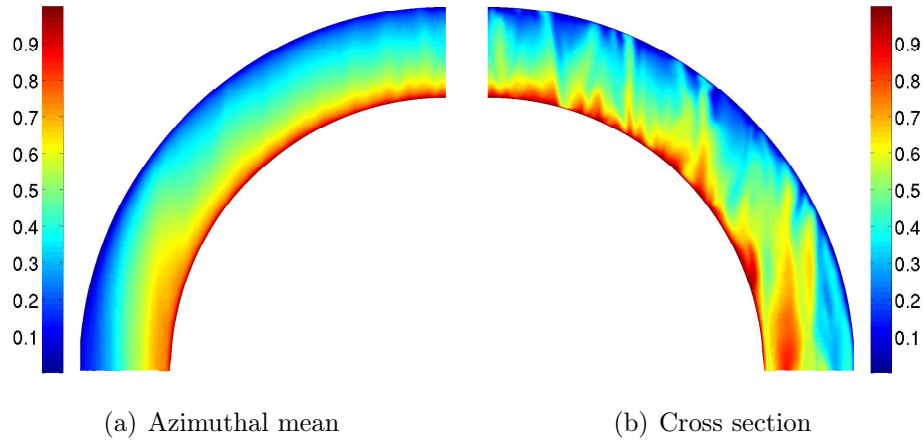
Figure 5.10: 3D temperature plotted in the $s - z$ plane. On the left (5.10(a)) are the azimuthal mean values and on the right (5.10(b)) is a cross section for an arbitrarily chosen meridian, depicted as a black line in figure 5.11.

Summary

In summary, the 3D results feature a strong prograde equatorial jet and several weaker jets at higher latitudes, the highest latitude of which are not concentric with the rotation axis. The Nusselt number is roughly constant with latitude, having a value of $\sim 6 - 8$.

For all of the variables examined, the axially averaged quantities and mid-shell values are quite similar, which supports the assumption of a dominantly rigid flow utilized in our QG model. The averaged values tend to have some-what smaller amplitudes and less small scale structure, which is expected due to random variations about the rigid values across the shell. The cross sections also show that the flow is mostly rigid, though there is some departure from rigidity, particularly near the shell boundaries. However, these non-rigidities are largely explainable in terms of boundary layer dynamics, the effects of which have been parameterized in our QG model. In the case of the tem-

(a) Axial mean   (b) Mid-shell
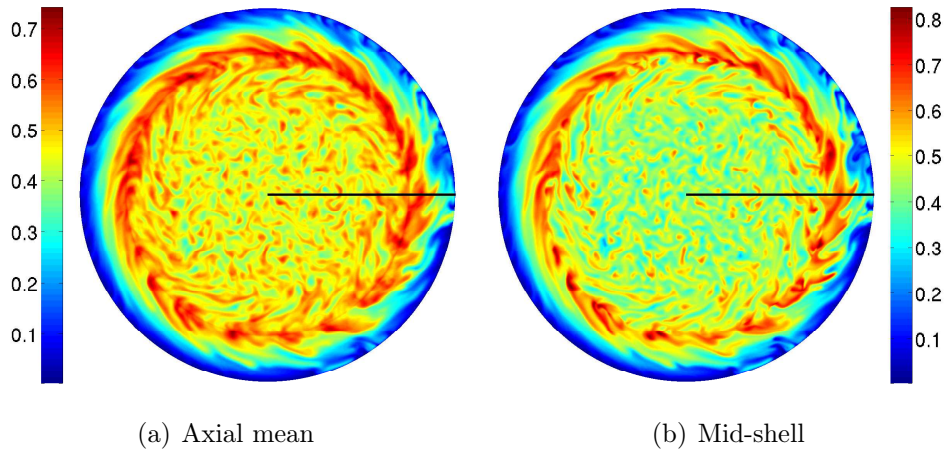
Figure 5.11: 3D temperature plotted in the $\phi - s$ plane. On the left (5.11(a)) are the axially averaged values and on the right (5.11(b)) are the mid-shell values ($z = \frac{L^- + L^+}{2}$). The black line represents the location of the cross section plotted in figure 5.10(b).

perature, only the thermal perturbations are rigid, taking the form of plumes extending from the boundary across the shell.

The linear in z axial flow predicted due to the boundary conditions, as parameterized by the beta-effect in our QG model, is also visible outside the TC. Meanwhile, the axial flow inside the TC is predominantly rigid and fed by boundary flows, which supports our addition of a rigid axial flow component to the QG model here. The tilted convection cells thought to drive jet generation are visible in the planforms of the flow and temperature. Additionally, the axisymmetric cylindrical radial and axial velocities are both an order of magnitude smaller than their non-axisymmetric components, which justifies neglecting them in our QG framework.

The flow features localized structures for the axial flow and thermal perturbations inside the TC, and elongated structures tilted in the prograde direction outside the TC. This is consistent with our QG parameterization of
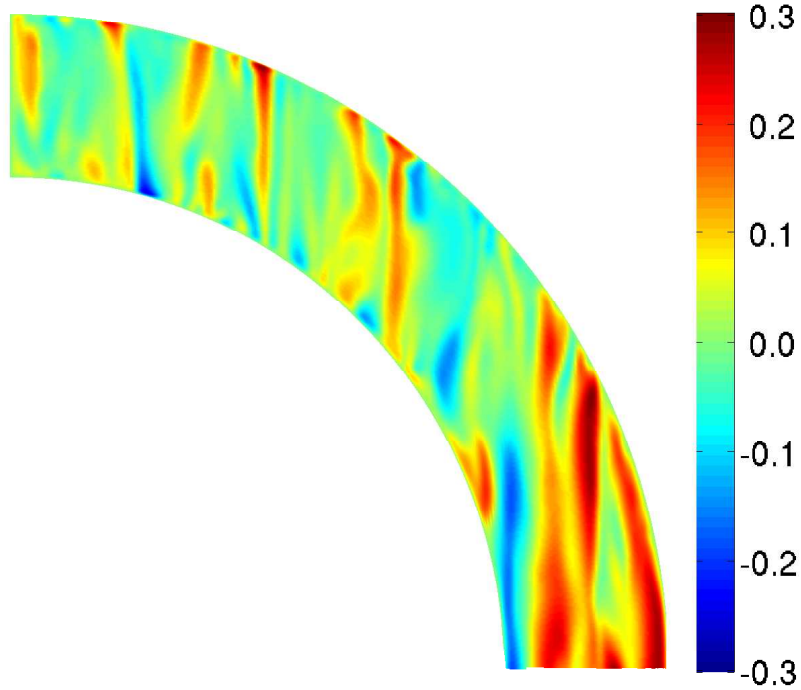
Figure 5.12: 3D non-axisymmetric temperature plotted in the $s - z$ plane. This is a cross section for an arbitrarily chosen meridian, depicted as a black line in figure 5.13.

axial plumes convecting inside the TC, and beta-effect induced axial flow from tilted convection cells outside the TC.

There are a few features of the 3D results which are not consistent with the present numerical implementation of our QG model. The 3D results feature significant horizontal flow across the pole, which is not permitted in our QG code due to the boundary conditions chosen. The poloidal circulation near the pole also cannot be captured since we do not model an axisymmetric azimuthal velocity. However, the later flow has a quite low amplitude so neglecting it is probably not significant. Finally, the cylindrical radial velocity does not vanish at the TC as assumed by our model.

(a) Axial mean　　　　　　　　　　(b) Mid-shell
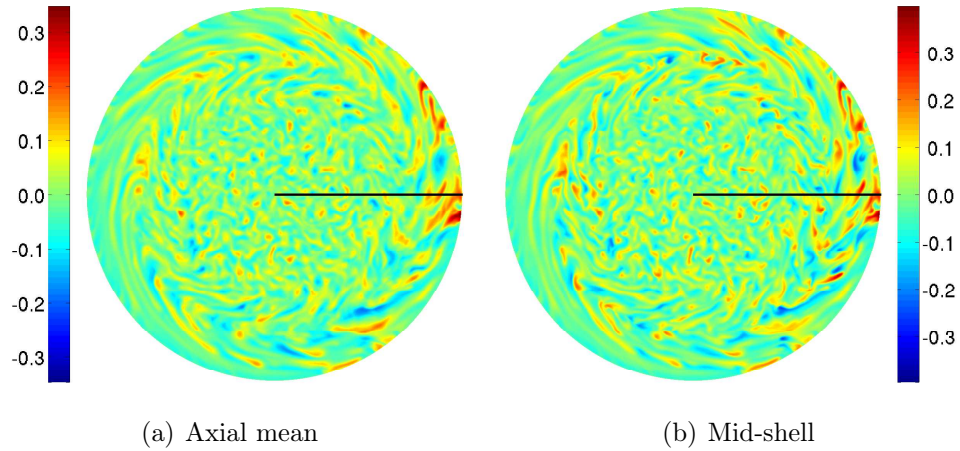
Figure 5.13: 3D non-axisymmetric temperature plotted in the $\phi - s$ plane. On the left (5.13(a)) are the axially averaged values and on the right (5.13(b)) are the mid-shell values ($z = \frac{L^- + L^+}{2}$). The black line represents the location of the cross section plotted in figure 5.12.
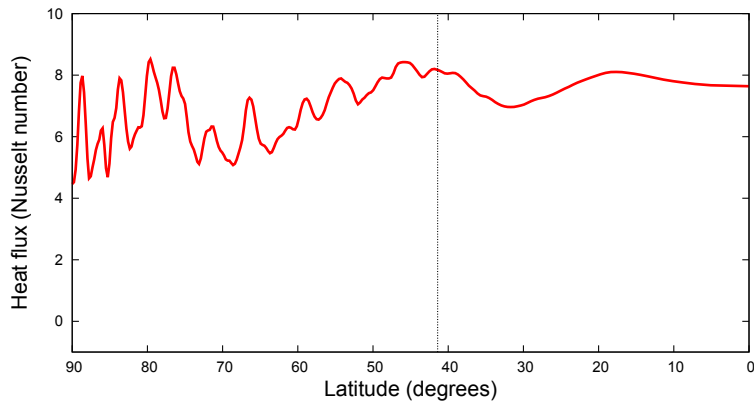
Figure 5.14: Spherical radial Nusselt number at the external surface plotted versus latitude for the 3D model. The dotted line is the tangent cylinder.

5.1.2 Two dimensional results

We will now compare the results of the 3D model presented in the previous subsection to the results from our 2D QG model with identical non-dimensional parameters. For this run we have utilized 521 cylindrical radial grid points, a maximal azimuthal mode of $M_{Max} = 255$ and a time step of $dt = 5 \times 10^{-3}$. To ensure that we get a Nusselt number of roughly $6-8$, as in the 3D results, an effective convective heat flux of half the physical value is utilized when calculating the midplane axial thermal gradient Γ in equation 3.77.

Figure 5.15 shows a planform of the azimuthal velocity. When compared with the 3D results in figure 5.2, both feature strongly axisymmetric flow of similar magnitudes. The azimuthally averaged zonal wind is plotted versus latitude in figure 5.16. Like the 3D results in figure 5.3, the maximal zonal wind occurs at the equator, and is of comparable amplitude. The central jet is less axisymmetric in the 2D case, so while the maximal azimuthal velocity is very similar between the two cases, the mean zonal wind is roughly a factor of 2 smaller in the 2D results. The absolute minimum zonal velocity for both sets of results occurs for the first retrograde jet, which is located at the TC. Again, the 2D jet is about half the amplitude of its 3D counterpart. At higher latitudes, within the TC, the 2D model produces a single jet which spans the entire region, while the 3D results features several alternating jets. The first high latitude jet in the 3D results is quite similar in amplitude to the 2D high latitude jet.

The structure of the non-axisymmetric azimuthal velocity, in figure 5.17, is quite similar with comparable amplitudes to the 3D results in figure 5.5. In both we see localized regions of enhanced convection, primarily near the
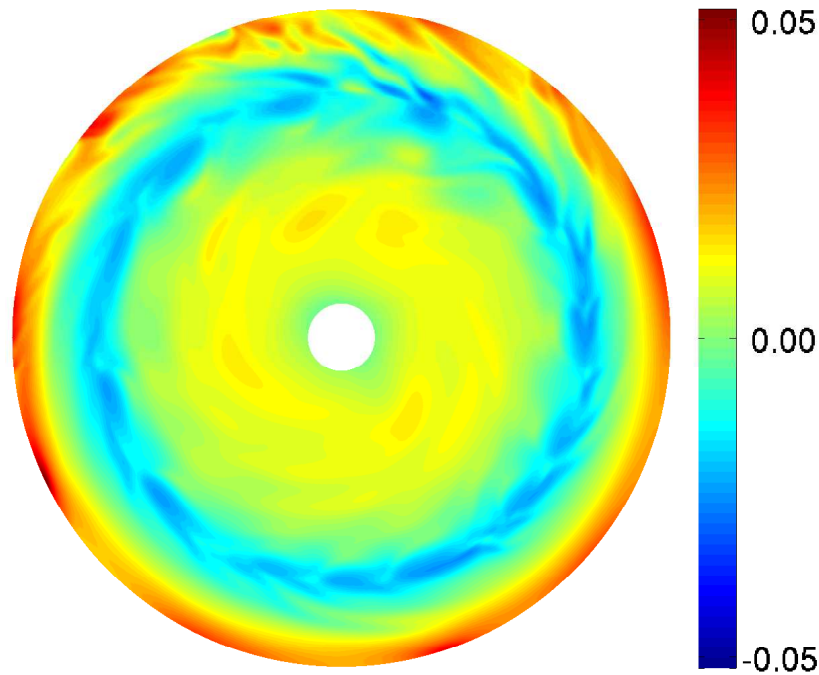
Figure 5.15: 2D azimuthal velocity.

boundary. While in the 3D case this is located on the right hand side of the image, in the 2D case it is at the top of the image. The equations of motion are axisymmetric, so the longitudinal location of this feature is not significant. The chaotic nature of convection will lead to its appearance at different locations at different snapshots in time. The azimuthal tilting of the convection cells can also be observed in both images. The amplitude of the flow is somewhat less at high latitudes in the 2D results relative to those from the 3D model, and there is not as much small scale flow here.

Figure 5.18 shows the cylindrical radial velocity for the 2D model. Outside the TC the flow is quite similar to the 3D results in figure 5.7, with comparable amplitudes and structures. Both results feature prominent convection cells
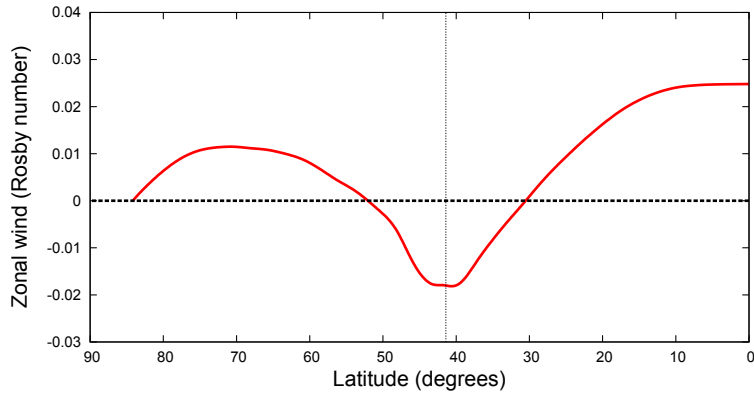
Figure 5.16: 2D zonal flow plotted versus latitude.

located at the TC and equator, which are enhanced in the regions where convection is more vigorous. We can again see evidence of these convection cells being tilted. However, there are notable differences between the 3D and 2D results. The previously observed large order one structure at the pole in the 3D results is clearly absent in the 2D results, as expected. More generally, the amplitude of the flow inside the TC is significantly smaller in the 2D results than in the 3D results. The 3D results also have more small scale structure than the 2D results at high latitudes.

The axial velocity depicted in figure 5.19 is somewhat different than the 3D results in figure 5.9. The 2D results are dominated by a large order one flow near the pole that is completely absent in the 3D flow. The amplitude of this mode is approximately five times larger than the maximal axial flow in the 3D case. This feature could be a consequence of how the boundary layer flow is parameterized in our QG model. When flow enters the boundary layer it is forced to break the rigidity constraints. However, this boundary layer flow
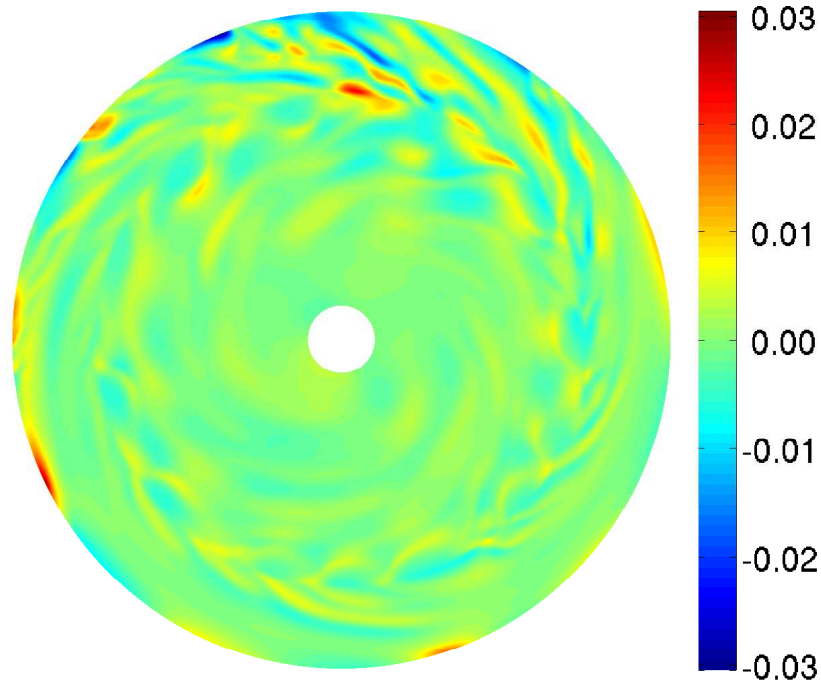
Figure 5.17: 2D non-axisymmetric azimuthal velocity.

is still subject to Coriolis forces which prevent the non-rigidity from growing too large. Since in the 2D case we do not explicitly model the flow within the boundary layer, and only parameterize the flow that crosses into or out of the bulk, these forces are not accounted for. The QG model assumes that at a given cylindrical radius all the upwelling flow downwells elsewhere at the same radius. This ensure the incompressibility of the flow and justifies neglecting the axisymmetric axial flow. For higher order modes this is a reasonable approach, as axial convection cells will exchange flow with their azimuthal neighbours. However, for the lowest modes near the pole this is a less physically realistic assumption. A more likely scenario is that the return flow in the boundary layer crosses the pole.
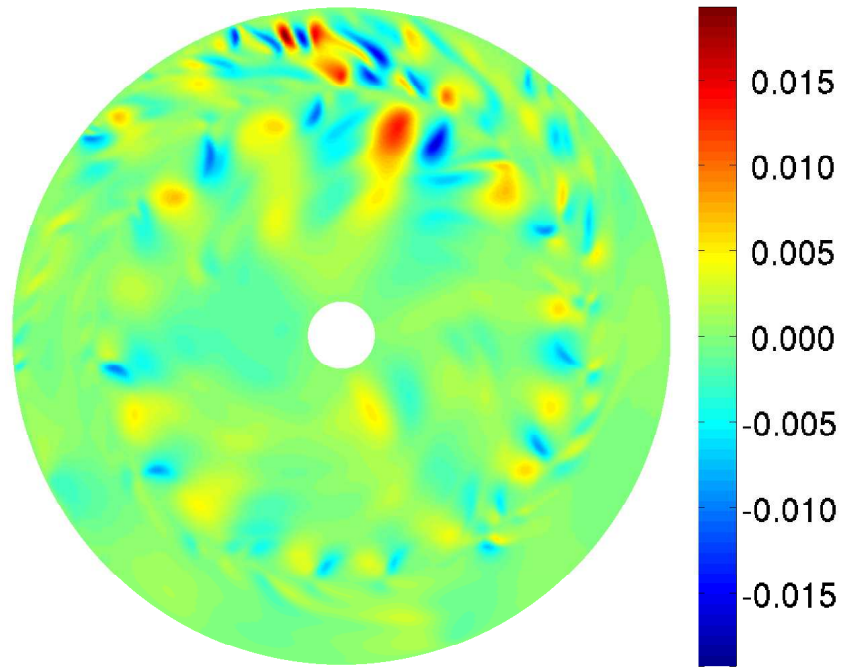
Figure 5.18: 2D cylindrical radial velocity.

The order one axial flow observed in the 2D results would require significant flow across the pole in the boundary layers. Not considering the Coriolis forces on this boundary flow would allow the antisymmetric axial flow to grow larger than it should. This could also explain both the origin and absence of the order one cylindrical radial flow in the 3D results. In the 3D case, since the boundary flows are dynamically modeled not only would the Coriolis forces prevent an antisymmetry in the axial flow from growing large, but any antisymmetry in the axial flow would drive an order one cylindrical radial flow in the bulk. Since the boundary flows are not explicitly modeled in the 2D model this feedback mechanism would not be captured, so we would expect to see the order one flow in the axial flow rather than the cylindrical radial flow. Away from the

pole, where a low order flow cannot be connected with a return flow over the pole, this effect would be negligible.

When the 2D results are filtered to remove the low order modes ($m \leq 8$), the results much more closely resemble the 3D results, both in terms of the amplitudes and structure. The amplitude of the 2D flow is roughly twice as large. However, the 2D results tend to feature more elongated structures than the 3D results, which has more localized features. The 2D images do not feature any axial flow outside the TC. This is due to the fact that the rigid axial flow is assumed to be zero here. However, if we add the half-plane average of the boundary induced axial flow from the topographic beta-effect, depicted in figure 5.19(c), we see some of the elongated structures with comparable magnitude outside the TC as seen in the 3D results of figure 5.9.

Finally, the thermal structure is shown in figure 5.20. Compared with the 3D results in figure 5.13 we can already see that although the mean structure is similar, the amplitude of the thermal perturbations are significantly smaller inside the TC. These thermal perturbations are more visible in the plot of the non-axisymmetric temperature in figure 5.21. Outside the TC the temperature is quite similar to the 3D results, with large perturbations of comparable amplitude near the boundary in the regions of enhanced convection, and elongated and lower amplitude structures elsewhere. The thermal perturbations are clearly tilted here like the convection cells they are associated with. Inside the TC we see smaller amplitude perturbations and an absence of the small scale localized perturbations that the 3D results featured.

Figure 5.22 shows the axisymmetric heat flux in the spherical radial direction from the 2D model as a function of latitude. Like the 3D results in figure 5.14, the Nusselt number is mostly constant with latitude inside the TC

(a) Full velocity

(b) High pass filtered velocity

(c) Boundary induced flow included
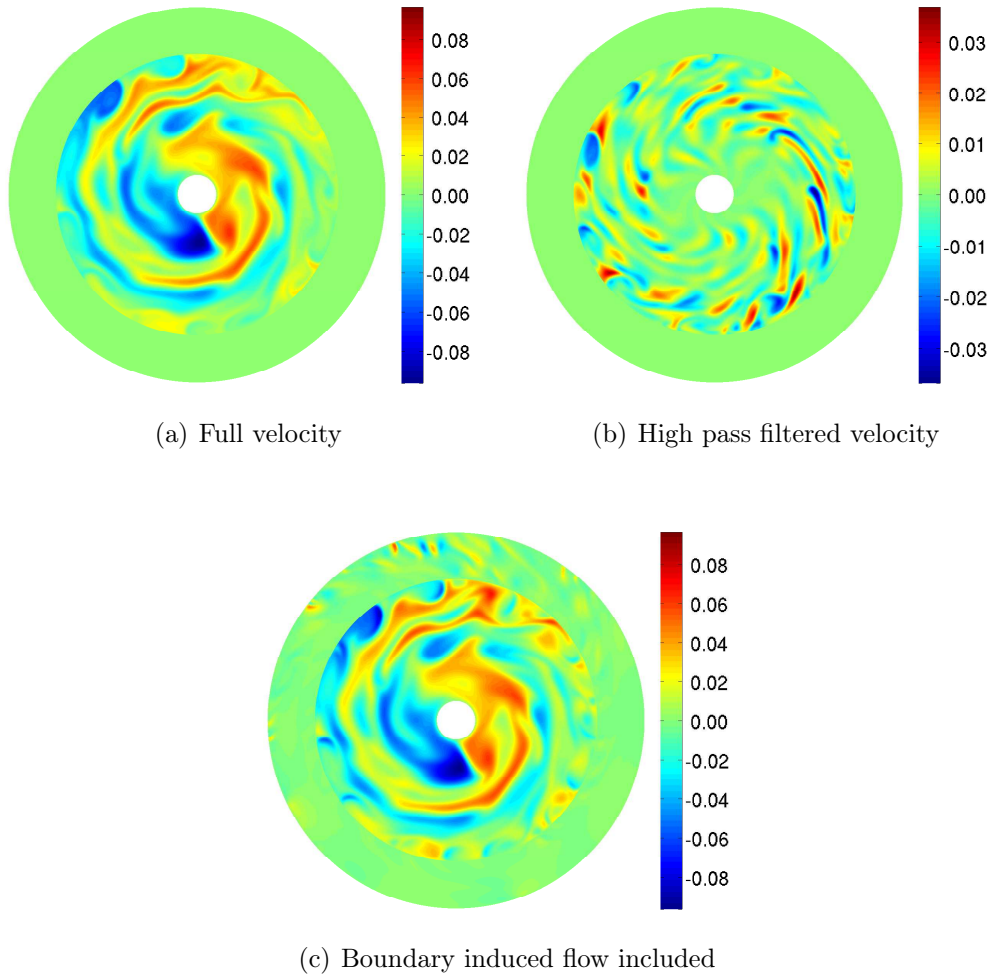
Figure 5.19: 2D axial velocity. On the top left (5.19(a)) is the full velocity, and on the top right (5.19(b)) is the velocity with low order modes ($m \leq 8$) filtered out. On the bottom (5.19(c)) the axial average of the boundary induced ageostrophic flow is included.

with a value of $6 - 8$. This value is a consequence of our choice of how to parameterize the saturation of the axial thermal profile Γ, which dictates the steady state axial heat flux. However, the Nusselt number drops off significantly across the TC. This could be due to the fact that we did not consider axial convection outside the TC. Additionally, the prohibition of flow across the TC would artificially decrease the heat flux here. Another potential cause

134
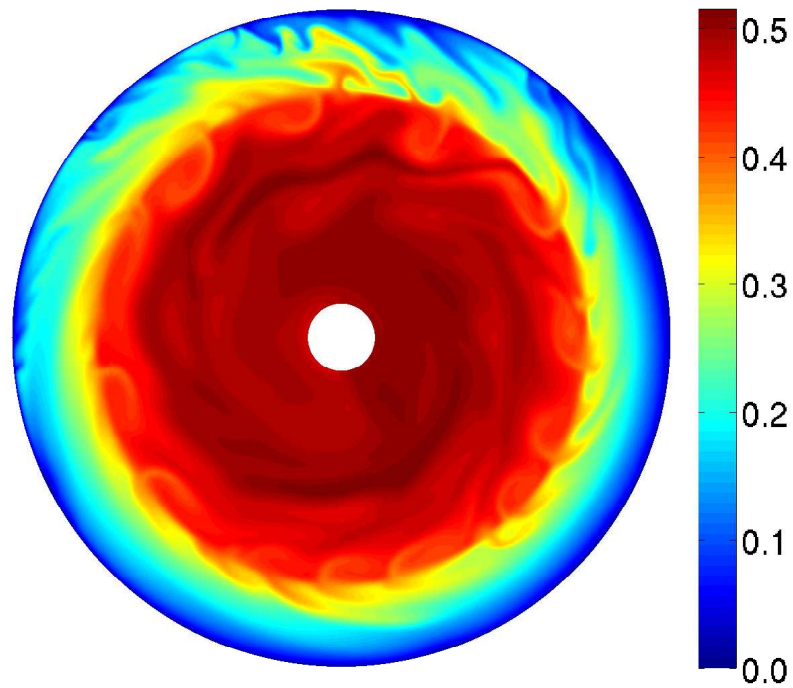
Figure 5.20: 2D temperature.

of this discrepancy is the difficulty defining a 2D reference conducting profile to normalize the heat flux with outside the TC.

Figure 5.23 shows the evolution of the various forms of energy of the system through the course of the simulation. After an initial burst of convection, the energies all equilibrate within several hundred planetary rotations.
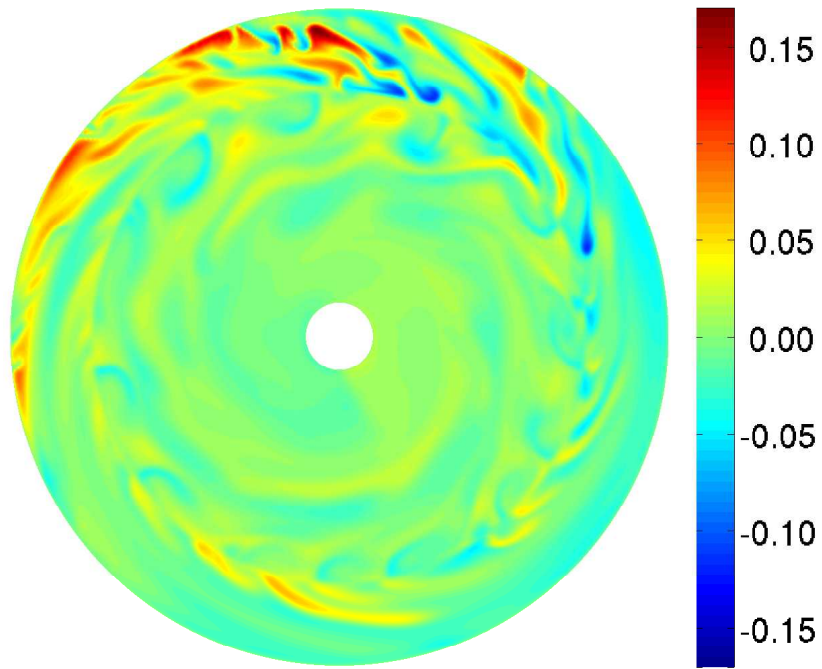
Figure 5.21: 2D non-axisymmetric temperature.
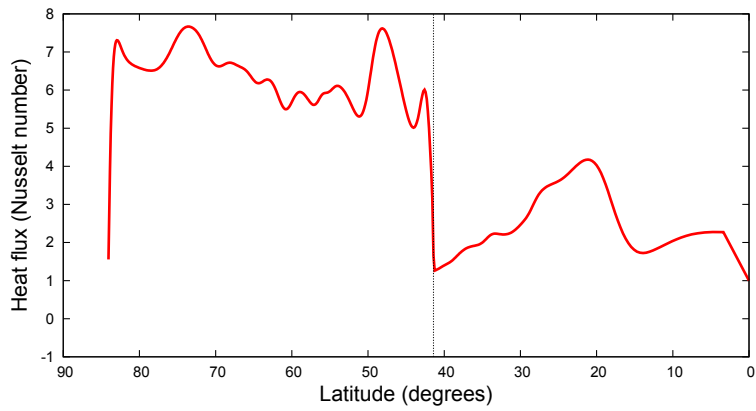
Figure 5.22: Nusselt number in the spherical radial direction for the 2D QG model as a function of latitude. The dotted line is the tangent cylinder.
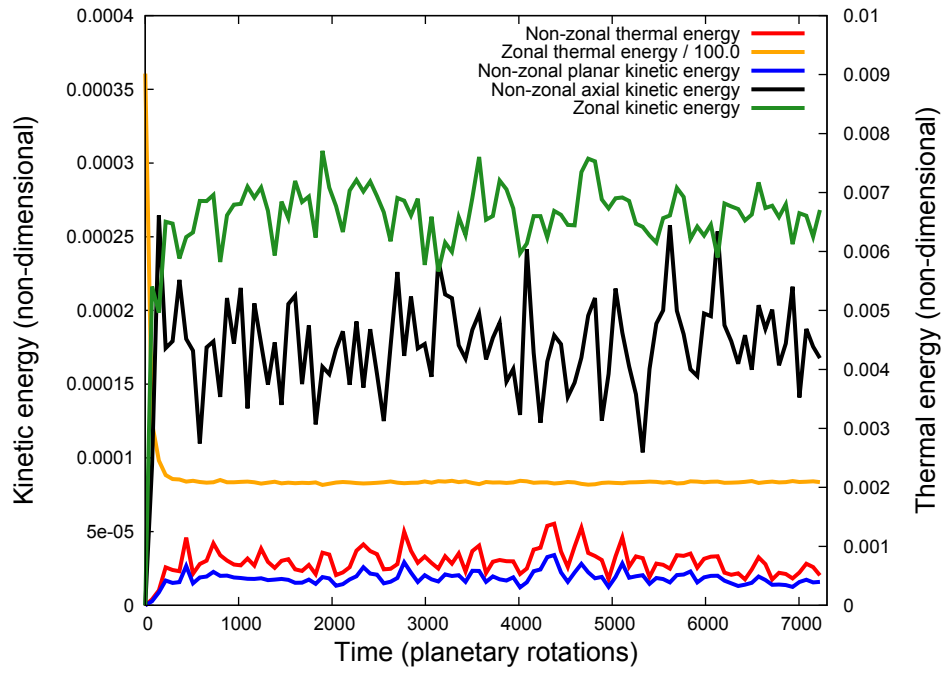
Figure 5.23: Temporal evolution of the various energy components in the 2D QG model.

Summary

The 2D QG model is able to reproduce many of the features of the 3D results. The tilted convection cells which drive jet formation are clearly visible in planforms of several of the system variables. The amplitudes of all the variables in the 2D results are within an order of magnitude of the 3D results, and most are much closer than that. However, at high latitudes the amplitudes are noticeably smaller in the 2D results. Generally, the horizontal length scale of the features in the 2D results is larger than the 3D results, again especially at high latitudes.

Both sets of results feature a broad prograde equatorial zonal jet and alternating jets of smaller amplitude at higher latitude, though the jets in the 2D results are roughly half the amplitude of the 3D results. The smaller amplitude central jet is likely due to the more gradual thermal conducting profile utilized outside the TC in the 2D model due to our choice of a non-cuspy profile. While the 3D model produced several alternating jets at high latitudes, the 2D model featured a single jet spanning the entire region. This could be a consequence of the small amplitude of the planar velocities at high latitudes. Convection cells do not grow large enough for the beta-effect to be the limiting factor preventing jet growth. Instead, the fluid at high latitudes is sped up by viscous forcing from lower latitude jets, eventually producing a single broad jet.

As expected, the large order one flow across the pole in the 3D results is not reproduced by the 2D model. However, an order one axial flow, which was not present in the 3D results, is produced in the 2D results. This discrepancy could be explainable by the fact that the QG model only parameterizes the

E	3×10^{-8}	Ra	5.56×10^{11}
Pr	0.1	χ	0.9

Table 5.3: Non-dimensional parameters used for the results in Section 5.2.

boundary layer flow, without directly simulating it.

The Nusselt number is comparable between the models inside the TC, though in the 2D results, unlike in the 3D case, it drops off outside the TC. This could be due to the fact that the QG model does not consider axial convection outside the TC.

5.2 Small Ekman number run

In this section, more aggressive non-dimensional parameters, equivalent to those specified by Heimpel [49], are utilized including a thinner convecting shell. The values are given in Table 5.3, and lead to $Ra^* \sim 0.005$. A grid of 1451 radial points and maximal spectral component of 559 was used. For these parameters, an eightfold symmetry is imposed on the flow to reduce the computational time required to reach convergence.

Figure 5.24 shows the azimuthal velocity produced by our 2D simulation. Only an eighth of the 2D plane has be plotted since with the eightfold symmetry imposed on the flow this uniquely specifies the results. This flow can be envisioned to be repeated eight times to produce a full plane solution. As with the 3D results, the azimuthal flow is strongly axisymmetric. The zonally averaged azimuthal flow is plotted versus latitude in figure 5.25. A strong prograde equatorial jet, of very similar amplitude to the results of the 3D numerical model seen in figure 1.8, is clearly evident. Like in the modest parameter regime in the last section, the absolute minimum zonal wind occurs

at the first retrograde jet located near the TC. The first 2D retrograde jet is somewhat stronger than in the 3D results. While at the modest parameter regime the QG model produced only a single broad jet inside the TC, using the aggressive parameters the results feature several jets of alternating directions at higher latitudes. The 3D model produced four and five high latitude maximums of the zonal wind in the two hemispheres respectively, while using our 2D model we get three. This difference could be explained by the fact that the 3D model simulated the full shell, while our QG model had a restricted domain external to $s = 0.1$ for numerical reasons. In the 3D results there is a prograde jet very close to the pole in both hemispheres. The amplitude of the high latitude jets is consistent with the 3D results.
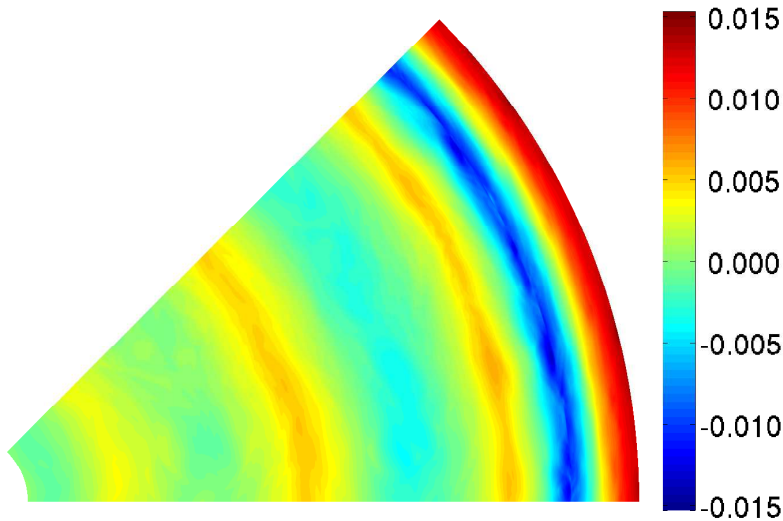
Figure 5.24: 2D azimuthal velocity.

The measured widths of the jets, and the predicted jet widths from Rhines scaling, are plotted versus latitude in figure 5.26. The jet boundaries are taken to be the locations of a local minimum of the absolute value of the azimuthal
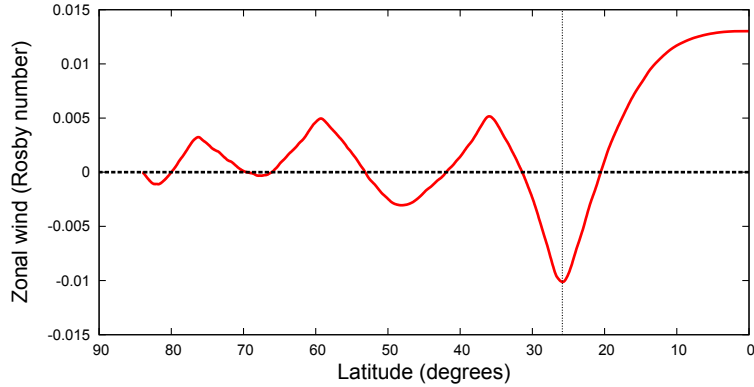
Figure 5.25: 2D zonal flow plotted versus latitude.

velocity. This corresponds to latitudes where either the azimuthal velocity is zero, or its derivative with latitude is zero. The Rhines wavelengths are calculated using equation 1.7, with β equal to the topographical beta defined in equation 3.46 and U equal to the average magnitude of the zonal flow over the jet. The jet widths are taken to correspond to half the wavelength. Figure 5.26 shows that the predicted and measured jet widths are quite comparable, which supports the theory that their widths are limited by the generation of Rossby waves. The measured central jet is roughly 50% larger than predicted, while the highest latitude jet is smaller, but this is consistent with the 3D results.

The non-axisymmetric azimuthal velocity is plotted in figure 5.27. This component of the flow is strongest near the TC, where it is organized such that it is elongated in the latitudinal direction but quite thin in the cylindrical radial direction. Alternating prograde and retrograde structures line the TC.

The cylindrical radial velocity is plotted in figure 5.28. Here we see several

141
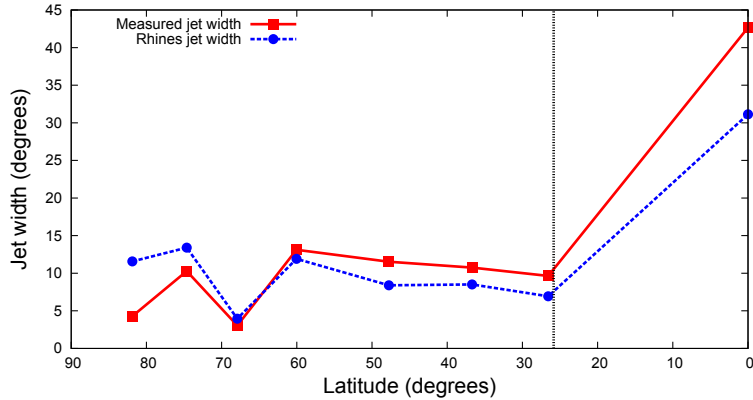
Figure 5.26: A plot of the measured jet widths (solid red line with square points) and the jet widths predicted by Rhines scaling (dashed blue line with circle points). The TC is marked with a dashed black line.

rings of convection cells, the most prominent of which is the one just inside the TC. Comparing this image with the azimuthal flow in figure 5.27 we can see that the TC is acting as a barrier to cylindrical radial flow. Outward moving fluid parcels are deflected into the azimuthal direction at the TC due to our prescription of an impenetrable boundary here. The physical explanation for this is that fluid parcels which cross the TC break the rigidity constraints imposed by rotation since outside the TC flow spans both hemispheres while inside it is restricted to a single hemisphere. Unlike in the modest parameter results, the cylindrical radial velocity remains large at high latitudes. Outside the TC the cylindrical radial velocity is smaller and is primarily smaller scale. Generally the scale of the flow is smaller than in the modest parameter regime, which is expected since the typical size of the planar flow should scale as $E^{\frac{1}{3}}$.

Unlike in the modest parameter regime we no longer see the order one flow dominating the axial flow in figure 5.29. In fact, the typical horizontal
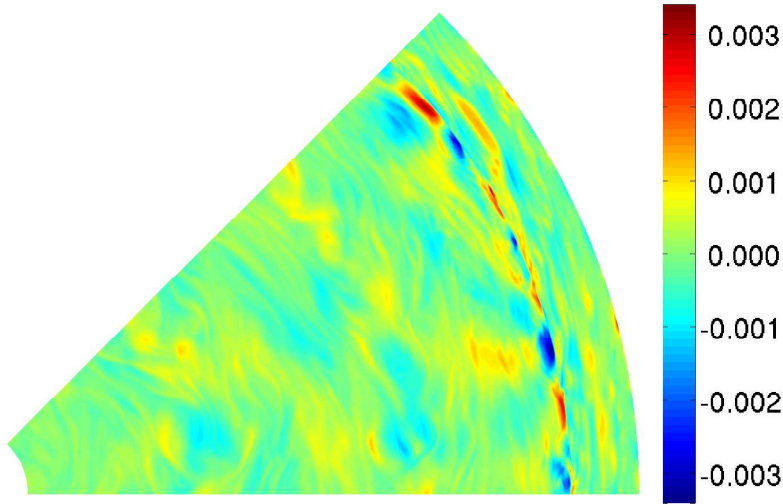
Figure 5.27: 2D non-axisymmetric azimuthal velocity.

scale of the axial velocity is much smaller than the horizontal flow. However the structures are still more elongated than the localized plume-like structures seen in the 3D results of the modest parameter regime.

As with the modest parameter regime, the temperature, plotted in figure 5.30, contains very small perturbations. When removing the axisymmetric thermal component, plotted in figure 5.31, it can be seen that the largest perturbations are located near the TC and external to it. The perturbations are generally quite elongated. Tilted thermal structures are quite visible in this image near the TC, prograde outside and retrograde inside due to the change in sign of beta. Aside from the axisymmetric zonal jets, the longitudinal extent of all the flow structures examined is significantly smaller than the simulated azimuthal domain, which suggests that the imposed eightfold symmetry should not drastically alter the results.

Plotting the spherical radial Nusselt number versus latitude in figure 5.32
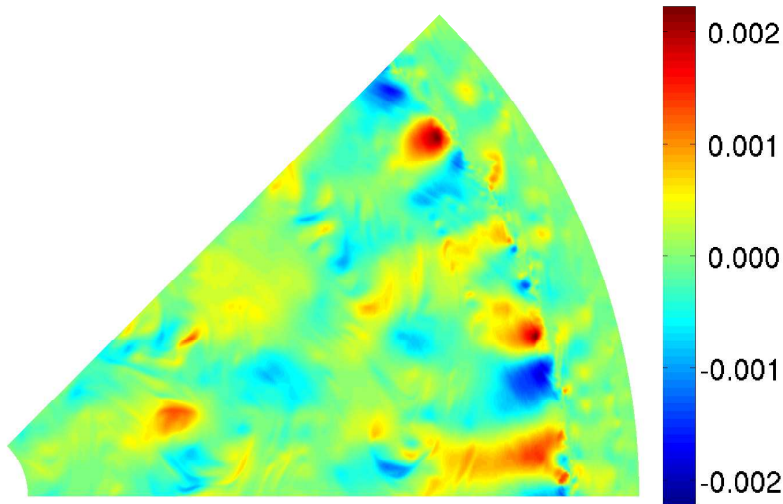
Figure 5.28: 2D cylindrical radial velocity.

shows that like in the modest parameter regime the heat flux is mostly constant inside the TC, with the value of the Nusselt number in this case roughly equal 3. Again, the Nusselt number drops off significantly outside the TC. This decrease in heat flux outside the TC is consistent with the 3D results at comparable parameters, and is likely due to the deflection of thermal plumes by the zonal wind [4]. The drop off is somewhat sharper at the TC in the 2D results, which can likely be explained by the same factors as described in the modest parameter regime: no axial flow outside the TC and no flow across the TC. Inside the TC axial plumes are aligned with contours of constant zonal flow, while outside the TC they must cross them, which inhibits their ability to transport heat efficiently across the shell.

Finally, figure 5.33 shows the evolution of the energies during the simulation. Using these parameters, convergence took significantly longer both in terms of wall-clock time and the number of planetary rotations. While the

144
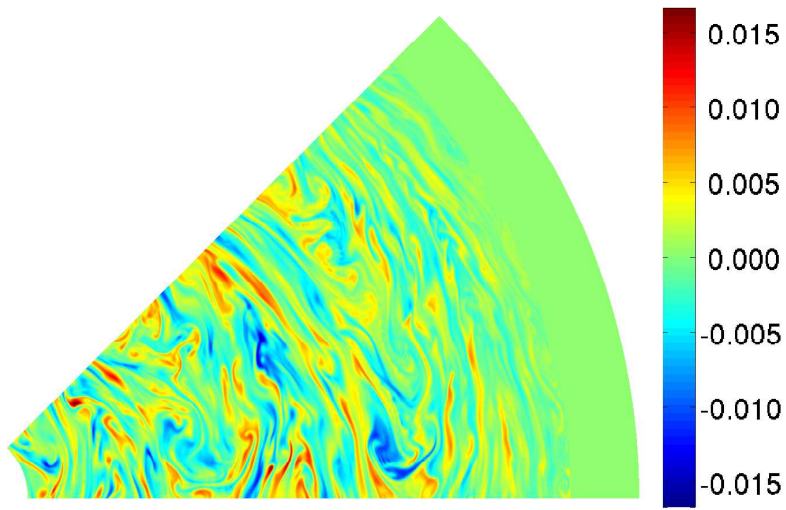
Figure 5.29: 2D axial velocity.

thermal and non-zonal mechanical energies quickly stabilized after an initial burst of convection, the zonal kinetic energy took an extended period of time to build up and eventually stabilize.
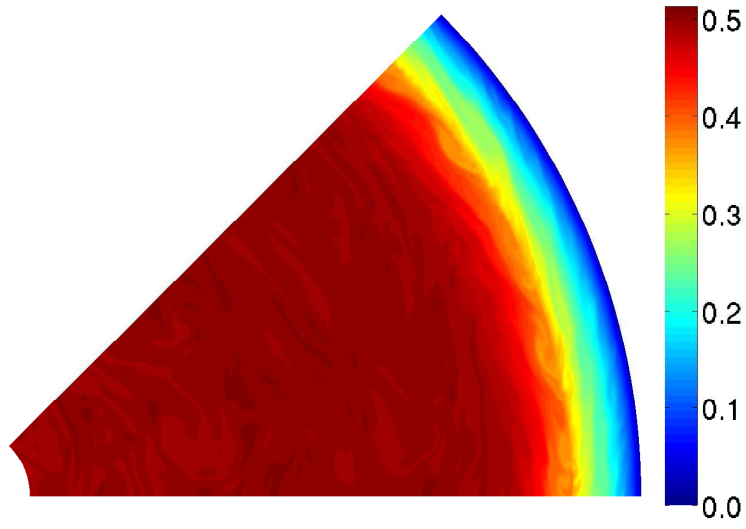
Figure 5.30: 2D total temperature.
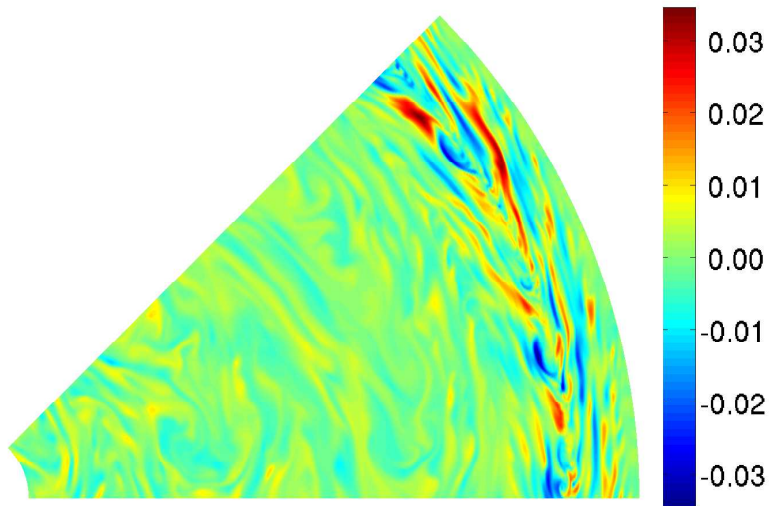
Figure 5.31: 2D non-axisymmetric temperature components.
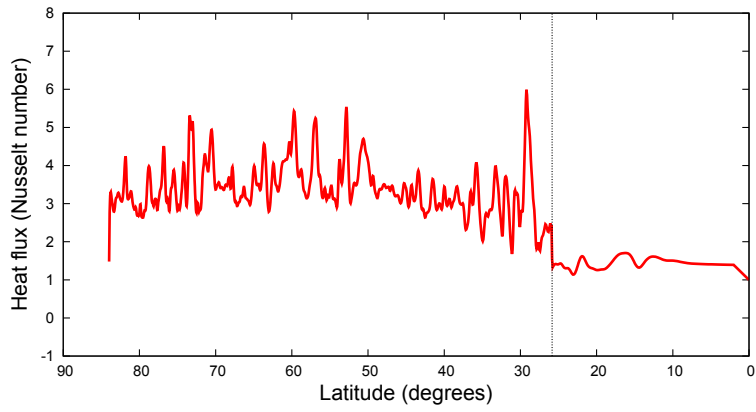
Figure 5.32: Spherical radial Nusselt number for the 2D model.
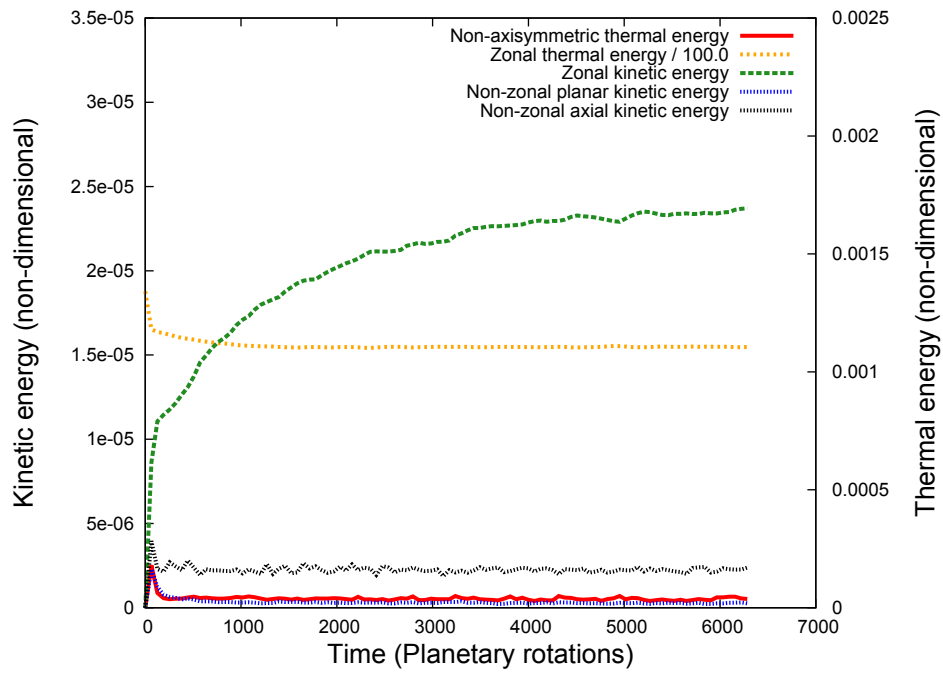
Figure 5.33: Temporal evolution of the various energy components in the 2D QG model.

Chapter 6

Conclusions

A complete understanding of the origin of Jupiter's mean zonal flow has yet to emerge. Both observations and numerical models suggest that the surface flow is a consequence of convection deep within the planet. If this picture is correct then the structure of the surface zonal flows provides a good way to probe the internal dynamics of the planet. However, due to computational limits, existing numerical models of zonal wind generation are restricted to parameter regimes which are many orders of magnitude more modest than is thought to exist in Jupiter. In order to study this phenomenon at more realistic physical parameters, a simplified two dimensional quasigeostrophic model of the flow in a spherical shell was constructed in this thesis. Such models assume that due to the rapid planetary rotation the primary force balance of the flow is geostrophic, between the Coriolis force and pressure gradient, which leads to dominantly rigid flow, invariant parallel to the rotation axis. To exploit this structure, the equations of motion were integrated over Taylor columns in the axial direction, with only the axially mean values being dynamically simulated. This required the generalization of existing QG models to account

for flow inside the tangent cylinder and buoyancy in the axial direction, which leads to axial convection. Neither has been considered in the past.

Results from a numerical implementation of our QG model demonstrate that it captures many of the important features of fully 3D simulations, including zonal wind generation. The general structure of Jupiter's observed zonal wind, a large central jet and jets of alternating direction at higher latitudes, can readily be reproduced using this model. The amplitudes of the flow variables are all of the same order of magnitude as the 3D values. The results are especially good outside the TC, where the scale and morphology of the flow structures are very similar. Inside the TC the amplitudes tend to be smaller and the scale of the flow structures more elongated than the more localized structures seen in the 3D results.

As this work represents a first approach to the development of a QG model of convection inside the TC, there are naturally several avenues available for further improvement to the model. First and foremost is to consider the effects of the variations in z of the geostrophic pressure due to the thermal wind, as discussed in Section 3.1.3, and the resulting non-rigid vorticity that this entails. If the non-rigid vorticity becomes large enough it will begin to tear the rigid vorticity apart. This could be incorporated into the model by specifying a second stream function, which is linear in z, and deriving an independent equation of motion for it. The linear stream function would then feed back on the equations for the other flow variables. Preliminary results suggest that this extension of the model prevents the large axial flow from developing in the large Ekman number runs, as in Figure 5.19(a). As a result, more localized structures in the axial flow and thermal perturbations are produced, in much better agreement with the 3D results.

The development of an improved parameterization of Γ, which models the saturation of the background thermal profile which drives axial convection, would also likely improve the results. In the present implementation saturation occurs when the axial Nusselt number at a given cylindrical radius becomes sufficiently large. However, one drawback of this approach is that all modes at a given radius saturate simultaneously. Both small scale and large scale heat flux can lead to saturation. It is quite possible that this could tend to produce thermal and axial flow structures which are extended in the azimuthal direction, as observed in the 2D results, rather than the more localized structures observed in the 3D results.

Including the axial flow outside the TC, which would require a parameterization of how it is fed by non-rigid flow along the equatorial plane, would lead to a better match of the heat flux with 3D results here. Additionally, a more realistic model of the flow within the boundary layers, and allowing for the possibility of axisymmetric axial flow into the boundary layer, would likely go a long way to improving the results. A relaxation of the strict impenetrability condition at the TC, which has been utilized to ensure stability at a point where β diverges, could lead to more realistic results as well. One possible method to accomplish this is to devise an effective beta parameter which does not diverge at the TC. However, some inhibition of flow across the TC is almost certainly required since such flow breaks the rigidity constraints imposed by rotation, so a parameterization of this effect, without completely prohibiting it, is needed.

Bibliography

[1] D. H. Atkinson, J. B. Pollack, and A. Seiff. The Galileo probe doppler wind experiement: measurement of the deep zonal winds on Jupiter. *Journal of Geophysics research*, 103:22911–22928, 1998.

[2] J. Aubert, N. Gillet, and P. Cardin. Quasigeostrophic models of convection in rotating spherical shells. *Geochemistry Geophysics, Geosystems*, 4:1052, 2003.

[3] J. Aurnou and M. Heimpel. Zonal jets in rotation convection with mixed mechanical boundary conditions. *Icarus*, 169:492–498, 2004.

[4] J. Aurnou, M. Heimpel, L. Allen, E. King, and J. Wicht. Convective heat transfer and the pattern of thermal emission on the gas giants. *Geophysics Journal International*, 173:793–801, 2008.

[5] J. Aurnou, M. Heimpel, and J. Wicht. The effects of vigorous mixing in a convective model of zonal flow on the ice giants. *Icarus*, 190(1):110–126, 2007.

[6] J. Aurnou and P. Olson. Strong zonal winds from thermal convection in a rotating spherical shell. *Geophysical Research Letters*, 28(13):2557–2559, 2001.

[7] H. Bénard. Les tourbillons cellulaires dans une nappe liquide: Description générale des phénomènes. *Revue Générale des Sciences pures et appliquées*, 11:1261–1271, 1900.

[8] H. Bénard. Les tourbillons cellulaires dans une nappe liquide: Procédés méchaniques et optiques d'examen; lois numériques des phénomènes. *Revue Générale des Sciences pures et appliquées*, 11:1309–1328, 1900.

[9] G. Boffetta. Energy and enstrophy fluxes in the double cascade of two-dimensional turbulence. *Journal of Fluid Mechanics*, 589:253–260, 2007.

[10] J. Boussinesq. *Théorie analytique de la chaleur mise en harmonie avec la thermodynamique et avec la théorie mécanique de la lumière*. Gauthier-Villars, 1903.

[11] S. C. Brown. Count Rumford discovers thermal convection. *Daedalus*, 86(4):340–343, 1957.

[12] U. Burr and W. Kinzelbach. Is the turbulent wind in convective flows driven by fluctuations? *Physics of Fluids*, 15(8):2313–2320, 2003.

[13] F. H. Busse. Thermal instabilities in rapidly rotating systems. *Journal of Fluid Mechanics*, 44(3):441–460, 1970.

[14] F. H. Busse. A simple model of convection in the Jovian atmosphere. *Icarus*, 20:255–260, 1976.

[15] F. H. Busse. Generation of mean flows by thermal convection. *Physica D: Nonlinear Phenomena*, 9(3):287–299, 1983.

[16] F. H. Busse. A model of mean zonal flows in the major planets. *Geophysical & Astrophysical Fluid Dynamics*, 23:153–174, 1983.

[17] F. H. Busse. Convection driven zonal flows and vortices in the major planets. *Chaos*, 4(2):123–134, 1994.

[18] F. H. Busse. Convective flows in rapidly rotating spheres and their dynamo action. *Physics of Fluids*, 14:1301–1214, 2002.

[19] F. H. Busse and C. R. Carrigan. Convection induced by centrifugal buoyancy. *Journal of Fluid Mechanics*, 62(3):579–592, 1974.

[20] F. H. Busse and C. R. Carrigan. Laboratory simulation of thermal convection in rotating plantes and stars. *Science*, 191(4222):81–83, 1976.

[21] F. H. Busse and P. G. Cuong. Convection in rapidly rotation spherical fluid shells. *Geophysical & Astrophysical Fluid Dynamics*, 8:17–44, 1977.

[22] C. R. Carrigan and F. H. Busse. An experimental and theoretical investigation of the onset of convection in rotating spherical shells. *Journal of Fluid Mechanics*, 126:287–305, 1983.

[23] S. Chandrasekhar. The instability of a layer of fluid heated below and subject to Coriolis forces. *Proceedings of the Royal Society of London Series A*, 217(1130):306–327, 1953.

[24] S. Chandrasekhar. *Hydrodynamic and Hydromagnetic Stability*. Oxford University Press, 1961.

[25] S. Chandrasekhar and D. D. Elbert. The instability of a layer of fluid heated below and subject to Coriolis forces II. *Proceedings of the Royal Society of London Series A*, 231(1185):198–210, 1955.

[26] D. Chen and G. H. Jirka. Experimental study of plane turbulent wakes in a shallow water layer. *Fluid Dynamics Research*, 16:11–41, 1995.

[27] J. Y.-K. Cho and L. M. Polvani. The emergence of jets and vortices in freely evolving, shallow-water turbulence on a sphere. *Physics of Fluids*, 8(6):1531–1552, 1996.

[28] J. Y.-K. Cho and L. M. Polvani. The morphogenesis of bands and zonal winds in the atmospheres on the giant outer planets. *Science*, 273:335–337, 1996.

[29] U. Christensen. Zonal flow driven by deep convection in the major planets. *Geophysical Research Letters*, 28(13):2553–2556, 2001.

[30] M. Evonuk. The role of density stratification in generating zonal flow structures in a rotating fluid. *Astrophysical Journal*, 673:1154–1159, 2008.

[31] M. Evonuk and G. Glatzmaier. 2D studies of various approximations used for modeling convection in giant planets. *Geophysical and Astrophysical Fluid Dynamics*, 98(3):241–255, 2004.

[32] B. Favier, L. J. Silvers, and M. R. E. Proctor. Inverse cascade and symmetry breaking in rapidly-rotating Boussinesq convection. *Physics of Fluids*, 26, 2014.

[33] M. Frigo and S. G. Johnson. *FFTW*. fftw.org, 3.3.3 edition, 2012.

[34] U. Frisch and P. L. Sulem. Numerical simulation of the inverse cascade in two-dimensional turbulence. *Physics of Fluids*, 27(8):1921–1923, 1984.

[35] O. U. V. Fuentes. Kelvin's discovery of Taylor columns. *European Journal of Mechanics B/Fluids*, 28:469–472, 2009.

[36] B. Galperin, S. Sukoriansky, and H.-P. Huang. Universal n^{-5} spectrum of zonal flows on giant planets. *Physics of Fluids*, 13(6):1545–1548, 2001.

[37] T. Gastine, M. Heimpel, and J. Wicht. Zonal flow scaling in rapidly-rotating compressible convection. *Physics of the Earth and Planetary Interiors*, 232:36–50, 2014.

[38] T. Gastine and J. Wicht. Effects of compressibility on driving zonal flow in gas giants. *Icarus*, 219:428–442, 2012.

[39] T. Gastine, J. Wicht, L. D. V. Duarte, M. Heimpel, and A. Becker. Explaining Jupiter's magnetic field and equatorial jet dynamics. *Geophysical Research Letters*, 41(15):5410–5419, 2014.

[40] N. Gillet and C. A. Jones. The quasi-geostrophic model for rapidly rotating spherical convection outside the tangent cylinder. *Journal of Fluid Mechanics*, 554:343–369, 2006.

[41] P. A. Gilman. Linear simulations of boussinesq convection in a deep rotating spherical shell. *Journal of the Atmospheric Sciences*, 32:1331–1352, 1975.

[42] P. A. Gilman and G. A. Glatzmaier. Compressible convection in a rotating spherical shell. I. Anelastic equations. *Astrophysical Journal*, 45:335–349, 1981.

[43] G. A. Glatzmaier, M. Evonuk, and T. Rogers. Differential rotation in giant planets maintained by density-stratified turbulent convection. *Geophysical and Astrophysical Fluid Dynamics*, 103(1):31–51, 2009.

[44] D. Goluskin, H. Johnston, G. R. Flierl, and E. A. Spiegel. Convectively driven shear and decreased heat flux. *Journal of Fluid Mechanics*, pages 360–385, 2014.

[45] C. Guervilly, D. W. Hughes, and C. A. Jones. Large-scale vortices in rapidly rotating Rayleigh-Bérnard convection. *Journal of Fluid Mechanics*, 758:407–435, 2014.

[46] T. Guillot. The interiors of giant planets: models and outstanding questions. *Annual Review of Earth and Planetary Sciences*, 33:493–530, 2005.

[47] T. Guillot, D. J. Stevenson, W. Hubbard, and D. Saumon. *Jupiter: the planet, satellites and magnetosphere*, chapter The interior of Jupiter, pages 35–37. Cambridge University Press, Cambridge, 2004.

[48] R. A. Hanel, B. J. Conrath, L. W. Herath, V. G. Kunde, and J. S. Pirraglia. Albedo, internal heat, and energy balance of Jupiter: Preliminary results of the Voyager infrared investigation. *Journal of Geophysical Research*, 86:8705–8712, 1981.

[49] M. Heimpel and J. Aurnou. Turbulent convection in rapidly rotating spherical shells: a model for equatorial and high latitude jets on Jupiter and Saturn. *Icarus*, 187(2):540–557, 2007.

[50] M. Heimpel, J. Aurnou, and J. Wicht. Simulation of equatorial and high-latitude jets on Jupiter in a deep convection model. *Nature*, 438:193–196, 2005.

[51] R. Hide and P. J. Mason. Sloping convection in a rotating fluid. *Advances in Physics*, 24(1):47–100, 1975.

[52] G. Holloway and M. Hendershott. Stochastic closure for nonlinear rossby waves. *Journal of Fluid Mechanics*, 82:747–765, 1977.

[53] S. S. Hough. On the application of harmonic analysis to the dynamical theory of tides. Part I. On Laplace's "Oscillations of the first species," and on the dynamics of ocean currents. *Philosophical transactions of the Royal Society of London. Series A.*, 189:201–257, 1897.

[54] A. P. Ingersoll and D. Pollard. Motion in the interios and atmospheres of Jupiter and Saturn: Scale analysis, anelastic equations, barotropic stability criterion. *Icarus*, 52:62–80, 1982.

[55] C. A. Jones. A dynamo model of Jupiter's magnetic field. *Icarus*, 241:148–159, 2014.

[56] C. A. Jones and K. M. Kuzanyan. Compressible convection in the deep atmospheres of giant planets. *Icarus*, 204(1):227–238, 2009.

[57] K. Julien, A. M. Rubio, I. Grooms, and E. Knobloch. Statistical and physical balances in low Rossby number Rayleigh-Bénard convection. *Geophysical and Astrophysical Fluid Dynamics*, 106(4-5):392–428, 2012.

[58] H. Kellay and W. Goldburg. Two-dimensional turbulence: a review of some recent experiments. *Reports on Progress in Physics*, 65:845–894, 2002.

[59] E. M. King, S. Stellmach, and J. M. Aurnou. Heat transfer by rapidly rotating Rayleigh-Bénard convection. *Journal of Fluid Mechanics*, 691:568–582, 2012.

[60] E. M. King, S. Stellmach, J. Noir, U. Hansen, and J. M. Aurnou. Boundary layer control of rotating convection systems. *Nature*, 457:301–304, 2009.

[61] R. H. Kraichnan. Inertial ranges in two-dimensional turbulence. *The Physics of Fluids*, 10(7):1417–1423, 1967.

[62] R. H. Kraichnan and D. Montgomery. Two-dimensional turbulence. *Reports in Progress in Physics*, 43:547–619, 1980.

[63] R. Krishnamurti and L. N. Howard. Large-scale flow generation in turbulent convection. *Proceedings of the National Academy of Science of the United States of America*, 78(4):1981–1985, 1981.

[64] Y. Lian and A. P. Showman. Deep jets on gas-giant planets. *Icarus*, 194(2):597–615, 2008.

[65] S. S. Limaye. Jupiter - new estimates of the mean zonal flow at the could level. *Icarus*, 65:335–352, 1986.

[66] J. Liu. Constraints on deep-seated zonal winds inside Jupiter and Saturn. *Icarus*, 196(2):653–664, 2008.

[67] M. E. Maltrud and G. K. Vallis. Energy spectra and coherent structures in forced two-dimensional and beta-plane turbulence. *Journal of Fluid Mechanics*, 228:321–342, 1991.

[68] T. Martin. The experimental researches of Benjamin Thompson, Count Rumford. *Bulletin of the British Society for the History of Science*, 1(6):144–158, 1951.

[69] J. Paret and P. Tabeling. Intermittency in the two-dimensional inverse cascade of energy: experimental observations. *Physics of Fluids*, 10(12):3126–3136, 1998.

[70] J. Pedlosky. *Geophysical fluid dynamics*. Springer, 1987.

[71] J. Pedlosky. *Ocean Circulation Theory*. Springer, 1996.

[72] J. A. Pirraglia. Meridional energy balance of Jupiter. *Icarus*, 59:169–176, 1984.

[73] C. C. Porco et al. Cassini imaging of Jupiter's atmosphere, satellites and rings. *Science*, 299:1541–1547, 2003.

[74] W. H. Press, S. A. Teukolsky, W. T. Vetterling, and B. P. Flannery. *Numerical Recipes: The Art of Scientific Computing*. Cambridge University Press, Third edition, 2007.

[75] J. Proudman. On the motion of solids in a liquid possessing vorticity. *Proceedings of the Royal Society of London Series A*, 92(642):408–424, 1916.

[76] L. Rayleigh. On convection currents in a horizontal layer of fluid, when the higher temperature is on the under side. *Philosophical Magazine*, 32(192):529–546, 1916.

[77] P. L. Read, Y. H. Yamazaki, S. R. Lewis, P. D. Williams, K. Miki-Yamazaki, J. Sommeria, H. Didelle, and A. Fincham. Jupiter's and Saturn's convectively driven banded jets in the laboratory. *Geophysical Research Letters*, 31(22), 2004.

[78] P. B. Rhines. Waves and turbulence on a beta-plane. *Journal of Fluid Mechanics*, 69:417–443, 1975.

[79] P. H. Roberts. On the thermal instability of a highy rotating fluid sphere. *Astrophysical Journal*, 141:240–250, 1965.

[80] P. H. Roberts. On the thermal instability of a rotating-fluid sphere containing heat sources. *Philosophical Transactions of the Royal Society of London Series A*, 263(1136):93–117, 1968.

[81] A. M. Rubio, K. Julien, E. Knobloch, and J. B. Weiss. Upscale energy transfer in three-dimensional rapidly rotating turbulent convection. *Physical Review Letters*, 112, 2014.

[82] N. Schaeffer and P. Cardin. Rossby-wave turbulence in a rapidly rotating sphere. *Nonlinear Processes in Geophysics*, 12:947–953, 2005.

[83] N. Schaeffer and P. Cardin. Quasi-geostrophic kinematic dynamos at low magnetic prandtl number. *Earth and Planetary Science Letters*, 245(3-4):595–604, 2006.

[84] R. K. Scott and L. M. Polvani. Forced-dissipative shallow-water turbulence on the sphere and the atmospheric circulation of the giant planets. *Journal of the Atmospheric Sciences*, 64:3158–3176, 2007.

[85] R. K. Scott and L. M. Polvani. Equatorial superrotation in shallow atmospheres. *Geophysical Research Letters*, 35, 2008.

[86] C. A. Smith, K. G. Speer, and R. W. Griffiths. Multiple zonal jets in a differentially heated rotating annulus. *Journal of Physical Oceanography*, 44:2273–2291, 2014.

[87] J. Sommeria. Experimental study of the two-dimensional inverse energy cascade in a square box. *Journal of Fluid Mechanics*, 170:139–168, 1986.

[88] J. Sommeria and R. Moreau. Why, how, and when, MHD turbulence becomes two-dimensional. *Journal of Fluid Mechanics*, 118:507–518, 1982.

[89] M. Sprague, K. Julien, E. Knobloch, and J. Werne. Numerical simulation of an asymptotically reduced system for rotationally constrained convection. *Journal of Fluid Mechanics*, 551:141–174, 2006.

[90] P. Tabeling. Two-dimensional turbulence: a physicist approach. *Physics Reports*, 362:1–62, 2002.

[91] G. I. Taylor. Motion of solids in fluids when the flow is not irrotational. *Proceedings of the Royal Society of London Series A*, 93(648):99–113, 1917.

[92] G. I. Taylor. Experiments with rotating fluids. *Proceedings of the Royal Society of London Series A*, 100(703):114–121, 1921.

[93] G. I. Taylor. The motion of a sphere in a rotating liquid. *Proceedings of the Royal Socienty of London. Series A.*, 102(715):180–189, 1922.

[94] G. I. Taylor. Experiments on the motion of solid bodies in rotating fluids. *Proceedings of the Royal Society of London. Series A.*, 104(725):213–218, 1923.

[95] G. K. Vallis and M. E. Maltrud. Generation of mean flows and jets on a beta plane and over topography. *Journal of Physical Oceanography*, 23:1346–1362, 1993.

[96] A. R. Vasavada and A. P. Showman. Jovian atmospheric dynamics: an update after Galileo and Cassini. *Report on Progress in Physics*, 68(8):1935–1996, 2005.

[97] J. Verhoeven and S. Stellmach. The compressional beta effect: A source of zonal winds in planets? *Icarus*, 237:143–158, 2014.

[98] G. P. Williams. Planetary circulations: 1. Baratropic representation of Jovian and terrestrial turbulence. *Journal of the Atmospheric Sciences*, 35:1399–1426, 1978.

[99] G. P. Williams. Jovian dynamics - Part III - Multiple, migrating, and equatorial jets. *Journal of the Atmospheric Sciences*, 60:1270–1296, 2003.

[100] C. T. Yap and C. W. van Atta. Experimental studies of the development of quasi-two-dimensional turbulence in stably stratified fluid. *Dynamics of Atmospheres and Oceans*, 19:289–323, 1993.

Appendices

Appendix A

Vorticity equation

We want to find an equation for the time evolution of the vorticity. This is accomplished by taking the curl of the momentum equation 2.28, giving

$$
\frac{\partial \boldsymbol{\omega}}{\partial t} + \underbrace{\boldsymbol{\nabla} \times [(\mathbf{u} \cdot \boldsymbol{\nabla}) \, \mathbf{u}]}_{(1)} + 2 \underbrace{\boldsymbol{\nabla} \times (\hat{\mathbf{z}} \times \mathbf{u})}_{(2)}
$$
$$
= - \underbrace{\boldsymbol{\nabla} \times \boldsymbol{\nabla} P}_{(3)} + E \underbrace{\boldsymbol{\nabla} \times (\boldsymbol{\nabla}^2 \mathbf{u})}_{(4)} - Ra^* \underbrace{\boldsymbol{\nabla} \times (g_r \Theta \hat{\mathbf{g}})}_{(5)}. \qquad (A.1)
$$

Evaluating each term individually, using vector calculus identities and the incompressibility of the flow, gives

$$
\begin{aligned}
(1) \quad &= \boldsymbol{\nabla} \times [(\mathbf{u} \cdot \boldsymbol{\nabla}) \, \mathbf{u}] \\
&= \boldsymbol{\nabla} \times \left[\frac{1}{2} \boldsymbol{\nabla} (\mathbf{u} \cdot \mathbf{u}) - \mathbf{u} \times (\boldsymbol{\nabla} \times \mathbf{u}) \right] \\
&= \frac{1}{2} \boldsymbol{\nabla} \times \boldsymbol{\nabla} u^2 - \boldsymbol{\nabla} \times (\mathbf{u} \times \boldsymbol{\omega}) \\
&= 0 - \mathbf{u} (\boldsymbol{\nabla} \cdot \boldsymbol{\omega}) + \boldsymbol{\omega} (\boldsymbol{\nabla} \cdot \mathbf{u}) - (\boldsymbol{\omega} \cdot \boldsymbol{\nabla}) \, \mathbf{u} + (\mathbf{u} \cdot \boldsymbol{\nabla}) \, \boldsymbol{\omega}
\end{aligned}
$$

$$= - \left(\boldsymbol{\omega} \cdot \boldsymbol{\nabla} \right) \mathbf{u} + \left(\mathbf{u} \cdot \boldsymbol{\nabla} \right) \boldsymbol{\omega}, \tag{A.2}$$

$$(2) \qquad = \boldsymbol{\nabla} \times \left(\hat{\mathbf{z}} \times \mathbf{u} \right)$$

$$= \hat{\mathbf{z}} \left(\boldsymbol{\nabla} \cdot \mathbf{u} \right) - \mathbf{u} \left(\boldsymbol{\nabla} \cdot \hat{\mathbf{z}} \right) + \left(\mathbf{u} \cdot \boldsymbol{\nabla} \right) \hat{\mathbf{z}} - \left(\hat{\mathbf{z}} \cdot \boldsymbol{\nabla} \right) \mathbf{u}$$

$$= - \frac{\partial \mathbf{u}}{\partial z}, \tag{A.3}$$

$$(3) \qquad = \boldsymbol{\nabla} \times \boldsymbol{\nabla} P = \mathbf{0}, \tag{A.4}$$

$$(4) \qquad = \boldsymbol{\nabla} \times \left(\boldsymbol{\nabla}^2 \mathbf{u} \right)$$

$$= \boldsymbol{\nabla} \times \left[\boldsymbol{\nabla} \left(\boldsymbol{\nabla} \cdot \mathbf{u} \right) - \boldsymbol{\nabla} \times \boldsymbol{\nabla} \times \mathbf{u} \right]$$

$$= 0 - \boldsymbol{\nabla} \times \boldsymbol{\nabla} \times \boldsymbol{\omega}$$

$$= - \boldsymbol{\nabla} \left[\boldsymbol{\nabla} \cdot \boldsymbol{\omega} \right] + \boldsymbol{\nabla}^2 \boldsymbol{\omega}$$

$$= \boldsymbol{\nabla}^2 \boldsymbol{\omega}, \tag{A.5}$$

$$(5) \qquad = \boldsymbol{\nabla} \times \left(g_r \Theta \hat{\mathbf{g}} \right)$$

$$= \frac{1}{s} \frac{\partial}{\partial \phi} \left(g_r \Theta \hat{\mathbf{g}} \cdot \hat{\mathbf{z}} \right) \hat{\mathbf{s}}$$

$$+ \left[\frac{\partial}{\partial z} \left(g_r \Theta \hat{\mathbf{g}} \cdot \hat{\mathbf{s}} \right) - \frac{\partial}{\partial s} \left(g_r \Theta \hat{\mathbf{g}} \cdot \hat{\mathbf{z}} \right) \right] \hat{\boldsymbol{\phi}}$$

$$- \frac{1}{s} \frac{\partial}{\partial \phi} \left(g_r \Theta \hat{\mathbf{g}} \cdot \hat{\mathbf{s}} \right) \hat{\mathbf{z}}. \tag{A.6}$$

These results allow us to write equation A.1 as

$$\frac{\partial \boldsymbol{\omega}}{\partial t} - \left(\boldsymbol{\omega} \cdot \boldsymbol{\nabla} \right) \mathbf{u} + \left(\mathbf{u} \cdot \boldsymbol{\nabla} \right) \boldsymbol{\omega} - 2 \frac{\partial \mathbf{u}}{\partial z} = E \boldsymbol{\nabla}^2 \boldsymbol{\omega} - Ra^* \boldsymbol{\nabla} \times \left(g_r \Theta \hat{\mathbf{g}} \right). \tag{A.7}$$

In cylindrical coordinates, the z components of the vector Laplacian and material derivative of a vector are equal to their scalar equivalents of the z component of the vector. Thus,

$$(\boldsymbol{\nabla}^2\boldsymbol{\omega})_z = \boldsymbol{\nabla}^2\omega_z$$

$$((\boldsymbol{\omega} \cdot \boldsymbol{\nabla})\,\mathbf{u})_z = (\boldsymbol{\omega} \cdot \boldsymbol{\nabla})\,u_z \qquad ((\mathbf{u} \cdot \boldsymbol{\nabla})\,\boldsymbol{\omega})_z = (\mathbf{u} \cdot \boldsymbol{\nabla})\,\omega_z, \qquad \text{(A.8)}$$

which allows us to write the z-component of equation A.7 as

$$\frac{\partial \omega_z}{\partial t} + (\mathbf{u} \cdot \boldsymbol{\nabla})\,\omega_z - (\boldsymbol{\omega} \cdot \boldsymbol{\nabla})\,u_z - 2\frac{\partial u_z}{\partial z} = E\boldsymbol{\nabla}^2\omega_z + Ra^*\hat{\mathbf{g}} \cdot \hat{\mathbf{s}}\frac{g_r}{s}\frac{\partial \Theta}{\partial \phi}. \qquad \text{(A.9)}$$

This is equation 3.80 which governs the time evolution of the axial vorticity.

Appendix B

Boundary conditions

To solve the differential equations of the system, boundary conditions for the dynamic variables on the shell are required. Assuming an impenetrable shell boundary gives

$$u_n(L^\pm) \equiv \mathbf{u} \cdot \hat{\mathbf{n}}_{bc}|^{L^\pm} = 0. \tag{B.1}$$

The boundary is also assumed to be stress free. This allows us to set the shear components of the non-dimensional stress tensor equal to zero

$$\sum_j \left(\tau_{ij} \left(\hat{\mathbf{n}}_{bc} \cdot \hat{\mathbf{j}} \right) \right) = \sum_j \left((-P\delta_{ij} + 2Ee_{ij}) \left(\hat{\mathbf{n}}_{bc} \cdot \hat{\mathbf{j}} \right) \right) = 0. \tag{B.2}$$

Here τ_{ij} is the stress tensor, δ_{ij} is the Kronecker delta, e_{ij} is the strain rate tensor and $\hat{\mathbf{j}}$ is the unit vector in the j direction. Equation B.2 is a vector equation which gives three scalar conditions, one for each value of i.

For a spherical shell, equation B.2 with $i = \phi$ and $i = \theta$ gives the conditions

$$e_{\phi r} = \frac{r}{2} \frac{\partial}{\partial r} \left(\frac{u_\phi}{r} \right) + \frac{1}{2r \sin \theta} \frac{\partial u_r}{\partial \phi} = 0$$

$$\left.\frac{\partial u_\phi}{\partial r}\right|^{L^\pm} = \frac{u_\phi}{r}, \tag{B.3}$$

and

$$e_{\theta r} = \frac{r}{2}\frac{\partial}{\partial r}\left(\frac{u_\theta}{r}\right) + \frac{1}{2r}\frac{\partial u_r}{\partial \theta} = 0$$

$$\left.\frac{\partial u_\theta}{\partial r}\right|^{L^\pm} = \frac{u_\theta}{r}. \tag{B.4}$$

Here we have used the impenetrability of the boundary. This gives boundary conditions for the zonal flow of

$$\left.\frac{\partial}{\partial r}\left(\frac{\overline{u_\phi}}{s}\right)\right|^{L^\pm} = \left.\frac{\partial}{\partial r}\left(\frac{\overline{u_\phi}}{r\sin\theta}\right)\right|^{L^\pm} = \left.\frac{1}{\sin\theta}\frac{\partial}{\partial r}\left(\frac{\overline{u_\phi}}{r}\right)\right|^{L^\pm} = 0. \tag{B.5}$$

In spherical coordinates the vorticity is

$$\boldsymbol{\omega} = \begin{cases} \dfrac{1}{r\sin\theta}\left(\dfrac{\partial}{\partial\theta}(u_\phi\sin\theta) - \dfrac{\partial u_\theta}{\partial\phi}\right)\hat{\mathbf{r}} \\[2ex] \dfrac{1}{r}\left(\dfrac{1}{\sin\theta}\dfrac{\partial u_r}{\partial\phi} - \dfrac{\partial}{\partial r}(ru_\phi)\right)\hat{\boldsymbol{\theta}} \\[2ex] \dfrac{1}{r}\left(\dfrac{\partial}{\partial r}(ru_\theta) - \dfrac{\partial u_r}{\partial\theta}\right)\hat{\boldsymbol{\phi}} \end{cases}. \tag{B.6}$$

After applying the impenetrability and stress free conditions for a spherical shell, the boundary values of the vorticity are

$$\boldsymbol{\omega}(L^\pm) = \begin{cases} \dfrac{1}{r\sin\theta}\left(\dfrac{\partial}{\partial\theta}(u_\phi\sin\theta) - \dfrac{\partial u_\theta}{\partial\phi}\right)\hat{\mathbf{r}} \\[2ex] -\dfrac{2u_\phi}{r}\hat{\boldsymbol{\theta}} \\[2ex] \dfrac{2u_\theta}{r}\hat{\boldsymbol{\phi}} \end{cases}. \tag{B.7}$$

Thus, the boundary conditions on the vorticity equation are

$$\left.\frac{\partial \omega_r}{\partial r}\right|^{L^{\pm}} = 0, \qquad \omega_\theta(L^{\pm}) = -\frac{2u_\phi(L^{\pm})}{r}, \qquad \omega_\phi(L^{\pm}) = \frac{2u_\theta(L^{\pm})}{r}. \qquad \text{(B.8)}$$

The current thesis utilizes free-slip boundary conditions on both the outer and inner boundaries. While approximating the outer boundary of a planetary atmosphere as a free surface is reasonable, it is possible that the inner boundary would be more realistically modeled as a no-slip boundary. This depends on the precise properties of the phase transition which inhibits the development of a zonal wind at depth, which is presently not well understood. No-slip boundary conditions could be implemented by considering an Ekman layer over which the velocity of the fluid in the bulk smoothly adjusts to zero at the boundary. By moving the boundary to the edge of the Ekman layer we could still apply free-slip boundary conditions to the bulk velocity. However the no-penetration condition would need to be altered to account for Ekman pumping, which models the effects of the boundary layer on the bulk of the flow.

Appendix C

Z-averaged equations

We need to calculate the z-average of several equations of the general form

$$\left\langle \frac{\partial f}{\partial t} + \mathbf{u} \cdot \boldsymbol{\nabla} f = E_f \nabla^2 f \right\rangle, \tag{C.1}$$

where E_f is the non-dimensional diffusion coefficient. The evaluation of the first term is trivial, since time derivatives and z-averaging commute. This leaves us with the advection and Laplacian terms to evaluate. When calculating these averages we will assume that the velocities are all dominantly rigid and that we can thus estimate the z-average of their products as the products of their averages. However, we will not assume the same for the s and z-derivatives of these variables, since the derivative of a dominantly rigid variable need not itself be dominantly rigid. For temporal and azimuthal derivatives, which commute with axial averaging, this is not an issue.

C.1 Velocities

In Section 3.2 it was argued that the flow contains a rigid geostrophic component and non-rigid ageostrophic component. By imposing no the penetration boundary condition and incompressibility of the flow, a parameterization of the ageostrophic flow in terms of the geostrophic flow was found in Section 3.4. Equations 3.52-3.54 give the flow on the boundaries at $z = L^{\pm}$ under this parameterization as

$$u_z(L^{\pm}) = u_z^g + u_z^a(L^{\pm}) = \pm \langle u_z \rangle + \frac{\partial L^{\pm}}{\partial s} \langle u_s \rangle \tag{C.2}$$

$$u_s(L^{\pm}) = u_s^g + u_s^a(L^{\pm}) = \langle u_s \rangle \pm \frac{\langle u_z \rangle}{\frac{\partial L^{\pm}}{\partial s}} \tag{C.3}$$

$$u_\phi(L^{\pm}) = u_\phi^g + u_\phi^a(L^{\pm}) = \langle u_\phi \rangle, \tag{C.4}$$

where the sign is positive inside the TC and on the upper boundary outside the TC, and negative outside the TC on the lower boundary due to the anti-symmetry of u_z here.

These identities allow us to calculate the axial average of the z-derivatives of the velocities over the entire shell, giving

$$\left\langle \frac{\partial u_z}{\partial z} \right\rangle = \left(\frac{u_z(L^+) - u_z(L^-)}{\Delta L} \right)$$

$$= \frac{\left(\langle u_z \rangle + \frac{\partial L^+}{\partial s} \langle u_s \rangle \right) - \left(\pm \langle u_z \rangle + \frac{\partial L^-}{\partial s} \langle u_s \rangle \right)}{\Delta L}$$

$$\equiv \beta \langle u_s \rangle + \frac{(1 \mp 1)}{\Delta L} \langle u_z \rangle, \tag{C.5}$$

$$\left\langle \frac{\partial u_s}{\partial z} \right\rangle = \left(\frac{u_s(L^+) - u_s(L^-)}{\Delta L} \right)$$

$$
= \frac{\left(\langle u_s \rangle + \frac{\langle u_z \rangle}{\frac{\partial L^+}{\partial s}} \right) - \left(\langle u_s \rangle \pm \frac{\langle u_z \rangle}{\frac{\partial L^-}{\partial s}} \right)}{\Delta L}
$$

$$
= \frac{\left(\frac{\partial L^-}{\partial s} \mp \frac{\partial L^+}{\partial s} \right)}{\Delta L \left(\frac{\partial L^+}{\partial s} \frac{\partial L^-}{\partial s} \right)} \langle u_z \rangle
$$

$$
\equiv \eta \langle u_z \rangle , \tag{C.6}
$$

where we have defined $\eta \equiv \frac{\left(\frac{\partial L^-}{\partial s} \mp \frac{\partial L^+}{\partial s} \right)}{\Delta L \left(\frac{\partial L^+}{\partial s} \frac{\partial L^-}{\partial s} \right)}$. If we take $\langle u_z \rangle = 0$ outside the TC, these can be simplified.

The average of the s-derivative of the axial velocity inside the TC is equal to

$$
\begin{aligned}
\left\langle \frac{\partial u_z}{\partial s} \right\rangle &= \frac{\partial \langle u_z \rangle}{\partial s} + \beta \langle u_z \rangle - \frac{1}{\Delta L} \left(u_z(L^+) \frac{\partial L^+}{\partial s} - u_z(L^-) \frac{\partial L^-}{\partial s} \right) \\
&= \frac{\partial \langle u_z \rangle}{\partial s} + \beta \langle u_z \rangle - \frac{1}{\Delta L} \left(\frac{\partial L^+}{\partial s} \left(\langle u_z \rangle + \frac{\partial L^+}{\partial s} \langle u_s \rangle \right) \right) \\
&\quad + \frac{1}{\Delta L} \left(\frac{\partial L^-}{\partial s} \left(\langle u_z \rangle + \frac{\partial L^-}{\partial s} \langle u_s \rangle \right) \right) \\
&= \frac{\partial \langle u_z \rangle}{\partial s} + \beta \langle u_z \rangle - \beta \langle u_z \rangle - \frac{1}{\Delta L} \left(\left(\frac{\partial L^+}{\partial s} \right)^2 - \left(\frac{\partial L^-}{\partial s} \right)^2 \right) \langle u_s \rangle \\
&= \frac{\partial \langle u_z \rangle}{\partial s} - \beta \left(\frac{\partial L^+}{\partial s} + \frac{\partial L^-}{\partial s} \right) \langle u_s \rangle \\
&\equiv \frac{\partial \langle u_z \rangle}{\partial s} - \lambda \langle u_s \rangle , \tag{C.7}
\end{aligned}
$$

where $\lambda \equiv \beta \left(\frac{\partial L^+}{\partial s} + \frac{\partial L^-}{\partial s} \right)$. Outside the TC the antisymmetry of the axial flow means that its integral across the shell vanishes, however the boundary terms give

$$
\left\langle \frac{\partial u_z}{\partial s} \right\rangle = - \frac{1}{\Delta L} \left(\frac{\partial L^+}{\partial s} + \frac{\partial L^-}{\partial s} \right) \langle u_z \rangle - \lambda \langle u_s \rangle . \tag{C.8}
$$

Finally, the average of the s-derivative of the cylindrical radial flow is

$$
\begin{aligned}
\left\langle \frac{\partial u_s}{\partial s} \right\rangle =& \frac{\partial \langle u_s \rangle}{\partial s} + \beta \langle u_s \rangle - \frac{1}{\Delta L} \left(u_s(L^+) \frac{\partial L^+}{\partial s} - u_s(L^-) \frac{\partial L^-}{\partial s} \right) \\
=& \frac{\partial \langle u_s \rangle}{\partial s} + \beta \langle u_s \rangle - \frac{1}{\Delta L} \left(\frac{\partial L^+}{\partial s} \left(\langle u_s \rangle + \frac{\langle u_z \rangle}{\frac{\partial L^+}{\partial s}} \right) \right) \\
& + \frac{1}{\Delta L} \left(\frac{\partial L^-}{\partial s} \left(\langle u_s \rangle \pm \frac{\langle u_z \rangle}{\frac{\partial L^-}{\partial s}} \right) \right) \\
=& \frac{\partial \langle u_s \rangle}{\partial s} + \beta \langle u_s \rangle - \beta \langle u_s \rangle - \frac{1}{\Delta L} \left(\langle u_z \rangle \mp \langle u_z \rangle \right) \\
=& \frac{\partial \langle u_s \rangle}{\partial s} - \frac{\langle u_z \rangle}{\Delta L} \left(1 \mp 1 \right).
\end{aligned}
\tag{C.9}
$$

C.2   Advection terms

Consider an advection term of the form

$$
\langle \mathbf{u} \cdot \boldsymbol{\nabla} f \rangle = \left\langle u_s \frac{\partial f}{\partial s} + u_\phi \frac{1}{s} \frac{\partial f}{\partial \phi} + u_z \frac{\partial f}{\partial z} \right\rangle,
\tag{C.10}
$$

where f is a scalar function. This can be written as

$$
\begin{aligned}
\langle \mathbf{u} \cdot \boldsymbol{\nabla} f \rangle =& \langle \boldsymbol{\nabla} \cdot (f \mathbf{u}) - f \boldsymbol{\nabla} \cdot \mathbf{u} \rangle \\
=& \left\langle \frac{1}{s} \frac{\partial}{\partial s} (s f u_s) + \frac{1}{s} \frac{\partial}{\partial \phi} (f u_\phi) + \frac{\partial}{\partial z} (f u_z) - 0 \right\rangle.
\end{aligned}
\tag{C.11}
$$

Since it contains a s-derivative, the first term in equation C.11 must be evaluated using the Leibniz integral theorem (equation 3.47). The terms in

equation C.11 can be evaluated as

$$
\left\langle \frac{1}{s}\frac{\partial}{\partial s}\left(sfu_s\right)\right\rangle = \frac{1}{s}\left(\frac{\partial}{\partial s}\left\langle sfu_s\right\rangle + \beta\left\langle sfu_s\right\rangle\right) - \frac{1}{s\Delta L}\left(sf(L^+)u_s(L^+)\frac{\partial L^+}{\partial s}\right)
$$
$$
+ \frac{1}{s\Delta L}\left(sf(L^-)u_s(L^-)\frac{\partial L^-}{\partial s}\right), \tag{C.12}
$$

$$
\left\langle \frac{1}{s}\frac{\partial}{\partial \phi}\left(fu_\phi\right)\right\rangle = \frac{1}{s}\frac{\partial}{\partial \phi}\left\langle fu_\phi\right\rangle, \tag{C.13}
$$

$$
\left\langle \frac{\partial}{\partial z}\left(fu_z\right)\right\rangle = \left(\frac{f(L^+)u_z(L^+) - f(L^-)u_z(L^-)}{\Delta L}\right). \tag{C.14}
$$

Using the parameterizations of equations 3.52-3.54 for the flow on the boundary at $z = L^{\pm}$, and the identities for the z-average of the derivatives of the flow derived in Appendix C.1, equation C.12 yields

$$
\left\langle \frac{1}{s}\frac{\partial}{\partial s}\left(sfu_s\right)\right\rangle = \frac{1}{s}\left(\frac{\partial}{\partial s}\left(s\left\langle f\right\rangle\left\langle u_s\right\rangle\right) + \beta s\left\langle f\right\rangle\left\langle u_s\right\rangle\right)
$$
$$
- \frac{1}{s\Delta L}\left(sf(L^+)\frac{\partial L^+}{\partial s}\right)\left(u_s^g(L^+) + u_s^a(L^+)\right)
$$
$$
+ \frac{1}{s\Delta L}\left(sf(L^-)\frac{\partial L^-}{\partial s}\right)\left(u_s^g(L^-) + u_s^a(L^-)\right)
$$
$$
= \frac{1}{s}\left(\frac{\partial}{\partial s}\left(s\left\langle f\right\rangle\left\langle u_s\right\rangle\right) + \beta s\left\langle f\right\rangle\left\langle u_s\right\rangle\right)
$$
$$
- \frac{f(L^+)}{\Delta L}\frac{\partial L^+}{\partial s}\left(\left\langle u_s\right\rangle + \frac{\left\langle u_z\right\rangle}{\frac{\partial L^+}{\partial s}}\right) + \frac{f(L^-)}{\Delta L}\frac{\partial L^-}{\partial s}\left(\left\langle u_s\right\rangle \pm \frac{\left\langle u_z\right\rangle}{\frac{\partial L^-}{\partial s}}\right)
$$
$$
= \frac{1}{s}\left(\frac{\partial}{\partial s}\left(s\left\langle f\right\rangle\left\langle u_s\right\rangle\right) + \beta s\left\langle f\right\rangle\left\langle u_s\right\rangle\right)
$$
$$
- \frac{\left\langle u_s\right\rangle}{\Delta L}\left(f(L^+)\frac{\partial L^+}{\partial s} - f(L^-)\frac{\partial L^-}{\partial s}\right)
$$
$$
- \frac{\left\langle u_z\right\rangle}{\Delta L}\left(f(L^+) \mp f(L^-)\right). \tag{C.15}
$$

The axial average of the z-derivative term in equation C.14 is equal to

$$
\left\langle \frac{\partial}{\partial z} (f u_z) \right\rangle = \left(\frac{f(L^+)(u_z^g(L^+) + u_z^a(L^+)) - f(L^-)(u_z^g(L^-) + u_z^a(L^-))}{\Delta L} \right)
$$

$$
= \left(\frac{f(L^+)\left(\langle u_z \rangle + \langle u_s \rangle \frac{\partial L^+}{\partial s}\right) - f(L^-)\left(\pm \langle u_z \rangle + \langle u_s \rangle \frac{\partial L^-}{\partial s}\right)}{\Delta L} \right)
$$

$$
= \frac{\langle u_s \rangle}{\Delta L} \left(f(L^+)\frac{\partial L^+}{\partial s} - f(L^-)\frac{\partial L^-}{\partial s} \right)
$$

$$
+ \frac{\langle u_z \rangle}{\Delta L} \left(f(L^+) \mp f(L^-) \right). \tag{C.16}
$$

From equation C.16 it can be observed that the average of the z-derivative term cancels the boundary terms from the average of the s-derivative in equation C.15. Note that this depends only on our choice of parameterization of the flow, and is true for any choice of f and its boundary values. Therefore, the z-average of the total advection term in equation C.10 is

$$
\langle \mathbf{u} \cdot \boldsymbol{\nabla} f \rangle = \frac{1}{s} \left(\frac{\partial}{\partial s} \left(s \langle f \rangle \langle u_s \rangle \right) + \beta s \langle f \rangle \langle u_s \rangle \right) + \frac{1}{s}\frac{\partial}{\partial \phi} \langle f u_\phi \rangle
$$

$$
= \langle f \rangle \frac{1}{s}\frac{\partial}{\partial s} \left(s \langle u_s \rangle \right) + \langle u_s \rangle \frac{\partial \langle f \rangle}{\partial s} + \langle f \rangle \left\langle \frac{\partial u_z}{\partial z} \right\rangle
$$

$$
+ \langle f \rangle \frac{1}{s}\frac{\partial \langle u_\phi \rangle}{\partial \phi} + \langle u_\phi \rangle \frac{1}{s}\frac{\partial \langle f \rangle}{\partial \phi}
$$

$$
= \langle f \rangle \langle \boldsymbol{\nabla} \cdot \mathbf{u} \rangle + \langle \mathbf{u}_\perp \rangle \cdot \boldsymbol{\nabla}_\perp \langle f \rangle
$$

$$
= \langle \mathbf{u}_\perp \rangle \cdot \boldsymbol{\nabla}_\perp \langle f \rangle, \tag{C.17}
$$

where $\mathbf{u}_\perp$ and $\boldsymbol{\nabla}_\perp$ are the projections of $\mathbf{u}$ and $\boldsymbol{\nabla}$ respectively into the 2D equatorial plane.

One subtlety that we must consider is the single hemisphere average utilized in the axial velocity equation outside the TC. Here, since $\langle u_z \rangle$ should

175

be antisymmetric about the equatorial plane we only average over one hemi-sphere. In this case the lower bound is not the shell boundary but rather $L^- = L^{1/2} = 0$. Additionally, since the equatorial plane is completely horizon-tal we must have $u_z(L^-) = 0$ to ensure no penetration across the plane. These two choices, with the original prescription for the upper boundary, leads to an identical result as equation C.17 for the two hemisphere average.

Equation C.17 is used in both the axial vorticity and axial velocity equa-tions. However, for the advection term in the thermal equation a modification is necessary since as discussed in Section 3.3.1 the limits of integration for this equation differ. Equation C.17 is a direct result of the impenetrability of the flow across the boundary. This is equivalent to assuming that there is no flux of the rigid $\langle f \rangle$ into or out of the system through advection across the system boundary. When $f = \omega_z$ or $f = u_z$ this is a sensible assumption. With free-slip boundary conditions both variables should remain largely rigid across the entire shell, and the mechanical boundary conditions, which control the flow variables, prevent flux into or out of the system.

However, the thermal perturbations are only expected to be rigid across the bulk of the fluid, where heat is carried by convection. Within the thermal boundary layer, where heat flow is predominantly conductive, the rigidity must break down. The dynamics of the rigid thermal perturbations are dictated by their interaction with the thermal boundary layer. Heat can be injected (or ejected) into fluid columns in the bulk through axial plumes emanating from within the thermal boundary layers. These plumes are fed by circulation within the boundary layer.

To capture this effect, which should be important inside the TC, the limits of integration for the thermal equation are not taken at the shell boundary

176

at $z = L^\pm$, but rather at the interface between the bulk of the fluid and the thermal boundary layer. Internal to the thermal boundary layers the thermal perturbations should be rigid. At this interface the radial flow need not vanish, and thus the relationship between u_s and u_z derived based upon impenetrable flow is no longer valid. Since the boundary layer should be relatively thin compared to the full shell this distinction will only play a role in the evaluation of the boundary terms.

If we assume that the flow is perfectly rigid across the shell, and only consider the variations in f, averaging over the bulk of the flow gives

$$
\begin{aligned}
\langle \mathbf{u} \cdot \boldsymbol{\nabla} f \rangle &= \langle \mathbf{u} \rangle \cdot \langle \boldsymbol{\nabla} f \rangle \\
&= \langle u_s \rangle \left(\frac{\partial \langle f \rangle}{\partial s} + \beta \langle f \rangle - \frac{1}{\Delta L} \left(f(L^+) \frac{\partial L^+}{\partial s} - f(L^-) \frac{\partial L^-}{\partial s} \right) \right) \\
&\quad + \langle u_\phi \rangle \frac{1}{s} \frac{\partial \langle f \rangle}{\partial \phi} + \langle u_z \rangle \left(\frac{f(L^+) - f(L^-)}{\Delta L} \right) \\
&= \langle \mathbf{u}_\perp \rangle \cdot \boldsymbol{\nabla}_\perp \langle f \rangle + \frac{1}{\Delta L} \left(f(L^+) - \langle f \rangle \right) \left(\langle u_z \rangle - \frac{\partial L^+}{\partial s} \langle u_s \rangle \right) \\
&\quad - \frac{1}{\Delta L} \left(f(L^-) - \langle f \rangle \right) \left(\langle u_z \rangle - \frac{\partial L^-}{\partial s} \langle u_s \rangle \right),
\end{aligned}
\tag{C.18}
$$

inside the TC.

This approach yields two new terms, involving the sum of velocity components equal to the spherical radial velocity at the boundaries. These new terms capture the flux of f transported by advection into or out of the bulk of the fluid from the boundary layer. If f is rigid, so that $\langle f \rangle = f(L^+) = f(L^-)$, then these new terms do not contribute. While the non-axisymmetric thermal perturbations are expected to be rigid, the axisymmetric component is not inside the TC due to the imposed thermal gradient across the shell. Here we expect that $f(L^-) \sim 1$ and $f(L^+) \sim 0$.

In the present thesis the advection term in the thermal equation is modeled as a hybrid of the approaches presented in equations C.17 and C.18. Inside the TC the non-rigid axial flow induced by the rigid $\langle u_s \rangle$ by the boundaries is accounted for. However, the rigid $\langle u_z \rangle$ is assumed to be fed by thermal plumes and non-rigid flow confined to the thermal boundary layer. Allowing the axial flow to penetrate into the boundary layer is equivalent to using the boundary flows

$$u_z(L^{\pm}) = \langle u_z \rangle + \frac{\partial L^{\pm}}{\partial s} \langle u_s \rangle \tag{C.19}$$

$$u_s(L^{\pm}) = \langle u_s \rangle, \tag{C.20}$$

in the preceding derivation. In this case the resulting averaged advection term is

$$\langle \mathbf{u} \cdot \boldsymbol{\nabla} f \rangle = \langle \mathbf{u}_{\perp} \rangle \cdot \boldsymbol{\nabla}_{\perp} \langle f \rangle + \left(\frac{f(L^+) - f(L^-)}{\Delta L} \right) \langle u_z \rangle. \tag{C.21}$$

Thus, only axial advection of f across the boundary layer interface is considered. Inside the TC this should be the dominant contribution due to the direction of buoyancy. When $f = T$, only the axisymmetric component of the temperature contributes to this term since the non-axisymmetric components are rigid. Also, since we do not consider an axisymmetric $\langle u_z \rangle$, it only acts as a source to the non-axisymmetric components of the temperature equation. Outside the TC, since we assume that the rigid axial velocity is negligible and do not model it, this term does not contribute.

C.3   Vorticity generation

We now evaluate the z-average of $(\boldsymbol{\omega} \cdot \boldsymbol{\nabla})\, u_z$,

$$
\begin{aligned}
\langle (\boldsymbol{\omega} \cdot \boldsymbol{\nabla})\, u_z \rangle &= \langle \boldsymbol{\nabla} \cdot (u_z \boldsymbol{\omega}) - u_z \boldsymbol{\nabla} \cdot \boldsymbol{\omega} \rangle \\
&= \left\langle \frac{1}{s}\frac{\partial}{\partial s}\left(s \omega_s u_z \right) + \frac{1}{s}\frac{\partial \left(\omega_\phi u_z \right)}{\partial \phi} + \frac{\partial \left(\omega_z u_z \right)}{\partial z} - 0 \right\rangle .
\end{aligned} \tag{C.22}
$$

In this section for simplicity we will only perform the calculation under the assumption that $\langle u_z \rangle = 0$ outside the TC, so that the $\pm$ signs can be dropped in equations 3.52-3.54.

Since we are assuming that there is no ageostrophic azimuthal velocity, we can write $\omega_s = \left(\frac{1}{s}\frac{\partial u_z}{\partial \phi} - \frac{\partial u_\phi}{\partial z} \right) \sim \frac{1}{s}\frac{\partial u_z}{\partial \phi}$. The first term is equal to

$$
\begin{aligned}
\left\langle \frac{1}{s}\frac{\partial}{\partial s}\left(s \omega_s u_z \right) \right\rangle &= \frac{1}{s}\left(\frac{\partial \langle s \omega_s u_z \rangle}{\partial s} + \beta s\, \langle \omega_s u_z \rangle \right) \\
&\quad - \frac{1}{\Delta L}\left((\omega_s u_z)^+\,\frac{\partial L^+}{\partial s} - (\omega_s u_z)^-\,\frac{\partial L^-}{\partial s} \right) \\
&= \left(\frac{1}{s}\frac{\partial}{\partial s} + \frac{\beta}{s} \right) \left\langle \frac{\partial u_z}{\partial \phi} u_z \right\rangle \\
&\quad - \frac{1}{\Delta L}\frac{1}{s}\frac{\partial}{\partial \phi}\left(\langle u_z \rangle + \frac{\partial L^+}{\partial s}\,\langle u_s \rangle \right)\left(\langle u_z \rangle + \frac{\partial L^+}{\partial s}\,\langle u_s \rangle \right)\frac{\partial L^+}{\partial s} \\
&\quad + \frac{1}{\Delta L}\frac{1}{s}\frac{\partial}{\partial \phi}\left(\langle u_z \rangle + \frac{\partial L^-}{\partial s}\,\langle u_s \rangle \right)\left(\langle u_z \rangle + \frac{\partial L^-}{\partial s}\,\langle u_s \rangle \right)\frac{\partial L^-}{\partial s} \\
&= \left(\frac{1}{s}\frac{\partial}{\partial s} + \frac{\beta}{s} \right)\left(\frac{\partial \langle u_z \rangle}{\partial \phi}\,\langle u_z \rangle \right) - \frac{\beta}{s}\,\langle u_z \rangle\,\frac{\partial \langle u_z \rangle}{\partial \phi} \\
&\quad - \frac{\lambda}{s}\left(\langle u_s \rangle\,\frac{\partial \langle u_z \rangle}{\partial \phi} \right) - \frac{\lambda}{s}\left(\langle u_z \rangle\,\frac{\partial \langle u_s \rangle}{\partial \phi} \right) \\
&\quad - \frac{1}{\Delta L}\left(\left(\frac{\partial L^+}{\partial s} \right)^3 - \left(\frac{\partial L^-}{\partial s} \right)^3 \right)\langle u_s \rangle\,\frac{1}{s}\frac{\partial \langle u_s \rangle}{\partial \phi} .
\end{aligned} \tag{C.23}
$$

Here we have defined $\lambda \equiv \beta \left(\frac{\partial L^+}{\partial s} + \frac{\partial L^-}{\partial s} \right)$.

The average of the azimuthal derivative term is

$$
\begin{aligned}
\left\langle \frac{1}{s} \frac{\partial (\omega_\phi u_z)}{\partial \phi} \right\rangle =& \frac{1}{s} \frac{\partial}{\partial \phi} \left\langle u_z \left(\frac{\partial u_s}{\partial z} - \frac{\partial u_z}{\partial s} \right) \right\rangle \\
=& \frac{1}{s} \frac{\partial}{\partial \phi} \left\langle \frac{\partial (u_z u_s)}{\partial z} - u_s \frac{\partial u_z}{\partial z} - \frac{1}{2} \frac{\partial (u_z u_z)}{\partial s} \right\rangle \\
=& \frac{1}{s} \frac{\partial}{\partial \phi} \left\langle \frac{\partial (u_z u_s)}{\partial z} + u_s \frac{\partial u_s}{\partial s} + u_s \frac{u_s}{s} + u_s \frac{1}{s} \frac{\partial u_\phi}{\partial \phi} - \frac{1}{2} \frac{\partial (u_z^2)}{\partial s} \right\rangle \\
=& \frac{1}{s} \frac{\partial}{\partial \phi} \left\langle \frac{\partial (u_z u_s)}{\partial z} + \frac{1}{2} \frac{\partial (u_s^2)}{\partial s} + \frac{u_s^2}{s} + \frac{u_s}{s} \frac{\partial u_\phi}{\partial \phi} \right\rangle \\
& - \frac{1}{s} \frac{\partial}{\partial \phi} \left\langle \frac{1}{2} \frac{\partial (u_z^2)}{\partial s} \right\rangle,
\end{aligned}
\tag{C.24}
$$

where we have used the incompressibility of the flow. Evaluating each term in equation C.24 gives

$$
\begin{aligned}
\left\langle \frac{\partial (u_z u_s)}{\partial z} \right\rangle =& \frac{\left(\langle u_z \rangle + \frac{\partial L^+}{\partial s} \langle u_s \rangle \right) \left(\langle u_s \rangle + \frac{\langle u_z \rangle}{\frac{\partial L^+}{\partial s}} \right)}{\Delta L} \\
& - \frac{\left(\langle u_z \rangle + \frac{\partial L^-}{\partial s} \langle u_s \rangle \right) \left(\langle u_s \rangle + \frac{\langle u_z \rangle}{\frac{\partial L^-}{\partial s}} \right)}{\Delta L} \\
=& \beta \langle u_s \rangle^2 + \eta \langle u_z \rangle^2,
\end{aligned}
\tag{C.25}
$$

$$
\begin{aligned}
\left\langle \frac{\partial (u_s^2)}{\partial s} \right\rangle =& \frac{\partial \langle u_s^2 \rangle}{\partial s} + \beta \langle u_s^2 \rangle \\
& - \frac{1}{\Delta L} \left(\left(\langle u_s \rangle + \frac{\langle u_z \rangle}{\frac{\partial L^+}{\partial s}} \right)^2 \frac{\partial L^+}{\partial s} - \left(\langle u_s \rangle + \frac{\langle u_z \rangle}{\frac{\partial L^-}{\partial s}} \right)^2 \frac{\partial L^-}{\partial s} \right) \\
=& \frac{\partial \left(\langle u_s \rangle^2 \right)}{\partial s} + \beta \langle u_s \rangle^2 - \beta \langle u_s \rangle^2 - \eta \langle u_z \rangle^2 \\
=& \frac{\partial \left(\langle u_s \rangle^2 \right)}{\partial s} - \eta \langle u_z \rangle^2,
\end{aligned}
\tag{C.26}
$$

180

$$\left\langle \frac{\partial \left(u_z^2\right)}{\partial s} \right\rangle = \frac{\partial \left\langle u_z^2 \right\rangle}{\partial s} + \beta \left\langle u_z^2 \right\rangle - \frac{1}{\Delta L} \left(\langle u_z \rangle + \frac{\partial L^+}{\partial s} \langle u_s \rangle \right)^2 \frac{\partial L^+}{\partial s}$$

$$+ \frac{1}{\Delta L} \left(\left(\langle u_z \rangle + \frac{\partial L^-}{\partial s} \langle u_s \rangle \right)^2 \frac{\partial L^-}{\partial s} \right)$$

$$= \frac{\partial \left(\langle u_z \rangle^2 \right)}{\partial s} + \beta \langle u_z \rangle^2 - \beta \langle u_z \rangle^2 - 2\lambda \langle u_z \rangle \langle u_s \rangle$$

$$- \frac{1}{\Delta L} \left(\left(\frac{\partial L^+}{\partial s} \right)^3 - \left(\frac{\partial L^-}{\partial s} \right)^3 \right) \langle u_s \rangle \langle u_s \rangle$$

$$= \frac{\partial \left(\langle u_z \rangle^2 \right)}{\partial s} - 2\lambda \langle u_z \rangle \langle u_s \rangle$$

$$- \frac{1}{\Delta L} \left(\left(\frac{\partial L^+}{\partial s} \right)^3 - \left(\frac{\partial L^-}{\partial s} \right)^3 \right) \langle u_s \rangle^2. \tag{C.27}$$

Finally, the average of the z-derivative term in equation C.22 is equal to

$$\left\langle \frac{\partial \left(\omega_z u_z \right)}{\partial z} \right\rangle = \frac{\left(\frac{1}{s} \frac{\partial \left(s \langle u_\phi \rangle \right)}{\partial s} - \frac{1}{s} \frac{\partial}{\partial \phi} \left(\langle u_s \rangle + \frac{\langle u_z \rangle}{\frac{\partial L^+}{\partial s}} \right) \right) \left(\langle u_z \rangle + \frac{\partial L^+}{\partial s} \langle u_s \rangle \right)}{\Delta L}$$

$$- \frac{\left(\frac{1}{s} \frac{\partial \left(s \langle u_\phi \rangle \right)}{\partial s} - \frac{1}{s} \frac{\partial}{\partial \phi} \left(\langle u_s \rangle + \frac{\langle u_z \rangle}{\frac{\partial L^-}{\partial s}} \right) \right) \left(\langle u_z \rangle + \frac{\partial L^-}{\partial s} \langle u_s \rangle \right)}{\Delta L}$$

$$= \beta \langle \omega_z \rangle \langle u_s \rangle - \eta \langle u_z \rangle \frac{1}{s} \frac{\partial \langle u_z \rangle}{\partial \phi}. \tag{C.28}$$

The remaining terms can be trivially evaluated to give the total

$$
\begin{aligned}
\langle \boldsymbol{\omega} \cdot \boldsymbol{\nabla} u_z \rangle =& \left(\frac{1}{s} \frac{\partial}{\partial s} + \frac{\beta}{s} \right) \left(\frac{\partial \langle u_z \rangle}{\partial \phi} \langle u_z \rangle \right) - \frac{\beta}{s} \langle u_z \rangle \frac{\partial \langle u_z \rangle}{\partial \phi} - \frac{\lambda}{s} \left(\langle u_s \rangle \frac{\partial \langle u_z \rangle}{\partial \phi} \right) \\
& - \frac{\lambda}{s} \left(\langle u_z \rangle \frac{\partial \langle u_s \rangle}{\partial \phi} \right) - \frac{1}{\Delta L} \left(\left(\frac{\partial L^+}{\partial s} \right)^3 - \left(\frac{\partial L^-}{\partial s} \right)^3 \right) \langle u_s \rangle \frac{1}{s} \frac{\partial \langle u_s \rangle}{\partial \phi} \\
& + \frac{1}{s} \frac{\partial}{\partial \phi} \left(\beta \langle u_s \rangle^2 + \eta \langle u_z \rangle^2 + \frac{1}{2} \left(\frac{\partial \left(\langle u_s \rangle^2 \right)}{\partial s} - \eta \langle u_z \rangle^2 \right) + \frac{\langle u_s \rangle^2}{s} \right) \\
& + \frac{1}{s} \frac{\partial}{\partial \phi} \left(\frac{\langle u_s \rangle}{s} \frac{\partial \langle u_\phi \rangle}{\partial \phi} - \frac{1}{2} \left(\frac{\partial \left(\langle u_z \rangle^2 \right)}{\partial s} - 2\lambda \langle u_z \rangle \langle u_s \rangle \right) \right) \\
& + \frac{1}{s} \frac{\partial}{\partial \phi} \left(\frac{1}{2} \left(\frac{1}{\Delta L} \left(\left(\frac{\partial L^+}{\partial s} \right)^3 - \left(\frac{\partial L^-}{\partial s} \right)^3 \right) \langle u_s \rangle^2 \right) \right) \\
& + \beta \langle \omega_z \rangle \langle u_s \rangle - \eta \langle u_z \rangle \frac{1}{s} \frac{\partial \langle u_z \rangle}{\partial \phi} \\
=& \frac{1}{s} \frac{\partial}{\partial \phi} \left(\langle u_s \rangle \left(\beta \langle u_s \rangle + \frac{\partial \langle u_s \rangle}{\partial s} + \frac{\langle u_s \rangle}{s} + \frac{1}{s} \frac{\partial \langle u_\phi \rangle}{\partial \phi} \right) \right) + \beta \langle \omega_z \rangle \langle u_s \rangle \\
=& \beta \langle \omega_z \rangle \langle u_s \rangle , && \text{(C.29)}
\end{aligned}
$$

where the last step follows from the 2D incompressibility equation. Thus, even though the full expansion of $(\boldsymbol{\omega} \cdot \boldsymbol{\nabla}) u_z$ in terms of our system variables and geometry is quite complicated, z-averaging reduces it to the simple expression

$$
(\boldsymbol{\omega} \cdot \boldsymbol{\nabla}) u_z = \beta \langle \omega_z \rangle \langle u_s \rangle . \qquad \text{(C.30)}
$$

C.4 Laplace term

We now evaluate the z-average of the Laplacian of a general variable f,

$$
\langle \nabla^2 f \rangle = \left\langle \frac{1}{s} \frac{\partial}{\partial s} \left(s \frac{\partial f}{\partial s} \right) + \frac{1}{s^2} \frac{\partial^2 f}{\partial \phi^2} + \frac{\partial^2 f}{\partial z^2} \right\rangle . \qquad \text{(C.31)}
$$

The second term can be trivially evaluated to give

$$\left\langle \frac{1}{s^2}\frac{\partial^2 f}{\partial \phi^2}\right\rangle = \frac{1}{s^2}\frac{\partial^2 \langle f\rangle}{\partial \phi^2}, \tag{C.32}$$

while the third term equals

$$\left\langle \frac{\partial^2 f}{\partial z^2}\right\rangle = \frac{1}{\Delta L}\int_{L^-}^{L^+}\frac{\partial^2 f}{\partial z^2}dz = \frac{1}{\Delta L}\left(\left.\frac{\partial f}{\partial z}\right|^{L^+} - \left.\frac{\partial f}{\partial z}\right|^{L^-}\right). \tag{C.33}$$

Evaluating the first term,

$$
\begin{aligned}
\left\langle \frac{1}{s}\frac{\partial}{\partial s}\left(s\frac{\partial f}{\partial s}\right)\right\rangle =& \frac{1}{s}\left(\frac{\partial}{\partial s}\left(s\left\langle\frac{\partial f}{\partial s}\right\rangle\right) + \beta s\left\langle\frac{\partial f}{\partial s}\right\rangle\right)\\
&- \frac{1}{s\Delta L}\left(s\frac{\partial L^+}{\partial s}\left.\frac{\partial f}{\partial s}\right|^{L^+} - s\frac{\partial L^-}{\partial s}\left.\frac{\partial f}{\partial s}\right|^{L^-}\right)\\
=& \frac{1}{s}\frac{\partial}{\partial s}\left(s\left(\frac{\partial \langle f\rangle}{\partial s} + \beta\langle f\rangle\right)\right)\\
&- \frac{1}{s}\frac{\partial}{\partial s}\left(s\left(\frac{1}{\Delta L}\left(\frac{\partial L^+}{\partial s}f(L^+) - \frac{\partial L^-}{\partial s}f(L^-)\right)\right)\right)\\
&+ \beta\left(\frac{\partial \langle f\rangle}{\partial s} + \beta\langle f\rangle - \frac{1}{\Delta L}\left(\frac{\partial L^+}{\partial s}f(L^+) - \frac{\partial L^-}{\partial s}f(L^-)\right)\right)\\
&- \frac{1}{\Delta L}\left(\frac{\partial L^+}{\partial s}\left.\frac{\partial f}{\partial s}\right|^{L^+} - \frac{\partial L^-}{\partial s}\left.\frac{\partial f}{\partial s}\right|^{L^-}\right)\\
=& \frac{1}{s}\frac{\partial}{\partial s}\left(s\frac{\partial \langle f\rangle}{\partial s}\right) + 2\beta\frac{\partial \langle f\rangle}{\partial s} + \left(\frac{\beta}{s} + \frac{\partial \beta}{\partial s} + \beta^2\right)\langle f\rangle\\
&- \frac{1}{\Delta L}\left(\frac{1}{s} - \beta + \beta\right)\left(\frac{\partial L^+}{\partial s}f(L^+) - \frac{\partial L^-}{\partial s}f(L^-)\right)\\
&- \frac{1}{\Delta L}\left(\frac{\partial^2 L^+}{\partial s^2}f(L^+) - \frac{\partial^2 L^-}{\partial s^2}f(L^-)\right)\\
&- \frac{1}{\Delta L}\left(\frac{\partial L^+}{\partial s}\left(\left.\frac{\partial f}{\partial s}\right|^{L^+} + \frac{\partial}{\partial s}f(L^+)\right)\right)\\
&+ \frac{1}{\Delta L}\left(\frac{\partial L^-}{\partial s}\left(\left.\frac{\partial f}{\partial s}\right|^{L^-} + \frac{\partial}{\partial s}f(L^-)\right)\right)
\end{aligned}
$$

183

$$
\begin{aligned}
={}& \frac{1}{s}\frac{\partial}{\partial s}\left(s\frac{\partial\langle f\rangle}{\partial s}\right) + 2\beta\frac{\partial\langle f\rangle}{\partial s} + \left(\frac{\beta}{s} + \frac{\partial\beta}{\partial s} + \beta^2\right)\langle f\rangle \\
& - \frac{1}{\Delta L}\left(\left(\frac{1}{s}\frac{\partial L^+}{\partial s} + \frac{\partial^2 L^+}{\partial s^2}\right)f(L^+)\right) \\
& + \frac{1}{\Delta L}\left(\left(\frac{1}{s}\frac{\partial L^-}{\partial s} + \frac{\partial^2 L^-}{\partial s^2}\right)f(L^-)\right) \\
& - \frac{1}{\Delta L}\left(\frac{\partial L^+}{\partial s}\left(\left.\frac{\partial f}{\partial s}\right|^{L^+} + \frac{\partial}{\partial s}f(L^+)\right)\right) \\
& + \frac{1}{\Delta L}\left(\frac{\partial L^-}{\partial s}\left(\left.\frac{\partial f}{\partial s}\right|^{L^-} + \frac{\partial}{\partial s}f(L^-)\right)\right).
\end{aligned}
\tag{C.34}
$$

Here equation 3.45 has been used twice, first with the function $f_0 = s\frac{\partial f}{\partial s}$.

Putting this all together gives

$$
\begin{aligned}
\langle\nabla^2 f\rangle ={}& \frac{1}{s}\frac{\partial}{\partial s}\left(s\frac{\partial\langle f\rangle}{\partial s}\right) + \frac{1}{s^2}\frac{\partial^2\langle f\rangle}{\partial\phi^2} + 2\beta\frac{\partial\langle f\rangle}{\partial s} + \left(\frac{\beta}{s} + \frac{\partial\beta}{\partial s} + \beta^2\right)\langle f\rangle \\
& - \frac{1}{\Delta L}\left(\left(\frac{1}{s}\frac{\partial L^+}{\partial s} + \frac{\partial^2 L^+}{\partial s^2}\right)f(L^+) - \left(\frac{1}{s}\frac{\partial L^-}{\partial s} + \frac{\partial^2 L^-}{\partial s^2}\right)f(L^-)\right) \\
& - \frac{1}{\Delta L}\left(\frac{\partial L^+}{\partial s}\left(\left.\frac{\partial f}{\partial s}\right|^{L^+} + \frac{\partial}{\partial s}f(L^+)\right)\right) \\
& + \frac{1}{\Delta L}\left(\frac{\partial L^-}{\partial s}\left(\left.\frac{\partial f}{\partial s}\right|^{L^-} + \frac{\partial}{\partial s}f(L^-)\right)\right) + \frac{1}{\Delta L}\left(\left.\frac{\partial f}{\partial z}\right|^{L^+} - \left.\frac{\partial f}{\partial z}\right|^{L^-}\right) \\
={}& \nabla^2_\perp\langle f\rangle + 2\beta\frac{\partial\langle f\rangle}{\partial s} + \left(\frac{\beta}{s} + \frac{\partial\beta}{\partial s} + \beta^2\right)\langle f\rangle \\
& - \frac{1}{\Delta L}\left(\left(\frac{1}{s}\frac{\partial L^+}{\partial s} + \frac{\partial^2 L^+}{\partial s^2}\right)f(L^+) - \left(\frac{1}{s}\frac{\partial L^-}{\partial s} + \frac{\partial^2 L^-}{\partial s^2}\right)f(L^-)\right) \\
& - \frac{1}{\Delta L}\left(\frac{\partial L^+}{\partial s}\left(\left.\frac{\partial f}{\partial s}\right|^{L^+} + \frac{\partial}{\partial s}f(L^+)\right)\right) \\
& + \frac{1}{\Delta L}\left(\frac{\partial L^-}{\partial s}\left(\left.\frac{\partial f}{\partial s}\right|^{L^-} + \frac{\partial}{\partial s}f(L^-)\right)\right) \\
& + \frac{1}{\Delta L}\left(\left.\frac{\partial f}{\partial z}\right|^{L^+} - \left.\frac{\partial f}{\partial z}\right|^{L^-}\right),
\end{aligned}
\tag{C.35}
$$

where $\nabla_\perp^2 \langle f \rangle = \frac{1}{s}\frac{\partial}{\partial s}\left(s\frac{\partial \langle f \rangle}{\partial s}\right) + \frac{1}{s^2}\frac{\partial^2 \langle f \rangle}{\partial \phi^2}$ is the Laplacian operator in the equatorial plane.

The boundary gradient terms,

$$-\frac{1}{\Delta L}\left(\frac{\partial L^+}{\partial s}\frac{\partial f}{\partial s}\bigg|^{L^+} - \frac{\partial L^-}{\partial s}\frac{\partial f}{\partial s}\bigg|^{L^-}\right) + \frac{1}{\Delta L}\left(\frac{\partial f}{\partial z}\bigg|^{L^+} - \frac{\partial f}{\partial z}\bigg|^{L^-}\right), \quad (C.36)$$

can be combined by writing them in terms of the gradient, and unit normal vector $\hat{\mathbf{n}}_{bc}$, perpendicular to the surface, which has no ϕ component for an axisymmetric boundary as has been assumed. The gradient normal to the surface is equal to

$$\boldsymbol{\nabla} f \cdot \hat{\mathbf{n}}_{bc}\big|^{L^\pm} = \left(\frac{\partial f}{\partial s}\hat{\mathbf{s}}\cdot\hat{\mathbf{n}}_{bc}\right)^{L^\pm} + \left(\frac{\partial f}{\partial z}\hat{\mathbf{z}}\cdot\hat{\mathbf{n}}_{bc}\right)^{L^\pm}$$

$$= \hat{\mathbf{z}}\cdot\hat{\mathbf{n}}_{bc}\big|^{L^\pm}\left(\frac{\hat{\mathbf{s}}\cdot\hat{\mathbf{n}}_{bc}}{\hat{\mathbf{z}}\cdot\hat{\mathbf{n}}_{bc}}\frac{\partial f}{\partial s} + \frac{\partial f}{\partial z}\right)^{L^\pm}. \quad (C.37)$$

Therefore,

$$\frac{\boldsymbol{\nabla} f \cdot \hat{\mathbf{n}}_{bc}}{\hat{\mathbf{z}}\cdot\hat{\mathbf{n}}_{bc}}\bigg|^{L^\pm} = -\frac{\partial L^\pm}{\partial s}\frac{\partial f}{\partial s}\bigg|^{L^\pm} + \frac{\partial f}{\partial z}\bigg|^{L^\pm}, \quad (C.38)$$

where we have used equation 3.36 for the unit normal to the boundary. Thus the boundary terms in equation C.36 can be written as

$$\frac{1}{\Delta L}\left(\frac{\boldsymbol{\nabla} f \cdot \hat{\mathbf{n}}_{bc}}{\hat{\mathbf{z}}\cdot\hat{\mathbf{n}}_{bc}}\bigg|^{L^+} - \frac{\boldsymbol{\nabla} f \cdot \hat{\mathbf{n}}_{bc}}{\hat{\mathbf{z}}\cdot\hat{\mathbf{n}}_{bc}}\bigg|^{L^-}\right). \quad (C.39)$$

In this form it is clear that these terms represent the net diffusion of f into the system through the boundaries.

185

Thus, the average of the Laplacian for general boundary geometry is

$$
\begin{aligned}
\left\langle \nabla^2 f \right\rangle =& \nabla_\perp^2 \left\langle f \right\rangle + 2\beta \frac{\partial \left\langle f \right\rangle}{\partial s} + \left(\frac{\beta}{s} + \frac{\partial \beta}{\partial s} + \beta^2 \right) \left\langle f \right\rangle \\
& + \frac{1}{\Delta L} \left(\left. \frac{\boldsymbol{\nabla} f \cdot \hat{\mathbf{n}}_{bc}}{\hat{\mathbf{z}} \cdot \hat{\mathbf{n}}_{bc}} \right|^{L^+} - \left. \frac{\boldsymbol{\nabla} f \cdot \hat{\mathbf{n}}_{bc}}{\hat{\mathbf{z}} \cdot \hat{\mathbf{n}}_{bc}} \right|^{L^-} \right) \\
& - \frac{1}{\Delta L} \left(\left(\frac{1}{s} \frac{\partial L^+}{\partial s} + \frac{\partial^2 L^+}{\partial s^2} \right) f(L^+) - \left(\frac{1}{s} \frac{\partial L^-}{\partial s} + \frac{\partial^2 L^-}{\partial s^2} \right) f(L^-) \right) \\
& - \frac{1}{\Delta L} \left(\frac{\partial L^+}{\partial s} \frac{\partial}{\partial s} f(L^+) - \frac{\partial L^-}{\partial s} \frac{\partial}{\partial s} f(L^-) \right).
\end{aligned}
\tag{C.40}
$$

To this equation we must apply boundary conditions on f, namely to the value of f at all points on the boundary, $f(L^\pm)$, the derivative of this value with respect to s, and the boundary value of the gradient in the $\hat{\mathbf{r}}$ direction.

C.4.1 Boundary terms

The boundary terms depend on the 3D values of f and its derivatives at the boundary. Since in our 2D framework we only simulate the axially averaged variables, we must relate the boundary values of quantities to their z-averaged values. Working under the assumption that the dynamic variables should be dominantly rigid, we take $f(L^+) = \left\langle f \right\rangle = f(L^-)$. This will be referred to as rigidity boundary conditions. This choice reduces the Laplacian to

$$
\left\langle \nabla^2 f \right\rangle = \nabla_\perp^2 \left\langle f \right\rangle + \beta \frac{\partial \left\langle f \right\rangle}{\partial s} + \frac{1}{\Delta L} \left(\left. \frac{\boldsymbol{\nabla} f \cdot \hat{\mathbf{n}}_{bc}}{\hat{\mathbf{z}} \cdot \hat{\mathbf{n}}_{bc}} \right|^{L^+} - \left. \frac{\boldsymbol{\nabla} f \cdot \hat{\mathbf{n}}_{bc}}{\hat{\mathbf{z}} \cdot \hat{\mathbf{n}}_{bc}} \right|^{L^-} \right).
\tag{C.41}
$$

Here we have used that $\frac{\partial}{\partial s} \left(\frac{1}{L^\pm} \right) = \frac{s}{L^{\pm 3}}$ and $\frac{\partial}{\partial s} \left(\frac{1}{\Delta L} \right) = -\frac{s}{\Delta L L^+ L^-}$.

For spherical geometry, where the outward pointing unit normal is equal to $\hat{\mathbf{n}}_{bc}\big|^{L^\pm} = \pm\hat{\mathbf{r}}$ with the minus on the inner boundary inside the TC, this is

equal to

$$\left\langle \nabla^2 f \right\rangle = \nabla^2_\perp \left\langle f \right\rangle + \beta \frac{\partial \left\langle f \right\rangle}{\partial s} + \frac{1}{\Delta L} \left(\frac{r^+}{L^+} \left. \frac{\partial f}{\partial r} \right|^{L^+} - \frac{r^-}{L^-} \left. \frac{\partial f}{\partial r} \right|^{L^-} \right). \tag{C.42}$$

The conditions on the gradients of f at the boundary differ depending on the variable being modeled. Each will be discussed in separate subsections below.

Axial vorticity

For the case of $f = \omega_z$ we apply free-slip boundary conditions. Formally, as calculated in Appendix B, this implies that $\frac{\partial \omega_r}{\partial r} = 0$, but for simplicity we will assume that we can take $\frac{\partial \omega_z}{\partial r} = 0$. Thus the full z-averaged Laplacian is

$$\left\langle \nabla^2 \omega_z \right\rangle = \nabla^2_\perp \left\langle \omega_z \right\rangle + \beta \frac{\partial \left\langle \omega_z \right\rangle}{\partial s} \equiv \nabla^2_\beta \left\langle \omega_z \right\rangle, \tag{C.43}$$

where we have defined $\nabla^2_\beta \left\langle f \right\rangle = \nabla^2_\perp \left\langle f \right\rangle + \beta \frac{\partial \left\langle f \right\rangle}{\partial s}$.

Zonal flow

For the case of $f = \tilde{\omega}$, as calculated in Appendix B free-slip boundary conditions give that $\frac{\partial \tilde{\omega}}{\partial r} = 0$. Thus the full z-averaged Laplacian is

$$\left\langle \nabla^2 \tilde{\omega} \right\rangle = \nabla^2_\beta \left\langle \tilde{\omega} \right\rangle. \tag{C.44}$$

Axial velocity

For $f = u_z$ it does not make sense to assume stress-free like conditions since inside the TC, where this variable is large, the axial velocity is predominantly

187

perpendicular to the boundary rather than tangential to it. Thus we will assume that

$$\left.\frac{\partial u_z}{\partial s}\right|^{L^{\pm}} \sim \frac{\partial \langle u_z \rangle}{\partial s}, \tag{C.45}$$

and

$$\left.\frac{\partial u_z}{\partial z}\right|^{L^{\pm}} \sim \mp \frac{\langle u_z \rangle}{\delta^{\pm}}, \tag{C.46}$$

where the boundary thicknesses, $\delta^{\pm}$, are as defined in equation 3.66. The latter is inspired by the assumption that the axial velocity, which is dominated by the rigid component in the bulk, should go to zero at the boundary. Thus the full z-averaged Laplacian is

$$\langle \nabla^2 u_z \rangle = \nabla_{\perp}^2 \langle u_z \rangle - \frac{\langle u_z \rangle}{\Delta L} \left(\frac{1}{\delta^+} + \frac{1}{\delta^-} \right). \tag{C.47}$$

Temperature

For the case of $f = T$ the gradients at the boundaries represent the heat flux into or out of our system. We do not want to fix the boundary gradients, since this would fix the heat flux through the system. Instead we will utilize the constant temperature boundary conditions to parameterize the boundary gradients in terms of the mean values. This is done using the heat flux through the bulk of the shell.

We expect the thermal profile of a well mixed fluid to look qualitatively like figure C.1, with a relatively thin boundary layer relative to the shell thickness.

(a) Inside the TC   (b) Outside the TC
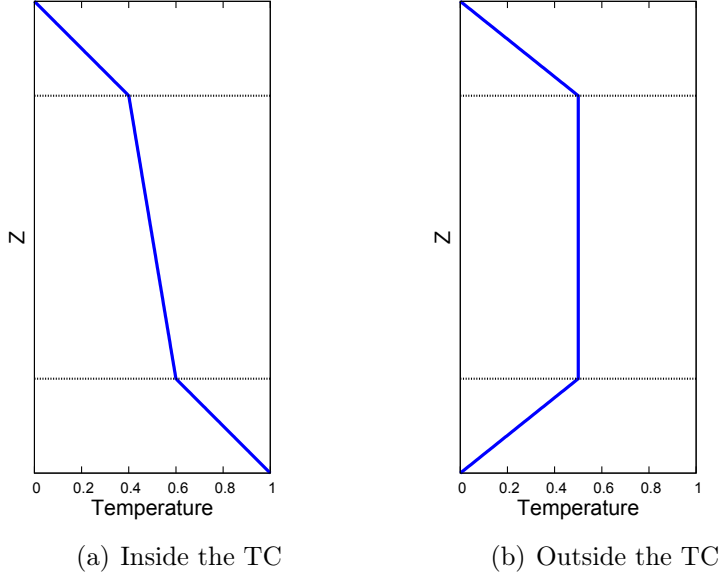
Figure C.1: Expected qualitative thermal profile in z. The dotted lines are the interface between the thermal boundary layer and the bulk of the fluid.

This allows us to estimate the boundary terms inside the TC by

$$\left.\frac{\partial T}{\partial r}\right|^{L^+} \sim \frac{T(L^+) - \langle T \rangle}{\delta^+}, \tag{C.48}$$

and

$$\left.\frac{\partial T}{\partial r}\right|^{L^-} \sim \frac{\langle T \rangle - T(L^-)}{\delta^-}, \tag{C.49}$$

where the boundary layer thickness is given by equation 3.66 in terms of the Nusselt number. Outside the TC the boundary gradients are given by

$$\left.\frac{\partial T}{\partial r}\right|^{L^\pm} \sim \frac{T(L^\pm) - \langle T \rangle}{\delta^\pm}. \tag{C.50}$$

While we previously took $T(L^+) = \langle T \rangle = T(L^-)$, doing so in this term would result in the boundary gradients being zero. These terms are necessary for generating a physically realistic thermal profile for the system; if they were

189

zero we would get a mean temperature of 0 throughout the shell. If we were to set $T(L^{\pm}) = T_e/T_i$, we would get a cuspy profile as in figure 3.2, which as argued previously is not desirable for a 2D model. Instead, we estimate the boundary gradients by taking $T(L^{\pm})$ equal to the average of the boundary values: $T(L^{\pm}) = 0$ outside the TC and $T(L^{+}) = T(L^{-}) = 0.5$ inside the TC. Thus when $\langle T \rangle \sim 0.5$ inside the TC the system is in equilibrium since the heat flux in the bottom is equal to the heat flux out the top, as expected. The geometrical effect of different surface areas at the two boundaries due to different slopes is taken into account by the different values of δ at the boundaries. Since the boundary value of the non-axisymmetric modes is 0, this term will force these modes to decay. We can envision that the region of integration is the region in which the temperature is rigid, and the gradients are conducting heat into and out of this region at the boundaries.

Under these assumptions the axisymmetric boundary gradients are

$$\frac{\partial \overline{T}}{\partial r}\bigg|^{L^+} = \begin{cases} \dfrac{0.5 - \overline{\langle T \rangle}}{\delta^+} & s < r_i \\[2ex] -\dfrac{\overline{\langle T \rangle}}{\delta^+} & s > r_i \end{cases}, \tag{C.51}$$

and

$$\frac{\partial \overline{T}}{\partial r}\bigg|^{L^-} = \begin{cases} \dfrac{\overline{\langle T \rangle} - 0.5}{\delta^-} & s < r_i \\[2ex] -\dfrac{\overline{\langle T \rangle}}{\delta^-} & s > r_i \end{cases}, \tag{C.52}$$

while the non-axisymmetric gradients are equal to

$$\frac{\partial T_m}{\partial r}\bigg|^{L^+} = -\frac{\langle T \rangle_m}{\delta^+} \qquad \forall s, \tag{C.53}$$

and

$$\frac{\partial T_m}{\partial r}\bigg|^{L^-} = \begin{cases} \dfrac{\langle T \rangle_m}{\delta^-} & s < r_i \\[2ex] -\dfrac{\langle T \rangle_m}{\delta^-} & s > r_i \end{cases}. \tag{C.54}$$

C.5 Buoyancy term

Depending on the symmetries of the system, the buoyancy term has different values. As discussed in Section 2.5, for a cylindrically symmetric system we have

$$g_r = \frac{s}{s_e} \qquad \hat{\mathbf{g}} = \hat{\mathbf{s}}, \tag{C.55}$$

where s_e is the cylindrical radius of the external boundary. For spherical symmetry we have two different cases. For a constant gravitational field

$$g_r = 1 \qquad \hat{\mathbf{g}} = -\hat{\mathbf{r}}, \tag{C.56}$$

and for a gravitational field which varies linearly with radius we have

$$g_r = \frac{r}{r_e} \qquad \hat{\mathbf{g}} = -\hat{\mathbf{r}}. \tag{C.57}$$

C.5.1 Vorticity equation

In cylindrical symmetry the gravitational component of the buoyancy term in the z-averaged vorticity equation, given by equation 3.81, can be calculated

191

by using C.55. It is equal to

$$\left\langle g_r \frac{\hat{\mathbf{g}} \cdot \hat{\mathbf{s}}}{s} \right\rangle = \left\langle g_r \frac{\hat{\mathbf{s}} \cdot \hat{\mathbf{s}}}{s} \right\rangle = \left\langle \frac{g_r}{s} \right\rangle = \frac{1}{s_e}, \tag{C.58}$$

which is z-independent. Meanwhile, in spherical symmetry,

$$\left\langle g_r \frac{\hat{\mathbf{g}} \cdot \hat{\mathbf{s}}}{s} \right\rangle = \left\langle -g_r \frac{\hat{\mathbf{r}} \cdot \hat{\mathbf{s}}}{s} \right\rangle = \left\langle -g_r \frac{s}{rs} \right\rangle = \left\langle -\frac{g_r}{r} \right\rangle. \tag{C.59}$$

If we take $g_r = \frac{r}{r_e}$ this can be trivially evaluated to the constant

$$\left\langle g_r \frac{\hat{\mathbf{g}} \cdot \hat{\mathbf{s}}}{s} \right\rangle = \left\langle -\frac{g_r}{r} \right\rangle = \left\langle -\frac{r}{rr_e} \right\rangle = -\frac{1}{r_e}. \tag{C.60}$$

Otherwise, if we assume that $g_r = 1$ then this can be evaluated to give

$$
\begin{aligned}
\left\langle g_r \frac{\hat{\mathbf{g}} \cdot \hat{\mathbf{s}}}{s} \right\rangle &= \left\langle -\frac{g_r}{r} \right\rangle = \left\langle -\frac{1}{r} \right\rangle \\
&= -\frac{1}{\Delta L} \left[\ln(2(r+z)) \right]_{L^-}^{L^+} \\
&= -\frac{1}{\Delta L} \left[\ln(2) + \ln(r^+ + L^+) - \ln(2) - \ln(r^- + L^-) \right] \\
&= -\frac{1}{\Delta L} \left[\ln\left(s \left(\sqrt{1 + \left(\frac{L^+}{s}\right)^2} + \left(\frac{L^+}{s}\right) \right) \right) \right] \\
&\quad + \frac{1}{\Delta L} \left[\ln\left(s \left(\sqrt{1 + \left(\frac{L^-}{s}\right)^2} + \left(\frac{L^-}{s}\right) \right) \right) \right] \\
&= -\frac{1}{\Delta L} \left[\ln\left(\sqrt{1 + \left(\frac{L^+}{s}\right)^2} + \left(\frac{L^+}{s}\right) \right) \right] \\
&\quad + \frac{1}{\Delta L} \left[\ln\left(\sqrt{1 + \left(\frac{L^-}{s}\right)^2} + \left(\frac{L^-}{s}\right) \right) \right] \\
&= -\frac{1}{\Delta L} \left[\operatorname{arcsinh}\left(\frac{L^+}{s}\right) - \operatorname{arcsinh}\left(\frac{L^-}{s}\right) \right]. \tag{C.61}
\end{aligned}
$$

Here we have used the relation $\text{arcsinh}(x) = \ln(x + \sqrt{x^2 + 1})$. Note that $\text{arcsinh}(-x) = -\text{arcsinh}(x)$, so this integral simplifies for a symmetric shell with $L^- = -L^+$ outside the TC.

C.5.2 Axial velocity equation

In cylindrical symmetry the buoyancy term in the z-averaged axial velocity equation 3.95 is given by

$$\langle g_r \hat{\mathbf{g}} \cdot \hat{\mathbf{z}} \Theta \rangle = \langle g_r \hat{\mathbf{s}} \cdot \hat{\mathbf{z}} \Theta \rangle = 0, \qquad (\text{C.62})$$

and in spherical geometry it is

$$\langle g_r \hat{\mathbf{g}} \cdot \hat{\mathbf{z}} \Theta \rangle = \langle -g_r \hat{\mathbf{r}} \cdot \hat{\mathbf{z}} \Theta \rangle = \left\langle -g_r \frac{z}{r} \Theta \right\rangle. \qquad (\text{C.63})$$

For linear gravity, with $g_r = \frac{r}{r_e}$, this can be approximated as

$$\langle g_r \hat{\mathbf{g}} \cdot \hat{\mathbf{z}} \Theta \rangle = \left\langle -g_r \frac{z}{r} \Theta \right\rangle = \left\langle -\frac{r}{r_e} \frac{z}{r} \Theta \right\rangle = \left\langle -\frac{z}{r_e} \Theta \right\rangle$$

$$\sim -\frac{\langle z \rangle}{r_e} \langle \Theta \rangle = -\frac{(L^+ + L^{1/2})}{2 r_e} \langle \Theta \rangle, \qquad (\text{C.64})$$

while for constant $g_r = 1$ it is

$$\langle g_r \hat{\mathbf{g}} \cdot \hat{\mathbf{z}} \Theta \rangle = \left\langle -g_r \frac{z}{r} \Theta \right\rangle = \left\langle -\frac{z}{r} \Theta \right\rangle \sim \left\langle -\frac{z}{r} \right\rangle \langle \Theta \rangle = -\frac{\Delta r}{\Delta z} \langle \Theta \rangle. \qquad (\text{C.65})$$

Inside the TC we have $\Delta z = \Delta L$ and $\Delta r = d$, while outside $L^{1/2} = 0$ and so the single hemisphere values are $\Delta z = L^+ - 0 = L^+$ and $\Delta r = 1 - s$.

A consequence of this is that for cylindrical gravitational forcing, as in a

193

rotationally dominated system, there is no component of $\hat{\mathbf{g}}$ in the $\hat{z}$ direction and thus the geostrophic axial flow will not be forced. Only in spherically symmetric systems, as in planetary scale gravity, will such flows be excited. This does not imply that the axial velocity is zero, as the impenetrable boundary conditions and the incompressibility of the flow will still lead to ageostrophic flow in the axial direction.

Appendix D

Axisymmetric cylindrical radial velocity

In section 3.8 it was argued that the axisymmetric cylindrical radial velocity is zero, $\overline{\langle u_s \rangle} = 0$, under the QG approximation This can be shown by integrating the divergence of the flow (which is zero from the incompressibility condition) over the volume bound by the convection shell boundaries on the top and bottom and cylinders concentric with the rotation axis with radii of $s = s_i$ and $s = s_o$. We will restrict our consideration to volumes such that s_i and s_o are either both inside or both outside the TC. Using the divergence theorem

$$0 = \iiint_V \boldsymbol{\nabla} \cdot \mathbf{u} \, dV = \iint_S \mathbf{u} \cdot \hat{\mathbf{n}} \, dS$$

$$0 = \iint_{s=s_i} \mathbf{u} \cdot (-\hat{\mathbf{s}}) s \, d\phi \, dz + \iint_{s=s_o} \mathbf{u} \cdot \hat{\mathbf{s}} s \, d\phi \, dz + \iint_{z=L^+} \mathbf{u} \cdot \hat{\mathbf{n}}_{bc} \, dS + \iint_{z=L^-} \mathbf{u} \cdot \hat{\mathbf{n}}_{bc} \, dS$$

$$0 = -\iint_{s=s_i} u_s s_i \, d\phi \, dz + \iint_{s=s_o} u_s s_o \, d\phi \, dz + \iint_{z=L^+} u_n \, dS + \iint_{z=L^-} u_n \, dS. \qquad \text{(D.1)}$$

Since $\mathbf{u} \cdot \hat{\mathbf{n}}_{bc}|^{L^{\pm}} = u_n(L^{\pm}) = 0$ due to the impenetrable boundary, this can be evaluated to give

$$2\pi \Delta L s_i \overline{\langle u_s \rangle}(s = s_i) = 2\pi \Delta L s_o \overline{\langle u_s \rangle}(s = s_o). \tag{D.2}$$

Taking $s_o = 1$ outside the TC we get $\overline{\langle u_s \rangle} = 0$ for all other s outside the TC since $\Delta L(s = 1) = 0$ and $u_s(s = 1) = 0$ due to the impenetrable boundary conditions. Likewise, taking $s_i = 0$ inside the TC we also get $\overline{u_s} = 0$ for all other s inside the TC. Hence $\overline{\langle u_s \rangle} = 0$ everywhere in the system.

This can also be seen by z and ϕ averaging the incompressibility equation

$$\overline{\langle 0 \rangle} = \overline{\langle \mathbf{\nabla} \cdot \mathbf{u} \rangle}$$

$$0 = \frac{1}{s} \overline{\left\langle \frac{\partial s u_s}{\partial s} \right\rangle} + \overline{\left\langle \frac{\partial u_z}{\partial z} \right\rangle} + \frac{1}{s} \overline{\left\langle \frac{\partial u_\phi}{\partial \phi} \right\rangle}$$

$$0 = \frac{1}{s} \frac{\partial \left(s \overline{\langle u_s \rangle} \right)}{\partial s} + \beta \overline{\langle u_s \rangle}. \tag{D.3}$$

Solving this first order homogeneous differential equation with variable coefficient gives

$$\int \frac{\partial \overline{\langle u_s \rangle}}{\partial s} ds = - \int \left(\frac{1}{s} + \beta \right) \overline{\langle u_s \rangle} ds$$

$$\overline{\langle u_s \rangle} = C e^{-\int \left(\frac{1}{s} + \beta \right) ds}$$

$$\overline{\langle u_s \rangle} = C e^{-\ln s - \ln \Delta L}$$

$$\overline{\langle u_s \rangle} = \frac{C}{s \Delta L(s)}, \tag{D.4}$$

where C is a constant of integration which can be determined from the boundary conditions. While the function diverges at the boundaries, where $u_s = 0$,

we can still consider it limit

$$\lim_{s \to 1} \overline{\langle u_s \rangle} = \lim_{s \to 1} \frac{C}{s \Delta L(s)} = 0. \qquad (\text{D.5})$$

Since $\Delta L(s) \to 0$ as $s \to 1$, the only way this boundary condition can be satisfied is if we take $C = 0$. Thus, $\overline{\langle u_s \rangle} = 0$ for all s.

Appendix E

Heat flux

To ensure that our 2D QG equations are consistent with the 3D equations, we will compare the heat flux through a cylindrical shell at an arbitrary location within the spherical shell, calculated for both the 2D and 3D heat equations.

E.1 Three dimensional equation

The full 3D heat equation is

$$\frac{\partial T}{\partial t} + \mathbf{u} \cdot \nabla T = \frac{E}{Pr} \nabla^2 T. \tag{E.1}$$

Using the fact that $\boldsymbol{\nabla} \cdot (\mathbf{u}T) = \mathbf{u} \cdot \boldsymbol{\nabla} T + T \boldsymbol{\nabla} \cdot \mathbf{u}$, where the second term is zero due to the incompressibility of the flow, the steady state heat equation can be rewritten as

$$0 = \boldsymbol{\nabla} \cdot (\mathbf{u}T) - \frac{E}{Pr} \nabla^2 T. \tag{E.2}$$

To find the heat flux through a surface, we integrate this equation over the volume bound by the surface and use the divergence theorem. In this case we

198

consider the volume bound by the tangent cylinder at $s = r_i$, another cylinder at $s = s_0$ and the endcaps at $z = L^{\pm}$. This gives

$$
\begin{aligned}
0 &= \oint_V \left(\boldsymbol{\nabla} \cdot (\mathbf{u}T) - \frac{E}{Pr} \nabla^2 T \right) dV \\
&= \oint_V \boldsymbol{\nabla} \cdot \left(\mathbf{u}T - \frac{E}{Pr} \boldsymbol{\nabla}T \right) dV \\
&= \oint_S \hat{\mathbf{n}} \cdot \left(\mathbf{u}T - \frac{E}{Pr} \boldsymbol{\nabla}T \right) dS,
\end{aligned}
\tag{E.3}
$$

where the last step follows from the divergence theorem. $\hat{\mathbf{n}}$ is the outward pointing unit vector normal to the surface bounding the volume of integration.

Expanding this, using the impenetrable boundary condition of the shell ($\hat{\mathbf{n}}_{bc} \cdot \mathbf{u} = 0$ on the endcaps) and the assumption that the TC is also impenetrable ($\hat{\mathbf{n}} \cdot \mathbf{u} = u_s = 0$ on the TC), gives

$$
\begin{aligned}
0 &= \int_{s=r_i} \hat{\mathbf{n}} \cdot \hat{\mathbf{s}} \left(-\frac{E}{Pr} \frac{\partial T}{\partial s} \right) r_i d\phi dz + \int_{s=s_0} \hat{\mathbf{n}} \cdot \hat{\mathbf{s}} \left(u_s T - \frac{E}{Pr} \frac{\partial T}{\partial s} \right) s_0 d\phi dz \\
&\quad - \frac{E}{Pr} \int_{r=r^+} \boldsymbol{\nabla}T \cdot \hat{\mathbf{n}}_{bc} dS - \frac{E}{Pr} \int_{r=r^-} \boldsymbol{\nabla}T \cdot \hat{\mathbf{n}}_{bc} dS \\
0 &= -2\pi \int_{s=r_i} \hat{\mathbf{n}} \cdot \hat{\mathbf{s}} \left(\frac{E}{Pr} \frac{\partial \overline{T}}{\partial s} \right) r_i dz + 2\pi \int_{s=s_0} \hat{\mathbf{n}} \cdot \hat{\mathbf{s}} \left(\overline{u_s T} - \frac{E}{Pr} \frac{\partial \overline{T}}{\partial s} \right) s_0 dz \\
&\quad - \frac{E}{Pr} \left(\int_{r=r^+} \boldsymbol{\nabla}T \cdot \hat{\mathbf{n}}_{bc} dS + \int_{r=r^-} \boldsymbol{\nabla}T \cdot \hat{\mathbf{n}}_{bc} dS \right).
\end{aligned}
\tag{E.4}
$$

Note that $\hat{\mathbf{n}} \cdot \hat{\mathbf{s}} = \pm 1$, with the sign dependent on the orientation of $\hat{\mathbf{n}}$: if s_0 is inside the TC it is equal to -1 and outside it is equal to $+1$. The first two terms represent the heat flux through the tangent cylinder (F_{s_i}) and cylinder at $s = s_0$ (F_{s_0}) respectively. The second two terms are the heat flux through the upper (F_{r+}) and lower (F_{r-}) endcaps respectively.

Performing the z-integrals over the two cylinders gives

$$
\begin{aligned}
F_s &= 2\pi \int_s \hat{\mathbf{n}} \cdot \hat{\mathbf{s}} \left(\overline{u_s T} - \frac{E}{Pr} \frac{\partial \overline{T}}{\partial s} \right) s\, dz \\
&= 2\pi s \left(\hat{\mathbf{n}} \cdot \hat{\mathbf{s}} \left(\overline{\langle u_s \rangle \langle T \rangle} \Delta L - \frac{E}{Pr} \Delta L \left\langle \frac{\partial \overline{T}}{\partial s} \right\rangle \right) \right) \Big|^s \\
&= 2\pi s \Delta L \left(\hat{\mathbf{n}} \cdot \hat{\mathbf{s}} \left(\overline{\langle u_s \rangle \langle T \rangle} - \frac{E}{Pr} \left(\frac{\partial \overline{\langle T \rangle}}{\partial s} + \beta \overline{\langle T \rangle} \right) \right) \right) \Big|^s \\
&\quad + 2\pi s \frac{E}{Pr} \left(\hat{\mathbf{n}} \cdot \hat{\mathbf{s}} \left(\overline{T} \left(L^+ \right) \frac{\partial L^+}{\partial s} - \overline{T} \left(L^- \right) \frac{\partial L^-}{\partial s} \right) \right) \Big|^s . \qquad \text{(E.5)}
\end{aligned}
$$

For the two endcap integrals we parameterize the surface integral in terms of polar coordinates. The surfaces, which are located at $z = L^\pm(s)$, can be parameterized as $\mathbf{x}(s, \phi) = (s \cos \phi, s \sin \phi, L^\pm(s))$. The surface area element is given by the magnitude of the cross product of the tangent vectors to the surface. The tangent vectors are equal to the directional derivatives of $\mathbf{x}$ tangent to the surface, and are notated $\mathbf{T}_s$ and $\mathbf{T}_\phi$. The surface area element is thus

$$
\begin{aligned}
|\mathbf{T_s} \times \mathbf{T}_\phi|^{L^\pm} &= \left| \frac{\partial \mathbf{x}(s, \phi)}{\partial s} \times \frac{\partial \mathbf{x}(s, \phi)}{\partial \phi} \right|^{L^\pm} \\
&= \left| \left(\cos \phi, \sin \phi, \frac{\partial L^\pm}{\partial s} \right) \times (-s \sin \phi, s \cos \phi, 0) \right|^{L^\pm} \\
&= \left| \left(-s \cos \phi \frac{\partial L^+}{\partial s}, +s \sin \phi \frac{\partial L^\pm}{\partial s}, s((\cos \phi)^2 + (\sin \phi)^2) \right) \right|^{L^\pm} \\
&= \left| s \left(-\cos \phi \frac{\partial L^+}{\partial s}, \sin \phi \frac{\partial L^+}{\partial s}, 1 \right) \right|^{L^\pm} \\
&= \left(s \sqrt{1 + ((\cos \phi)^2 + (\sin \phi)^2) \left(\frac{\partial L^+}{\partial s} \right)^2} \right)^{L^\pm} \\
&= \left(s \sqrt{1 + \left(\frac{\hat{\mathbf{n}}_{bc} \cdot \hat{\mathbf{s}}}{\hat{\mathbf{n}}_{bc} \cdot \hat{\mathbf{z}}} \right)^2} \right)^{L^\pm}
\end{aligned}
$$

200

$$= \left(s\sqrt{\frac{(\hat{\mathbf{n}}_{bc} \cdot \hat{\mathbf{z}})^2 + (\hat{\mathbf{n}}_{bc} \cdot \hat{\mathbf{s}})^2}{(\hat{\mathbf{n}}_{bc} \cdot \hat{\mathbf{z}})^2}} \right)^{L^{\pm}}$$

$$= \frac{s}{|\hat{\mathbf{n}}_{bc} \cdot \hat{\mathbf{z}}|^{L^{\pm}}}. \tag{E.6}$$

Here we have used the calculation of the unit normal to the surface $\hat{\mathbf{n}}_{bc}$ in equation 3.36. Provided the boundary is never vertical (except when crossing the equatorial plane), $\hat{\mathbf{n}}_{bc} \cdot \hat{\mathbf{z}}$ is positive on the upper boundary and negative on the lower boundary. For the lower boundary this is true outside the TC because it is at negative values of z, while inside the TC it is because the normal points outwards from the volume of integration, or into the centre of the body. Thus we can replace the absolute value signs with the multiplication by -1 on the lower endcap.

Putting this all together, the total heat flux is

$$0 = F_{s_i} + F_{s_0} + F_{r^+} + F_{r^-}, \tag{E.7}$$

where

$$F_{r_i} = -\left. 2\pi r_i \Delta L \left(\hat{\mathbf{n}} \cdot \hat{\mathbf{s}} \left(\frac{E}{Pr} \left(\frac{\partial \overline{\langle T \rangle}}{\partial s} + \beta \overline{\langle T \rangle} \right) \right) \right) \right|^{|s=r_i}$$
$$+ \left. 2\pi r_i \left(\hat{\mathbf{n}} \cdot \hat{\mathbf{s}} \left(\frac{E}{Pr} \left(\overline{T}\left(L^+\right) \frac{\partial L^+}{\partial s} - \overline{T}\left(L^-\right) \frac{\partial L^-}{\partial s} \right) \right) \right) \right|^{|s=r_i}, \tag{E.8}$$

$$F_{s_0} = \left. 2\pi s_0 \Delta L \left(\hat{\mathbf{n}} \cdot \hat{\mathbf{s}} \left(\overline{\langle u_s \rangle \langle T \rangle} - \frac{E}{Pr} \left(\frac{\partial \overline{\langle T \rangle}}{\partial s} + \beta \overline{\langle T \rangle} \right) \right) \right) \right|^{|s=s_0}$$
$$+ \left. 2\pi s_0 \left(\hat{\mathbf{n}} \cdot \hat{\mathbf{s}} \left(\frac{E}{Pr} \left(\overline{T}\left(L^+\right) \frac{\partial L^+}{\partial s} - \overline{T}\left(L^-\right) \frac{\partial L^-}{\partial s} \right) \right) \right) \right|^{|s=s_0}, \tag{E.9}$$

$$F_{r^+} = -\frac{E}{Pr} \int \left((\boldsymbol{\nabla} T \cdot \hat{\mathbf{n}}_{bc}) \frac{s}{|\hat{\mathbf{n}}_{bc} \cdot \hat{\mathbf{z}}|} \right)\Bigg|^{r=r^+} d\phi ds$$

$$= -2\pi \frac{E}{Pr} \int \left(\frac{\boldsymbol{\nabla}\overline{T} \cdot \hat{\mathbf{n}}_{bc}}{\hat{\mathbf{n}}_{bc} \cdot \hat{\mathbf{z}}} \right)\Bigg|^{r=r^+} s ds, \tag{E.10}$$

$$F_{r^-} = -\frac{E}{Pr} \int \left((\boldsymbol{\nabla} T \cdot \hat{\mathbf{n}}_{bc}) \frac{s}{|\hat{\mathbf{n}}_{bc} \cdot \hat{\mathbf{z}}|} \right)\Bigg|^{r=r^-} d\phi ds$$

$$= 2\pi \frac{E}{Pr} \int \left(\frac{\boldsymbol{\nabla}\overline{T} \cdot \hat{\mathbf{n}}_{bc}}{\hat{\mathbf{n}}_{bc} \cdot \hat{\mathbf{z}}} \right)\Bigg|^{r=r^-} s ds. \tag{E.11}$$

E.2 Two dimensional equation

We will now calculate the heat flux using the 2D QG equation through the same surface as in the previous section, and compare it with the result for the full 3D equation. The general steady state 2D heat equation is

$$
\begin{aligned}
0 = {} & \langle \mathbf{u}_\perp \rangle \cdot \boldsymbol{\nabla}_\perp \langle T \rangle + \langle u_z \rangle \left(\frac{T(L^+) - T(L^-)}{\Delta L} \right) \\
& - \frac{E}{Pr} \left(\nabla_\perp^2 \langle T \rangle + 2\beta \frac{\partial \langle T \rangle}{\partial s} + \left(\frac{\beta}{s} + \frac{\partial \beta}{\partial s} + \beta^2 \right) \langle T \rangle \right) \\
& - \frac{E}{Pr} \left(\frac{1}{\Delta L} \left(\frac{\boldsymbol{\nabla} T \cdot \hat{\mathbf{n}}_{bc}}{\hat{\mathbf{z}} \cdot \hat{\mathbf{n}}_{bc}} \Bigg|^{L^+} - \frac{\boldsymbol{\nabla} T \cdot \hat{\mathbf{n}}_{bc}}{\hat{\mathbf{z}} \cdot \hat{\mathbf{n}}_{bc}} \Bigg|^{L^-} \right) \right) \\
& + \frac{E}{Pr} \frac{1}{\Delta L} \left(\left(\frac{1}{s} \frac{\partial L^+}{\partial s} + \frac{\partial^2 L^+}{\partial s^2} \right) T(L^+) - \left(\frac{1}{s} \frac{\partial L^-}{\partial s} + \frac{\partial^2 L^-}{\partial s^2} \right) T(L^-) \right) \\
& + \frac{E}{Pr} \frac{1}{\Delta L} \left(\frac{\partial L^+}{\partial s} \frac{\partial}{\partial s} T(L^+) - \frac{\partial L^-}{\partial s} \frac{\partial}{\partial s} T(L^-) \right). \tag{E.12}
\end{aligned}
$$

To calculate the heat fluxes we multiply this equation by the column length, ΔL, and integrate over the area bounded by the tangent cylinder at $s = r_i$

and the cylinder at $s = s_0$. This gives six terms:

$$(1) = \Delta L \oint \langle \mathbf{u}_\perp \rangle \cdot \boldsymbol{\nabla}_\perp \langle T \rangle \, s d\phi ds, \tag{E.13}$$

$$(2) = \Delta L \oint \langle u_z \rangle \left(\frac{T(L^+) - T(L^-)}{\Delta L} \right) s d\phi ds, \tag{E.14}$$

$$(3) = -\frac{E}{Pr} \Delta L \oint \left(\nabla_\perp^2 + 2\beta \frac{\partial}{\partial s} + \frac{\beta}{s} + \frac{\partial \beta}{\partial s} + \beta^2 \right) \langle T \rangle \, s d\phi ds, \tag{E.15}$$

$$(4) = -\frac{E}{Pr} \oint \left(\frac{\boldsymbol{\nabla} T \cdot \hat{\mathbf{n}}_{bc}}{\hat{\mathbf{z}} \cdot \hat{\mathbf{n}}_{bc}} \bigg|^{L^+} - \frac{\boldsymbol{\nabla} T \cdot \hat{\mathbf{n}}_{bc}}{\hat{\mathbf{z}} \cdot \hat{\mathbf{n}}_{bc}} \bigg|^{L^-} \right) s d\phi ds, \tag{E.16}$$

$$(5) = \frac{E}{Pr} \oint \left(\frac{1}{s} \frac{\partial L^+}{\partial s} + \frac{\partial^2 L^+}{\partial s^2} \right) T(L^+) s d\phi ds$$

$$- \frac{E}{Pr} \oint \left(\frac{1}{s} \frac{\partial L^-}{\partial s} + \frac{\partial^2 L^-}{\partial s^2} T(L^-) \right) s d\phi ds, \tag{E.17}$$

$$(6) = \frac{E}{Pr} \oint \left(\frac{\partial L^+}{\partial s} \frac{\partial}{\partial s} T(L^+) - \frac{\partial L^-}{\partial s} \frac{\partial}{\partial s} T(L^-) \right) s d\phi ds. \tag{E.18}$$

The second term is trivially zero since we only allow for $m > 0$ contributions from the convective heat injection, and hence $\overline{\langle u_z \rangle} = 0$ for all s.

Evaluating the remaining terms gives

$$(1) = \oint \Delta L \langle \mathbf{u}_\perp \rangle \cdot \boldsymbol{\nabla}_\perp \langle T \rangle \, s d\phi ds$$

$$= \oint \Delta L \left(\boldsymbol{\nabla} \cdot (\langle \mathbf{u}_\perp \rangle \langle T \rangle) - \langle T \rangle \boldsymbol{\nabla} \cdot \langle \mathbf{u}_\perp \rangle \right) s d\phi ds$$

$$= \oint \Delta L \left(\boldsymbol{\nabla} \cdot (\langle \mathbf{u}_\perp \rangle \langle T \rangle) - \langle T \rangle \left(\langle \boldsymbol{\nabla} \cdot \mathbf{u} \rangle - \left\langle \frac{\partial u_z}{\partial z} \right\rangle \right) \right) s d\phi ds$$

$$= \oint \left(\boldsymbol{\nabla} \cdot (\langle \mathbf{u}_\perp \rangle \Delta L \langle T \rangle) - \langle T \rangle \langle \mathbf{u}_\perp \rangle \cdot \boldsymbol{\nabla} (\Delta L) \right) s d\phi ds$$

$$+ \oint (\Delta L \langle T \rangle \beta \langle u_s \rangle) s d\phi ds$$

$$= \oint \left(\boldsymbol{\nabla} \cdot (\langle \mathbf{u}_\perp \rangle \Delta L \langle T \rangle) - \langle T \rangle \langle u_s \rangle \beta \Delta L + \Delta L \langle T \rangle \beta \langle u_s \rangle \right) s d\phi ds$$

$$= \oint \boldsymbol{\nabla} \cdot (\langle \mathbf{u}_\perp \rangle \Delta L \langle T \rangle) s d\phi ds$$

$$= \int_{s=r_i} \hat{\mathbf{n}} \cdot \langle \mathbf{u}_\perp \rangle \, \Delta L \, \langle T \rangle \, r_i d\phi + \int_{s=s_0} \hat{\mathbf{n}} \cdot \langle \mathbf{u}_\perp \rangle \, \Delta L \, \langle T \rangle \, s_0 d\phi$$

$$= 2\pi \, \hat{\mathbf{n}} \cdot \hat{\mathbf{s}} \Delta L \overline{\langle u_s \rangle \langle T \rangle} r_i \Big|^{s=r_i} + 2\pi \, \hat{\mathbf{n}} \cdot \hat{\mathbf{s}} \Delta L \overline{\langle u_s \rangle \langle T \rangle} s_0 \Big|^{s=s_0}$$

$$= 0 + 2\pi \, \hat{\mathbf{n}} \cdot \hat{\mathbf{s}} \Delta L \overline{\langle u_s \rangle \langle T \rangle} s_0 \Big|^{s=s_0} , \tag{E.19}$$

$$(3) = -\frac{E}{Pr} \oint \Delta L \left(\nabla_\perp^2 + 2\beta \frac{\partial}{\partial s} + \frac{\beta}{s} + \frac{\partial \beta}{\partial s} + \beta^2 \right) \langle T \rangle \, s d\phi ds$$

$$= -\frac{E}{Pr} \oint \left(\boldsymbol{\nabla}_\perp \cdot (\Delta L \boldsymbol{\nabla}_\perp \langle T \rangle) \right) s d\phi ds$$

$$+ \frac{E}{Pr} \oint \left((\boldsymbol{\nabla}_\perp \Delta L) \cdot \boldsymbol{\nabla}_\perp \langle T \rangle \right) s d\phi ds$$

$$- \frac{E}{Pr} \oint \left(\Delta L \left(2\beta \frac{\partial}{\partial s} + \frac{\beta}{s} + \frac{\partial \beta}{\partial s} + \beta^2 \right) \right) \langle T \rangle \, s d\phi ds$$

$$= -\frac{E}{Pr} \oint \left(\boldsymbol{\nabla}_\perp \cdot (\Delta L \boldsymbol{\nabla}_\perp \langle T \rangle) \right) s d\phi ds$$

$$- \frac{E}{Pr} \oint \left(-\beta \Delta L \frac{\partial}{\partial s} + \Delta L \left(2\beta \frac{\partial}{\partial s} + \frac{\beta}{s} + \frac{\partial \beta}{\partial s} + \beta^2 \right) \right) \langle T \rangle \, s d\phi ds$$

$$= -\frac{E}{Pr} \oint \left(\boldsymbol{\nabla}_\perp \cdot (\Delta L \boldsymbol{\nabla}_\perp \langle T \rangle) \right) s d\phi ds$$

$$- \frac{E}{Pr} \oint \Delta L \left(\beta \frac{\partial}{\partial s} + \frac{\beta}{s} + \frac{\partial \beta}{\partial s} + \beta^2 \right) \langle T \rangle \, s d\phi ds$$

$$= -\frac{E}{Pr} \oint \left(\boldsymbol{\nabla}_\perp \cdot (\Delta L \boldsymbol{\nabla}_\perp \langle T \rangle) + \frac{\partial \left(\Delta L \beta \langle T \rangle \right)}{\partial s} \right) s d\phi ds$$

$$- \frac{E}{Pr} \oint \left(-\frac{\partial \left(\Delta L \beta \right)}{\partial s} \langle T \rangle + \Delta L \left(\frac{\beta}{s} + \frac{\partial \beta}{\partial s} + \beta^2 \right) \langle T \rangle \right) s d\phi ds$$

$$= -\frac{E}{Pr} \oint \left(\boldsymbol{\nabla}_\perp \cdot (\Delta L \boldsymbol{\nabla}_\perp \langle T \rangle) + \frac{\partial \left(\frac{s}{s} \Delta L \beta \langle T \rangle \right)}{\partial s} \right) s d\phi ds$$

$$+ \frac{E}{Pr} \oint \left(\beta \Delta L \beta + \Delta L \frac{\partial \beta}{\partial s} - \Delta L \left(\frac{\beta}{s} + \frac{\partial \beta}{\partial s} + \beta^2 \right) \right) \langle T \rangle \, s d\phi ds$$

$$= -\frac{E}{Pr} \oint \left(\boldsymbol{\nabla}_\perp \cdot (\Delta L \boldsymbol{\nabla}_\perp \langle T \rangle) + \boldsymbol{\nabla}_\perp \cdot (\hat{\mathbf{s}} \Delta L \beta \langle T \rangle) \right) s d\phi ds$$

$$+ \frac{E}{Pr} \oint \left(\frac{s \Delta L \beta \langle T \rangle}{s^2} - \Delta L \left(\frac{\beta}{s} \right) \langle T \rangle \right) s d\phi ds$$

$$= -\frac{E}{Pr}\left(\int_{s=r_i} \hat{\mathbf{n}}_{bc}\cdot\left(\Delta L\boldsymbol{\nabla}_\perp\langle T\rangle + \hat{\mathbf{s}}\Delta L\beta\langle T\rangle\right)r_i d\phi\right)$$

$$-\frac{E}{Pr}\left(\int_{s=s_0} \hat{\mathbf{n}}_{bc}\cdot\left(\Delta L\boldsymbol{\nabla}_\perp\langle T\rangle + \hat{\mathbf{s}}\Delta L\beta\langle T\rangle\right)s_0 d\phi\right)$$

$$= -2\pi\frac{E}{Pr}\left.\left(\hat{\mathbf{n}}_{bc}\cdot\hat{\mathbf{s}}\Delta L\left(\frac{\partial\overline{\langle T\rangle}}{\partial s} + \beta\overline{\langle T\rangle}\right)r_i\right)\right|^{s=r_i}$$

$$-2\pi\frac{E}{Pr}\left.\left(\hat{\mathbf{n}}_{bc}\cdot\hat{\mathbf{s}}\Delta L\left(\frac{\partial\overline{\langle T\rangle}}{\partial s} + \beta\overline{\langle T\rangle}\right)s_0\right)\right|^{s=s_0}, \qquad\text{(E.20)}$$

$$(4) = -\frac{E}{Pr}\oint\left(\left.\frac{\boldsymbol{\nabla}T\cdot\hat{\mathbf{n}}_{bc}}{\hat{\mathbf{z}}\cdot\hat{\mathbf{n}}_{bc}}\right|^{L^+} - \left.\frac{\boldsymbol{\nabla}T\cdot\hat{\mathbf{n}}_{bc}}{\hat{\mathbf{z}}\cdot\hat{\mathbf{n}}_{bc}}\right|^{L^-}\right)sd\phi ds$$

$$= -2\pi\frac{E}{Pr}\int\left(\left.\frac{\boldsymbol{\nabla}\overline{T}\cdot\hat{\mathbf{n}}_{bc}}{\hat{\mathbf{z}}\cdot\hat{\mathbf{n}}_{bc}}\right|^{L^+} - \left.\frac{\boldsymbol{\nabla}\overline{T}\cdot\hat{\mathbf{n}}_{bc}}{\hat{\mathbf{z}}\cdot\hat{\mathbf{n}}_{bc}}\right|^{L^-}\right)sds, \qquad\text{(E.21)}$$

$$(5)+(6) = \frac{E}{Pr}\oint\left(\frac{1}{s}\frac{\partial L^+}{\partial s} + \frac{\partial^2 L^+}{\partial s^2}\right)T(L^+)sd\phi ds$$

$$-\frac{E}{Pr}\oint\left(\frac{1}{s}\frac{\partial L^-}{\partial s} + \frac{\partial^2 L^-}{\partial s^2}\right)T(L^-)sd\phi ds$$

$$+\frac{E}{Pr}\oint\left(\frac{\partial L^+}{\partial s}\frac{\partial}{\partial s}T(L^+) - \frac{\partial L^-}{\partial s}\frac{\partial}{\partial s}T(L^-)\right)sd\phi ds$$

$$= \frac{E}{Pr}\oint\left(\frac{1}{s}\frac{\partial}{\partial s}\left(s\frac{\partial L^+}{\partial s}\right) + \frac{\partial L^+}{\partial s}\frac{\partial}{\partial s}\right)T(L^+)sd\phi ds$$

$$-\frac{E}{Pr}\oint\left(\frac{1}{s}\frac{\partial}{\partial s}\left(s\frac{\partial L^-}{\partial s}\right) + \frac{\partial L^-}{\partial s}\frac{\partial}{\partial s}\right)T(L^-)sd\phi ds$$

$$= \frac{E}{Pr}\oint\left(\frac{1}{s}\frac{\partial}{\partial s}\left(s\frac{\partial L^+}{\partial s}T(L^+)\right) - \frac{1}{s}\frac{\partial}{\partial s}\left(s\frac{\partial L^-}{\partial s}T(L^-)\right)\right)sd\phi ds$$

$$= \frac{E}{Pr}\oint\left(\boldsymbol{\nabla}_\perp\cdot\left(\hat{\mathbf{s}}\left(\frac{\partial L^+}{\partial s}T(L^+) - \frac{\partial L^-}{\partial s}T(L^-)\right)\right)\right)sd\phi ds$$

$$= \frac{E}{Pr}\left(\int_{s=r_i}\hat{\mathbf{n}}\cdot\hat{\mathbf{s}}\left(\frac{\partial L^+}{\partial s}T(L^+) - \frac{\partial L^-}{\partial s}T(L^-)\right)r_i d\phi\right)$$

$$+\frac{E}{Pr}\left(\int_{s=s_0}\hat{\mathbf{n}}\cdot\hat{\mathbf{s}}\left(\frac{\partial L^+}{\partial s}T(L^+) - \frac{\partial L^-}{\partial s}T(L^-)\right)s_0 d\phi\right)$$

$$
\begin{aligned}
=& 2\pi \frac{E}{Pr} \left(\left(\hat{\mathbf{n}} \cdot \hat{\mathbf{s}} \left(\frac{\partial L^+}{\partial s} \overline{T}(L^+) - \frac{\partial L^-}{\partial s} \overline{T}(L^-) \right) r_i \right) \Big|^{s=r_i} \right) \\
&+ 2\pi \frac{E}{Pr} \left(\left(\hat{\mathbf{n}} \cdot \hat{\mathbf{s}} \left(\frac{\partial L^+}{\partial s} \overline{T}(L^+) - \frac{\partial L^-}{\partial s} \overline{T}(L^-) \right) s_0 \right) \Big|^{s=s_0} \right) . \quad \text{(E.22)}
\end{aligned}
$$

Putting these all together we find

$$
\begin{aligned}
0 =& 2\pi\, \hat{\mathbf{n}} \cdot \hat{\mathbf{s}} \Delta L \overline{\langle u_s \rangle \langle T \rangle} s_0 \Big|^{s=s_0} - 2\pi \frac{E}{Pr} \left(\hat{\mathbf{n}} \cdot \hat{\mathbf{s}} \Delta L \left(\frac{\partial \overline{\langle T \rangle}}{\partial s} + \beta \overline{\langle T \rangle} \right) r_i \right) \Big|^{s=r_i} \\
& - 2\pi \frac{E}{Pr} \left(\hat{\mathbf{n}} \cdot \hat{\mathbf{s}} \Delta L \left(\frac{\partial \overline{\langle T \rangle}}{\partial s} + \beta \overline{\langle T \rangle} \right) s_0 \right) \Big|^{s=s_0} \\
& - 2\pi \frac{E}{Pr} \int \left(\frac{\boldsymbol{\nabla} \overline{T} \cdot \hat{\mathbf{n}}_{bc}}{\hat{\mathbf{z}} \cdot \hat{\mathbf{n}}_{bc}} \Big|^{L^+} - \frac{\boldsymbol{\nabla} \overline{T} \cdot \hat{\mathbf{n}}_{bc}}{\hat{\mathbf{z}} \cdot \hat{\mathbf{n}}_{bc}} \Big|^{L^-} \right) s\,ds \\
& + 2\pi \frac{E}{Pr} \left(\hat{\mathbf{n}} \cdot \hat{\mathbf{s}} \left(\frac{\partial L^+}{\partial s} \overline{T}(L^+) - \frac{\partial L^-}{\partial s} \overline{T}(L^-) \right) r_i \right) \Big|^{s=r_i} \\
& + 2\pi \frac{E}{Pr} \left(\hat{\mathbf{n}} \cdot \hat{\mathbf{s}} \left(\frac{\partial L^+}{\partial s} \overline{T}(L^+) - \frac{\partial L^-}{\partial s} \overline{T}(L^-) \right) s_0 \right) \Big|^{s=s_0} \\
=& - 2\pi r_i \Delta L \frac{E}{Pr} \left(\hat{\mathbf{n}} \cdot \hat{\mathbf{s}} \left(\frac{\partial \overline{\langle T \rangle}}{\partial s} + \beta \overline{\langle T \rangle} \right) \right) \Big|^{s=r_i} \\
& - 2\pi r_i \Delta L \frac{E}{Pr} \left(\hat{\mathbf{n}} \cdot \hat{\mathbf{s}} \left(-\frac{1}{\Delta L} \left(\frac{\partial L^+}{\partial s} \overline{T}(L^+) - \frac{\partial L^-}{\partial s} \overline{T}(L^-) \right) \right) \right) \Big|^{s=r_i} \\
& + 2\pi s_0 \Delta L \left(\hat{\mathbf{n}} \cdot \hat{\mathbf{s}} \left(\overline{\langle u_s \rangle \langle T \rangle} - \frac{E}{Pr} \left(\frac{\partial \overline{\langle T \rangle}}{\partial s} + \beta \overline{\langle T \rangle} \right) \right) \right) \Big|^{s=s_0} \\
& - 2\pi s_0 \Delta L \frac{E}{Pr} \left(\hat{\mathbf{n}} \cdot \hat{\mathbf{s}} \left(-\frac{1}{\Delta L} \left(\frac{\partial L^+}{\partial s} \overline{T}(L^+) - \frac{\partial L^-}{\partial s} \overline{T}(L^-) \right) \right) \right) \Big|^{s=s_0} \\
& - 2\pi \frac{E}{Pr} \int \left(\frac{\boldsymbol{\nabla} \overline{T} \cdot \hat{\mathbf{n}}_{bc}}{\hat{\mathbf{z}} \cdot \hat{\mathbf{n}}_{bc}} \right) \Big|^{L^+} s\,ds + 2\pi \frac{E}{Pr} \int \left(\frac{\boldsymbol{\nabla} \overline{T} \cdot \hat{\mathbf{n}}_{bc}}{\hat{\mathbf{z}} \cdot \hat{\mathbf{n}}_{bc}} \right) \Big|^{L^-} s\,ds \\
=& F_{r_i} + F_{s_0} + F_{r^+} + F_{r^-}. \quad \text{(E.23)}
\end{aligned}
$$

Thus our 2D equations give the same heat flux as the 3D equations.

Appendix F

Numerical implementation

F.1   Discretized derivatives

Derivatives are calculated on the grid based on a second order centred finite difference method. These are derived from a Taylor expansion about the point s, keeping up to second derivatives

$$f\left(s + h^+\right) = f(s) + h^+ f'(s) + \frac{(h^+)^2}{2} f''(s) \tag{F.1}$$

$$f\left(s - h^-\right) = f(s) - h^- f'(s) + \frac{(-h^-)^2}{2} f''(s) \tag{F.2}$$

$$f'\left(s + \frac{h^+}{2}\right) = f'(s) + \frac{h^+}{2} f''(s) \tag{F.3}$$

$$f'\left(s - \frac{h^-}{2}\right) = f'(s) - \frac{h^-}{2} f''(s). \tag{F.4}$$

Here $h^\pm$ is the grid spacing in the positive/negative direction from s, which in general is allowed to vary for a non-homogeneously spaced grid.

The difference of equations F.1 and F.2 gives

$$f'(s) = \frac{f(s + h^+) - f(s - h^-)}{h^+ + h^-} - \left(\frac{(h^+)^2 - (h^-)^2}{2(h^+ + h^-)}\right) f''(s), \qquad \text{(F.5)}$$

while the difference of equations F.3 and F.4 yields

$$f''(s) = \frac{f'(s + \frac{h^+}{2}) - f'(s - \frac{h^-}{2})}{\left(\frac{h^+}{2} + \frac{h^-}{2}\right)}. \qquad \text{(F.6)}$$

Substituting the former into the latter gives

$$
\begin{aligned}
f''(s) = & \frac{2}{(h^+ + h^-)} \left(\frac{f\left(s + \frac{h^+}{2} + \frac{h^+}{2}\right) - f\left(s + \frac{h^+}{2} - \frac{h^+}{2}\right)}{\left(\frac{h^+}{2} + \frac{h^+}{2}\right)}\right) \\
& - \frac{2}{(h^+ + h^-)} \left(\frac{\left(\frac{h^+}{2}\right)^2 - \left(\frac{-h^+}{2}\right)^2}{2\left(\frac{h^+}{2} + \frac{h^+}{2}\right)}\right) f''\left(s + \frac{h^+}{2}\right) \\
& - \frac{2}{(h^+ + h^-)} \left(\frac{f\left(s - \frac{h^-}{2} + \frac{h^-}{2}\right) - f\left(s - \frac{h^-}{2} - \frac{h^-}{2}\right)}{\left(\frac{h^-}{2} + \frac{h^-}{2}\right)}\right) \\
& + \frac{2}{(h^+ + h^-)} \left(\frac{\left(\frac{h^-}{2}\right)^2 - \left(\frac{-h^-}{2}\right)^2}{2\left(\frac{h^-}{2} + \frac{h^-}{2}\right)}\right) f''\left(s - \frac{h^-}{2}\right) \\
= & \frac{2}{(h^+ + h^-)} \left(\left(\frac{f(s + h^+) - f(s)}{h^+}\right) - \left(\frac{f(s) - f(s - h^-)}{h^-}\right)\right) \\
= & \frac{2}{(h^+ + h^-)} \left(\frac{f(s - h^-)}{h^-} + \frac{f(s + h^+)}{h^+}\right) - \frac{2f(s)}{h^+ h^-}. \qquad \text{(F.7)}
\end{aligned}
$$

Substituting this back into equation F.5 for the first derivative gives

$$f'(s) = \frac{f(s + h^+) - f(s - h^-)}{h^+ + h^-} - \left(\frac{(h^+)^2 - (h^-)^2}{2(h^+ + h^-)}\right) f''(s)$$

$$=\frac{f(s+h^+)-f(s-h^-)}{h^++h^-}$$
$$-\left(\frac{(h^+-h^-)(h^++h^-)}{2(h^++h^-)}\right)\left(\frac{2}{(h^++h^-)}\left(\frac{f(s-h^-)}{h^-}+\frac{f(s+h^+)}{h^+}\right)\right)$$
$$+\left(\frac{(h^+-h^-)(h^++h^-)}{2(h^++h^-)}\right)\frac{2f(s)}{h^+h^-}$$
$$=\left(\frac{1}{h^++h^-}\right)\left(f(s+h^+)-f(s-h^-)\right)$$
$$-\left(\frac{h^+-h^-}{h^++h^-}\right)\left(\frac{f(s-h^-)}{h^-}-\frac{(h^++h^-)f(s)}{h^+h^-}+\frac{f(s+h^+)}{h^+}\right)$$
$$=-\left(\frac{1}{h^++h^-}\right)\left(\frac{h^-+h^+-h^-}{h^-}\right)f(s-h^-)+\frac{(h^+-h^-)}{h^+h^-}f(s)$$
$$+\left(\frac{1}{h^++h^-}\right)\left(\frac{h^+-(h^+-h^-)}{h^+}\right)f(s+h^+)$$
$$=-\left(\frac{h^+}{h^-(h^++h^-)}\right)f(s-h^-)+\left(\frac{h^+-h^-}{h^+h^-}\right)f(s)$$
$$+\left(\frac{h^-}{h^+(h^++h^-)}\right)f(s+h^+)$$
$$=\frac{\left(-(h^+)^2 f(s-h^-)+(h^-)^2 f(s+h^+)\right)}{h^+h^-(h^++h^-)}+\left(\frac{h^+-h^-}{h^+h^-}\right)f(s). \qquad (F.8)$$

Thus the first and second derivatives in s are evaluated on the grid, respectively, by

$$f'(s)=\frac{\left(-(h^+)^2 f(s-h^-)+(h^-)^2 f(s+h^+)\right)}{h^+h^-(h^++h^-)}+\left(\frac{h^+-h^-}{h^+h^-}\right)f(s), \quad (F.9)$$
$$f''(s)=\frac{2}{(h^++h^-)}\left(\frac{f(s-h^-)}{h^-}+\frac{f(s+h^+)}{h^+}\right)-\frac{2f(s)}{h^+h^-}. \qquad (F.10)$$

F.2   Axisymmetric non-linear terms

If only the axisymmetric component of a non-linear term is required, it can be calculated directly without having to perform any costly Fourier transforms. As shown in Section 4.3, only the cross products of Fourier coefficients in which

$l = m + n = 0$, or $n = -m$, where m and n are the spectral modes of the two variables being multiplied, contribute to the axisymmetric mode. The amplitude of the axisymmetric component of the product is thus

$$\overline{h(\phi)} = \overline{f(\phi)g(\phi)}$$

$$= h_0$$

$$= \sum_{m=-M_{max}}^{+M_{max}} (f_{-m}g_m)$$

$$= f_0g_0 + \sum_{m=1}^{+M_{max}} (f_{-m}g_m + f_m g_{-m})$$

$$= f_0g_0 + \sum_{m=1}^{+M_{max}} (f_m^* g_m + f_m g_m^*)$$

$$= f_0g_0 + \sum_{m=1}^{+M_{max}} 2\Re(f_m g_m^*)$$

$$= f_0g_0 + \sum_{m=1}^{+M_{max}} 2(\Re(f_m)\Re(g_m) + \Im(f_m)\Im(g_m)). \qquad \text{(F.11)}$$